Study of delta-doped quantum wells

Energy levels and applications in the terahertz region

Volodymyr Akimov
Anton Tiutiunnyk
Roman Demediuk
Viktor Mykolayovych Tulupenko
Erika Yazmin Soto Gómez
Juan Camilo Cortés Peñaranda
Pedro Alejandro Orellana Dinamarca
Judith Helena Ojeda Silva
John Alexander Gil Corrales
José Carlos León González
Rafael Guillermo Toscano Negrette
Dahana Caicedo Paredes
Miguel Eduardo Mora Ramos
Juan Carlos Martínez Orozco
Ricardo León Restrepo Arango
Álvaro Luis Morales Aramburo
Carlos Mario Duque Jiménez
Carlos Alberto Duque Echeverri

©2022 Editorial Instituto Antioqueño de Investigación
Medellín – Antioquia

Study of delta-doped quantum wells

Energy levels and applications in the terahertz region

First Edition

Volodymyr Akimov
Anton Tiutiunnyk
Roman Demediuk
Viktor Mykolayovych Tulupenko
Erika Yazmin Soto Gómez
Juan Camilo Cortés Peñaranda
Pedro Alejandro Orellana Dinamarca
Judith Helena Ojeda Silva
John Alexander Gil Corrales
José Carlos León González
Rafael Guillermo Toscano Negrette
Dahana Caicedo Paredes
Miguel Eduardo Mora Ramos
Juan Carlos Martínez Orozco
Ricardo León Restrepo Arango
Álvaro Luis Morales Aramburo
Carlos Mario Duque Jiménez
Carlos Alberto Duque Echeverri

ISBN: 978-628-95135-1-6

©2022 Editorial Instituto Antioqueño de Investigación
Medellín – Antioquia

Catalogación en la publicación – Biblioteca Nacional de Colombia

Akimov, Volodymyr, autor
Study of delta-doped quantum wells: Energy levels and applications in the terahertz region / Volodymyr Akimov [y otros diecisiete]. -- First edition. – Medellín: Editorial Instituto Antioqueño de Investigación, 2022.
1 recurso en línea : archivo de texto: PDF.

Incluye datos curriculares de los autores -- Incluye referencias bibliográficas

ISBN 978-628-95135-1-6

1. Puntos cuánticos 2. Semiconductores 3. Electrónica cuántica 4. Radiación I. Tiutiunnyk, Anton, autor II. Demediuk, Roman, autor III. Mykolayovych Tulupenko, Viktor, autor IV. Soto Gómez, Erika Yazmin, autor V. Cortés Peñaranda, Juan Camilo, autor VI. Orellana Dinamarca, Pedro Alejandro, autor VII. Ojeda Silva, Judith Helena, autor VIII. Gil Corrales, John Alexander, autor IX. León González, José Carlos, autor X. Toscano Negrette, Rafael Guillermo, autor XI. Caicedo Paredes, Dahana, autor XII. Mora Ramos, Miguel Eduardo, autor XIII. Martínez Orozco, Juan Carlos, autor XIV. Restrepo Arango, Ricardo León, autor XV. Morales Aramburo, Álvaro Luis, autor XVI. Duque Jiménezm Carlos Mario, autor XVII. Duque Echeverri, Carlos Alberto, autor XVIII.

CDD: 621.38152 ed. 23 CO-BoBN– a1100732

Investigación Científica
ISBN: 978-628-95135-1-6
DOI:
Hecho el depósito legal digital

Study of delta-doped quantum wells - Energy levels and applications in the terahertz region
Serie: Ingeniería y Ciencia
Editorial Instituto Antioqueño de Investigación
Edición 1: Octubre 2022
Publicación electrónica gratuita

©2022 Instituto Antioqueño de Investigación IAI™. Salvo que se indique lo contrario, el contenido de esta publicación está autorizado bajo Creative Commons Licence CC BY-NC-SA 4.0 (https://creativecommons.org/licenses/by-nc-sa/4.0/)

Editorial Instituto Antioqueño de Investigación es Marca Registrada del Instituto Antioqueño de Investigación. El resto de marcas mencionadas en el texto pertenecen a sus respectivos propietarios.

La información, hallazgos, puntos de vista y opiniones contenidos en esta publicación son responsabilidad de los autores y no reflejan necesariamente los puntos de vista del Instituto Antioqueño de Investigación IAI; no se garantiza la exactitud de la información proporcionada en este texto.

Ni los autores, ni la Editorial, ni el IAI serán responsables de los daños causados, o presuntamente causados, directa o indirectamente por el contenido en este libro.

Maquetación: Instituto Antioqueño de Investigación IAI
Diseño, edición y publicación: Editorial Instituto Antioqueño de Investigación
Financiador de la publicación: Universidad de Antioquia

Instituto Antioqueño de Investigación IAI
http://fundacioniai.org
contacto@fundacioniai.org

Editorial Instituto Antioqueño de Investigación
http://fundacioniai.org/index.php/editorial.html
editorial@fundacioniai.org

Universidad de Antioquia
https://www.udea.edu.co
cduque_echeverri@yahoo.es
alvaro.morales@udea.edu.co

©2022 Editorial Instituto Antioqueño de Investigación
Medellín – Antioquia

Preface

Quantum wells, quantum wires, quantum dots. These are terms that have become familiar not only to specialists in physics and semiconductor technology but also to the common public. But these structures of nanoscopic dimensions appeared several decades ago in the vision of renowned specialists in these materials and, as a reality, after it was possible to develop epitaxial crystal growth techniques and methodologies that allow ultra-precise control of the deposition of atomic monolayers. The 1980s witnessed a steady increase in research work on these structures. The subsequent decades have seen the consolidation of a branch that has redefined solid-state physics and, in particular, semiconductor physics.

Although these three classes of systems began to be studied, at least from a theoretical point of view, almost simultaneously, the attention of the first years was much more inclined towards quantum wells. These semiconductor heterostructures with rectangular profiles or other geometric shapes obtained through the use of modulation in the composition, guarantee a spatial confinement for the movement of charge carriers along one direction by combining semiconductor materials with different bandgap widths. For this reason, they are often referred to as quasi-two-dimensional quantum systems. A multitude of theoretical and experimental works have allowed a broad knowledge of its properties to be achieved and allowed the development of various applications in the fields of electronics and optoelectronics. Thus, the first and fourth chapters of this book deal with particularities of the study of charge carrier states in semiconductor quantum wells. In chapter 1 the authors deal with the case in which the potential energy profile in the conduction band of these heterostructures is affected by the presence of a high-density donor doping spread over a very narrow region both inside and out, at the edges of the potential well (deltaic doping). In this situation, the characteristics of the optical response in the THz range associated with the electron states in the system, taking into account the influence of elements such as the application of electric fields and the change in the concentration of ionized impurities in the doping region. Considering the particular case of Si-Ge quantum wells, a new class of modeling device is proposed that would work in the mentioned spectral zone.

A key element in determining the electronic structure of semiconductor quantum wells is to solve the characteristic differential problem for the envelope wave function within the effective mass formalism. This also means finding the eigenvalues of the corresponding energy operator. When the geometry of the potential profile departs from the model of abrupt interfaces with rectangular quantum wells, the analytical solution of this problem reduces to some very specific cases in terms of special functions of Mathematical Physics. In a vast majority of situations, quantum states must be obtained by computational numerical schemes. Chapter 4 details the procedure known as the Numerov method, which is particularly suitable for solving second-order ordinary differential equations of the Schrödinger type, leading to an equivalent matrix problem from which the allowed states of energy result when solving the problem of corresponding eigenvalues. Using several typical examples, the authors explain the algorithm and show how it works. Furthermore, they provide the complete Python code to the interested reader.

Further progress in crystal growth methods made it possible to produce structures in which the movement of charge carriers in the nanostructure is restricted in two or three spatial directions. In this way, the possibility of having unlimited displacement is reduced to one dimension (in the case of quantum wires) or to none. In this last situation, the energy spectrum is completely discrete and we have what have been called quantum dots. Given this circumstance, we can speak of systems whose behavior is equivalent to a kind of artificial atoms. Given their unusual properties, ideas about the applications of quantum dots in practical life go beyond electronics and optoelectronics and reach areas such as biomedicine. Chapter 2 briefly describes some properties of quantum transport through quantum dots and quantum wires. In this framework, the transmission probability in a quantum wire system with an impurity (or quantum dot) is calculated through the tight-binding method. These same transport properties can be treated with various formalisms.

The use of Green's functions in the most diverse areas of Physics has made it possible to provide accurate theoretical explanations for many phenomena inherent to this science. Its use allows the determination of electronic, optical, thermal, transport and other properties in solid systems and also in the case of semiconductor nanostructures. Chapter 3 of this book is dedicated to exposing in sufficient detail the use of this formalism to investigate quantum transport properties -in particular the so-called transmission probability- in ensembles of two or three quantum dots with different geometries.

Speaking of optical properties, it should be noted that in semiconductor nanostructures the nonlinear components of the response of each system to the incidence of light usually have remarkably large amplitudes compared to the bulk semiconductors themselves. Moreover, in several of these systems, the characteristics of the energy spectrum allow theoretical descriptions analogous to those used to explain the optical response of atoms or molecules. A nonlinear optical property that often occurs in semiconductor nanostructures is electromagnetically induced transparency. In the chapter 5 of the book, the authors have decided to give a detailed description of the derivation process of the expressions that allow evaluating the dielectric susceptibility in a system of three energy levels coupled to two external electromagnetic fields in the configuration typically known as type-λ. This kind of treatment is relevant to investigate this kind of nonlinear phenomenon in wells and quantum dots.

In the final chapter have described the procedure for corrections of first and third order to the optical absorption and changes in the refractive index for two-level system. Clearly in a multi-level system should make a sum over all possible transitions involving all initial and final states. In that case it is very important to consider the occupation of levels considering the statistic that applies to the case of low temperatures or finite values of temperature.

Readers interested in the topics presented in this book will be able to find information, in several cases, detailed on different methods and procedures to study the electronic structure of low-dimensional semiconductor nanostructures and for the calculation of optical and transport properties in said systems.

Miguel Eduardo Mora Ramos
Cuernavaca, Estado de Morelos, México
March 2022

Cite this book as following: V. Akimov, A. Tiutiunnyk, R. Demediuk, V. Tulupenko, E. Soto-Gómez, J. C. Cortés-Peñaranda, P. A. Orellana, J. H. Ojeda, J. A. Gil-Corrales, J. C. León-González, R. G. Toscano-Negrette, D. Caicedo-Paredes, M. E. Mora-Ramos, J. C. Martínez-Orozco, R. L. Restrepo, A. L. Morales, C. M. Duque, and C. A. Duque. Study of delta-doped quantum wells: Energy levels and applications in the terahertz region. Editorial Instituto Antioqueño de Investigación, Medellín-Antioquia, Colombia (2022).

About the authors

Volodymyr Akimov

it-ogo@yandex.ru

University of Medellin, Colombia.

Born in Kramatorsk, Donetsk region, USSR. In 1998 obtained the title of Systems Engineer in the specialty of Computer Aided Design Systems, at the Donbass State Engineering Academy DSEA, Kramatorsk, Ukraine. Subsequently, did postgraduate studies in the Physics Department of the DSEA, and worked as an engineer, assistant professor, junior researcher, and senior professor in the Department of Information Technologies and the Physics Department of the DSEA. Between 2003 and 2005 worked as a researcher at the University of Lecce, Italy, now the University of Salento, in the Department of Innovation Engineering. The work has been carried out within the framework of the European Union Project Single PrOTein NanObioSEnsor griD array IST-2001-38899-SPOT-NOSED. In 2011 obtained a doctorate degree in biophysics from Kharkiv V. N. Karazin National University, Ukraine. Until August 2014 worked as a professor at the Department of Information Technologies at DSEA, Kramatorsk, Ukraine. From September 2014 to December 2016, worked as a postgraduate researcher at the University of Antioquia, Colombia. From February 2016 to date, works as a full-time professor at the University of Medellín, Colombia.

Anton **Tiutiunnyk**

tyutyunnyk.a.m@academicos.uta.cl

University of Tarapaca, Chile.

Ph.D. in Physics, University of Antioquia (Colombia). Master in Applied Physics, The Yuriy Fedkovych National University of Chernivtsi (Ukraine)

Roman **Demediuk**

demediuk.roman@gmail.com

Donbass State Engineering Academy, Ukraine.

Candidate of Science (comparable to the Academic Degree of Doctor of Philosophy), V.Ye. Lashkaryov Institute of Semiconductor Physics of National Academy of Sciences of Ukraine. Master of mathematics, Donbass State Pedagogical University (Ukraine).

Viktor Mykolayovych Tulupenko

viktor.tulupenko@gmail.com

Head of the Department of Physics and Laboratory of Solid State Quantum Electronics in the Donbass State Engineering Academy, Kramatorsk, Ukraine. Official Physics Expert of the Ministry of Science and Education and the Foundation for Fundamental Research of Ukraine. Member of Condensed Matter Group-UdeA, Colombia. Master of Radiophysics from Donetsk State University, Ukraine. PhD in Semiconductor Physics and Dielectrics of the Leningrad Polytechnic Institute, Russia. Doctor of Physics and Mathematics Sciences, Kyiv National University, Ukraine.

Erika Yazmín Soto Gómez

erikayazmin.soto@uptc.edu.co

Pedagogical and Technological University of Colombia UPTC, Colombia.

Physics, Master in Sciences-Physics and Ph.D student in Sciences-Physics. She has experience as a professor of physics, research and formulation of projects on dye-sensitized solar cells. She is linked to the research groups Química-Física Molecular y Modelamiento Computacional (QUIMOL) of the UPTC and Ciencias Básicas Aplicación e Innovación (CIBAIN) of the Unitópico. Her research areas are molecular electronics, quantum transport and electrical, thermal and magnetic properties in low-dimensional systems, also studies on organic molecular systems and their applications in photovoltaic devices.

Juan Camilo Cortés Peñaranda

juancamilo.cortes@uptc.edu.co

Pedagogical and Technological University of Colombia UPTC, Colombia

Physicist and Master of Science-Physics student at the Pedagogical and Technological University of Colombia. Research area in molecular electronics and quantum dots, studies of electrical, thermal and magnetic transport properties applying the Green Functions method.

Pedro Alejandro Orellana Dinamarca

pedro.orellana@usm.cl

Technical University Federico Santa María (USM), Chile

Bachelor in Physics PUC 1989. Ph.D. in Physics from the Pontificia Universidad Católica de Chile (PUC) (1994). Actually, he is a full professor at the USM; 1997 - 2013 Associated Professor Universidad Católica del Norte (UCN) - Antofagasta; 1996 Postdoctoral researcher at USACH- Chile; 1995 Postdoctoral researcher at CNPqRj-Brazil. His research line is Electronic Transport and Photonics in the Nanoscale.

Judith Helena Ojeda Silva

judith.ojeda@uptc.edu.co

Pedagogical and Technological University of Colombia UPTC, Colombia.

Bachelor of Science in Physical Education and Mathematics, Specialist in Physics Teaching, Master of Science in Physics, Doctor of Science in Physics, Postdoctoral Experience at the University of Tarapacá, Chile. Actually, she is a titular professor at the Universidad Pedagógica y Tecnológica de Colombia; at the same university: April 2018 and April 2021 coordinator of the Ph.D. and M.Sc. postgraduate programs in Physical Sciences; February 2016 - August 2018 coordinator of the M.Sc. in Physical Sciences; February 2015- February 2016 director Physics Department; January 2014 Postdoctoral researcher at Universidad de Tarapacá, Chile; August 2010 - December 2013 director of the Postgraduate School of the Faculty of Sciences; January 2004 - June 2012 Assistant Professor; January 2003 - December 2003 Assistant professor at Universidad de Cundinamarca, Colombia; January 2002 - December 2002 Auxiliary professor at Universidad Santo Tomás, Colombia. Her research lines are Quantum Transport, spintronics, molecular systems, electrical and magnetic properties in low dimensional systems. She is affiliated to the research groups: Materials Physics Group and the Chemistry-Molecular Physics and Computational Modeling Group Quimol of the UPTC, and to the Condensed Matter Group of the University of Antioquia.

John Alexander Gil Corrales

jalexander.gil@udea.edu.co

University of Antioquia, Colombia.

Physicist from the University of Antioquia and Ph.D. in Physics from the same college. He is a member of the Condensed Matter-UdeA group, where he has developed works on characterization of low-dimensional structures and analysis of electronic transport properties in heterostructures, among others.

Juan Carlos Martínez Orozco

jcmartinez@uaz.edu.mx

Autonomous University of Zacatecas UAZ, México.

Has a degree in Physics from the Autonomous University of Zacatecas (UAZ) in 2000 and a Doctor of Science (Physics) from the Autonomous University of the State of Morelos, in its direct Doctorate modality, obtaining the degree in August 2007 and He made a postdoctoral stay in 2014, through the CONACyT project, at the University of Antioquia, in Medellín, Colombia and is currently assigned to the Physics Academic Unit of the UAZ. Product of his academic and research activities, among which are around 50 undergraduate and postgraduate courses, director of four doctoral theses (one more in process), two master's theses (four in process) and about a dozen undergraduate level.

He has published more than 60 internationally indexed research articles and about 15 extensive publications. Which have earned him recognition as a member of the national system of researchers at level II and his admission to the Mexican Academy of Sciences in 2019. Finally, in the management part, Dr. Martínez Orozco has been technically responsible for at least 5 research projects of both the SEP and CONACyT. He is coordinator of the Doctorate in Basic Sciences at the Autonomous University of Zacatecas, served as president of the solid-state division of the Mexican Society of Physics in the period 2017-2018 and is a member of the Mexican Society of Physics, of the American Society of Physics, of the Mexican Society of Materials, of the Colombian Society of Physics, among others.

José Carlos León González

jose.leong@udea.edu.co

University of Antioquia, Colombia.

He was born in the city of Montería, Colombia, where he studied primary and secondary school at the Villa Cielo educational institution. He entered the University of Córdoba to study Physics. He is currently doing Ph.D. studies in Physics at the University of Antioquia, where he studies the properties of low-dimensional semiconductor heterostructures. In addition, he is a professor at the University of Córdoba, Colombia.

Rafael Guillermo Toscano Negrette

rafael.toscano@udea.edu.co

University of Antioquia, Colombia.

I was born in the city of Montería-Cordoba in 1993. I began my training in secondary school at the municipality of Puerto Escondido-Córdoba, and I finished secondary school at the Mercedes Abrego institution, in the city of Cartagena-Bolívar. In 2011 I entered the University of Córdoba to study Physics, and in July 2017 I received the diploma that accredited me as a professional in Physics. In the year 2020, motivated to learn and delve deeper into physics, I began my Ph.D. studies in Physics at the University of Antioquia, where I am currently studying. In the workplace, in August 2017, I started working as a laboratory assistant at the University of Córdoba, and I am currently working in the same place.

Dahana Caicedo Paredes

dahana.caicedo@udea.edu.co

University of Antioquia, Colombia.

She was born in Bajo Baudó, Chocó, on December 27, 1997. She is the sixth daughter of seven siblings, her father is a fisherman and her mother is a laboratory assistant.

At the age of 17, she moved to the city of Medellin to study materials engineering at the University of Antioquia, she is about to graduate. She was part of the Condensed Matter research group between the years 2019-2021. Among her hobbies are playing sports, cooking, traveling, reading and spending time with her loved ones.

Miguel Eduardo Mora Ramos

memora@uaem.mx

Autonomous University of Morelos State UAEM, México

Born in Havana, Cuba. Major in physics (B. Sc., 1984) AND Ph.D in physics (1995) from University of Havana. Assistant professor of theoretical physics, University of Havana (1984-1996). Associate professor of theoretical physics, autonomous University of Zacatecas, Mexico (1996-1997). Associate researcher, center for optical research, Aguascalientes, Mexico (1997-1998). Professor (full) of theoretical physics and mathematics (UAEM, 1998-), since 1998 full pro.

Ricardo León Restrepo Arango

ricardo.restrepo@eia.edu.co

EIA University, Colombia.

Physicist, Master in Physics and Doctor in Physics. He is director of the EIA-Theoretical and Applied Physics research group, and a member of the Colombian Physics Society. His areas of interest are Condensed Matter Physics, Interaction of light with matter, photonics.

Álvaro Luis Morales Aramburo

alvaro.morales@udea.edu.co

University of Antioquia, Colombia.

Academic degrees Physicist, M.Sc. In Physics, Ph.D. in Physics. Member of the Condensed Matter-UdeA and Solid State groups at Universidad de Antioquia. Docent/researcher at Universidad de Antioquia since 1970. Member of the Colombian Academy of Exact, Physical, and Natural Sciences.

Carlos Mario Duque Jiménez

cduque1987@gmail.com

Max Planck Institute of Molecular Cell Biology and Genetics, Germany.

Physicist, Master in Physics, Ph.D. in Physics, Ph.D. University of Massachusetts Amherst, USA.

Carlos Alberto Duque Echeverri
carlos.duque1@udea.edu.co
University of Antioquia, Colombia.

Ph.D. in Physics, Universidad del Valle. Master in Physics, University of Antioquia. Undergraduate Physicist, University of Antioquia. Coordinator of the Condensed Matter Group-UdeA.

Table of Contents

1 Adjusting energies of intersubband optical transitions in delta-doped quantum wells 1

1.1 Introduction 1

1.1.1 Semiconductor quantum wells 2

1.1.2 Intersubband transitions in QWs 3

1.1.3 THz radiation 5

1.1.4 Impurities in semiconductor nanostructure optical devices 7

1.1.5 Concept of the new kind of tunable THz device 8

1.1.6 General and specific objectives 10

1.2 Object 11

1.2.1 SiGe quantum wells structure 11

1.2.2 Assumptions and limitations 13

Delta-layer Impurity concentration 13

Internal stress in the well material 15

Central cell effect 16

1.3 Methods 16

1.3.1 Energy subband positions and wave functions . 16

1.3.2 Fermi level 18

1.3.3 Hartree potential 19

1.3.4 Impurity binding energy 19

1.3.5 Self-consistent method 22

1.3.6 Particular case: background impurities 23

Fermi level 23

Modification of the algorithm 27

1.3.7 Linear and nonlinear optical effects based on intersubband transitions 29

1.3.8 Many-body effects 30

1.4 Results and discussion 31
1.4.1 Energy positions and wave functions 31
1.4.2 Linear absorption peak changes. Estimation of tuning ranges. 34
1.4.3 Influence of nonlinearity on the absorption and refraction 39
1.4.4 New type of THz modulator 41
1.4.5 Influence of transversal electric field 45
1.4.6 Influence of background impurity 49
Transition to the limit of undisturbed rectangular QW 49
Results at temperature 4K 50
Higher temperatures. IBEs and the electron concentrations 52
Energy distances at higher temperatures 56
Shallower QW 57
1.5 Conclusions 58
References 61

2 Review: A Look Into QD and QW 70
2.1 A brief introduction to electronic transport through quantum dots and wires 70
2.2 Review and analysis of electronic transport through a quantum wire (QW) with an impurity or quantum dot (QD). 72
References 86

3 Green's functions and Quantum transport properties 89
3.1 Introduction to Green's functions 89
3.2 Properties of quantum transport through systems with QD_s and QW using Green's functions. 95
3.2.1 Transmission probability through a quantum dot (QD). 95
3.3 Transmission probability through two QD_s. 97
3.4 Comparison with a system of wells and barriers 104
3.5 One-dimensional system of three QD_s 107
3.6 T-shaped System with two QD_s between leads. 112

3.7 T-shaped System with three QD_s between leads. 116
3.8 Three-QD_s system with cross-coupling-leads at the intermediate site 120
References 124

4 Derivation and Applications of the Numerov Method 127
4.1 Definition and derivation of the method 127
4.1.1 Application of the method to the one-dimensional Schr¨odinger equation 130
4.2 Application of the method to quantum wells of different shapes 131
4.2.1 Finite Potential Well 131
4.2.2 V-shaped Potential Well 133
4.2.3 Parabolic Potential 135
4.2.4 Asymmetric Potential Well 137
4.2.5 Sawtooth potencial 139
4.3 Conclusions 141
4.4 Algorithm implementation 141
References 146

5 Electromagnetically Induced Transparency (EIT) 148
References 163

6 Nonlinear optical properties 164
6.1 Introduction 164
6.2 Density Matrix Equations 164
6.3 Linear and non-linear absorption coefficients 172
6.4 Linear and non-linear changes in the refractive index . 175
6.5 Non-linear optical rectification, second and third harmonic generator 177
References 180

Chapter 1

Adjusting energies of intersubband optical transitions in delta-doped quantum wells

List of abbreviations

1D – 1-dimensional
2D – 2-dimensional
2DEG – 2-dimensional electron gas
3D – 3-dimensional
BI – Background Impurities
CVD – Chemical Vapor Deposition
IBE – Impurity Binding Energies
IR – Infrared
MBE – Molecular Beam Epitaxy
ME – Matrix Element
MQW – Multiple Quantum Wells
QCL – Quantum Cascade Laser
QW – Quantum Well
QWIP – Quantum Well Infrared Photodetectors
THz – Terahertz
WF – Wave Function

1.1 Introduction

A new configuration of semiconductor quantum well optical devices based on intersubband optical transitions is proposed. The idea of

doping into the well allows tuning energy separations between size-quantized levels (that is the working frequency of the device) by controlling the degree of impurity ionization. The proposed idea is grounded by the extensive numerical study of a $Si_{0.8}Ge_{0.2}/Si$ structures with a number of varying parameters including geometrical ones. Self-consistent calculations that include a calculation of impurity binding energy as a part of iteration are used as a method. The positions and wave functions of size quantized energy levels within quantum well are found and studied as well as linear and non-linear absorption coefficient and refractive index change connected with intersubband transitions.

1.1.1 Semiconductor quantum wells

Semiconductor heterostructures are monosrystallic compositions of different semiconductor materials with the same type of crystal lattice. They are produced using such technologies as Molecular Beam Epitaxy [1] and Chemical Vapor Deposition [2] and made in the way that inside a crystal there are regions of different materials. The materials have different bandgap and form heterojunctions. The difference of the bandgap on the border of the regions with different materials provide a band discontinuity. The technologies and activity to obtain semiconductor heterostructures with a given geometrical parameters is called Bandgap Engineering. The relative positions of the band edges of the materials forming the heterojunction is usually treated as the fundamental property of the material couple [3]. For the simplicity and specificity in the following explanations, we speak about the conduction band only and neglect the valence band. If the materials (1) form three plane layers, (2) the width of the second (central) layer is comparable to de Broglie wavelength of the conduction electron and (3) conduction band edges of the first and the third (bordering) layers are higher in energy than the one of the central layer, than the conduction band, energy profile forms a well (see Fig. 1.1). Here bordering materials form barriers and central material forms potential well. In the well, the conduction electrons may have states quantized in one direction (perpendicular to the layer) and continuous in two other spatial dimensions. Such electronic structure is called Quantum Well (QW). The direction perpendicular to the layers is called

heterostructure growth direction (for technological reasons) and traditionally denoted as z-direction. The dimensions in plane of QW are denoted as x and y. The electrons moving in (x,y) plane and confined in z-direction within the QW are called **quasi** two-dimensional electron gas in analogy to three-dimensional electron gas in bulk semiconductor crys-tals. The 2D continuum of electronic states attached to the specific size-quantized level is called a subband. So the quantum well forms a number of size-quantized subbands that can be filled with 2DEG in addition to 3D continuum of electronic states in the bulk crystal.

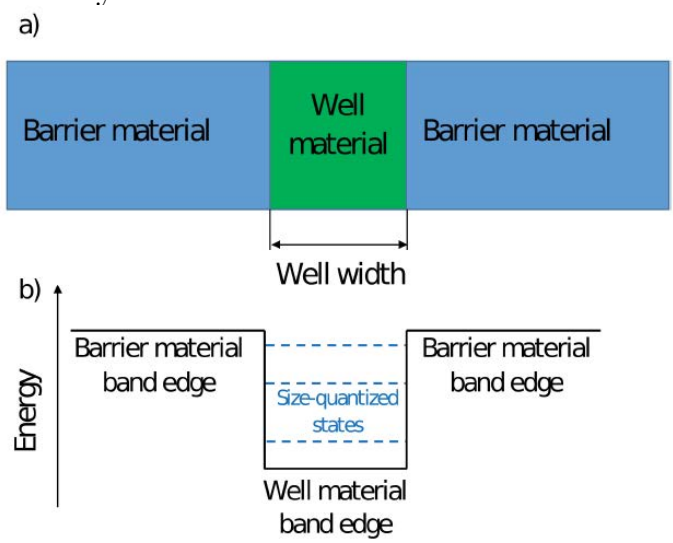

Figure 1.1: Semiconductor quantum well heterostructure (a) and its conduction band energy profile (b).

Applications of the semiconductor heterostructures [4] can be divided in two big groups, namely production of electronic and optical devices. The most commonly known example of semiconductor optical device are light-emitting diodes (LEDs) [5]. Electronic applications covers among the others monolithic integrated circuits or computer chips.

1.1.2 Intersubband transitions in QWs

Most optical devices based on semiconductor heterostructures exploit interband transitions. That is the transitions between valence and conduction bands. Energies of such transitions are determined mainly by the bandgap of the material. However, optical transitions between the different states within the same band (intraband transitions [6])

are also possible. A particular kind of intraband electronic transitions are optical transitions between the quantum wells subbands [7], which are called intersubband optical transitions. Here "optical" means that the transition occurs with the absorption or emission of a photon (see Fig. 1.2) so that such transitions have the influence on the absorption or emission spectra of the semiconductor heterostructure and can be used to construct an optical device.

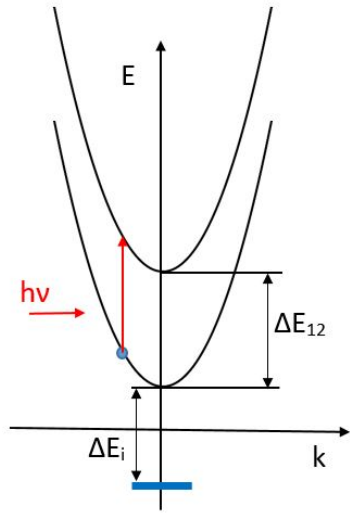

Figure 1.2: Absorptive intersubband optical transition. E – energy, k – wave vector, lower horizontal fat line – impurity state, parabolas – dispersion of subbands, ΔE_i – impurity binding energy, ΔE_{12} – energy distance between two lower subbands, h ($= \Delta$ E $_{12}$) – photon energy.

One can speak about two most important types of quantum well-based optical devices on intersubband transitions: Quantum Well Infrared Photodetectors [8] (passive ones, based on absorption) and Quantum Cascade Lasers [9, 10] (active ones, based on stimulated emission). Many implementations of the mentioned designs are commercially available and have many applications. However, they mostly work at one given frequency (in other words lack tunability), which is considered as the crucial disadvantage. Here we propose the way that kind of devices can be tuned by influencing the degree of impurity ionization so that the existing devices can be modified and the new designs of tunable optical devices working in THz regions like filters and modulators can be created.

Notably, in both QWIP and QCL designs the transverse electric field is used (that is the field applied in the direction of QW growth or perpendicular to QW plane).

1.1.3 THz radiation

For the commonly used semiconductor materials the typical working frequencies for the intersubband optical transitions lie between mid IR and TeraHertz ranges. The lower frequencies, namely microwaves and below, normally cannot be obtained with photonic methods and are normally discussed in terms of electronics terminology. Particularly, if we speak in terms of photonics, in case of intersubband transitions if two subbands are so close in energy that the difference corresponds to microwaves (below 300GHz or 1 meV) then the transitions between the subbands are defined by the acoustic phonon rates and the uncertain-ties of different kind (statistical as well as fundamental Heizenberg) does not allow to obtain pronounced peaks in optical properties. The limit of higher energies is defined by the band discontinuities that can be obtained for the given materials. Generally, they are considered about one order of magnitude less than the characteristic bandgap of the materials.

Currently, in the mentioned range, the most attractive for engineers as well as the most problematic technically is the TeraHertz range, which is on the brink between optics and electronics [11], see Fig. 1.3

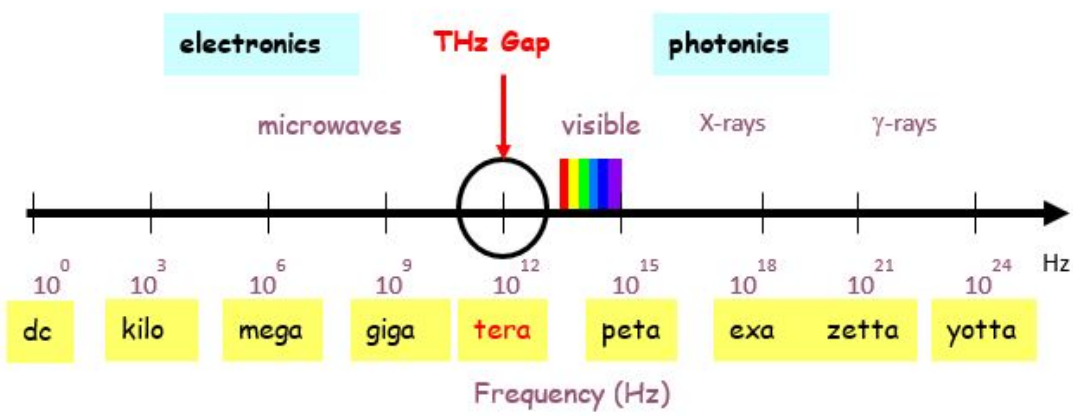

Figure 1.3: TeraHertz frequency range

The term terahertz literally implies the frequency $= 1$ THz $= 10^{12}$ Hz and accordingly, the period 10^{-12} s $= 1$ ps. The corresponding vacuum wavelength is 300 µm and wave number is 33.3 cm^{-1}. The energy of 1 THz photon is 4.1meV and equivalent temperature is T = 48K. The THz range has no strict definition in the literature as the different authors refer to the different ranges. Some consider THz range to be from

0.1 to 10 THz (with wavelength from 3 mm to 30 µm), others define it between 0.1 and 50 THz. Other definitions are also possible. We believe that the most appropriate would be the range with wavelength from 0.4 mm to 40 µm or with frequencies from 0.75 THz to 7.5 THz. On the one hand, it completely covers the band of a so-called THz gap. And on the other hand, there are physical reasons for the individualization of the very mentioned spectral band. The point is that on both sides of the frequency (wavelength) range different physical approaches for creating active devices, which depend on the value of wavelength, are used. The long-wavelength edge borders to the part of the entire electromagnetic wave spectrum (sometimes it is also called as a submillimeter range), which within the concept of the wave-particle duality, fits the definition of a wave rather than a particle. Accordingly, classical electronic ways of generation of electromagnetic radiation (in which the radiation is treated as an electromagnetic wave) are efficiently used in submillimeter and in the longer wavelength ranges

The reasons for the peculiarities of THz range are the following. Firstly, it has a small photon energy. At room temperatures the mean kinetic energy of molecules or free electrons in solids or the mean oscillation energy of atoms is 27 meV. At the liquid nitrogen temperature of 77K (which is practically very important) it is about 7 meV. Compare it to the photon energy photon of 1 THz, which is 4.1 meV. Such a relationship makes very difficult the creation of stable inversion population of electrons (or holes) at these temperatures as any carrier distribution is destroyed by the Brownian motion. Also, a large thermal noise in the background makes difficult processing information provided by THz radiation. Actually, most of the energy emitted by the objects at 300K or 77K objects is not in the THz range, and basically, it is quite possible to block this radiation with optical filters. However, any object with non-zero temperature does emit THz radiation. Secondly, radiation in THz range is well absorbed by the atmosphere of the Earth as one can see, for example, in Fig 14 of the paper [12]. The water vapor is the main absorbent for that spectrum. Therefore, the effective propagation of THz radiation in the Earth is limited by the vacuum or specific waveguides. Additionally, the vibrational and rotational spectra of many other molecules are also in THz range. Thirdly,

the THz radiation penetrates through many materials such as ceramics, plastics and dress clothing. And, last but not least, THz photons do not harm human tissue that along with their notable penetrating ability makes THz perspective for use in medicine. That feature is the consequence of the first tree mentioned above, but we put it separately for its practical importance.

THz radiation has many perspective applications in medicine [13–15], security [16–18], atmosphere monitoring [18], material inspection, control of quality [19] etc.

1.1.4 Impurities in semiconductor nanostructure optical devices

The importance of semiconductor nanostructures as both active and passive optical devices in contemporary science and technology is difficult t o o verestimate. T he p roblems c onnected t o t he i mpurity positioning and characteristics Impurity has always been in the center of interest in physics and engineering of semiconductors and semiconductor heterostructures. It determines many key features of a majority of semiconductor devices. (From now on when speaking about semi-conductor heterostructures or nanostructures mainly and by default we will refer to the rectangular semiconductor quantum wells, which are the object of our study.) Technological progress resulted in some shift of attention towards the impurity-related properties. The first task was to increase electron mobility so for that reason the impuri-ties were sought to remove from QW. On the way the principal points were modulation doping [20] and delta-doping to the barrier [21] that allowed to combine the high mobility and high concentration of carri-ers. On the other hand, big oscillator strengths for the optical transi-tions between size-quantized subbands encouraged creation of both the emission-based optical devices (e.g. quantum cascade lasers [9], and absorption-based ones (like quantum well infrared photodetectors [22]. Such structures often are doped heavily, though the impurities played there an auxiliary role. So up to now in our knowledge the action of no actual device is based on the impurity properties in QW. In fact, impurities in quantum well are interesting to study. The impu-rity binding energy is quite sensitive to the changes of practically all the parameters of QW. In the pioneering in this area work [23], the

case of infinitely deep QWs was considered. It was shown that IBE depends both on the well width and on the position of impurity inside the well. Since then was confirmed the IBE dependence on the depth and width of QW [24, 25], the barrier width in case of MQW structures [26], the dispersion law nonparabolicity [27], effective mass difference in the barriers and well [28], the mismatch of dielectric constant between the well and barrier materials [29], and free electrons screening [30, 31]. Also, the influence of many external factors on the IBE, like electric and magnetic fields, uniaxial stress [32–39], hydrostatic strain [40–42], and the incident laser radiation [43–46] was in the focus of attention. Additionally, the effect of temperature was studied by introducing temperature-dependent electron effective masses, dielectric constants and well depth [47–49].

1.1.5 Concept of the new kind of tunable THz device

If we put the delta-layer of impurity inside the quantum well, it may be used as to control the energies of the optical transitions between size-quantized subbands of QW. And that is the way to regulate the working frequencies of the intersubband transitions-based optical devices by an external electric field applied in the plane of the QW. In such a structure without field applied and for the relatively low temperatures, the impurity is not ionized. So there are no carriers and no charged impurity center so the well has a shape designed by the material composition only, like the traditional rectangular shape. When we apply the electric field in QW plane, the current arises and ionizes the impurity in the delta-layer. Initially neutral impurity centers now provide free electrons to the subbands, that spread their negative charge in the border of QW and positive ionized atoms concentrated in the delta-layer. As a result, redistribution of charge in space changes the shape of the structure energy profile as well as the optical transition energies, and, accordingly, the frequency of the peak optical response. The effect is illustrated in Fig. 1.4.

Obviously, the described above effect depends on the number (and fraction) of ionized impurity atoms, that we call the impurity ionization degree, which statistically depends on impurity binding energy

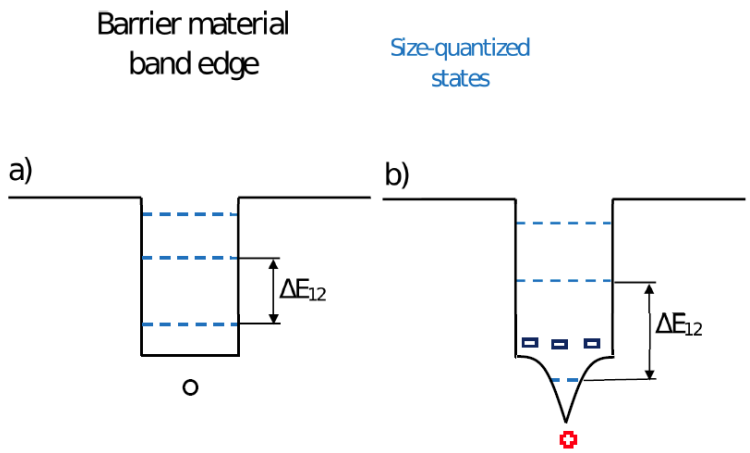

Figure 1.4: QW profile with non-ionized (a) and partly ionized (b) impurity with an impurity delta-layer positioned in the center of the well. ΔE_{12} – energy separation between two lower levels. Black circle – neutral impurity, red cross – ionized impurity centers, blue minuses – electrons in subbands.

(IBE). The bigger is IBE, the more difficult is to ionize the impurity, the less is the ionization degree. In the semiconductor science and engineering for the most purposes, the IBE in the heterostructures is taken equal to the one in corresponding bulk material, which is known for the common semiconductor materials. However, in quantum wells (and other kinds of semiconductor nanostructures), the IBE differs notably from the one of the bulks and depends on the spatial position in the structure [23]. Existing semiconductor devices, based on intersubband optical transitions, normally are doped to the passive regions as it somewhat improves the quality of the structure and allows to avoid calculation complexities. In this case the only function of impurity is to provide free electrons to the structure, and the possible changes in the IBE do not influence much the key characteristics of the device. However, our proposed design implies the varying of the energy profile in the active region with a key factor of ionization degree and the IBE became crucial for correct quantitative and even qualitative description of the device performance.

IBE within the quantum wells of different characteristics and under different external conditions is studied numerically in many works like [50–52] and others. The features that differs our approach from the most of them are the following. First, we use the modified auto consistent method that embeds the calculation of IBE, which is especially impor-tant in our case as the IBE has the crucial influence on the ionization

degree of impurities. The energy profile shape, delta-layer impurity ionization, charge distribution along the growth direction of the structure and IBE are mutually influencing, so we take into account that influence by introducing iterative converging calculation process based on Hartree self-consistent concept. Second, instead of common variational methods it uses an expansion approach and may be used as an independent reference for the comparison to other works.

1.1.6 General and specific objectives

The general objective of this work is the complex numerical study of all the effects and regularities arising in delta-doped within QW semiconductor nanostructures from the point of view of their band and optical properties keeping in mind the final goal to design new types of tunable optical devices based on intersubband transitions between space quantized levels inside such quantum wells. The specific objectives of the work are the following.

1. To propose and ground the materials and geometrical parameters of the semiconductor heterostructure optimal to obtain the tunability effect for THz or/and far IR active and passive optical devices.

2. To design and implement the self-consistent numerical procedure for the simulation of band and optical properties of the delta-doped QW structure that incorporates calculation of impurity binding energy. To define and pronounce the ranges of applicability of the method.

3. To design and implement the modifications of the method to the particular cases of transverse electric field and infinite barriers with background impurity.

4. To study numerically the behavior of the position of energy subbands, energy distances, Fermi level and impurity binding energy depending on such parameters as geometrical sizes, impurity concentration and ionization degree. To verify and agree the results with the ones existing in the literature.

5. To calculate and analyze the optical linear and nonlinear properties connected to the intersubband transitions in the structures under study.
6. To estimate the possible tuning frequency range of the possible optical devices of the proposed design. To discuss the perspectives of implementation of the particular kinds of device.
7. To study numerically and discuss the influence of transverse electric field applied to the structure on the basic characteristics of the structures above and possible performance of optical devices.
8. To study numerically and discuss the ranges of possible influence of technological background impurity structure on the basic characteristics of the structures above and possible performance of optical devices.

1.2 Object

1.2.1 SiGe quantum wells structure

As the object study we use the $Si_{0.8}Ge_{0.2}/Si/Si_{0.8}Ge_{0.2}$ QW structures, delta-doped with phosphorus to the center or edge of QW, see Figure 1.5. The reason of such a choice is the following. First, the n-type QW is easier to calculate then p-type one and involves less risky assumptions. Second, the shallow impurity binding energy for the center-doped silicon QW have a magnitude around 30-40 meV [53], and, according to many references [23–25, 28, 35], for the edge-doped structures must be less about by half. So in the temperature range of interest the degree of impurity ionization changes noticeably that allows to use it for the phenomenon under study. Additionally, the structure is composed from commonly used in electronics materials and should be relatively easy to produce. Finally, this structure has been studied numerically in [53]. It means that we can check our results against those obtained in that work when it is possible. Their authors took the parameters of the structure taken from [54] and we made the same. Therefore, the barrier heights was taken as 200meV in accordance with [54], despite of some new data in the literature [55–57].

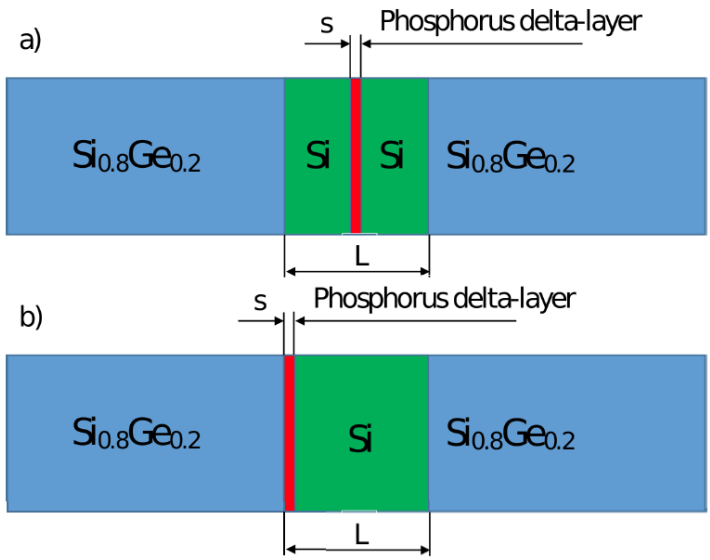

Figure 1.5: Schematic representation of the heterostructure under study a) doped to the center, b) doped to the well. s – delta-layer width, L – well width

For some studies the well width L is variable but as a reference point we took two well widths of 10 and 20 nm. Such widths allow us to obtain intersubband transition energies corresponding to THz region of spectrum. The selection of widths is also grounded in the assump-tions and limitations section. Delta-layer widths s we took as 1 nm, which is achievable technologically and corresponds to about 2 lattice parameters.

We considered two configurations. In most part of the study we imply the MQW configuration, where the structure is periodical and infinite. QWs in the structure are far enough from each other to neglect the coupling between bound states and close enough to assume that the Fermi level of the structure is defined by the impurities in delta-layers and neglect the background impurities and intrinsic carriers. Another configuration is a single quantum well with infinite barriers. This configuration implies that the Fermi level is defined by the bulk part of the heterostructure and is used to study the possible influence of the backgroung impurity in its extreme cases. For both configurations the crystal is considered infinite in all directions so that we neglect the influence of superficial states on the Fermi level.

The temperatures we took for the most calculations are 300K, 77K and 4K, which are traditional reference points in solid state physics as they refer to the environment, liquid nitrogen and liquid helium

temperatures. T=4K actually corresponds to the case of zero delta-layer impurity ionization and is our equivalent of zero temperature but for the numerical reasons it was taken a non-zero value.

1.2.2 Assumptions and limitations

We use the effective mass approximation to find the impurity binding energy. Like in the work [53] a small difference in lateral masses $m_{||}$ and dielectric constants for the well and barrier materials is neglected. We assume that subband dispersion laws are parabolic in the plane of QW and isotropic. The assumption is based on the work [27]; it shows that if QW width L is greater or equal two Bohr radii a_B then the nonparabolicity influence on the impurity ground state is negligible. In our work this condition is true with a good margin for the used delta-doping concentrations 0.6, 1.2 and 2.4×10^{12} cm^{-2}. These values allow us to consider the charge of ionized impurity centers to be distributed uniformly in the plane of delta-layer at $T = 300$ K. On the other hand, it also satisfies the condition from[30] that mean distance between impurity atoms $a_I > 2\times 1.3 a_B$ that allows neglecting many-body effects and treat impurity centers as isolated. In this work we use delta layer width s=1 nm as the typical width for similar experimentally studied structures [58].

Delta-layer Impurity concentration

Obviously, to obtain a pronounced effect from tuning the ionization degree of a delta layer, the impurity concentrations should be big enough. Again, the concept of constant in lateral plane Hartree potential implies big enough concentration, at room and liquid nitrogen temperatures. On the other hand, the concentration should not be high enough to form the impurity minibands by the overlap of the impurity wave functions, or arising tails of the density of states in the gap. That is concentration should be small enough to use a single impurity approach that makes possible manipulate the concept of IBE and the degree of ionization of the delta layer. The natural restriction here is the Mott metal-semiconductor transition. The critical value n_M can be deduced from the relation $a_B n_M^{1/2} = 0.37$ [59], and for our material $a_B \cong 2\ nm$, and $n_M = 3.4 \times 10^{12}$ cm^{-2}.

The concentration lower limit to avoid the potential fluctuations in plane of quantum well can be found from the following. We know [60] that impurities can cause fluctuating potential with a maximum size r_s that has to be included to the Hamiltonian of the problem. In our structure, when the background impurity concentration is negligible, the number of subband electrons equals the number of ionized delta-layer impurity centers N_d^+. Therefore [60] the maximum fluctuation size is the average distance between ionized donors $r_s = d^+ = 1/\sqrt{N_d^+}$. So, the fluctuations can be neglected if the configuration of the ionized donors is volatile, that is constantly varies over time, since the atoms are ionizing randomly. And if anywhere along the delta layer a potential fluctuation arises then (i) it gets shielded to some degree by free electrons, and (ii) the ionization impurity probabilities in the adjacent area get smoothed. The mentioned processes have characteristic time order of $\tau \sim 10^{-10}$ s. This is the conduction band electron lifetime with respect to the capture by impurity [61] within the range of temperatures 4...100 K. Using this lifetime, the lower limit of the impurity concentration can be found from the statement that the mean distance between the ionized impurity centres d^+ should not be greater than the mean free path of the electron $d^+ \leq l$ ($l \cong \upsilon\tau \approx \sqrt{k_b T/m_{||}}\tau$, k_b is the Boltzmann's constant). A stronger condition can be imposed taking into account that the concept of electron mean free path makes sense only if it is greater or equal the de Broglie wavelength $\lambda = \frac{h}{p} \approx \frac{h}{\sqrt{mk_bT}}$ [62] (h is Plank's constant, and p is electron momentum). As a result, the lower concentration limit can be estimated as: $N_d^+ \geq \frac{m_{||}k_bT}{h^2}$ and now it depends on temperature. For example, for T=77 K $N_d^+ \geq 4.2\times10^{10}$ cm^{-2}, and for T=300 K $N_d^+ = 1.6\times10^{11}$ cm^{-2}. Again, in reality the lower limit of impurity concentration should be less in the same degree as the de Broglie electron wavelength is less than its mean free path. Therefore, in solving the task of finding IBE, the fluctuating potential can be omitted in the Hamiltonian. The estimation can be formalized as

$$sN_\delta > \frac{m_{||}k_bT\left(1 + 2\exp\left(\frac{E_F - E_\delta}{k_bT}\right)\right)}{h^2} \tag{1.1}$$

As a result of all the considerations above the delta-layer impurity concentration has been chosen as 0.6×, 1.2×, and 2.4×10^{12} cm^{-2}.

Internal stress in the well material

In this work we consider the structure grown in crystallographic direction [100]. The well width (L=20nm) we chose from the following considerations. First, in the work [63] it was shown that the influence of the delta layer ionization on the IBE is bigger for the wider QW. Second, there is a critical well width [56], the higher limit, after which the well cannot be treated as tense anymore. That is the stain due to a lattice constant mismatch between well and barrier materials cannot be considered uniform. The well width of 20 nm looks like a good compromise between these two limits. Our QW has an internal strain because the lattice constant of $SiGe$ alloy in barriers is larger than that of Si. It means that the well can be considered as uniaxially strained in the direction of structure growth z. The strain magnitude depends on the fraction of Ge in the material. (Also, it relates to the QW depth, which is 202 meV in our case.) It is known that uniaxial strain damages the crystal symmetry [64], as a result the degeneracy of electron valleys in Si is removed. For the case of the structure grown in [100] crystallographic direction, the energy difference between two lower in energy valleys and four upper ones is greater than 110 meV [56,63,65]. Such difference allows us to consider only *2* lowest valleys. The electron effective masses there appear to be $m_{||} = 0.19m_0$ in plane of QW, and $m_{\perp} = 0.92m_0$ in the growth direction, where m_0 is a free electron mass.

Additionally, a relatively wide well allows us neglecting the nonparabolicity of the QW size quantization levels. The work [27] showed that for the well width more than two Bohr radii, the influence of nonparabolicity on the impurity ground state is negligible. For the Bohr radius of about 2 nm [63] it is well satisfied. Also, we do not account for the splitting in our IBE calculations. Instead, following [53] we discuss the joint influence of splitting and central cell effect on IBE later.

Central cell effect

It is known that effective mass approach when calculating impurity ground state does not allow to take into account the central cell effect (also known as chemical shift). It becomes especially important in case of silicon-based structures. The effective mass calculation of Phosphorus impurity binding energy (shallow donor in Si) provides the value of 29 meV [66], while the experimental study gives 45.6 meV (see, for example, [67]). The notable difference of 16.6 meV is attributed to the central cell effect. So, to agree the results of effective mass calculations with the experiment the necessary corrections should be introduced. Here we propose to make the addition of 8 meV to all the obtained results. The proposition is based on the work [63], where such an addition to IBE was grounded for the similar structure as ours with well width of 7 nm and more.

1.3 Methods

1.3.1 Energy subband positions and wave functions

Size quantized in z-direction energy levels E_j and corresponding wave functions $\xi_j(z)$ were found as the eigenvalues and eigenfunctions of z-dependent Hamiltonian:

$$H_0 = -\frac{\mathrm{h}^2}{2m_\perp}\frac{\partial^2}{\partial z^2} + V(z) + e\varphi(z), \tag{1.2}$$

here $m_\perp$ is the transverse effective mass (in z direction), $V(z)$ is an undisturbed rectangular potential profile of QW (without background impurities and at zero temperature): $V(z) = \left\{ \begin{array}{ll} 0, & |z| > L/2 \\ -V_b & |z| \leq L/2 \end{array} \right\}$, $\varphi(z)$ in the Hartree potential (electrostatic potential provided by charge redistribution), e is a unit charge. Schrödinger equation for the problem can be written as [68]:

$$H_0 \xi j(z) = Ej \xi j(z) \tag{1.3}$$

The equation was solved numerically using shooting method [69]. The differences of effective masses between the materials of the well

and the barriers were neglected. Accordingly, the Ben Daniel-Duke boundary conditions [68] at the interfaces are interpreted as the continuity of the wave functions and their first derivatives. The number of energy levels N accounted for (j=1,2... N) has been chosen from the following considerations. First, the difference between the energies of the first and the last considered levels should be greater than $3kT$, so that absolute majority of electrons in subbands are accounted for. Second, the IBE calculated with N and N-1 levels should not be greater than 0.1 meV (convergence condition of the method). The maximum of two options above was taken as actual N. Numerically we got N=9 for the first condition (for T=300 K) and N=7 for the second one. So, we used 9 levels for the room temperature and 7 levels for the temperatures of 4 and 77 K.

In case of the applied transverse electric field, the equation *1.2* is transformed into

$$H_0 = -\frac{\hbar^2}{2m_\perp}\frac{\partial^2}{\partial z^2} + V(z) + e\varphi(z) + eEz. \tag{1.4}$$

That is a term of a constant electric field is added. This term provides additional complications for the numerical method. For the large enough integration range over z the potential on one of the borders can become less than some of the eigenvalues for the necessary number of eigenfunctions. Technically it means that the electronic state is not localized and time-independent Schrodinger equation is not applicable. In that case we overcame that problem on the numerical level by introducing Big Quantum Box method, that is by modifying the well potential as

$$V(z) = \left\{ \begin{array}{ll} 0, & \frac{L_1}{2} > |z| > \frac{L}{2} \\ -V_b, & \frac{L}{2} \geq |z| \\ \infty, & |z| \geq \frac{L_1}{2} \end{array} \right\}, \tag{1.5}$$

Where L_1 is the width of a Big Quantum Box with infinite barriers, $L_1 > L$.

L_1 was selected manually during the calculation process in a way that (i) the finite barrier width is at least comparable with the well width; and (ii) of the center of mass of all the squared eigenfunctions taken into account should be deep within the well. Actually it was

the criterion, when the delocalization of the WFs can be neglected.

As the result of the numerical solution of the equation *1.3*, we ob-tain the series of the bound in the direction z energy states E_i and wave functions i, describing corresponding subbands. Here i=1, 2, 3. . . that is the ground state corresponds to i=1.

1.3.2 Fermi level

The Fermi level was found from the condition of electro neutrality for the structure:

$$\int_{-\infty}^{\infty} N^{\pm}(z)\, dz = 0 \tag{1.6}$$

The charge concentration $N^{\pm}(z)$ is the concentration difference of the ionized impurity $N_D^+(z)$ and subband electrons $N^-(z)$:

$$N^{\pm}(z) = N_D^+(z) - N^-(z) \tag{1.7}$$

The holes were neglected as it is an type structure. Ionized impurity concentration in the delta layer were found from Fermi statistics:

$$N_D^+(z) = \begin{cases} N_\delta^+(z) = \frac{N_\delta}{1+2exp\left(\frac{E_F-E_\delta}{k_bT}\right)}, & |z| < \frac{s}{2} \\ 0 - \text{otherwise} \end{cases} \tag{1.8}$$

s is the delta layer width. Here we use the following assumptions. First, the impurity distribution within the delta layer is uniform: $N_\delta(z) = \begin{cases} N_\delta = \frac{n_\delta}{s}, & |z| < s/2 \\ 0, & |z| \geq s/2 \end{cases}$ It is grounded in the work [63]. Second, the binding energy does not change within the delta-layer. We believe it is acceptable, as the width of delta layer is small in comparison to the well width. The electron concentration $N^-(z)$ is a sum of the concentrations in each subband:

$$N^-(z) = N_{QW}(z) = \frac{m_{||} k_b T}{\pi \hbar^2} \sum_j^N ln\left(1 + \exp\frac{E_F - E_j}{k_b T}\right) |\xi_j(z)|^2 \tag{1.9}$$

Accordingly, the sheet concentration of electrons is:

$$n_{QW}=\int_{-\infty}^{\infty} N_{QW}\left(z\right) dz=\frac{m_{||}k_bT}{\pi\hbar^2}\sum_{j}^{N} ln\left(1+\exp\frac{E_F-E_j}{k_bT}\right), \quad (1.10)$$

As the result of the numerical solution of the equation *1.6*, we obtain the Fermi level E_F. The equation was solved using bisection method.

1.3.3 Hartree potential

Hartree potential $\varphi(z)$ in Eq. *1.2* was obtained from the solution of Poisson equation for the QW area, with non-uniform charge distribution along z:

$$\frac{\partial^2\varphi}{\partial z^2}=\frac{e}{\varepsilon\varepsilon_0}N^{\pm}\left(z\right). \quad (1.11)$$

The distribution of charge $N^{\pm}\left(z\right)$ was discussed in the section above. The equation is solved by the numerical integration with Runge-Kutta method.

1.3.4 Impurity binding energy

We find the binding energy of impurity atoms in delta layer by adding the Coulomb potential to the Hamiltonian H_0 (*1.2*). Assuming that the effective mass in plane of QW is isotropic, the problem has a cylindrical symmetry, so we use the cylindrical coordinates R, θ, z, as in [70]. We write the complete wave function $\Psi\left(R,\theta,z\right)$ as

$$\Psi\left(R,\theta,z\right)\equiv\exp\left(im\theta\right)\ \psi_m\left(R,z\right), \quad (1.12)$$

were i is an imaginary unit and m is the azimuthal quantum number. We present the complete Hamiltonian as a sum of the part depending on z only H_0 – the same as in *1.2* - and the part, depending on all three coordinates H_1

$$H=H_0+\ H_1 \quad (1.13)$$

$$H_1=-\frac{\hbar^2}{2m_{||}}\left(\frac{\partial^2}{\partial R^2}+\frac{1}{R}\frac{\partial}{\partial R}+\frac{1}{R^2}\frac{\partial^2}{\partial\theta^2}\right)-\frac{e^2}{4\pi\varepsilon\varepsilon_0\sqrt{R^2+\left(z-z_D\right)^2}} \quad (1.14)$$

Here $m_{||}$ is the electron effective mass in (x,y) plane, z_D is the impurity center z position. Then the eigenfunction of the complete Hamiltonian H (*1.13*) can be expanded over a series of wavefunctions $\xi_j(z)$ of the Hamiltonian H_0:

$$\Psi\left(R,\theta,z\right) \equiv \exp\left(im\theta\right)\ \sum_j f_j^m\left(R,z\right)\xi_j(z). \tag{1.15}$$

Then according to the Schrodinger equation with the complete Hamiltonian *H:*

$$\left[H_0 - \frac{\hbar^2}{2m_{||}}\left(\frac{\partial^2}{\partial R^2} + \frac{1}{R}\frac{\partial}{\partial R} + \frac{1}{R^2}\frac{\partial^2}{\partial\theta^2}\right) - \frac{e^2}{4\pi\varepsilon\varepsilon_0\sqrt{R^2+(z-z_D)^2}}\right]\Psi\left(R,\theta,z\right) = E\Psi\left(R,\theta,z\right) \tag{1.16}$$

Then we differentiate *Eq. 1.16* with respect to θ, multiply by $\xi^*_N(z)$, $(N = 0, 1, 2\ldots)$ and integrate with respect to z. The result is:

$$\left[\frac{d^2}{dR^2} + \frac{1}{R}\frac{d}{dR} + \left(k_N^2 - \frac{m^2}{R^2}\right)\right] f_N^m\left(R\right) = U_{Nn}\left(R\right) f_n^m, \tag{1.17}$$

were $U_{Nn}\left(R\right) = \frac{2m_{||}}{\hbar^2}\frac{1}{4\pi\varepsilon\varepsilon_0}\int \xi_N^*\left(z\right)\frac{e^2}{\sqrt{R^2+(z-z_D)^2}}\xi_n\left(z\right)dz$, $k_N^2 = \frac{2m_{||}}{\hbar^2}(E-E_N)$, and E_N (N=1,2,3...) are the eigenvalues of H_0. If there is no Coulomb term in *1.17* then it becomes a Bessel type order m equation, the wave function is only allowed for $E > E_N$ and the solution can be written as

$$f_N^m\left(R\right) = C_N J_m\left(k_N R\right) + S_N N_m\left(k_N R\right), \tag{1.18}$$

where J_m and N_m are first and second kind Bessel functions respectively, C_N and S_N are constants. Second kind Bessel functions are singular at zero coordinate, so S_N=0, and

$$\Psi\left(R,\theta,z\right) = C_N \exp\left(im\theta\right)\ J_m(k_N R)\xi_N(z). \tag{1.19}$$

Now let us solve *1.17* for $E < E_N$ (that is $k_N^2 < 0$). In this situation instead of *1.17* we have

$$\left[\frac{d^2}{dR^2} + \frac{1}{R}\frac{d}{dR} - \left(k_N^2 + \frac{m^2}{R^2}\right)\right] f_N\left(R\right) = \sum_n U_{Nn}\left(R\right) f_n\ . \tag{1.20}$$

By definition in [71] the solution of *1.20* is the solution of

$$\left[\frac{d^2}{dR^2}+\frac{1}{R}\frac{d}{dR}-\left(k_N^2+\frac{m^2}{R^2}\right)\right]G_N\left(R,R^{'},E\right)=\frac{1}{R}\delta(R-R^{'}). \quad (1.21)$$

where $G_N(R,R',E)$ is the Green function. Accordingly [70, 71]

$$G_N\left(R,R^{'},E\right)=\begin{cases} -K_m\left(k_NR^{'}\right)I_m\left(k_NR\right), & R<R' \\ -I_m\left(k_NR^{'}\right)K_m\left(k_NR\right), & R>R' \end{cases} \quad (1.22)$$

with modified Bessel functions K_m and I_m. So, from Green function definition

$$\begin{array}{c} f_N\left(R\right)=\int_0^\infty R'dR'G_N\left(R,R^{'},E\right)\sum_n U_{Nn}\left(R^{'}\right)f_n\left(R^{'}\right)= \\ -K_m\left(k_NR\right)\int_0^R R^{'}dR'I_m\left(k_NR^{'}\right)\sum_n U_{Nn}\left(R^{'}\right)f_n\left(R^{'}\right) \\ -I_m\left(k_NR\right)\int_R^\infty R'dR'K_m\left(k_NR^{'}\right)\sum_n U_{Nn}\left(R^{'}\right)f_n\left(R^{'}\right). \end{array} \quad (1.23)$$

It can be written more conveniently like 1.18:

$$f_N\left(R\right)=C_NJ_m\left(k_NR\right)+S_NN_m\left(k_NR\right), \quad (1.24)$$

where

$$\begin{array}{c} C_N\left(R\right)=-\int_R^\infty R'dR'K_m(k_NR^{'})\sum_n U_{Nn}(R^{'})f_n(R^{'}) \\ S_N\left(R\right)=-\int_0^R R'dR'I_m(k_NR^{'})\sum_n U_{Nn}(R^{'})f_n(R^{'}) \end{array}. \quad (1.25)$$

After differentiating with respect to the variable upper limit (over parameter R), from 1.25 we obtain

$$\begin{array}{c} \frac{dC_N}{dR}=RK_m\left(k_NR\right)\sum_n U_{Nn}\left(R\right)f_n\left(R\right) \\ \frac{dS_N}{dR}=-RI_m(k_NR)\sum_n U_{Nn}\left(R\right)f_n\left(R\right) \end{array}. \quad (1.26)$$

Then substituting *1.24* into *1.26* we obtain the system of differential equations, which can be numerically solved. Here we assume the following. First, the number of equations is not infinite, so that the number of subbands in QW has to be limited to a reasonable value. Second, the numerical integration over R is performed for a finite range from 0 to some R_{max}. The wave function for $R>R_{max}$ is negligibly small (in our calculations $R_{max}=6a_B$). Third, we have to adopt starting values for $C_N(R)$ and $S_N(R)$. Because of the modified Bessel functions properties, $C_N\left(\infty\right)=S_N\left(R_{max}\right)=S_N\left(0\right)=0$ and

another side of boundary conditions $C_N(0) = S_N(R_{max}) = \delta_{Nn}$. The conditions for R=R_{max} and R=0 and are only correct at some discrete energies. To obtain those energies the shooting method is used. It means, we choose an initial R_0 ($0<R_0<R_{max}$), integrate numerically from 0 to R_0 for all n and obtain $C_{Nn}(R_0\text{-})$ and $S_{Nn}(R_0\text{-})$. Similarly we obtain $C_{Nn}(R_{0+})$ and $S_{Nn}(R_{0+})$ by integration back from R_{max} to R_0. We took R_0 as a half of R_{max}. Now as the functions are continuous the obtained values should be the same, so, following [70] we obtain a system of linear algebraic equations:

$$\begin{array}{l} \sum_n \mathrm{C}_{Nn}(R_{0-})\, C_n(0) = \sum_n \mathrm{C}_{Nn}(R_{0+})\, S_n(R_{max}) \\ \sum_n S_{Nn}(R_{0-})\, C_n(0) = \sum_n S_{Nn}(R_{0+})\, S_n(R_{max}) \end{array} \tag{1.27}$$

Here the variables are $C_N(0)$ and $S_N(R_{max})$. The determinant of the system depends on the energy and when it is equal to zero, the solutions can be found numerically. In case of 9 subbands taken into account, the determinant order is 18.

1.3.5 Self-consistent method

The 1D self-consistent Schrodinger-Poisson method in application to 2D semiconductor heterostructures is widely used and has many numerical implementations in commercially available software. However, to our knowledge up to now all those implementations do not imply the possibility to include the calculation of IBE to the self-consistent procedure, which is a crucial point in our case. The IBE has a drastic effect on the degree of ionization which is a key factor for our idea to regulate the working frequency of the optical device. Within our model and parameters IBE has a strong mutual influence on the Hartree potential and electronic structure and, accordingly, cannot be assumed a constant during calculations. Therefore, we implemented a modified self-consistent procedure that embeds the calculation of IBE as its part performed at each iteration. The variant of the classical schematic of the method is presented in Fig. 1.6. It includes the following steps, described in the sections above. 1. Solution of Schrodinger equation that uses the potential profile as an input data and gives away energy levels of subbands and their wave functions (Section 1.3.1). 2. Solution of electroneutrality equation for a given energy profile, subband

positions and wave functions, that provides with Fermi level, and, accordingly, charge distribution (Section 1.3.2). Normally this step uses IBE as a constant. 3. Solution of the Poisson equations based on the charge distribution, which gives the Hartree potential that modifies the energy potential for the step 1 (Section 1.3.3).

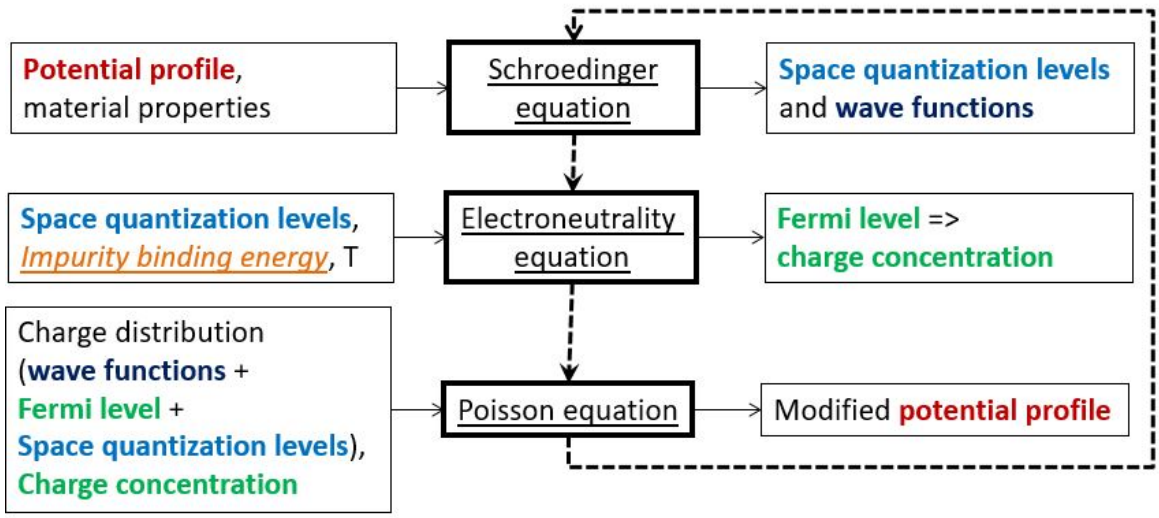

Figure 1.6: General scheme of the self-consistent calculation method of 1D Schrödinger-Poisson problem

In our method (Fig. 1.7) we introduced the calculation of IBE based on the wave functions and energy positions of subbands (Section 1.3.4). As a criterion of convergence was taken the condition that IBE for the two last iterations does not change more than 0.1 meV.

1.3.6 Particular case: background impurities

In the case of background impurity, the specificity of the problem requires the modifications of the method, which are described below.

Fermi level

Obtaining the Hartree potential and the heterostructure energy profile by solving Poisson equation requires knowledge of the Fermi level. In the most cases we assume the periodic n-type MQW structure so that the Fermi level is determined by the impurities in the delta layers and the electro neutrality equation can be written for a period, which

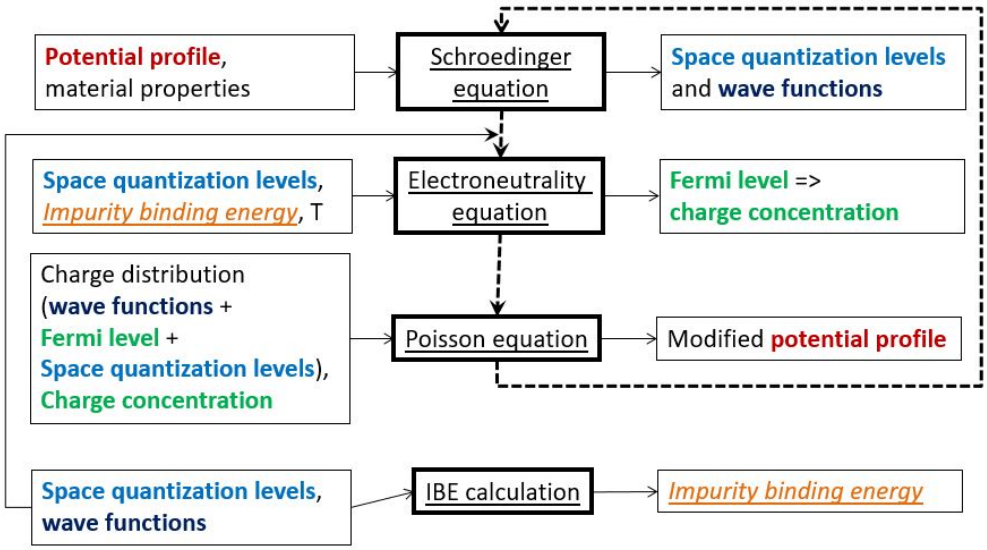

Figure 1.7: General scheme of **our modification** of self-consistent calculation method of 1D Schrödinger-Poisson problem.

includes the well and its relatively close proximity. The different situation is when the barriers are infinite and the well is single. In this case the Fermi level is defined by the bulk area outside the well, that includes background impurity. So we find it as for the uniformly n-doped bulk barrier material as follows (see the textbook [72]). The electro neutrality equation is:

$$N_0^- = N_b^+ + P_0, \tag{1.28}$$

where N_0^-, N_b^+ and P_0 are volumetric concentrations of electrons, ionized impurity centers and holes correspondingly. Within the Fermi statistics they are found as:

$$N_0^- = \frac{2}{\sqrt{\pi}} N_c \phi_{\frac{1}{2}} \left(\frac{E_F - E_c}{k_b T} \right), \quad P_0 = \frac{2}{\sqrt{\pi}} N_v \phi_{\frac{1}{2}} \left(\frac{E_v - E_F}{k_b T} \right) \tag{1.29}$$

$$N_b^+ = \frac{N_b}{1 + 2exp\left(\frac{E_F - E_b}{k_b T}\right)} \tag{1.30}$$

Here $\phi_{\frac{1}{2}}$ is the Fermi-Dirac integral, the E_c and E_v are gap edges, the N_c and N_v are the effective densities of states. Subindexes c and v denote conduction and valence bands correspondingly. N_b is the impurity concentration and E_b ground state of background impurity. For

the detailed explanations and deduction of these equations see [72]. To find the Fermi energy from *1.28* we need the gap and IBE magnitudes for the bulk barrier material, which is $Si_{0.8}Ge_{0.2}$ alloy. The bandgap was taken as 1.08 eV (from [73] for 77 K) and the influence of tempera-ture was neglected because our numerical estimations showed that for the temperatures between 4 and 300K it practically does not change (means for the same temperature the variation of the bandgap has no notable influence on E_F). IBE here was taken as ε_b = 39meV, as obtained in [74], and accordingly E_b=E_c-ε_b. The acceptors were not accounted for, so the impurity concentration here can be understood as the difference between background donors and background acceptors.

So, in this case in the algorithm, we use the electro neutrality equation *1.6* not to find the Fermi level, which is known from the above, but to calculate the half depletion layer width Z_0, which is used as a limit for integration in the calculation of Hartree potential and the numerical solution of the Schrödinger equation (see Fig. 1.8). We suppose that the many barrier electrons from the area around the well move to the well. So, by depletion layer we mean the area, where the charge is distributed non-uniformly along z axis. For the symmetric QW the electro-neutrality condition is:

$$\int_{z=-Z_0}^{0} N^{\pm}(z)\,dz = 0 \tag{1.31}$$

Solving this equation provides us with the depletion region length Z_0.

The equation for ionized donors *1.8* now includes not only delta-layer impurity centers $N_\delta^+(z)$, but also those in barriers $N_b^+(z)$:

$$N_D^+(z) = \begin{cases} N_b^+(z) = \frac{N_b}{1+2exp\left(\frac{E_F-E_b-e\varphi(z)}{k_bT}\right)}, & |z| > \frac{L}{2} \\ N_\delta^+(z) = \frac{N_\delta}{1+2exp\left(\frac{E_F-E_\delta}{k_bT}\right)}, & |z| < \frac{s}{2} \\ 0 - \text{otherwise} \end{cases} \tag{1.32}$$

Here we assume that the contribution of BI inside the well is negligible even for the biggest concentration (10^{17}cm^{-3}) at all temperatures.

The equation *1.9* for the free electrons also changes. Now it includes not only 2DEG in the well subbands but also electron gas in 3D

continuum:

$$N^{-}(z) = N_{QW}(z) + N_{3D}(z). \tag{1.33}$$

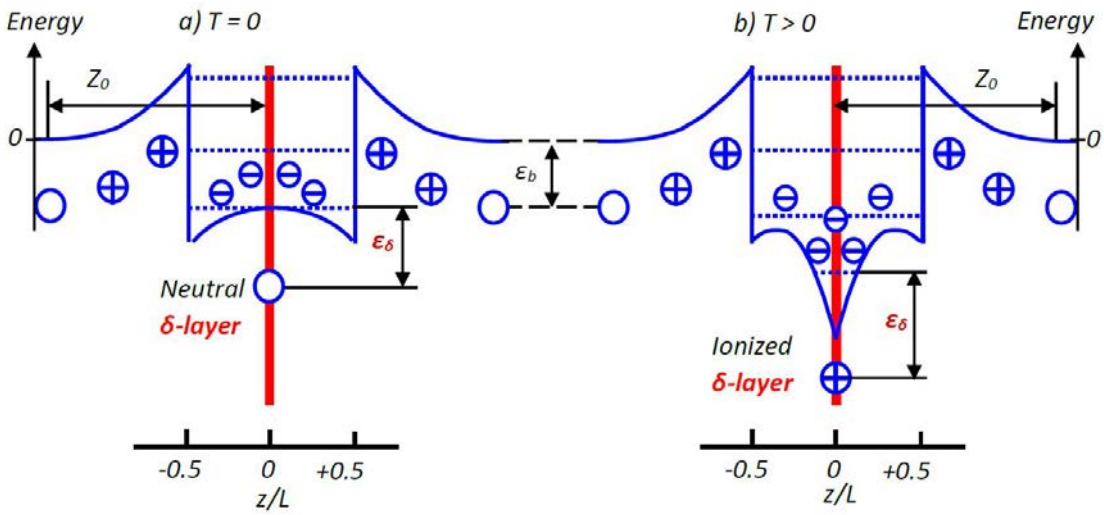

Figure 1.8: Schematic representation of a center delta-doped QW with residual impurities of concentration N_b in barriers at low – *a)* and higher – *b)* temperatures T. Z_0 is the depletion layer length, that is the distance between heterojuction and a point where band bending becomes zero. ε_b and $\boldsymbol{\varepsilon_\delta}$ are the binding energies of background impurities and impurities in the delta layer accordingly.

Here the concentration of electrons N_{3D} (see *1.29*) is

$$N_{3D}(\mathrm{z}) = \begin{cases} \frac{2}{\sqrt{\pi}} N_c \phi_{1/2}\left(\frac{E_F - e\varphi(z) - E_c}{k_b T}\right), \ |z| > L/2 \\ \frac{2}{\sqrt{\pi}} N_c^* \phi_{1/2}\left(\frac{E_F - E_m}{k_b T}\right), |z| \leq \frac{L}{2}, T = 300K, \ m > 9 \\ 0, \ |z| \leq \frac{L}{2}, T = 4 \ or \ 77K \end{cases} \tag{1.34}$$

For the room temperature (1.34, second line) we account for 9 first subbands. Totally there are 14 subbands but the upper ones have very few electrons. Also, they are poorly localized. So we treat the energies above the 9-th subband as a part of 3D continuum and $N_c^* = N_c/3$ because the material within the well ($z \leq L/2$) is uniaxially stressed and we have there only 2 electron valleys instead of 6 in unstressed barriers. Again, as was mentioned before, to find IBE with 0.1 meV precision, 9 energy levels were enough. All the electrons in subbands above the 9-th are used only for the correct solution of Poisson equation. And at lower temperatures (line 3 of 1.34) the number of electrons above the QW is absolutely negligible.

Modification of the algorithm

In our calculations of this modification zero of energy corresponds to the conduction band edge of the bulk barrier material. So the nega-tive energy solutions for the subbands obtained by shooting method in z direction $E_j < 0$, correspond to the perfectly localized states. Positive energy solutions strictly speaking do not exist for time-independent Schrodinger equation if we try to solve for the whole depletion region, because the potential on the borders is zero and the wave functions should be complex that corresponds to the moving electron. However the states within the well can be separated by large enough barriers formed by Hartee potential and treated as quasilocal. To deal with this kind of problem numerically, in some literature [75, 76] the quantum box technique is used. Roughly, we put an infinite potential barrier on the borders and thus obtain the solutions. However, if the region is large enough, most of the solutions obtained will have corresponding WFs mostly outside the well, which do not correspond to the quasilocal states off the well. Therefore, we limit the quantum box by the area, which includes the well ant the parts of barriers, where the potential is greater than the solution. Mathematically it means that to find $E_j > 0$ we integrate over z between z=-t_j and 0, where t_j is found from the equation $e\varphi(-t_j)=E_j$. So, our quantum box limits are variable in the process of shooting method solution and depend on the energy. Obviously, this method can produce an error which is bigger for the higher energies (and narrower Hartree barriers), however in our calculations the minimum t fas as big as 22 nm. In the material used ($Si_{0.8}Ge_{0.2}$) this length is big enough to neglect electron tunneling through the barrier of such width. To make an example from the literature, in [62] for barriers more than 15 nm in silicon the tunneling was neglected. The work [78] used the same approximation. Finally, the uniaxial stress induced electron valley splitting in our material is always bigger than the difference between the first and the last accounted for subbands: Δ_4 - Δ_2 > E_9-E_1, so that we continue neglecting the upper valleys.

The specificity of the self-consistent algorithm for calculation the case of infinitely wide barriers with background doping is the following. First, the Fermi level is constant. Second, there are two impurity binding energies: for the barrier, and for the delta-layer in the

well. The first one is taken as constant and the second one is variable and incorporated to the calculus as was described before. Third, it uses depletion layer width $2Z_0$ as a variable. Initially depletion zone length was taken as for the p-n junction at zero temperature $Z_0 \approx \left(\frac{2\varepsilon_0 \varepsilon V}{e^2 N_b}\right)^{\frac{1}{2}}$. The starting value for the IBE of the donors in the layer was taken as the one obtained before for the same combination of parameters but without background impurity [79]. For the algorithmic reasons at the first iteration the 3D electrons in the depletion layers were neglected ($N_{3D}(z)$=0 in *eq. 1.33*). Also, for the first iteration the electrons distribution within the QW width was considered uniform:

$$N_{QW}(z) = \begin{cases} 2\left(\int_{z=-\frac{L}{2}}^{0} N_b(z')\,dz' + n_\delta^+\right)/L & ,|z| < L/2 \\ 0, & \lfloor z \rfloor \geq L/2 \end{cases} \tag{1.35}$$

The very self-consistent process starts from the calculation of Fermi energy as described in 1.3.6 in bulk barrier material. Then the iterative process is performed in the following way.

1. The depletion zone half-length Z_0 is calculated solving the electro neutrality equation *1.31*. It is made along with Schrödinger equation 1.3 solution as follows:

1a. The left-hand side of equation 1.31 is found for a given Z_0 by solving numerically the Poisson equation 1.11 by direct integration over z from $-Z_0$ to 0. At first iteration, after $z = -L/2$ the N_{3D}(z) is calculated from 1.34, and is used for the further integration. In the following iterations instead of 1.34 we use 1.35 with the data obtained from the previous iteration.

1b. We solve *1.3* obtaining E_j and ζ_j(z) using Hartree potential $\varphi(z)$ from the previous step. We calculate the left-hand side of Eq. 1.31 for a given Z_0, then a new Z_0 is selected from the bisection algorithm. Then $1a$ and $1b$ are repeated in the internal loop until the charge concentration from Eq. 1.31 is small enough (10^9 cm^{-2}).

2. IBE in the well ε_δ is calculated (see section 1.3.4).

3. Steps 1 and 2 are repeated in outer loop until $\varepsilon_\delta^k - \varepsilon_\delta^{k-1} \leq 0.1$ meV (convergence criterium). In practice to reach the condition 3 to 7 iterations of the outer loop was performed depending on the temperature. The inner loop normally was performed about 30 times.

1.3.7 Linear and nonlinear optical effects based on intersubband transitions

The complete absorption for the transitions between subbands i and j is found as a sum of the linear and Kerr-type nonlinear parts $\alpha_{i,j}^{(1)}(\omega)$ and $\alpha_{i,j}^{(3)}(\omega, I)$ correspondingly. We use a model proposed in [80] with reference to [81]:

$$\alpha_{ij}^{(1)}(\omega) = \frac{\omega\mu_0 c}{n}|M_{ji}|^2 \frac{\sigma_{ij}\Gamma}{(E_{ji}-\omega)^2+\Gamma^2} \alpha_{ij}^{(3)}(\omega, I) = -\frac{\omega\mu_0 I}{2n^2\varepsilon\varepsilon_0}|M_{ji}|^2 \frac{\sigma_{ij}\Gamma}{\left\{(E_{ji}-\omega)^2+\Gamma^2\right\}^2} \times$$

$$\left[4|M_{ji}|^2 - \frac{|M_{jj}-M_{ii}|^2\left\{(E_{ji}-\omega)^2-\Gamma^2+2E_{ji}(E_{ji}-\omega)\right\}}{{E_{ji}}^2-\Gamma^2}\right] \qquad (1.36)$$

Here ω is the angular frequency of the incident radiation photon, μ_0 is the vacuum permeability constant, $n=\sqrt{\varepsilon}$ is the material refractive index (3.4926 as for the bulk silicon), E_i and E_j are energies corresponding to the edges of the initial and final states of absorptive, E_{ji}=E_j-E_i is the transition energy difference, I is an optical intensity of the incident radiation (I= 0.5 MW/cm^2 for all frequencies as a reasonable value), absorption peak proadening in energy units for all transition was taken as Γ=2meV [82]). σ_{ij} is the difference between volumetric electron concentrations of i-th and j-th subbands,

$$\sigma_{ij} = \frac{m^* k_b T}{L\pi^2} ln\left\{\frac{1+e^{(E_f-E_i)/k_bT}}{1+e^{(E_f-E_j)/k_bT}}\right\}, \qquad (1.37)$$

where m^* is the density-of-states effective mass of electrons, L is a QW width. Other quantities and constants were mentioned before.

Matrix element of the intersubband transitions is of dipole type:

$$M_{ab} = \int \xi_a^*(z)\,|e|\,z\xi_b(z)dz(a,b = 1..N_S), \qquad (1.38)$$

N_S is a subbands number taken into account.

The total absorption coefficient is

$$\alpha(\omega, I) = \alpha^{(1)}(\omega) + \alpha^{(3)}(\omega, I). \qquad (1.39)$$

Here

$$\alpha^1(\omega) = \sum_{i=1}^{N_s-1} \sum_{j=i+1}^{N_s} \alpha_{ij}^{(1)}(\omega) \quad and \quad \alpha^3(\omega, I) = \sum_{i=1}^{N_s-1} \sum_{j=i+1}^{N_s} \alpha_{ij}^{(3)}(\omega, I). \tag{1.40}$$

The transitions between the subbands i and j provide refractive index change that consists of the linear $\frac{\Delta n_{ij}^{(1)}(\omega)}{n}$ and nonlinear part $\frac{\Delta n_{ij}^{(3)}(\omega,I)}{n}$ [80]:

$$\frac{\Delta n_{ij}^{(1)}(\omega)}{n} = \frac{1}{2n^2\varepsilon\varepsilon_0}|M_{ji}|^2 \frac{\sigma_{ij}(E_{ji}-\omega)}{(E_{ji}-\omega)^2+\Gamma^2} \tag{1.41}$$

$$\frac{\Delta n_{ij}^{(3)}(\omega, I)}{n} = -\frac{\mu_0 c I}{4n^3\varepsilon\varepsilon_0}|M_{ji}|^2 \frac{\sigma_{ij}}{\left\{(E_{ji}-\omega)^2+\Gamma^2\right\}^2} \times$$

$$\left[4\left(E_{ji}-\omega\right)|M_{ji}|^2 - \frac{(M_{jj}-M_{ii})^2}{{E_{ji}}^2+\Gamma^2} \times \left\{\left(E_{ji}-\omega\right)\left[\left(E_{ji}-\omega\right)E_{ji}-\Gamma^2\right] - \Gamma^2\left[2E_{ji}-\omega\right]\right\}\right] \tag{1.42}$$

And the total change of refractive index is:

$$\frac{\Delta n\ (\omega, I)}{n} = \frac{\Delta n^{(1)}(\omega)}{n} + \frac{\Delta n^{(3)}(\omega, I)}{n}, \tag{1.43}$$

Where both linear and nonlinear part were found as a sum for all possible intersubband transitions:

$$\frac{\Delta n^{(1)}(\omega)}{n} = \sum_{i=1}^{N_s-1} \sum_{j=i+1}^{N_s} \frac{\Delta n_{ij}^{(1)}(\omega)}{n}, \quad and \quad \frac{\Delta n^{(3)}(\omega, I)}{n} = \sum_{i=1}^{N_s-1} \sum_{j=i+1}^{N_s} \frac{\Delta n_{ij}^{(3)}(\omega, I)}{n} \tag{1.44}$$

The input data, namely wave functions, subband energy positions and Fermi level were calculated with the self-consistent method as described in other subsections of this section.

1.3.8 Many-body effects

To make our results more realistic, we accounted for depolarization shift γ as described in [83, 84]:

$$\tilde{E}_{ji}^2 = E_{ji}^2\left(1 + \gamma_{ji}\right). \tag{1.45}$$

In the equation above E_{ji}=E_j-E_i is the intersubband transition energy without depolarization shift, found solving the Schrödinger equation, and $\tilde{E}_{ji}$ is the modified transition energy, that was actually used in the ecuations of absorption and refraction. γ_{ji} was calculated as [83,84] :

$$\gamma_{ji} = \frac{2e^2\sigma_{ij}}{\varepsilon_0\varepsilon E_{ji}} \int_{-\infty}^{\infty} dz \left(\int_{-\infty}^{z} \xi_i\left(z'\right) \xi_j\left(z'\right) dz' \right)^2, \tag{1.46}$$

where ε=11.7 is the silicon dielectric constant.

When the exchange-correlation effects cannot be neglected, the usual way to take them into account in 2DEG systems is to add a z-dependent potential to the Hamiltonian.

$$V_{xc} = -\left(\frac{9\pi}{4}\right)^{1/3} \frac{2}{\pi r_s} \left[1 + \frac{B}{A} r_s \ln\left(1 + \frac{A}{r_s}\right)\right] \frac{e^2}{8\pi\varepsilon\varepsilon_0 a_B} \tag{1.47}$$

$$r_s = \left[\frac{4\pi}{3} a_B^3 N\left(z\right)\right]^{-1/3} \tag{1.48}$$

This expression was obtained first in the work [85] within the Kohn-Sham density functional theory [86]. Parameters A and B can be taken from many later works.

However, in this work the exchange-correlation interaction was neglected for the reasons explained in [63].

1.4 Results and discussion

1.4.1 Energy positions and wave functions

For a given heterostructure, the spectrum of intersubband absorption and emission depend on such factors as the optical transition energies, impurity concentration, impurity ionization degree, which are presented in Tables 1.1, to 1.3. We start from comparing optical transition energies for the undisturbed wells with rectangular profile R and the same wells with the addition of Hartree potential R+H in Table 1.1. The changes in optical transition energies due to the depolarization shift are very similar for both considered profiles. So, the changes

Well profile	T, K	Center doping						Edge doping					
		L=10 nm			L=20 nm			L=10 nm			L=20 nm		
		1-2	2-3	3-4	1-2	2-3	3-4	1-2	2-3	3-4	1-2	2-3	3-4
R	77,300	11	17	24	3	5	7	11	17	24	3	5	7
R+H	77	11	17	24	4	5	7	11	15	26	7	5	7
R+H	300	15	17	25	12	7	7	18	17	24	20	12	7

Table 1.1: Transition energies between i-th and j-th subbands (in meV) for QWs doped to the center and edge of QWs at temperatures T and with different widths L. R means rectangular energy profile, R+H means a profile modified with Hartee potential. Sheet concentration of impurities is $1.2\times10^{12}cm^{-2}$.

Well profile	n_d, 10^{11}cm^{-2}	Center doping			Edge doping		
		1-2	2-3	3-4	1-2	2-3	3-4
R	6-24	3	5	7	3	5	7
R+H	6	8	5	7	15	9	6
	12	12	7	7	20	12	7
	24	17	7	8	26	14	9

Table 1.2: Transition energies between i-th and j-th subbands (in meV) for QWs doped to the center and edge of QWs with different sheet concentration of impurity n_d. Temperature 300 K, well width $L = 20$ nm. R means rectangular energy profile, R+H means a profile modified with Hartee potential

that we see here are almost exceptionally due to the Hartree potential of the delta-doped QWs. We assume that there are no changes for the rectangular energy profile within the temperature from 77 to 300 K with the error margin of 1 meV. In the table we show only the first three energies, as the others apparently do not depend on the temperature. One can see that in case of center-doped well of 10 nm, no change is exhibited at 77 K in energies, and at 300 K only the transition energy between first and second subbands is increased. The changes are more apparent for for the well of 20 nm, especially for the case of edge-doping at 300 K.

Here we see big enough changes for the energy differences 1-2 and 2-3. Also, for the different temperatures we can compare the shifts for complete energy profiles. Table 1.1 shows that the biggest changes appear in the case of wide wells, doped to the edge at room temperature. Table 1.2 shows the energies for different sheet concentrations of delta layer impurity. One can see that the concentration increase leads

n_d, 10^{11} cm^{-2}	Center doping		Edge doping	
	T=77K	T=300K	T=77K	T=300K
6	14	82	21	81
12	9	70	14	65
24	7	55	9	50

Table 1.3: Ionization degree $\frac{n_d^+}{n_d}(\%)$ for well width L=20 nm, different sheet concentrations of impurity n_d, and temperatures T.

T, K	Well profile	Center doping						Center doping					
		1-2	2-3	3-4	4-5	5-6	6-7	1-2	2-3	3-4	4-5	5-6	6-7
L=10 nm													
77,300	R	3.9	4.6	4.8	5.0	5.2	5.5	3.9	4.6	4.8	5.0	5.2	5.5
77	R+H	3.8	4.6	4.8	5.0	5.2	5.5	3.8	4.5	4.8	4.9	5.2	5.5
300	R+H	3.0	4.9	4.9	5.1	5.2	5.5	1.6	3.9	4.5	4.8	5.1	5.6
L=20 nm													
77,300	R	14	17	17	18	18	18	14	17	17	18	18	18
77	R+H	11	18	18	18	18	18	4	13	16	17	17	18
300	R+H	4	14	19	20	19	19	1.3	4	9	14	16	17

Table 1.4: Squares of matrix elements (10^{-18}m^2) for the neighboring (from i-th to j-th) subbands transitions, for the different well widths L and temperatures T. Delta layer impurity sheet concentration n_d=1.2×10^{12}cm^{-2}. R means rectangular energy profile, R+H means a profile modified with Hartee potential.

to the increase of the transition energies. The biggest growth again is for the transition between two first subbands for the case of edge doping. Table 1.3 demonstrates that the fraction of ionized impurities decreases for bigger concentration.

The dipole matrix elements for the transitions between neighboring subbands with R+H profile depend on temperature in greater degree than corresponding energy separations. Table 1.4 shows squared MEs for the first six optical transitions. For example, big enough changes in the MEs for the disturbed and undisturbed energy profiles for the wide edge doped well are demonstrated for the first five transitions while the energies changes only for the two first ones (Table 1.1). For the transitions 1-2 MEs always decrease with temperature in Table 1.4, and the biggest decrease is for the edge-doped wide well at room temperature. In the meantime, for the higher transitions, center-doped well MEs for the disturbed potential can be bigger than that for the undisturbed one. Obviously, it is due to the change in the wave functions spread in the V-shaped part of profile that changes the overlap (see Fig. 1.9).

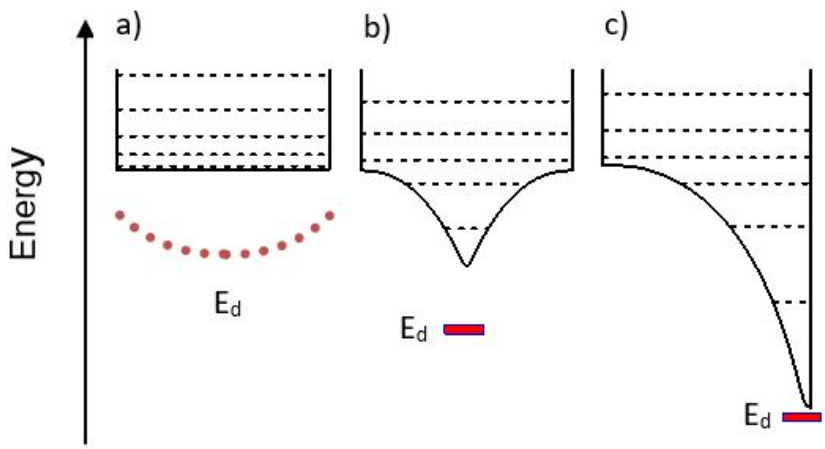

Figure 1.9: Representations of a QW energy profiles (solid lines) with a several first space- quantized energy levels (dashed lines) at temperatures 4K – a), and at elevated temperature – b), and c). Dotted line in a) show schematic dependence of a donor ground state energy E_d on the position within a QW. E_d in b) and c) show the same for center-, and edge-doped QWs.

1.4.2 Linear absorption peak changes. Estimation of tuning ranges.

Let us compare the linear absorption for the undoped (undisturbed profile) and delta-doped (disturbed profile) wells. One can see in the Table 1.1 that the biggest changes can be expected for the wide well with bigger concentration of impurity at room temperature. In Fig. 1.10 the absorption curves with mentioned parameters are shown for the rectangular profile (R), center doping (C), and edge doping (E). The vertical arrows of colors corresponding to the curves, point out the positions of the most important transition energies. For the case of center doping, the biggest peak around 10 meV, is about the same as for the rectangular well, the only exception is 2-3 absorption line, which has greater transitions energy than the others not pointed out shown in Fig. 1.10, and the largest energy is for 1-2 transition, which is the result of delta layer ionization. The delta layer in the well center does not change the structure symmetry and so the selection rules are the same for rectangular and center-doped wells. In turn, the edge-doped well absorption strongly differs both in amplitude and shape from that of the rectangular well, which is also the result of the delta-layer ionization. Mostly it exhibits in the blue shift the two first absorption lines. Table 1.4 shows that MEs of all considered transitions in case of edge doping are lesser than ones for the case of center doping so the peaks for edge doped well are smaller. Edge doping breaks the

symmetry of the well, so the selection rules change and the transitions between states of the same parity are now allowed.

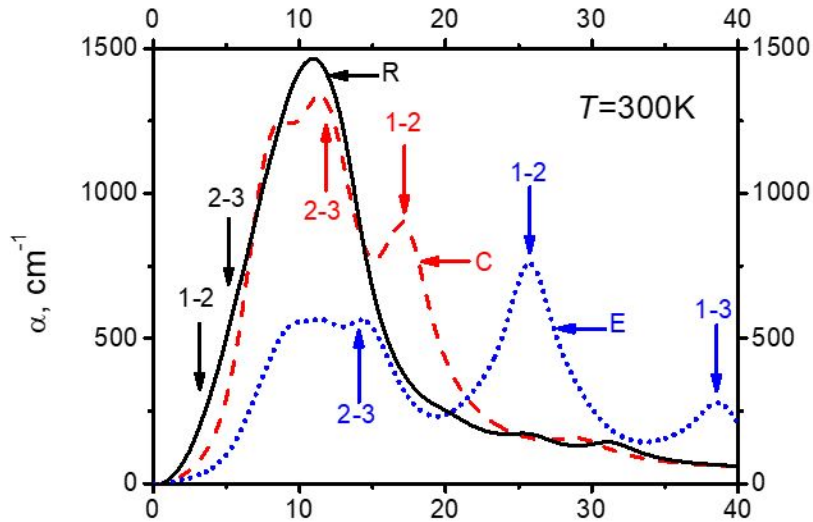

Figure 1.10: Absorption coefficients for: R - pure rectangular QW; C - center-doped QW; E – edge-doped QW. Vertical arrows show the optical transitions between 1-2, 2-3, and 1-3 energy subbands. QW width $L = 20$ nm. Impurity concentration $N_d = 2.4\times10^{12}\text{cm}^{-2}$.

Now let us see how the degree of ionization of the delta layer impurity influence the absorption of both the edge- and center-doped structuress. The numerical results are presented in Fig. 1.11. We marked the graphs and some transition energies with horizontal and vertical arrows in the same way as in Fig. 1.10. Letter "C" corresponds to center doping, letter "E" – to the edge doping. The ionization degrees for the cases of Fig. 1.11 one can see in the in Table 1.3. We used the different scales for the absorption coefficient for the room and nitrogen temperatures, as in these two situations the number of carriers participating in intersubband transitions is very different due to Fermi statistics and so the absorption coefficient changes very much as well. One can see that the absorption coefficient behaves differently for the center- and edge-doped wells all along the spectral scale at both temperatures. Let us see why it happens. In the left side of the figure one can see that at nitrogen temperature the absorption for the smaller energies up to 5 meV center-doped QW is higher than that for the edge-doped one at the "red" end of the spectrum is greater for the center doped well. Though the ionization degree is greater for the case of edge doping – see the Table1.3 The reason for that is the center-case smallest transition energy is of 4 meV, while the edge-case one

is of 5 meV and the absorption amplitudes are approximately equal. From the Table 1.1 is seen that transition energies are increased starting from the first center-case transition, exactly like in rectangular wells. It means that Hartree addition there is relatively insignificant and increases 1-2 transition energy only slightly. However, in edge-case Hartree addition is deeper and now the first subband edge is deeply inside the V-shaped part of the well, so the first transition energy increases strongly and now is greater than the second (2-3) transition energy. All further transitions follows the rule of increasing energy in both cases and are within the range from 5 to 11 meV. Note that doping to the center-doping does not break the symmetry and does not alter selection rules while doping to the edge does. So, the forbidden for the symmetric wells transitions like 1-3 or 1-5 now are allowed. In the right side of the figure (and Table 1.1) we can see that the first transition has the biggest energy among the transitions for the closest subbands in both cases. So, the other transitions starting from the first subband also move to higher energies with temperature. For example, see the positions of 1-3 transitions for the edge–case in Fig. 1.11 a and b. Also, the absorption for the center-case is notably greater than that of the edge-case in the lower energies range, but later, after 17 meV, it is reversed. The explanation is given before, when we compare the matrix elements (see also Table 1.4).

To show the influence of the delta layer impurity concentration on the absorption we present the Fig. 1.12 with the results for edge-case with different concentrations. The corresponding concentration magnitudes in units of 10^{11}cm^{-2} are marked next to the horizontal arrows. With the vertical arrows we mark only 1-2 and 1-3 transitions, which are most influenced by the concentration of impurities. Other notable absorption lines have lesser energies for all the curves. We have already discussed the absorption for the edge-case with concentrations 12 and $24\times10^{11}\text{cm}^{-2}$ when considering the Fig. 1.10 and Fig. 1.11 b. Here we only can add that increasing concentration leads to the increasing transition energies mostly for the transitions from the ground state. Also the ionization degree is different even for the same room temperature (see Table 1.3). However the absolute charge concentration increases with impurity concentration anyway, and, accordingly, the disturbing potential grows bigger.

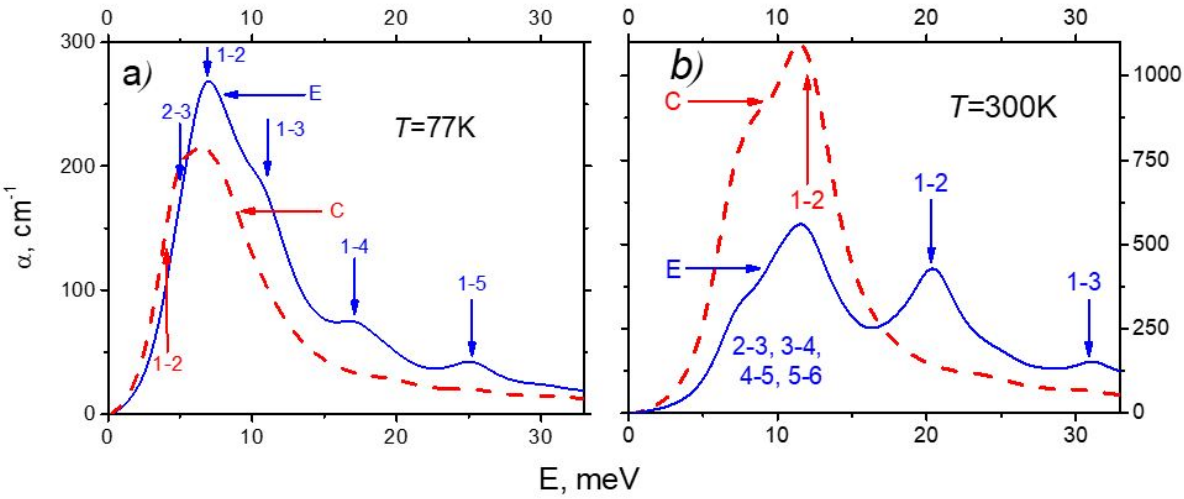

Figure 1.11: Absorption coefficients for center- (dashed lines), and edge-doped (solid lines) QWs for temperatures T = 77 K – left panel and T = 300 K – right panel. QW width L = 20 nm. Total impurity concentration N_d=1.2×10^{12}cm^{-2}. Letters E and C denote the optical transitions for edge-doped and center-doped QWs respectively. Note different vertical scales for left and right panels.

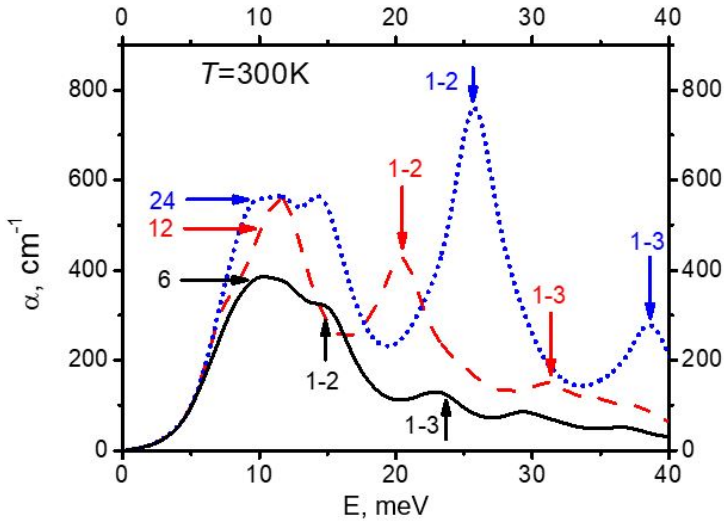

Figure 1.12: Absorption curves for edge-doped QW with different impurity concentrations, shown next to horizontal arrows in the units 10^{11}cm^{-2}. Vertical arrows show optical transitions. QW width L=20 nm.

The Fig. 1.13 demonstrates the influence of the delta doped well width on the absorption. Here one can see the curves of absorption coefficient for a narrow (marked with letter "N") and a wide (marked with letter "W") wells having respective widths of 10 and 20 nm. Both structures are doped to the edge of the well with sheet concentration of

Phosphorus n_d=1.2×10^{12} cm^{-2}. We have discussed the wide wells at nitrogen temperature in the comments for the 1.11 a for the edge-case. Here we mention that 3-4, 4-5, 5-6 energies occure between 2-3 and 1-3 lines for the wide well. Now, let us discuss a narrow well. One can see that all of the absorption lines have greater energies than the ones of the wide well. More interesting is that the sequence of the first three lines (1-2, 2-3 and 3-4) is "regular", while for a wide well, the lines 1-2 and 2-3 have the opposite order, despite of the ionization degrees are very similar, namely 14% for the wide well and 12% for the narrow one. Our results show for the wide well the ground level is inside the narrower V-shaped part of the well, while for the narrow well it is still in the rectangular part. So, the negatively charged electrons in the first subband in case of the wide well are concentrated in the narrower part of the well, more close to the positive ionized delta layer that makes the potential distortion deeper than the one of the narrower well. As a result the ground level goes deeper and first transition is bigger than the second for the wide well and lesser for the narrow one. Thus, ionized delta-layer has bigger influence on the wider well.

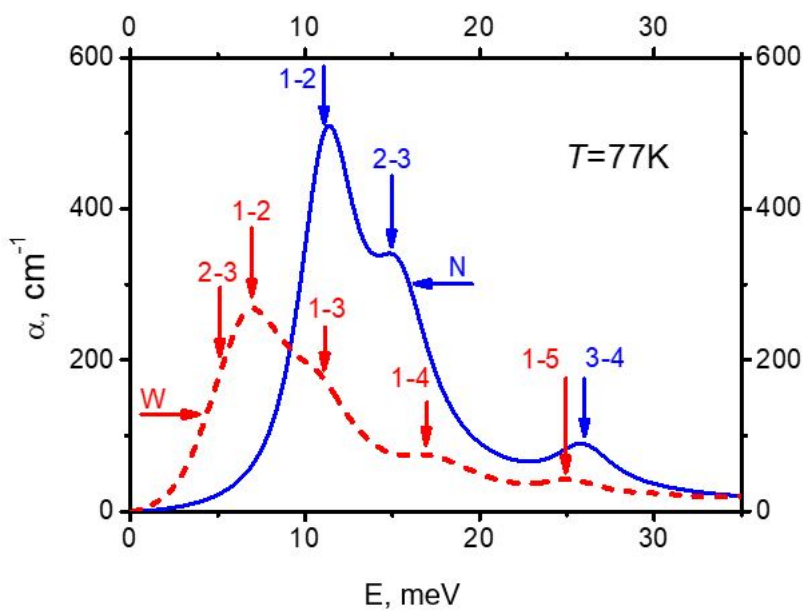

Figure 1.13: Absorption curves for a narrow – capital letter N above the horizontal arrow, and a wide – capital letter W above the horizontal arrow, QWs. The widths of the QWs: L = 10 nm and L = 20 nm for N and W letters correspondingly. Vertical arrows show some specific absorption lines. Degrees of ionization are 12% and 14% for narrow and wide QWs accordingly with total impurity concentration N_d=1.2×10^{12}cm^{-2}.

	Energy level, meV									n_d^+/n_d, %	n,10^{12} cm^{-2}
	E_f	E_1	E_2	E_3	E_4	E_5	E_6	E_7	E_D		
Center											
77K	-19.6	-0.7	3.1	7.6	14.3	22.6	33.0	45.2	-30	9	10.8
200K	-44.3	-9.2	-0.6	4.3	10.9	19.0	29.4	41.4	-32.6	50	60.0
300K	-72.4	-14.4	-3.3	2.6	9.1	17.1	27.4	39.4	-33.4	70	84.0
Edge											
77K	-15.0	-6.5	-0.3	4.1	10.4	18.7	28.9	41.0	-23.4	14	16.8
200K	-39.5	-26.0	-10.3	-1.8	4.1	11.6	21.3	33.2	-28.8	48	57.6
300K	-66.6	-35.5	-15.8	-4.6	2.1	9.1	18.6	30.2	-30.0	65	78.0

Table 1.5: Energy positions of size-quantized subbands, Fermi energy E_f, IBE E_D, degree of ionization n_d^+/n_d and free electrons surface density n for the center and edge-doped wells for different temperatures. E_D and E_f are given relative from the first subband E_1.

1.4.3 Influence of nonlinearity on the absorption and refraction

In Fig. 1.14 shows the energy profiles and wave functions of first 7 first subbands (that have been accounted for), zero of WFs correspond to the respective energy position: a) center-case, b) – edge-case. It is the biggest profile distortion at room temperature. Table 1.5 represents the calculated subband energies, Fermi level and impurity ionization degree for the temperatures of 77, 200, and 300K.

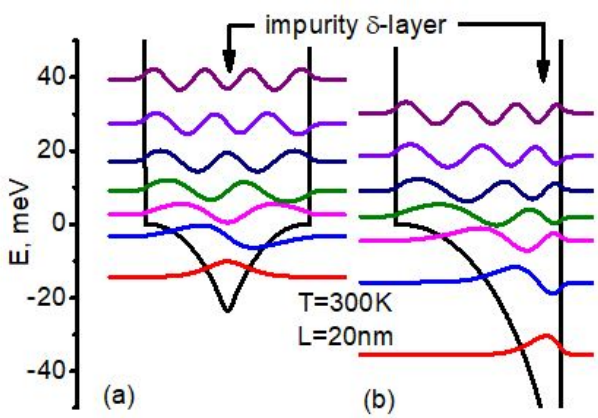

Figure 1.14: Energy profiles and first wave functions for our structures at T=300K.

The distortion potential of the positive delta-layer and negative electrons in subbands adds a V-shaped well inside the rectangular well formed by the material band discontinuity. As a result, the most notable differences between the two cases are the following. First, deeper V-shaped well in the edge-case that leads to the greater energy of the first transition. Second, the asymmetry of edge-doped well alters the selection rules and permits the transitions between the states of the

same parity. It is also true for the other temperatures though pronounced in a lesser degree. The Fig. 1.15 repeats some curves from the previous figures as for the linear absorption and adds the nonlinear part with a reasonable laser intensity I=0.5 MW/cm^2

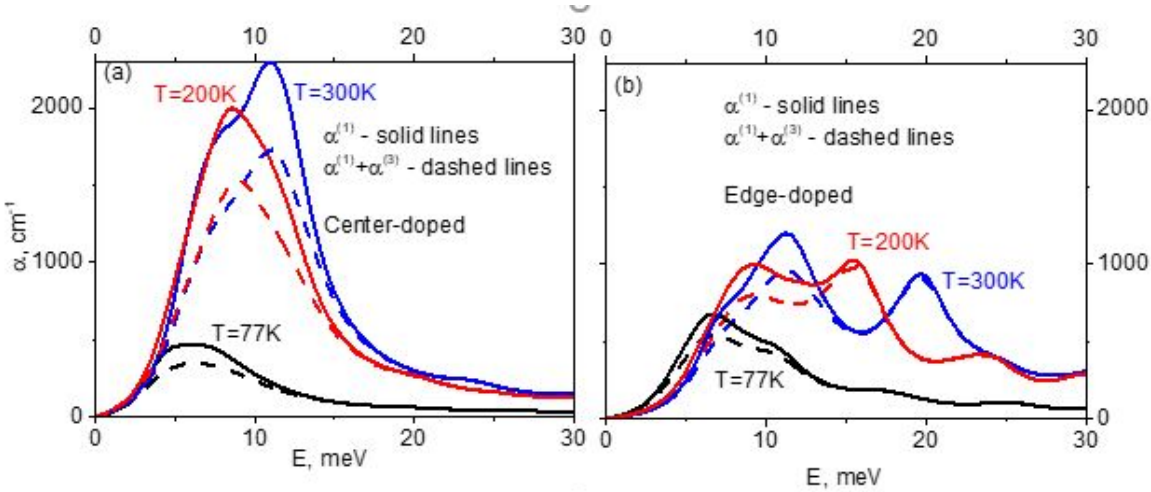

Figure 1.15: Absorption coefficient of the QW structures doped to the center (a) and edge (b) for the different temperatures. Solid lines – linear absorption, dashed lines – total absorption with Kerr-type nonlinear part, laser intensity I=0.5 MW/cm^2.

Nonlinear Kerr-type absorption is always negative. In our model it is proportional to the incident radiation intensity and can be extrapolated to different magnitudes of I. The selected intensity gives relatively big nonlinear part, but not enough big to make two absorption peaks of one like, for example, in [87]. For bigger intensities this model is hardly adequate. The nonlinear part of absorption makes biggest relative decrease in the vicinity of the absorption peaks. However, for the edge-case at high temperatures (see Fig. 1.15 b) the nonlinearity has lesser influence on the peak caused mainly by the first transition (1-2), than on the first peak (2-3, 3-4 etc.). This is because the nonlinearity percentage of the transitions between the higher levels is greater than for the lower levels. For the same reason the relative nonlinearity for the wide wells is bigger than that for two-level systems.

The change of refractive index due to nonlinearity (Fig.1.16) small and hardly should be accounted for in electronic devices. Surprisingly, the linear and nonlinear parts refractive index change have the same order of magnitude. However, within an accepted approximation [81] that the absorption is the imaginary part of complex susceptibility and the refraction change is the real part, the nonlinear part should

be lesser than the linear one, and this assumption is fulfilled. For the refractive index change, he result of the combination of linear and Kerr-type nonlinear parts, which have the opposite signs, the nonlinearity decreases the absolute value of the total change around in the maximum areas to a few percent. So, the whole complex structure of subbands makes many jumps.

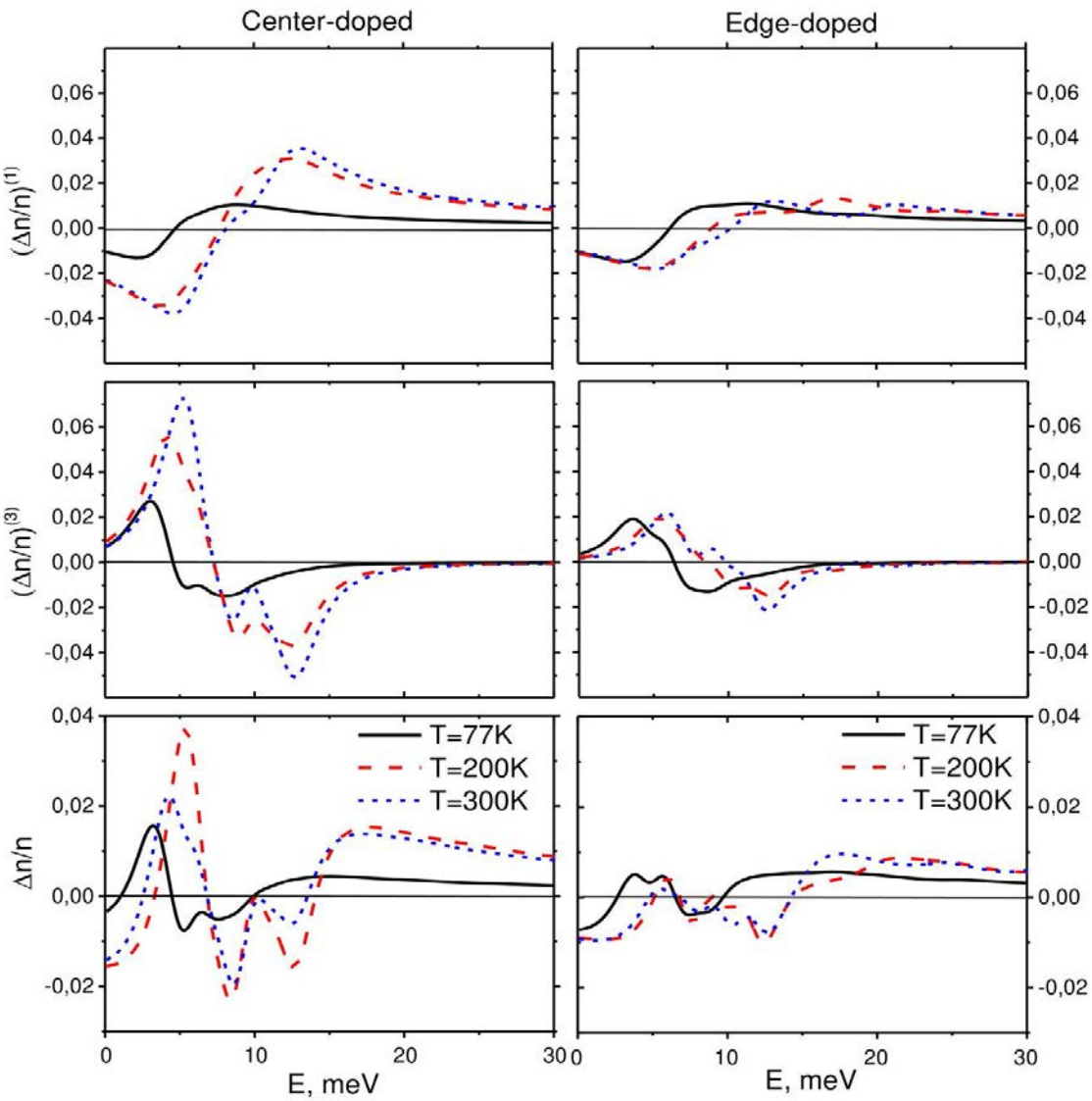

Figure 1.16: Linear, nonlinear and total (from up to down) relative refraction coefficient change of the QW structures doped to the center (left column) and edge (right column) for the different temperatures.

1.4.4 New type of THz modulator

The characteristic parameter of any modulator is the the ratio of maximum and minimum passing radiation intensities Imax/Imin. Ac-

cording to Beer's law it is proportional to $e^{(\alpha_{max}-\alpha_{min})L}$ with L being optical path in the active medium, α_{max} and α_{min} being the maxi-mum and minimum absorption coefficients for a given frequency. Let us see from this viewpoint on our results, which are shown in Figs. 1.17, 1.18 for narrow, and Figs. 1.19, 1.20 for wide wells (10 and 20 nm correspondingly). Obviously, the biggest influence of the impurity ionization degree on the relative structure transparency is expected for low temperatures, all electrons in equilibrium are not ionized and there is no intersubband absorption at all ($\alpha_{min} = 0$). On the other hand, the higher temperature of operation implies much larger range of po-tential applications. So, we calculated both for helium and nitrogen temperatures. To analyze the results, one should remember the following. First, two-dimensional electron gas in quantum well subbands can absorb only the photons polarized along z direction. Second, for the narrower well width the transition energies between the closest subbands are notably bigger than ones for the wider well. Third, here we assume that the electron effective temperature here defines the electron distribution in the subbands, but the impurity ionization degree is independent and may correspond to the equilibrium of much higher temperatures. Such situation can be achieved with application of very short impulses of longitudinal electric field, that ionizes the impurity.

The Fig. 1.17 depicts the absorption coefficients for the narrow well with two impurity ionization degrees for 4 and 77K, delta layer is in the center. As we expected, the largest ratio I_{max}/I_{min} is at 4K, which provides the maximum absorption difference for two impurity ionization degrees. Note that center doping does not alter the structure symmetry and the optical selection rules in a well are like in the rectangular well, that is transitions between the states with the same parity are prohibited. At nitrogen temperature all the excited electrons are in the ground subband and there is only absorption peak that corresponds to 1-2 transition. At nitrogen temperature some fraction of electrons appear in the higher subbands, and the is an addition from 2-3 and even 3-4 transitions. As a result, the biggest absorption line reduces in magnitude.

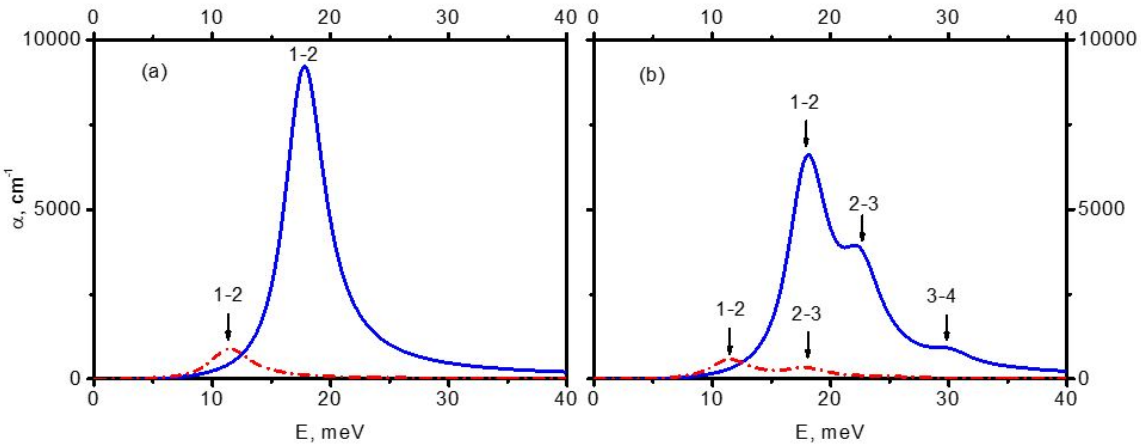

Figure 1.17: Absorption coefficients for center-doped 10nm-wide QW structure. Electron temperature T=4K (a) and 77K (b). Degree of ionization - 6% and 61% for dashed and solid curves accordingly. The peaks corresponding to intersubband optical transitions are also shown.

The edge-case results are shown in Fig. 1.18. Here for helium temperature (Fig. 1.18 a) appears the additional absorption line 1-3, which is now allowed due to the symmetry break (see Fig.1.9). Consequently, now the main peak is less in magnitude then the one in center-case. Higher temperature with the same impurity ionization degree (Fig. 1.18 b) leads to the electrons appearance in the higher subbands. As a result, the main peak decreases further, and 2-3 transitions appear.

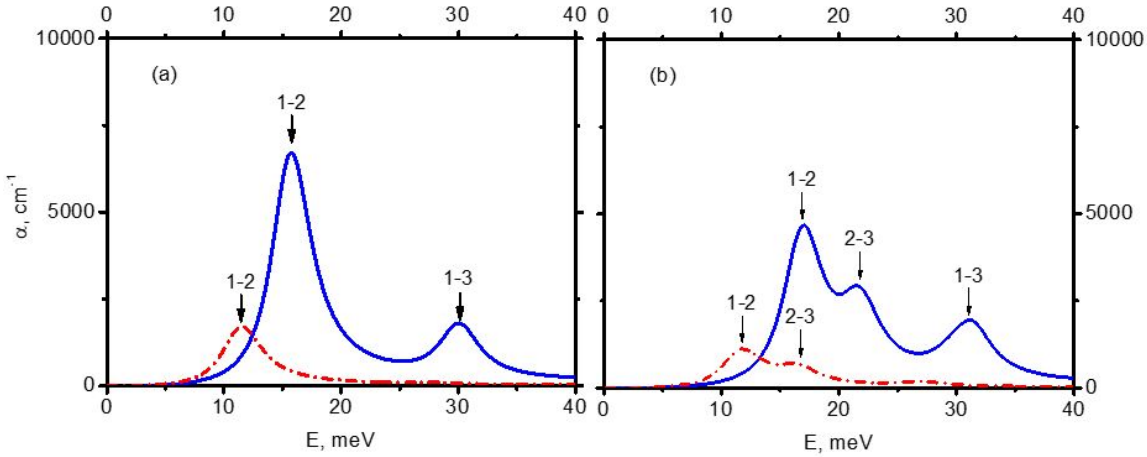

Figure 1.18: Absorption coefficients for edge-doped 10nm-wide QW structure. Electron temperature T=4K (a), and 77K (b). Degree of ionization - 63% for solid curves and 12% for dash-dot curves. The peaks corresponding to intersubband optical transitions are also shown.

Figs. 1.19 and 12 present the results for the wider well of 20 nm and are interesting to compare to the ones of 10 nm-wide well. Fig. 1.19 shows two additional relatively small peaks for 1-4 and 1-6 transitions in case of the higher ionization degree due to the decreased subband

distances in wider wells. The main peak energy (still corresponding mainly to 1-2 transition) has lesser energy for the same reason. On the other hand, the main peak now includes the effect of transitions 2-3, 3-4 and 4-5 that make it broader instead of presenting separate visible peaks.

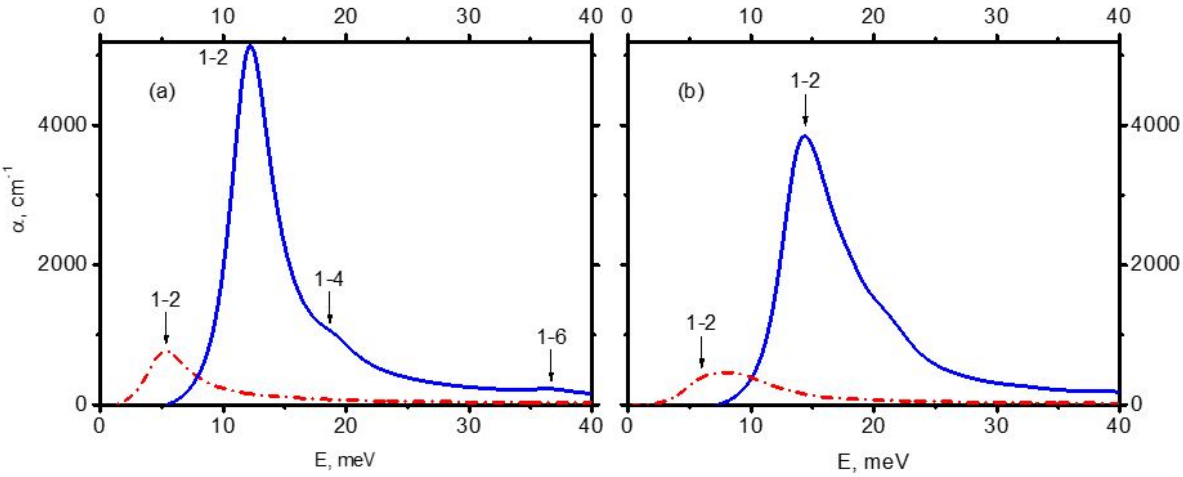

Figure 1.19: Absorption coefficients for center-doped 20nm-wide QW structure. Electron temperature T=4K (a) and 77K (b). Degree of ionization - 6% and 61% for dash-dot and solid curves accordingly. The peaks corresponding to some specific intersubband optical transitions are also shown.

Now let revise Fig. 1.20 with quite unusual results. On the left panel all the notable peaks are for the transitions from the ground subband, which is still in line with our previous analysis of Figs. 1.17-1.19. It is true for the right panel as well, however, for higher ionization degree all transition energies are now shifted about 8meV towards higher energies comparing to the left panel, while for the lower ionization degree of ionization the shift is about 2meV, nearly the same as in Figs. 1.18-1.19. It can be explained as follows. At helium temperature only the ground subband is occupied by electrons, and the negative charge mainly concentrates near QW center and the Hartree potential "digs" a very narrow v-shaped well. As a result the ground subband is pushed up in energy to the wider region of dug out by Hartree potential QW. So, the energy difference between the ground and the rest of subbands is not very different in comparison to the rectangular well. At nitrogen temperature electrons are distributed among few lower subbands and the charge is spread over the well width. It means that Hartree well becomes wider but still narrower than the big rectangular well. Now it contains more levels that have greater energy separations.

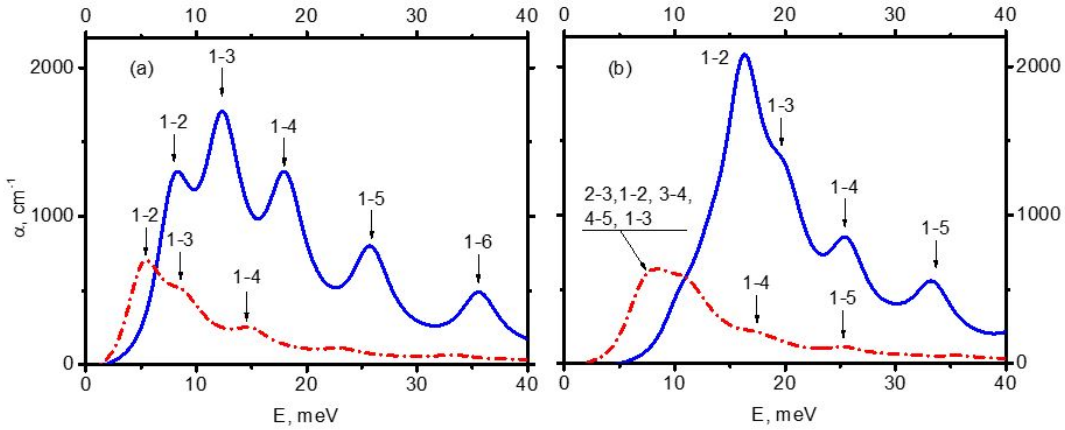

Figure 1.20: Absorption coefficients for edge-doped 20 nm-wide QW structure. Electron temperature T_0=4K (a) and 77K (b). Degree of ionization - 14% and 65% for dash-dot and solid curves accordingly. The peaks corresponding to some specific intersubband optical transitions are also shown.

Figs. 1.17-1.20 demonstrate two dominant peaks for two impurity ionization degrees. It shows that absorption tuning of the structure under study in the range that corresponds to the differences in peak positions can be performed by relatively small lateral electric field. Fig. 1.21 depicts the mentioned range of tuning according to our calculations. Each frequency presented case has its magnitude of ratio I_{max}/I_{min}. However, for some purposes the high ratio is required, for other purposes it more preferrable to have broader tuning band, while in some cases the goal is a simultaneous modulation of various lines. The goals can be reflected in particular features within the same general design framework. Note that additional tuning or adjustment to the particular environment condition can be done by varying temperature [88]. The probable complication in the implementation of the design can be instability at helium temperature due to the impurity breakdown in small electric fields [89]. Though the application of a small magnetic field [90], higher electric field allows to avoid this effect. At higher temperature it is not expected to be a problem.

1.4.5 Influence of transversal electric field

Fig. 3 of [53] depicts a binding energy of the impurity as a function of the width of the QW made of the same materials as in our work. We used that work as a numerical verification for our method. Fig. 1.22

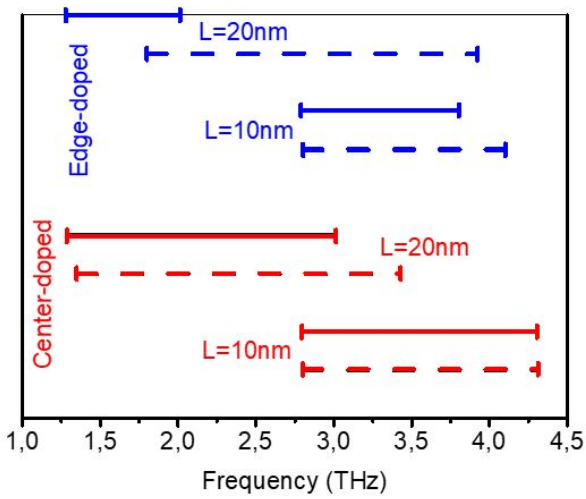

Figure 1.21: Spectral range of tuning for our structures (motion of the peak position with increasing ionization degree) for the considered degrees of impurity ionization: solid lines – T=4K, dashed lines – T=77K.

contains the comparison between our results and theirs, specifically, IBE in the well center for hydrogenic impurity. The graphs are in a good agreement if the well is narrow enough. For our maximum well width of 20 nm the correspondence is quite good. In the extreme situations of infinitely narrow and infinitely wide well IBE, obviously should be equal to the one of the bulk materials of the well and of the barrier correspondingly. In our calculations for narrow wells we used external quantum box with infinite barriers positioned at the distance of 10 nm from each heterojunction. As for the wide well limit, note that we make calculations for the case of uniformly stressed material, which is not true in case of bulk material or wider wells, and we believe that is the main reason of disagreement, starting after 20 nm.

Fig. 1.23 illustrates qualitatively and quantitatively what happens to the profile of our structure. The energy profile of QW under bias is shown there along with WFs of the two first subbands (zero WF corresponds to the subband energy position) and impurity level E_d for the non-ionized (temperature 4K) and ionized (temperature 300K) impurity delta-layer in the well center. The energy difference ΔE_{12}=E_2-E_1 characterizes the intersubband optical transition and its change corresponds to the tuning range. IBE is the distance between the impurity level and the first quantized subband E_1-E_d.

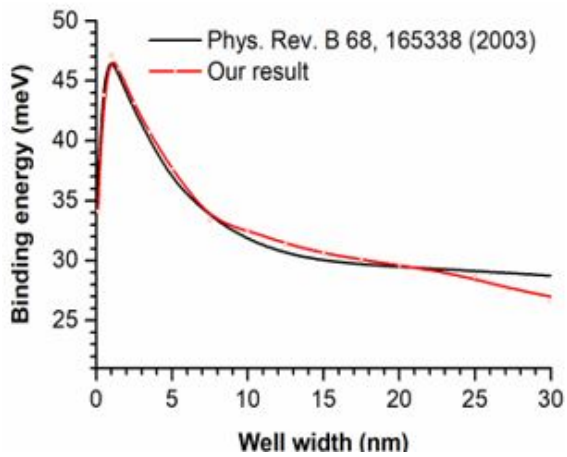

Figure 1.22: Impurity binding energy in the senter of $Si_{0.8}Ge_{0.2}/Si/Si_{0.8}Ge_{0.2}$ quantum well against well width. Comparison between our results (red) and the results from [15].

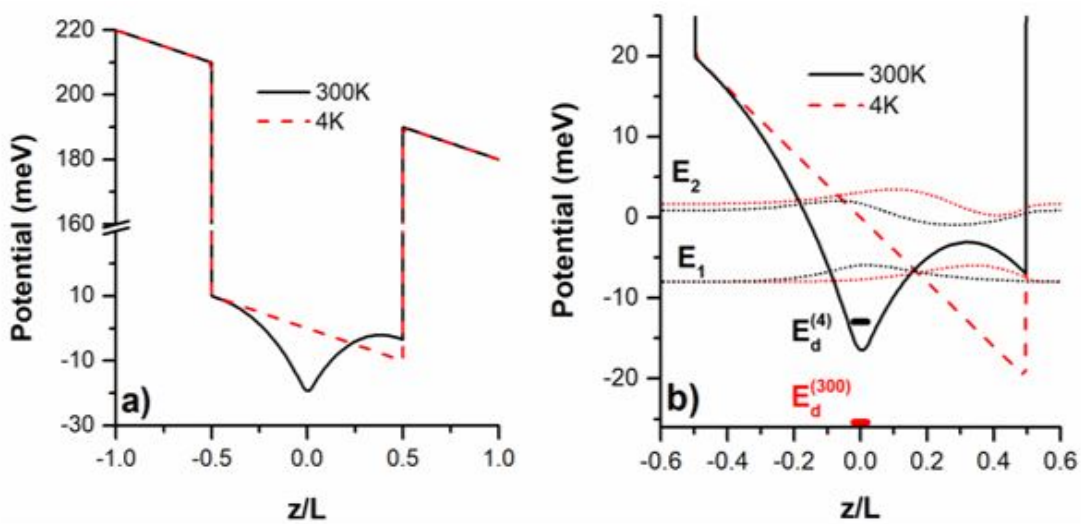

Figure 1.23: QW profile with the well width of 20 nm in the applied electric field of 20kV/cm. Red dash line correspond to the case of no ionized impurity. Black solid line correspond to the same well with an ionized impurity delta layer in the center with ionization degree and electron statistics corresponding to the equilibrium of room temperature. L is the width of the well. (b) is the zoomed in lower part of (a) with the addition of impurity levels and two first wave functions.

The results for 20 nm wide QW are shown in Table 1.6, for the ionized (T=300K) and non-ionized case for the different strengths of external electric field. ΔE_{ij}=E_j-E_i are the energy differences between subbands.

Analyzing the first energy distance, we can see that the electric field growth leads to its monotonous and strong increase for the case of 4K about 9 times, while its behavior for 300K is opposite: it decreases more than 2 times. Our qualitative interpretation of such a phenomenon is based on the concept of two mini-wells that appear in

T, K	E, kV/cm	ΔE_{12}, meV	ΔE_{23}, meV	ΔE_{34}, meV	ΔE_{45}, meV	ΔE_{56}, meV	ΔE_{67}, meV	ΔE_{78}, meV	ΔE_{89}, meV	E_d, meV
4	0	2.84	4.71	6.6	8.47	10.34	12.19	14.01	15.9	29.6
	10	6.12	5.46	6.51	8.39	10.34	12.25	14.13	15.97	26.35
	20	9.67	7.94	7.37	8.22	10.06	12.05	13.99	15.87	20.94
	50	17.78	14.56	12.87	11.77	11.17	11.56	13.13	15.16	9.93
300	0	11.09	5.83	6.53	7.97	10.36	11.96	14.09	15.73	33.86
	10	10.18	6.18	6.89	8.23	10.32	12.11	14.17	15.88	33.63
	20	8.81	7.27	7.7	8.66	10.05	12.1	14.02	15.86	33.35
	50	4.78	10.79	11.21	10.74	10.92	11.8	13.45	15.52	30.64

Table 1.6: IBE and intersubband energy distances in transverse electric field.

the bottom of our bigger well as a result of its distortion by the external field and the Hartree potential of delta-layer ionization. The Hartree well is formed in the middle of the bigger well, where the delta layer is positioned. Its mechanism is described in the previous sections. The field well appears at the right edge of the greater well result of applied bias (see Fig. 1.23). The first well grows with the ionization degree od delta-layer impurity (which can be regulated either by temperature or by the longitudinal electric field), while the second one grows with the transverse electric field. Each well is narrower then the originan and when one of them is dominant, the ground subband goes down to that dominant well and the energy of the first transition grows. However, when two mini-wells are comparable, the two first WFs distributes between them and the energy distance decreases.

According to the Table 1.6 the variation of the next energy distances gradually decreases that confirms our conclusions. Mini-wells influence strongly on the first few subbands, but the differences between the upper levels, which are far from bottom and are defined by the characteristics of the whole greater well, are stable.

So, if we try to design the structure that allows to obtain larger tuning range $|\Delta E_{12}|_{T=300K} - \Delta E_{12}|_{T=4K}|$, for such a configuration, we can manipulate external fields to balance the mini-wells to decrease the transition energy or disbalance them to increase the one. Interestingly, such a configuration permits much bigger tuning range in comparison to the situations in the previous sections and adds more flexibility for tuning. Moreover, in this case we don´t need to rely on lower temperatures like 4 or 77K to get the whole possible range.

As for the impurity binding energy, Table 1.6 shows that in 300K case it does not depend much on the field strength, while for the 4K case it decreases uniformly with the field, so that its final magnitude about three times less. We can explain it in terms of Coulomb interaction strength. Fig.1.23 demonstrates that under the bias the lower part of the well moves to the right, and energy levels descend with respect to the impurity position. As a result, most of the WFs moves away from the positively charged impurity and the Coulomb interaction weakens. Indirectly this logic can be confirmed by the fact ([53]) that in rectangular well the binding energy decreases near the edges, and here again we have the situation when electron WF moves away from the impurity ion. In the ionized case, the Hartree potential makes mini-well near the delta-layer and the electron WF now is localized there so the interaction is strong and IBE is big.

1.4.6 Influence of background impurity

Transition to the limit of undisturbed rectangular QW

First let us discuss the reliability of our model and results. In absence of experimental data that can be used as a reference point (we did not find any in literature), we used theoretical work [53], which used different method (full Hamiltonian diagonalization) to calculate IBE for the similar structure, but only rectangular profile. In that particular case our results are in good agreement with theirs (see the comparison in the previous section). Additionally, many other works [24,34,40,49,91] confirm that IBE at the edge of QW is significantly less than that at the center. It confirms the reliability of our method in particular cases so we can move further and account for the BI. So, to check the results obtained with BIs we can look for their convergence with the results without BIs. Therefore, we calculated the case of low BI concentrations at low temperatures, when the delta layer is not ionized and the profile for different BI concentrations looks like is shown in the main panel of Fig. 1.24.

Here we can see that for lower concentrations QW shape becomes indistinguishable from the rectangular, which is the conceptually obvious result. Table 1.7 demonstrates the IBE magnitudes (which is the difference between the ground subband and ground impurity state) for delta layer impurities both in the center (ε_δ^c) and in the edge (ε_δ^e)

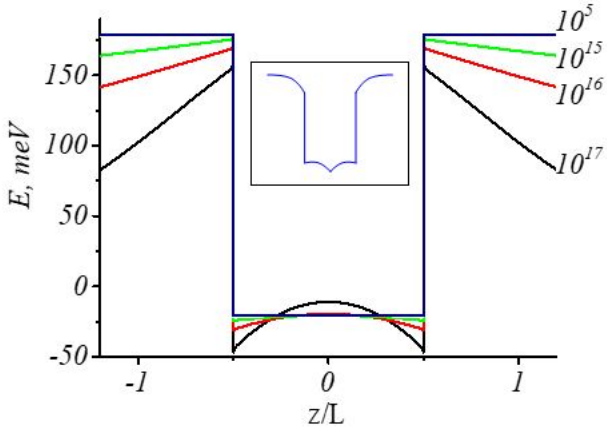

Figure 1.24: Energy profiles of QW at T=4K. The numbers next to curves indicate the concentrations of background impurities in cm^{-3}. In the insert in the center of the figure the QW energy profile for a concentration of 10^{12}cm^{-2} at a temperature of 300K is shown schematically.

of the well, energy distances between the neighboring subbands, and electron sheet concentrations electrons in the well (n_{QW}) for different BI concentrations. This well is relatively wide for a silicon and in case of center doping the well positioned IBE is almost the same as in bulk silicon (29.0 and 29.6 meV correspondingly) with the latter is obtained by variational technique within the effective mass theory [66], and it is the additional verification for our results. All the data of the Table 1.7 have a kind of limit in the case of N_b=0, that is a pure rectangular QW. Again, a reported good convergence was made possible only by accounting for the subbands positioned about bulk conductance band edge (positive energy subbands). It illustrates why exactly we needed the algorithmic complications described in the corresponding section. Second thing to note is that the energy differences are the same for two kinds of delta-layer positionind only at low temperature. For higher temperatures it is not the case.

Results at temperature 4K

Let us start from the delta layer impurity binding energies. Table 1.7 shows the biggest variation for highest BI concentration (last column): edge-case IBE is greater than for the center-case. It contradicts to the results without BIs (first column). We mentioned that edge-case IBE is lesser center-case ones for the rectangular well according to many sources. The decrease BI concentration leads to the change of their

N_b, cm^{-3}	*0*	*10^5*	*10^{12}*	*10^{15}*	*10^{16}*	*10^{17}*
ε_δ^c, meV	*29.6*	*29.5*	*29.5*	*28.9*	*28.1*	*25.6*
ε_δ^e, meV	*17.0*	*17.0*	*17.7*	*19.7*	*22.3*	*26.5*
ΔE_{21}, meV	*2.9*	*2.9*	*2.8*	*2.1*	*1.4*	*0.4*
ΔE_{32}, meV	*4.7*	*4.7*	*4.8*	*4.7*	*4.8*	*5.9*
ΔE_{43}, meV	*6.7*	*6.7*	*6.7*	*6.6*	*6.6*	*6.0*
n_{QW},cm^{-2}	*0*	*10^6*	*1.2×10^8*	*1.0×10^{11}*	*3.2×10^{11}*	*8.6×10^{11}*

Table 1.7: IBE for the wells delta-doped to center ε_δ^c, and edge ε_δ^e, sheet concentration of electrons in the well n_{QW}, and energy differences between nearest subbands ΔE_{ij}, for the different concentrations of BI N_b. T=4K.

behavior: center-case IBE increases, while edge-case one decreases and finally results in the regular "rectangular" behavior. So, we gained an uncommon result. Fig. 1.25 is used to explain it. There zero energy is the bottom of conduction band far from depletion region. We can compare the dynamics of the WF against BI concentration with the one of tunnel-coupled symmetric QW (for example, see [92]) with the variable middle barrier width. The profile distortion forms two pockets near the heterojunctions, that act as QWs, and a hill between them acts as a barrier that grows for bigger BI concentration [93, 94]. Something similar was presented in [95], but without proper discussion. As soon as all delta layer impurity centers at low temperature are neutral, the curves for the different delta layer concentrations are the same. Here we suppose that the influence of the first subband WF on the IBE is the biggest though for the numerical calculation we used 7 subbands (for lower temperatures).

It is seen in Fig. 1.25 that the electron WFs for the first subband are displaced towards the heterointerfaces with increasing BI concentrations, so the Coulomb interaction with impurity in QW center weakens and IBE decreases. For the edge impurity the situation is opposite: one of the electron density peaks moves toward the impurity, and IBE increases.

Now about the energy differences. Table 1.7 shows us that they don{t change much for BI concentrations from 10^5 to 10^{15}cm^{-3}, when the pockets near barriers are negligibly small (Fig. 1.24). For the

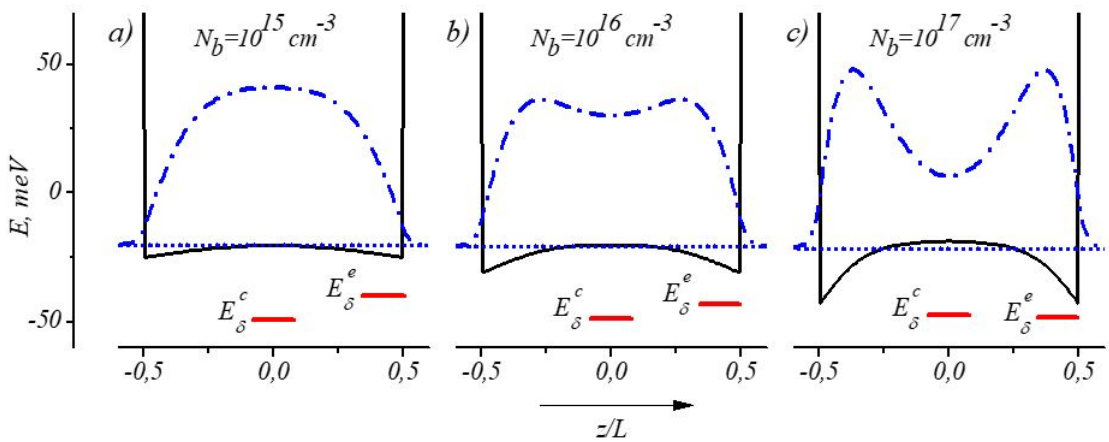

Figure 1.25: Energy profiles (solid black lines), first space quantized energy levels and their wave functions (blue dotted and dot-dashed lines accordingly), and ground impurity states for center-, and edge-doped QWs (short red solid lines) for the different concentrations of background impurities. Temperature T=4K. At this temperature each curve is the same for both concentrations of donors in the delta layer used: n_δ=0.6×, and 1.2×10^{12}cm^{-2}. All the wave functions are in the same scale. The zero of energy is at the bottom of the conduction band in barriers far away of the depletion layers.

upper levels the distances increase monotonically in the same way it happens in rectangular QW. Obvious alteration to this rule happens only for BI concentration of 10^{17} cm^{-3} , where ΔE_{12} is very small and ΔE_{23} is relatively big. This is the situation, when the first two levels correspond to the symmetric mini wells formed by pockets near barriers and the third level mainly belongs to the whole well. Therefore, small ΔE_{21} is a result of the degeneracy removing in two identic tunnel-coupled wells. Something similar, but to a lesser degree happens in case of BI 10^{16}cm^{-3} , while for 10^{15}cm^{-3} the first level does not with the central barrier the general rules for the rectangular well from now on are dominant.

The electron concentrations in the well (Table 1.7 last line) are controlled by the barrier impurities, so in this case we should expect a notable intersubband absorption even at helium temperature.

Higher temperatures. IBEs and the electron concentrations

Now let us discuss the case of partly ionized delta layer donors, the data is shown in the Table 1.8. There are IBEs (only for center-case), the sheet electron density in the well, ionized donor density in the delta-layer and Fermi level positions at different BI concentrations at T= 77

and 300K for two different delta layer donor concentrations. Note that Fermi level does not depend on delta layer donor concentration as it is defined by the bulk barrier material. For the cases marked (N_b=0) the Fermi level was found as for the MQW structure using different electro neutrality condition so we did not put it to the table to avoid confusion. Fig. 1.26 illustrates the situation discussed. In the upper part of the figure (a, b and c) the well energy profiles are shown in the same scale. (The specific case of very low BI concentration (10^{12}cm^{-3}) is discussed separately.) Like in Fig. 1.25 here we present only the lower part of the well profile as the most relevant for our discussion. The energy has the same scale multiplier everywhere, but the origin is shifted for better representation of our arguments as described in the figure caption.

In general, blue lines correspond to the room temperature, red ones to the nitrogen ones, solid lines correspond to the higher delta layer concentrations, dashed or dotted ones to the lower one. The lower part of the figure (d, e, f) depicts the wave functions of the ground energy level (again the same scale multiplier). We did not present the curves at T = 4K as they are indistinguishable from those at T = 77K. Besides, they are presented in the previous figure. From Fig. 1.26 we can conclude that the shape of QW bottom is determined by the electrons that come from two sources. First, there are electrons from BI in the barriers and they make the mini wells adjacent to the heterointerfaces. Second, there are electrons from the ionized delta-layer and they form the V-shaped potential well in the center (along with the ionized donors). So the that bigger BI concentration leads to the deeper "side pockets", while delta-layer ionization leads to the deeper central mini well.

At nitrogen temperature the delta layer ionization is less than 10% (see Table 1.8) and the well bottom shape is defined by the domination of side pockets near the heterointerfaces so that the situation is similar to that at helium temperature. Second, for the same reason in this case the profiles don´t depend much on the delta layer impurity concentration. Accordingly, WF don´t change much as well (see lower part of the figure). As a result, the IBEs for different n_δ no more than 0.3meV, which is on the brink of our numerical method precision. It

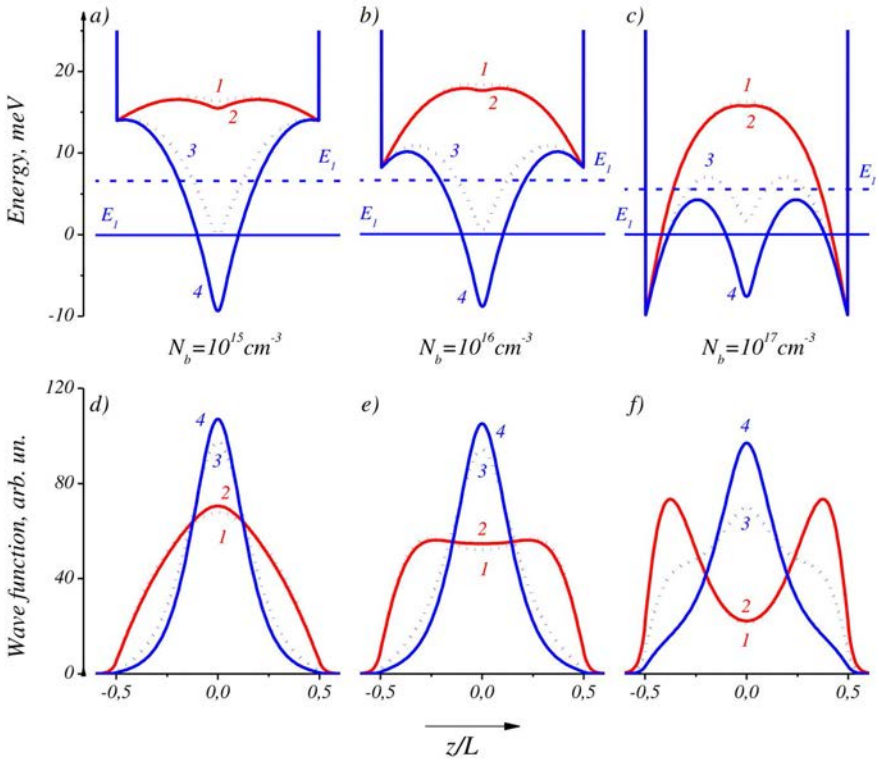

Figure 1.26: Energy profiles – *a), b), c)* (upper part of the figure), and wave functions of the first space quantized energy level – *d), e), f)* (lower part of the figure). Concentrations of background impurities, N_b, cm^{-3}:*a)* and *d)* – 10^{15};*b)* and *e)* – 10^{16}; *c)* and *f)* – 10^{17}. Temperature T, K: 1 and 2 – 77(red lines); 3 and 4 – 300(blue lines). The concentrations of donors in the delta layer n_δ, cm^{-2}: 1 (red) and 3 (blue) dashed lines – 0.6×10^{12}; 2 (red) and 4 (blue) solid lines – 1.2×10^{12}.The upper dashed (blue) horizontal straight lines (designated as E_1 at their right ends) correspond to the *1*-st space-quantized energy level for the N_δ=0.6×10^{12}cm^{-2} at T = 300K, and the lower solid (blue) ones (designated also as E_1, but at the left ends of the lines) show the 1-st space-quantized level for N_δ=1.2×10^{12}cm^{-2}at T = 300K. In the upper part the energy profiles for each N_b are shifted in such a way that E_1 is put as zero of energy for N_δ =1.2×10^{12} cm^{-2} and T=300K. All the curves in the *a), b),* and *c)* have the same energy scale factor. All the wave functions in the lower part are in the same scale as well.

can be explained in the same way for all BI concentrations. Table 1.8 shows that the number of ionized impurity centers in the delta layer (and, accordingly, electrons from this source in subbands) is two times greater for a higher n_δ. As a result the bottom part of the well energy profile for the bigger n is inside the same for the lesser n (Fig. 1.26 b). It means that the side mini wells are closer to each other. It has two consequences. First, the splitting between the levels belonging to the pockets because of the tunnel coupling should be slightly bigger for the bigger n_δ. It is confirmed by the Table 1.8 (see ΔE_{21}). Second, the wave function in the central barrier increases (Fig. 1.26 f) that leads

T, K	77							
2^*n_δ, cm^{-2}	6×10^{11}				12×10^{11}			
2^*N_b,cm^{-3}	10^{17}	10^{16}	10^{15}	0*	10^{17}	10^{16}	10^{15}	0* 10^{12}
$2^*\varepsilon_\delta$, meV	24.1	28.2	29.6	29.7	24.4	28.5	29.8	30.0 30.5
2^*n_{QW},10^{11} cm^{-2}	9.0	3.2	1.5	0.8	9.2	3.5	1.8	1.1 1.1
$2^*n_\delta{}^+$, 10^{11} cm^{-2}	0.2	0.3	0.5	0.8	0.4	0.6	0.8	1.1 1.1
2^*E_F, meV	-34	-43	-55		-34	-43	-55	-100
T, K	300							
2^*n_δ, cm^{-2}	6×10^{11}				12×10^{11}			
2^*N_b, cm^{-3}	10^{17}	10^{16}	10^{15}	0*	10^{17}	10^{16}	10^{15}	0* 10^{12}
$2^*\varepsilon_\delta$, meV	30.6	32.4	32.7	32.3	32.8	33.7	33.9	33.4 34.0
2^*n_{QW},10^{11} cm^{-2}	10.5	6.1	4.8	4.9	13.5	9.2	8.0	8.4 7.7
$2^*n_\delta{}^+$, 10^{11} cm^{-2}	4.4	4.8	4.9	4.9	7.7	8.2	8.4	8.4 8.5
2^*E_F, meV	-146	-205	-265		-146	-205	-265	-443

Table 1.8: IBEs (ε, meV), the complete sheet electron density in the well (n_{QW}, cm^{-2}), delta layer ionization ($n_\delta{}^+$, cm^{-2}), and Fermi level (E_F) for the two different delta layer impurity concentrations at T=77 and 300 K, and for the different BI concentrations (N_b, cm^{-3}).

to an increase of IBE. We believe that the ability to explain such small IBE variations is one more evidence of the calculation method reliability and that the IBE behavior is explained well enough with only the ground WF, that is the variation of the first term of expansion.

At room temperature the increase of delta layer ionization results in a bigger central V-shaped mini well, see Fig. 1.26 a and b. Interestingly, despite the notable difference in energy profiles for different n_δ, the corresponding WFs (Fig. 1.26 d and e) look very similar. IBE change is no more than 1.5 meV with lesser magnitude again for the lesser delta layer donor concentration. The reason is the bigger electron number, due to the bigger donor concentration, produces deeper central mini well. As a result, electron WFs are more localized around the well center that increases IBE.

Generally, the same is true about Fig. 1.26 c and f. However, the most notable thing here is the difference in WFs rather than in energy profiles. The WF difference is a result of different contributions of side mini wells as well to the charge redistribution of first subband electrons along z. It results in IBE difference of more than 2meV. So, one can see that the less different are the first subband WFs, the less is the IBE difference. And vice versa, a big (more than 6 meV) IBE difference follows the prominent distinction in WF shapes for T=77 and 300K (same n_δ), see Fig.1.26 f, and Table 1.8.

Also, Table 1.8 presents a behavior of ${n_\delta}^+$ against the IBE that at first may look counterintuitive. We can expect that the decrease of IBE should increase the ionization level, but the situation is opposite. To explain it we must remember that what directly influence on the ionization degree is the relative position of the Fermi level. And the position of Fermi level in our structure with infinitely wide barriers is determined by the BI concentration and temperature: the greater BI concentration, the closer it moves to the conductance band edge while higher temperature pushes it back to the bandgap. It explains why the number of ionized atoms in delta layer depends on BI concentration. However, the most remarkable thing in the Table 1.8 in our opinion is the fact that BI in barriers can increase the well electron concentration several times. In turn it can influence the efficiency of our presumable intersubband transition based optoelectronic devices. Note also that at 77K the fraction of electrons in the well that came from delta layer is always less than half. At room temperature this fraction increases and for the lower BI concentrations most electrons come to the well from the delta layer. The calculations show that at room temperature a notable part of electrons moves above the barriers and now belongs to a 3D continuum even being in the vicinity of the well and participating in profile distortion.

Energy distances at higher temperatures

In the Table 1.9 the energy distances between adjacent subbands for the room and nitrogen temperatures and different BI concentrations are presented. The data shows that in general their magnitudes for different BI concentrations are the same order as well as in case of

T, K	77								
2*n_δ, cm^{-2}	6×10^{11}				12×10^{11}				
2*N_b,cm^{-3}	10^{17}	10^{16}	10^{15}	0*	10^{17}	10^{16}	10^{15}		0*
2*ΔE_{21},meV	0.3	1.4	2.6	3.6	0.3	1.5	2.9		3.8
2*ΔE_{32},meV	7.1	4.7	4.5	4.5	6.9	4.6	4.4		4.5
2*ΔE_{43},meV	5.6	6.6	6.7	6.7	6.8	6.7	6.7		6.6
2*ΔE_{54},meV	8.2	8.4	8.5	8.4	8.1	8.4	8.5		8.4
T, K	300								
2*n_δ, cm^{-2}	6×10^{11}				12×10^{11}				
2*N_b,cm^{-3}	10^{17}	10^{16}	10^{15}	0*	10^{17}	10^{16}	10^{15}	10^{12}	0*
2*ΔE_{21},meV	2.1	6.5	7.8	4.9	5.8	10.1	11.2	11.5	11.1
2*ΔE_{32},meV	3.0	4.1	4.8	4.9	2.5	4.9	5.9	6.2	5.9
2*ΔE_{43},meV	7.5	6.6	6.6	6.6	6.8	6.3	6.6	6.4	6.5
2*ΔE_{54},meV	8.0	8.3	8.2	8.1	8.2	8.1	8.0	8.0	8.0

Table 1.9: Intersubband energy differences at nitrogen and room temperatures for different BI concentrations and two delta layer impurity concentrations

completely without BI. However, it is interesting that, for example, for N_b of 10^{15}cm^{-3} the change magnitude of the first difference ΔE_{12} with temperature is 11.2-2.9 = 8.4 meV while for N_b=0 it is 11.1-3.8 =7.3 meV. The similar thing happens in other cases. We mention it to emphasize a notable tuning range of intersubband transition energy in our structure design. As one can see BI do not prevent this effect and even, at come parameter combinations, can provide us with additional possibilities.

Shallower QW

There are different data on the depth QW with the same material combination in literature. Particularly, the works [55–57] estimate the depth as 120 meV. Here we analyze how our results can change for

QW with lower depth. First, regardless of the QW depth, the energy separation due to the internal stress between the four upper electron valleys and the two lower ones will be more than 110 meV [57], so the upper valleys are negligible anyway. Second, as is shown, the ground impurity state binding energy depends mainly on the first subband wave function and position, which, in turn, depends mainly on the QW bottom shape. We suppose, that it will be so independently from the well depth. As we say before, other subband WFs only refine ground impurity state energy. So, let us compare the structure of energy levels for both quantum wells using as an example the well with rectangular profile. The deep well has forteen subbands while the shallow one has eleven. The nineth level energy (the last we ccounted for in our calculations) is 76 meV with respect to the well bottom for the deep well and 73 meV for the shallow one. As is known, the closest intersubband energy difference increases with energy level and is the biggest for upper subband couples (unless very close to the barrier top). For the deep well the 8-9 difference is 16 meV and for the shallow one is 14 meV. So, as we see, the variation is minor, at least for the first nine subbands. We can conclude that the results for the well with lower depth are expected to be very much like what we got for the deeper one.

1.5 Conclusions

This work is built around the idea about the new design for semiconductor active and passive optical devices based on quantum wells delta-doped within the well. The introduction of impurity delta-layer permits tuning the working frequencies for such devices with external electric field. The device functioning is based on the intersubband optical transitions of electrons and may work in the spectral range from IR to THz regions. The most actual part of the spectrum is the THz region because there were technical problems in implementation of optical devices working in this range, which is known as THz gap. Existing designs of intersubband QW optical devices like QCL and QWIP can be modified using our idea that may increase their tunability. New types of optical devices, like modulators, can also be introduced.

To ground the idea numerically the self-consistent calculation method has been implemented. The peculiarity of our implementation of that method in comparison to the existing ones is the incorporation of the impurity binding energy calculation, which is crucial for our task.

We have proposed materials for the implementation of the concept, which is $Si_{0.8}Ge_{0.2}/Si/Si_{0.8}Ge_{0.2}$ heterostructures with shallow impurity of Phosphorus. Our choice is grounded theorically and confirmed with calculations. The calculation parameters are taken from literature, some of the particular results are confirmed by the works of another authors, that demonstrates the correctness of the method.

The method permitted to calculate the energy differences between lower subbands, position of Fermi level and wave functions of electrons in QW as a function of many parameters including QW width, electronic temperature, degree of impurity ionization, alloy content, impurity delta-layer position and concentration of impurity within the delta-layer. In addition, the possible influence on the tuning effect such factors as eternal transversal electric field and the presence of technological background impurity has been studied. The obtained results permit to calculate the linear and non-linear absorption coefficients of the structure and non-linear refraction change. Absorption spectra obtained for different impurity ionization degrees allowed to estimate frequency tuning ranges for the presumable devices.

As a result of the performed calculations and analysis the following most important conclusions can be made.

1. The best materials to implement the idea are Silicon and Germanium heterostructures because their shallow impurity is deep enough to obtain the tuning within acceptable temperature range and has enough small Bohr radius to use higher impurity concentrations for better effect without shifting to the metallic side of Mott transition.

2. The calculations show the viability of the proposed idea for the selected materials and configuration. It is fundamentally possible to create working tunable semiconductor optical device for THz or IR region based on the proposed design.

3. Absorption change in some calculated configurations demonstrate the possibility of tuning the working frequencies, for example, from 1.3 to 3.5 THz or from 2.6 to 4.3 THz for the same device.

4. Impurity binding energy for the different may change significantly, for example to decrease about 2-3 times. This effect does not prevent using the proposed design, however should be taken into account in quantitative estimations.

5. Nonlinear (Kerr-type) effects with reasonable magnitude of incident radiation and acceptable carrier concentrations may somewhat decrease the absorption peaks, however do not suppress them completely.

6. Applied transversal electric field (which is the necessary part of such devices as QCL and QWIP) at high magnitudes may modify the tuning effect significantly and should be taken into account in numerical estimations. Also, it provides additional possibility of tuning, that makes the design more flexible.

7. The introduction of technological background impurity has some effect on the tenability and at extremely high concentrations can make it impossible. However extreme cases can easily be avoided by technologic means.

References

[1] C.G. Smith, *Low-dimensional quantum devices*. Rep. Prog. Phys. **59**, 235-282 (1996).

[2] D. Dobkin, M.K. Zuraw. *Principles of Chemical Vapor Deposition*. Springer Science & Business Media, 2003, p. 273.

[3] W. Mönch, *Semiconductor Surfaces and Interfaces*. Springer-Verlag Berlin Heidelberg, New York, 2001, p. 548.

[4] Z.I. Alferov, *The history and future of semiconductor heterostructures*. Semiconductors **32**, 1–14 (1998).

[5] N. Zheludev, *The life and times of the LED: a 100-year history*. Nature Photonics. **1,** 189–192 (2007).

[6] E.L. Ivchenko, G.E. Pikus, *Interband Optical Transitions. In: Superlattices and Other Heterostructures*. Springer Series in Solid-State Sciences, Berlin, 1997, p. 39.

[7] J.Y. Duboz, P. Bois, E. Rosencher, *Intersubband Transitions in Quantum Wells.* Confined Electrons and Photons, New York, 1995, p. 20.

[8] H. Schneider, H. C. Liu, *Quantum Well Infrared Photodetectors. Physics and Applications*, Springer- Verlag Berlin Heidelberg, 2007, p. 248.

[9] J. Capasso, *Quantum Cascade Laser*, Science **264**, 553-556, (1994).

[10] Y. Zeng, B. Qiang, Q. J. Wang, *Photonic Engineering Technology for the Development of Terahertz Quantum Cascade Lasers*, Adv. Opt. Mat. **8**, p. 1900573, (2019).

[11] R. Han, *Filling the Gap: Silicon Terahertz Integrated Circuits Offer Our Best Bet*, IEEE Microwave Magazine, **20**, 80 – 93 (2019).

[12] C. Corsi, *Infrared: A Key Technology for Security Systems,* Advances in Optical Technologies **6**, p. 838752 (2012).

[13] V.P. Wallace, A.J. Fitzgerald, S. Shankar, R.J. Pye, D.D. Arnone, *Terahertz Pulsed Imaging of Basal Cell Carcinoma ex Vivo and in Vivo*, Br. J. Dermatol **151**, 424-432 (2004).

[14] A. J. Fitzgerald, V. P. Wallace, M. Jimenez-Linan, L. Bobrow, R. J. Pye, A. D. Purushotham, D. D. Arnone. *Terahertz pulsed imaging of human breast*, Radiology **239**, 533-540 (2006).

[15] O. Mitrofanov, M. Lee, J. W. P. Hsu, I. Brener, R. Harel, J. F. Federici, J. D. Wynn, L. N. Pfeiffer and K. W. West, *Collection-mode near-field imaging with 0.5-THz*, IEEE J. Sel. Top. Quantum Electron. **7**, 600-607 (2001).

[16] H.-B. Liu, H. Zhong, N. Karpowicz, Y. Chen, and X.-C. Zhang, *Terahertz Spectroscopy and Imaging for Defense and Security Applications,* Proc. IEEE, **95**, p. 1514-1527 (2007).

[17] Prof. Zhang X.-C. report at THz Symposium in Taiwan, 10/22/01.

[18] H. Zhan, K. Zhao, R. Bao, *Monitoring PM2.5 in the Atmosphere by Using Terahertz Time-Domain Spectroscopy.* J Infrared Milli Terahz Waves **37**, 929–938 (2016).

[19] F. Ellrich, M. Bauer, N. Schreiner, *Terahertz Quality Inspection for Automotive and Aviation Industries.* J Infrared Milli Terahz Waves **41**, 470–489 (2020).

[20] R. Dingle, H. L. Störmer, A. C. Gossard, *Electron Mobilities in Modulation Doped Semiconductor Heterojunction Superlattices.* Applied Physics Letters **33,** 656 – 667 (1978).

[21] E. F. Shubert, Shubert, *Delta doping of III–V compound semiconductors: Fundamentals and device applications.* J. Vac. Sci. Techn. **8,** p. 2980 (1990).

[22] B. F. Levine, *Quantum-well infrared photodetectors*, Applied Physics Letters **74,** (1993).

[23] G. Bastard, *Hydrogenic impurity states in a quantum well: A simple model*, Phys. Rev. B. **24**, p. 4714 (1981).

[24] C. Mailhiot, Y. C. Chang, and T. C. McGill, *Energy spectra of donors in GaAs-$Ga_{1-x}Al_xAs$ quantum well structures in the effective-mass approximation.* Phys. Rev. B. **26,** 4449-4457 (1982).

[25] W. T. Masselink, Y. C. Chang, H. Morkoc, *Binding energies of acceptors in GaAs- Al_xGa_{1-x} As quantum wells*, Phys. Rev. B**. 28,** p. 7373 (1983).

[26] S. Chaudhuri, *Hydrogenic-impurity ground state in multiple GaAs-Ga_{1-x} Al_xAs quantum-well structures,* Phys. Rev. B**. 28,** p. 4480 (1983).

[27] S. Chaudhuri and K. K. Bajaj, *Effect of nonparabolicity on the energy levels of hydrogenic donors in GaAs- Ga_{1-x} Al_xAs quantum-well structures,* Phys. Rev. B. **29**, p. 1803 (1984).

[28] C. Priester, G. Bastard, G. Allan, and M. Lannoo, *Binding energies of hydrogenic impurities in finite-quantum-well structures with effective-mass mismatch: Simple and accurate variational treatments*, Phys. Rev. B. **30,** p. 6029 (1984).

[29] S. Fraizzoli, F. Bassani, and R. Buczko, *Shallow donor impurities in GaAs- Ga_{1-x} Al_xAs quantum-well structures: Role of the dielectric-constant mismatch*, Phys. Rev. B. **41,** p. 5096 (1990).

[30] J. A. Brum, G. Bastard, and C. Guillemot, *Screened Coulombic impurity bound states in semiconductor quantum wells,* Phys. Rev. B**. 30,** p. 905 (1984).

[31] L. E. Oliveira and L. M. Falicov, *Energy spectra of donors and acceptors in quantum-well structures: Effect of spatially dependent screening*, Phys. Rev. B**. 34,** p. 8676 (1986).

[32] W. T. Masselink, Yia-Chung Chang, and H. Morkoç, *Acceptor spectra of Al_xGa_{1-x} As-GaAs quantum wells in external fields: Electric, magnetic, and uniaxial stress*, Phys. Rev. B**. 32,** p. 5190 (1985).

[33] J. A. Brum, C. Priester, and G. Allan, *Electric field dependence of the binding energy of shallow donors in GaAs- Ga_{1-x} Al_xAs quantum wells,* Phys. Rev. B. **32,** p. 2378 (1985).

[34] G.Weber, *Density of states and optical-absorption spectra of shallow impurities in quantum wells under the influence of a longitudinal electric field*, Phys. Rev. B. **41,** p. 10043 (1990).

[35] R. L. Greene and K. K. Bajaj, *Effect of magnetic field on the energy levels of a hydrogenic impurity center in* $GaAs/Ga_{1-x}\ Al_xAs$ *quantum-well structures,* Phys. Rev. B. **31**, p. 913 (1985).

[36] E. Kasapoglu, H. Sarı, and I. Sokmen, *Binding energy of hydrogenic impurities in a quantum well under the tilted magnetic field Solid State Commun,* Solid State Commun. **125**, 429-434 (2003).

[37] N. Raigoza, A. L. Morales, A. Montes, N. Porras-Montenegro, and C. A. Duque, *Stress effects on shallow-donor impurity states in symmetrical* $GaAs/Al_xGa_{1-x}As$ *double quantum wells*, Phys. Rev. B. **69,** p. 045323 (2004).

[38] J. P. Loehr and J. Singh, *Effect of biaxial strain on acceptor-level energies in* $In_yGa_{1-y}As/Al_xGa_{1-x}As$ *(on GaAs) quantum wells*, Phys. Rev. B**. 41,** p. 3695 (1990).

[39] Q. X. Zhao and M. Willander, *Theoretical study of shallow acceptor states under the influence of both a confinement potential and a deformation potential*, Phys. Rev. B. **57,** p. 13033 (1998).

[40] S. Y. Lopez, N. Porras-Montenegro, and C. A. Duque, *Absorción óptica relativa a impurezas donadoras en pozos cuánticos de GaAs-(Ga,Al)As bajo efectos de presión hidrostática,* Semicond. Sci. Technol. **18**, p. 718 (2003).

[41] G. J. Zhao, X. X. Liang, S. L. Ban, *Binding energies of donors in quantum wells under hydrostatic pressure*, Phys. Lett. A. **319**, 191-197 (2003).

[42] H. Panahi and M. Maleki, *Binding Energies of Donor States in GaAs-GaAlAs Quantum Wells Under Hydrostatic Pressure*, J. Appl. Sci. **8**, p. 636-641 (2008).

[43] Q. Fanyao, A. L. A. Fonseca, and O. A. C. Nunes, *Intense laser field effect on confined hydrogenic impurities in quantum semiconductors.* Phys. Status Solidi B. **197**, 349-357 (1996).

[44] F. Qu and P. C. Morais, *Hydrogenic Impurity States in n-Doped and Undoped Quantum Wells of GaAs–$Al_xGa_{1-x}As$ Embedded in Intense Laser Fields*, J. Phys. Soc. Jpn. **67**, 513-518 (1998).

[45] H. Sari, E. Kasapoglu, I. Sokmen, and N. Balkan, *Intense field effects on shallow donor impurities in graded quantum wells, Semicond.* Sci. Technol. **18**, p. 470 (2003).

[46] N. Radhakrishnan, A. J. Peter, *Polaronic effects on laser dressed donor impurities in a quantum well*, Physica E. **41,** 1841-1847 (2009).

[47] A. M. Elabsy, *Temperature dependence of shallow donor states in GaAs-$Al_xGa_{1-x}As$ compositional superlattice*, Physica Scripta **46**, p. 473 (1992).

[48] A. J. Peter and K. Navaneethakrishnan, *Simultaneous effects of pressure and temperature on donors in a GaAlAs/GaAs quantum wellSuperlattices Microstruct*, Superlattices Microstruct. **43,** 63-71 (2008).

[49] E. Kasapoglu, *The hydrostatic pressure and temperature effects on donor impurities in GaAs/$Ga_{1-x}Al_xAs$ double quantum well under the external fields*, Phys. Lett. A**. 373**, 140-143 (2008).

[50] H. Zhou, Z.-Y. Deng, *Electronic and hydrogenic impurity states in a corner under an applied electric field*, J. Phys.: Condens. Matter **9**, 1241–1248, (1997).

[51] E. Kasapoglu, H. Sari, I. Sokmen, *Binding energy of hydrogenic impurities in a quantum well under the tilted magnetic field*, Solid State Communications **125**, 17-22, (2003).

[52] K.H. Aharonyan, E.P. Kokanyan, M. Aillerie, *Screened shallow impurity properties of quantum well heterosystems with high-κ dielectric barrier environment*, Physica E. **113**, 47–53, (2019)

[53] A. Blom, M. A. Odnoblyudov, I. N. Yassievich, and K.-A. Chao, *Donor states in modulation-doped Si/SiGe heterostructures*, Phys.Rev.B. **68**, p. 165338, (2003).

[54] M. M. Rieger and P. Vogl, *Electronic-band parameters in strained $Si_{1-x}Ge_x$ alloys on $Si_{1-y}Ge_y$ substrates*, Phys. Rev. B. **48,** 14276, (1993)

[55] F. Schaffler, *High-Mobility Si and Ge Structures*, Semicond. Sci. Technol. **12,** 1515-1549, (1997)

[56] D. J. Paul, *Si/SiGe heterostructures: from material and physics to devices and circuits,* Semicond. Sci. Technol. **19,** p. R75, (2004)

[57] S. Sant, S. Lodha, U. Ganguly, S. Mahapatra, F. O. Heinz, L. Smith, V. Moroz and S. Ganguly, *Band gap bowing and band offsets in relaxed and strained $Si_{1-x}Ge_x$ alloys by employing a new nonlinear interpolation scheme*, J. Appl. Phys, **113**, p. 033708, (2013)

[58] D. Dutarte, P. Warren, I. Sagnes, P.A.Badoz,A. Perio, .C.Dupuis and G.Prudon, *Epitaxy and doping of Si and $Si_{1-x}Ge_x$ at low temperature by rapid thermal chemical vapor deposition*, J. Vac. Sci. Technol. B **11**, 1134-1139 (1993).

[59] A.G. Kyazym-zade, *Criteria for a Mott transition in two-dimensional latticesSemiconductors*, Semiconductors **29,** p. 10, (1995).

[60] B.I. Shklovskii and A.L. Efros, *Electronic Properties of Doped Semiconductors*, Springer-Verlag Berlin Heidelberg, 1984, p. 388.

[61] Yu. M. Sirenko, V. Mitin, *Phonon-assisted trapping and detrapping of an electron in quantum wells and wires by ionized impurity*, Journal of Luminescence **58**, 257-260 (1994).

[62] L. M. R. Scolfaro, D. Beliaev, R. Enderlein and J. R. Leite, *Electronic structure of n-type δ-doping multiple layers and superlattices in silicon*, Phys. Rev. B. **50,** p. 8699, (1994)

[63] V.Tulupenko, C. Duque, R. Demedyuk, *On some new effects in delta-doped QWs*, Physica E, **66**, 162-169, (2015).

[64] G.L. Bir and G.E. Pikus, *Symmetry and Strain-Induced Effects in Semiconductors*, Wiley, New York, (1974).

[65] V. Tulupenko, C. A. Duque, A. L. Morales, A. Tiutiunnyk, R. Demediuk, T. Dmytrychenko, O. Fomina, V. Akimov, R.

L. Restrepo and M. E. Mora-Ramos, *Background impurities in* $Si_{0.8}$ $Ge_{0.2}/Si/Si_{0.8}$ $Ge_{0.2}$ *n-type δ-doped QW*, Phys. Status Solidi B. **254**, p. 1600464, (2017)

[66] W. Kohn and J. M. Luttinger, *Theory of Donor States in Silicon*, Phys. Rev. **98,** p. 915, (1955)

[67] A. K. Ramdas and S. Rodriguez, *Spectroscopy of the solid-state analogues of the hydrogen atom: donors and acceptors in semicon-ductors*, Rep. Prog. Phys. **44,** p. 1297, (1981)

[68] D. J. BenDaniel and C. B. Duke, *Space-Charge Effects on Electron Tunneling*, Phys. Rev., **152,** p. 683, (1966)

[69] P. Harrison, *Quantum Wells, Wires and Dots.* Wiley-Interscience, N.Y, 2005.

[70] B. Vinter, *Influence of charged impurities on Si inversion-layer electrons*, Phys. Rev. B. **26**, p. 6808, (1982).

[71] J. D. Jacson, *Classical electrodynamics,* JohnWiley&Son INC. New York-London, 1962.

[72] D. A. Neamen, *Semiconductor physics and devices,* McGraw-Hill; 4ed., 2012

[73] R. Braunstein, A. R. Moore and F. Herman, *Intrinsic Optical Absorption in Germanium-Silicon Alloys*, Phys. Rev. **109,** p. 695,(1958)

[74] R. Krussmann, H. Vollmer and R. Labusch, *The Activation Energy of Phosphorus Donors in Silicon-Rich Silicon–Germanium Alloys*, Phys. Stat. Sol. B. **118,** p. 275, (1983)

[75] V. I. Zubkov, M. A. Melnik, A. V. Solomonov, E. O. Tsvelev, F. Bugge, M. Weyers and G. Tr¨ankle, *Determination of band offsets in strained* $In_xGa_{1-x}As/GaAs$ *quantum wells by capacitance-voltage profiling and Schr¨odinger-Poisson self-consistent simulation*, Phys. Rev. B. **70,** p. 075312, (2004)

[76] V. I. Zubkov, *Characterization of* $In_xGa_{1-x}As/GaAs$ *quantum-well heterostructures by C-V measurements: Band offsets, quantum-confinement levels, and wave functions,* Semiconductors **41,** 320-326,(2007)

[77] L. I. Shiff, *Quantum Meschanics*, McGraw-Hill, INC, New York-Toronto-London, 1949.

[78] I. Rodriguez-Vargas, and L. M. Gaggero-Sager, *Subband and transport calculations in double n-type δ-doped quantum wells in Si*, Journ. Appl. Phys. **99,** p. 033702, (2007)

[79] V. Tulupenko, A. Abramov, Ya. Belichenko, V. Akimov, *The influence of the ionized impurity delta-layer potential in the quantum well on impurity binding energy*, Journal of Applied Physics, **109**, p. 064303, (2011).

[80] K. J. Kuhn, G. U. Iyengar, and S. Yee, *Free carrier induced changes in the absorption and refractive index for intersubband optical transitions in AlxGa1−xAs/GaAs/AlxGa1−xAs quantum wells*, Journ. Appl. Phys. **70**, p. 5010 (1991).

[81] D. Ahn, S. L. Chuang, *Optical Transitions in a Parabolic Quantum Well with an Applied Electric Field-Analytical Solutions*, IEEE Journal of Quantum Electronics **23**, p. 2196 (1987).

[82] M. Virgilio, M. Ortolani, M. Teich, S. Winnerl, M. Helm, D. Sabbagh, G. Capellini, M. De Seta, *Combined effect of electron and lattice temperatures on the long intersubband relaxation times of Ge/Si_xGe_{1-x} quantum wells*, Phys. Rev. B**. 89**, p. 045311 (2014).

[83] M. Zachau, *Electronic eigenstates and inter-sub-band transitions in doped heterostructure superlattices*, Semicond. Sci. Technol. **3**, p. 879 (1988).

[84] H.C. Liu, F. Capasso, *Intersubband Transitions in Quantum Wells: Physics and Device Applications*, Academic Press, 1999, p. 309.

[85] L. Hedin and B. I. Lundqvist, *Explicit local exchange-correlation potentials*, J. Phys. C: Solid State Phys. **4,** p. 2064 (1971).

[86] W. Kohn and L. J. Sham, *Self-Consistent Equations Including Exchange and Correlation Effects*, Phys. Rev. **140**, p. A1133 (1965).

[87] E . Ozturk, Y. Ozdemir, *Linear and nonlinear intersubband optical absorption coefficient and refractive index change in n-type δ-doped GaAs structure*, Optics Communications **294**, 361–367 (2013).

[88] M. Rahm, J.-S. Li, W.J. Padilla, *THz Wave Modulators: A Brief Review on Different Modulation Techniques*, J. Infrared Milli. Terahz. Waves **34**, 1–27 (2013).

[89] G. Hüpper, K. Pyragas, E. Schöll, *Complex dynamics of current filaments in the low-temperature impurity breakdown regime of semiconductors*, Phys. Rev. B. **47,** p. 15515 (1993).

[90] R.V. Aldridge, K. Davis, M. Holloway, *An investigation of the effect of a magnetic field on the forward characteristics of some silicon diodes at low temperatures*, J. Phys. D. **8**, p. 64 (1975).

[91] M. Stopa and S. DasSarma, *Calculated shallow-donor-level binding energies in GaAs-$Al_xGa_{1-x}As$ quantum wells*, Phys. Rev B. **40,** p. 8466 (1989)

[92] E. Ozturk, H. Sari, Y. Ergun and I. Sokmen, *The effect of the donor distribution on the electronic structure of two coupled Si δ-doped layers in GaAs*, Phys. B. **334**, 1-8 (2003)

[93] I. H. Tan, G. L. Snider, L. D. Chang and E. L. Hu, *A Self-Consistent Solution of Schrödinger-Poisson Equations Using a Nonuniform Mesh*, J. Appl. Phys. **68,** p. 4071 (1990)

[94] G. Bastard, *Wave mechanics applied to semiconductor nanostructures*, Wiley-Interscience, 1ed, 1991.

[95] F. Ungan, E. Kasapoglu, H. Sarı, I. Sökmen, *Inter-sub-band transitions and binding energies of donor impurities in a modulation-doped quantum well in the presence of electric field*, Superlatt. Microst. **46,** 864-871 (2009)

Chapter 2

Review: A Look Into QD and QW

2.1 A brief introduction to electronic transport through quantum dots and wires

The ability to carry electrical charges through metals is determined by its electrical resistance R. Ohm's law establishes that the current I is proportional to the potential difference V and to the conductance G, which depends on the shape of the conductor, which together with the intrinsic property of macroscopic systems, called the conductivity of the material, can indicate if the material that makes up the sample is conductive or not. This Ohm's law loses its validity, when the size of the conductor approaches the atomic scale, more specifically, the electronic transport through a carbon nanotube, a quantum wire, a quantum dot, a heterostructure, or a molecule (for example) cannot respond to the same laws of charge transport that for a macroscopic system. The reason is that the distance which an electron travels between two scattering events, is usually much greater than the atomic size, i.e., the size of the system is less than some of the characteristic lengths such as *De Broglie's wavelength, or the mean free path*, thus producing confinement and quantization of the energy where the electrons pass ballistically through the conductor, generating that its resistance does not depend on the size of the system [1, 2].

These length scales vary widely from one material to another and are strongly affected by temperature, magnetic fields, and/or electric fields. We are, therefore, within a completely quantum limit, which we cannot describe with semi-classical arguments. On the other hand, when a mesoscopic system is at low temperatures or small applied

voltages, the transport properties are determined by the charge carriers on the Fermi energy.

Systems whose lengths are comparable to these characteristic lengths are usually called *mesoscopic or nanoscopic systems*. These systems have particular properties, which cannot be described by laws such as Drude's law, which particularly describes the electrical properties of macroscopic systems. This then makes it necessary to design circuits taking into account new transport regimes at nanoscopic scales.

The experimental investigation of these phenomena requires tools for manipulation and characterization of structures at the atomic and molecular scale, it is thus, that the construction of an electronic system using quantum wires and/or individual molecules is one of the fundamental goals of what we know today as the nanotechnology. During the last decades, important advances have been made in this regard, for example, the measurement, control, and understanding of the transport properties in a conductor that is between contacts have been the object of study in this field [3].

A main challenge for the theory is to derive the conductor conductance of the atomic size from microscopic principles, for this reason, the objective of this section is to review part of the basic theory to calculate the transport properties in mesoscopic conductors, especially through devices that are made up of quantum dots and quantum wires.

Initially, the work done by Ojeda *et al.* [4–6] will be taken as the main reference, where a general and simple vision of quantum transport in systems consisting of arrangements of quantum dots in one dimension is given, which are analyzed using wave functions.

The second system is an array of quantum dots coupled to a conducting quantum wire, where the transport properties were analyzed by Orellana *et al.* [7]. It should be noted that the analysis presented in this section was published and is the authorship of Orellana *et al.* [7], however, it is developed in detail here as a reproduction of their results, to take them as a fundamental theoretical basis and add some analyzes that have not been published, where parameters involved in the model are varied, and of which they are studied in order to compare them with results of the analysis of electronic transport through said systems using Green functions.

2.2 Review and analysis of electronic transport through a quantum wire (QW) with an impurity or quantum dot (QD).

The properties of electron transport such as the transmission probability (TP) and reflection probability (RP) through a quantum wire (QW) with an impurity are analyzed [8]. The electrical properties of this system are discussed, which is characterized by being of atomic size.

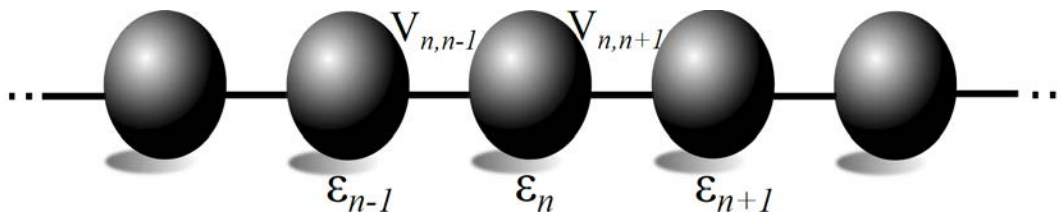

Figure 2.1: *Representation of a one-dimensional Quantum Wire (QW).*

The QW (See figure 2.1) is modeled by means of a Tight Binding Hamiltonian with interaction to first neighbors, which is given by [1, 9–11]:

$$\hat{H} = \sum_{n=1}^{N} \varepsilon_n c_n^\dagger c_n + \sum_{n=1}^{N} V_{n,n-1}, c_n^\dagger c_n \tag{2.1}$$

where ε_n is the energy of the nth atomic site (or quantum dot), $c_n^\dagger(c_n)$ is the creation (destruction) operator and $V_{n,n-1}$ is the coupling between the nth and $(n+1)^{th}$ site [12].

The eigen-states of said Hamiltonian $\hat{H}$ can be described by $|\psi\rangle = \sum_n a_n|n\rangle$, which satisfy periodic conditions[1], or its corresponding dual component ($\langle\psi| = \sum_{n'} a_{n'}\langle n'|$), where a_n is the probability amplitude to find an electron at the nth site of QW.

On the other hand, when determining the expected value of the Hamiltonian given by $\langle\psi|\hat{H}|\psi\rangle = \sum_{n'} a_{n'}\langle n'|\hat{H}\sum_n a_n|n\rangle$, and applying the respective properties of the creation operators[2] and destruction[3],

[1] Bloch states: describes the plane wave function of a particle (such as an electron) in a periodic medium (like a crystal lattice), multiplied by a periodic wave function due to the lattice, which allows describing the motion of several electrons from a single electron in a crystal lattice [13, 14]

[2] $c_n^\dagger|n\rangle = \sqrt{n+1}|n+1\rangle$

[3] $c_n|n\rangle = \sqrt{n}|n-1\rangle$

as well as the evaluation of the Kronecker delta[4], we get to obtain a dynamic or motion equation given by:

$$\varepsilon a_n = \varepsilon_n a_n + V_{n,n+1} a_{n+1} + V_{n,n-1} a_{n-1}, \tag{2.2}$$

where $\varepsilon = \varepsilon_n + 2V_{n,n\pm1} \cos k$, is known as the dispersion relation[5] that characterizes a monatomic linear chain (or QW).

For this case, the QW system is taken with all its atoms or QD_s characterized by having a site energy ε_A, the bonding or coupling to first neighbors is given by $V_{n,n\pm1} = V_{AA}$ and the dispersion relation is equal to $\varepsilon = \varepsilon_A + 2V_{AA} \cos k$. Now, considering said QW, with an

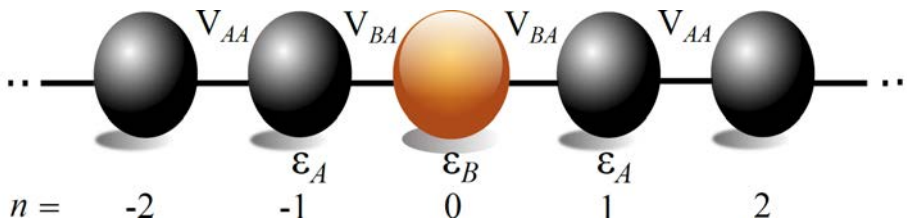

Figure 2.2: *QW with an impurity at the site $n = 0$.*

impurity located at the site $n = 0$ and energy $\varepsilon_0 = \varepsilon_B$ (see figure 2.2), and couplings to first neighbors (between impurity and QD) given by $V_{0,1} = V_{0,-1} = V_{BA} = V_c$ and $V_{n,n\pm1} = V_{AA} = V_a$ ($\forall\ n < -1\ and\ \forall\ n > 1$), the equation (2.2) becomes:

$$[(\varepsilon_A - \varepsilon_B) + 2V_a cosk]a_0 = V_c a_1 + V_c a_{-1} \tag{2.3}$$

Likewise, for $n = 1$ where $\varepsilon_1 = \varepsilon_A$ and for $n = -1$ where $\varepsilon_{-1} = \varepsilon_A$ the equation (2.2) is respectively given by:

$$(2V_a cosk)a_1 = V_a a_2 + V_c a_0 \tag{2.4}$$

and,

$$(2V_a cosk)a_{-1} = V_a a_{-2} + V_c a_0 \tag{2.5}$$

Taking into account the boundary conditions where is fulfilled that there is a wave incident by the left side of the impurity, giving place to a wave transmitted by the right side and another reflected by the left side, whose amplitudes defined as $t(\varepsilon)$ and $r(\varepsilon)$, respectively, are

[4] $\delta_{n,n'} = 1$ (si $n = n'$); $\delta_{n,n'} = 0$ (si $n \neq n'$); $\delta_{n',n+1} = \langle n'|n+1\rangle$; $\delta_{n',n-1} = \langle n'|n-1\rangle$

[5] This relation describes the effect that the dispersion of the medium has, in this case the monatomic linear chain, on the properties of the wave associated with the electron that travels within that medium. Where ε is the energy of the incident wave and k is the wave number equal to $2\pi/\lambda$ [13, 14].

given by [2, 10]:

$$a_n = \begin{cases} e^{ikn} + r(\varepsilon)e^{-ikn} & \text{for } n \leq -1 \\ t(\varepsilon)e^{ikn} & \text{for } n \geq 1 \end{cases} \tag{2.6}$$

The equations (2.4), (2.5) and (2.6) can be related to determine that the probability amplitude a_0 of finding an electron at the site $n = 0$, which is given by:

$$a_0 = \frac{V_a}{V_c} t(\varepsilon) = \frac{V_a}{V_c}(1 - r(\varepsilon)) \tag{2.7}$$

From the equation (2.7) can be inferred that $t(\varepsilon) = 1 - r(\varepsilon)$, and together with determining the amplitudes a_1 and a_{-1} the reflection coefficient is obtained by:

$$r(\varepsilon) = \frac{V_a\varepsilon_- + 2(V_a^2 - V_c^2)cosk}{2V_c^2 e^{ik} - (V_a\varepsilon_- + 2V_a^2 cosk)} \tag{2.8}$$

where $\varepsilon_- = \varepsilon_A - \varepsilon_B$.

With the reflection amplitude ($r(\varepsilon)$) of the equation (2.8), the reflection p robability R (ε) c an b e o btained b y m eans o f t he relation $R(\varepsilon) = rr^*$ given by:

$$R(\varepsilon) = \frac{[V_a\varepsilon_- + 2(V_a^2 - V_c^2)cosk]^2}{(V_a\varepsilon_- - 2V_c^2 cosk)[V_a\varepsilon_- + 2(V_a^2 - V_c^2)cosk] + 4V_c^4} \tag{2.9}$$

As these transmission and reflection probabilities comply with $T(\varepsilon)+ R(\varepsilon) = 1$, which is equivalent to the conservation of current, or in general of unitarity, that is, each incident particle will be transmitted or reflected with a probability $T(\varepsilon)$ o $R(\varepsilon)$ respectively, therefore, said transmission probability $T(\varepsilon)$ can also be determined by means of the relation $T(\varepsilon) = 1 - R(\varepsilon)$.

Figures 2.3(a) and 2.3(b) represent the reflection and transmission probability respectively, for a QW system with an impurity, taking into account that $\varepsilon_A = 0.3\ eV$, $\varepsilon_B = -0.3\ eV$ and the respective couplings are given by $V_a = -0.8\ eV$ and $V_c = -0.3\ eV$. Thus it is inferred that the electron probability transmission is maximum when the reflection probability is minimum [2, 15].

Is also saw, that the transmission probability through the quantum system with an impurity shows a resonant tunneling regime and,

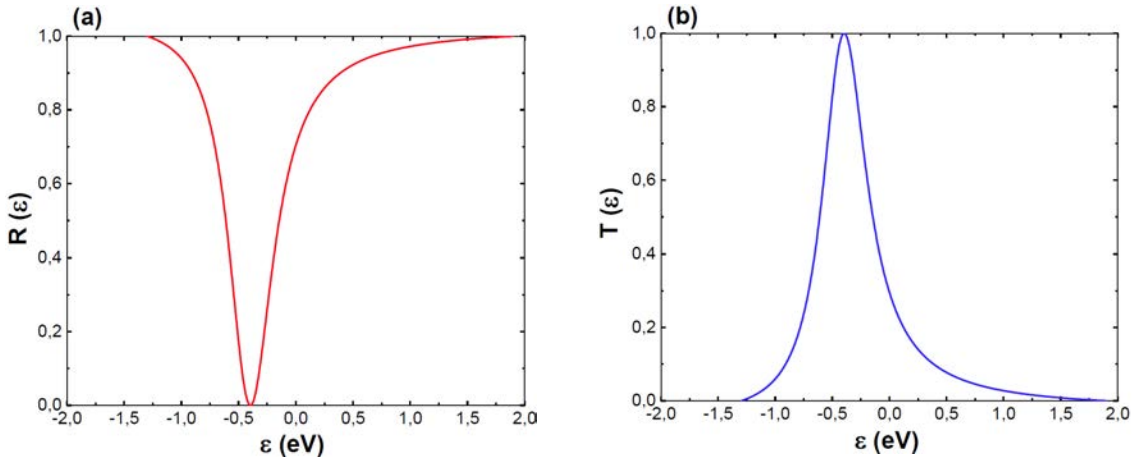

Figure 2.3: *(a) Reflection probability and (b) Transmission probability for a QW with an impurity.*

therefore, a unit peak in the transmission is observed. This resonant peak is associated with the eigenvalue of the impurity depending on the coupling with the atomic linear chain.

Now, the transport properties are analyzed considering the QW with an impurity, but this time in the form of a linear chain of quantum dots (QD_s) coupled perpendicularly to the QW forming a **T**, as was analyzed by Orellana *et al.* [20] and as is represented in the figure 2.4.

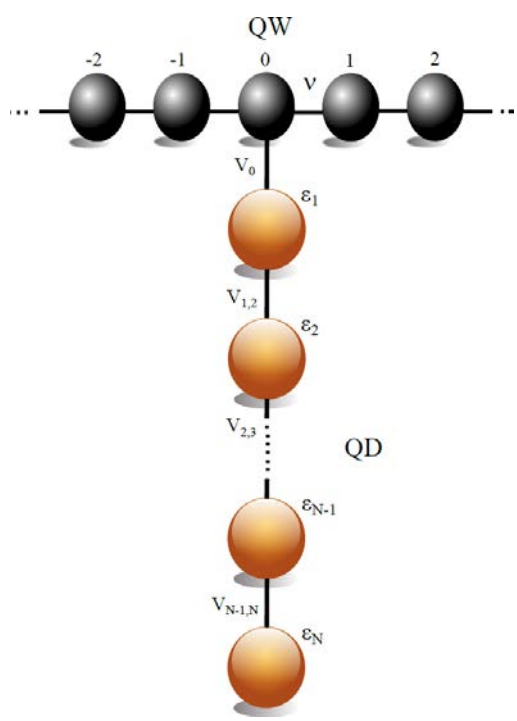

Figure 2.4: *QW with lateral coupling to an array of QD_s.*

At this point, it is important to clarify to the reader that the methodology and results of the transport's study through this sys-

tem were carried out by Orellana *et al.* [7]; for what is wanted in this section, to reproduce said results and from them vary some parameters of which were not done in the mentioned work. This is done in order to analyze the transport properties, observe other behaviors in addition to those reported and be able to compare them with those obtained for this same system but with Green functions in the next section of this document.

The formation of this system consists of N quantum dots, with energy levels or sites ε_l and connected by an interface V_0 through the atomic site $n = 0$ of QW [1, 16, 7].

The system is modeled using a non-interacting Anderson tunneling Hamiltonian ($\hat{H}$) [17] given by:

$$\hat{H} = \hat{H}_{QW} + \hat{H}_I + \hat{H}_{QD} \tag{2.10}$$

where,

$$\begin{aligned} \hat{H}_{QW} &= \nu \sum_{i \neq j} c_n^\dagger c_n \\ \hat{H}_{QD} &= \sum_{l=1}^{N} \varepsilon_l d_l^\dagger d_l + \sum_{l=1}^{N-1} (\ V_{l,l+1} d_l^\dagger d_{l+1} + h.c) \\ \hat{H}_I &= V_0 (d_1^\dagger c_0 + c_0^\dagger d_1) \end{aligned} \tag{2.11}$$

where $c_n^\dagger(c_n)$ is the operator creation (destruction) of an electron on the n site of the QW, ν is the coupling between the energetic sites in the QW, $d_l^\dagger(d_l)$ is the operator creation (destruction) of an electron on the site l of the impurity or array of QD_s, $V_{l,l+1}$ (where $l \neq 0$) is the coupling between the QD_s and V_0 is the coupling between the array of QD_s and the QW.

Taking into account that the eigenstates of $\hat{H}$ are given by $|\psi\rangle = \sum_{j=-\infty}^{\infty} a_j^k |j\rangle + \sum_{l=1}^{N} b_l^k |l\rangle$, where a_j^k is the probability amplitude of finding an electron at the site j del QW y b_j^k is the probability amplitude of finding an electron at site l in the array of QD_S in a k state [18], the expected value ($\langle\psi|\hat{H}|\psi\rangle$) is evaluated, arriving to a system of linear and independent equations given by:

$$\begin{aligned} \varepsilon a_j^k &= \nu(a_{j-1}^k + a_{j+1}^k) + V_0 b_1^k \delta_{j0} \\ \varepsilon b_l^k &= \varepsilon_l b_l^k + V_{l,l-1} b_{l-1}^k + V_{l,l+1} b_{l+1}^k, \end{aligned} \tag{2.12}$$

where $\varepsilon = 2\nu \cos k$, is the dispersion relation of a monatomic linear chain such as QW with $\varepsilon_a = 0$.

Taking the first equation of (2.12) with $j = 0$ and the second equation of (2.12) with $l = N$ we have respectively:

$$\begin{aligned} \varepsilon a_0^k &= \nu(a_{-1}^k + a_1^k) + V_0 b_1^k \\ \varepsilon b_N^k &= \varepsilon_N b_N^k + V_{N,N-1} b_{N-1}^k \end{aligned} \tag{2.13}$$

Taking into account that $b_0^k = a_0^k$ and $V_{1,0} = V_0$, the amplitudes b_N^k can be found recurrently, and especially for $N = 1$ with a continuous fraction is given by [8, 7].

$$b_1^k = \frac{V_0 a_0^k}{Q_N}, \tag{2.14}$$

where said continuous fraction is given by:

$$Q_N = \varepsilon - \varepsilon_1 - \cfrac{V_{1,2}^2}{\varepsilon - \varepsilon_2 - \cfrac{\quad}{\ddots \cfrac{\quad}{\varepsilon - \varepsilon_{N-1} - \cfrac{V_{N-1,N}^2}{\varepsilon - \varepsilon_N}}}} \tag{2.15}$$

Substituting the equation (2.14) in the first equation of (2.13) gives:

$$\varepsilon a_0^k = \nu(a_{-1}^k + a_1^k) + \frac{V_0^2}{Q_N} a_0^k \tag{2.16}$$

Knowing the amplitudes given by the equation (2.16), which as-sumes that electrons are described by an incident, reflected and trans-mitted wave for a k-state [9], it can be established that:

$$a_j^k = \begin{cases} e^{ikj} + re^{-ikj} & \text{for } j < 0 \\ te^{ikj} & \text{for } j > 0 \end{cases} \tag{2.17}$$

Evaluating the equation (2.17) for $j = -1, 1$ and $j = 0$ (from which is obtained that $t(\varepsilon) = 1 + r(\varepsilon)$) to replace it in the equation (2.16), the transmission ($t(\varepsilon)$) and reflection ($r(\varepsilon)$) amplitudes respectively

are found by:

$$\begin{aligned} t(\varepsilon) =& \frac{2iv\sin k}{2iv\sin k + \frac{V_0^2}{Q_N}} \\ r(\varepsilon) =& -\frac{\frac{V_0^2}{Q_N}}{2iv\sin k + \frac{V_0^2}{Q_N}} \end{aligned} \tag{2.18}$$

Taking into account that $\Gamma(\varepsilon) = \frac{V_0^2}{2\nu\sin(k)}$, the expressions for $t(\varepsilon)$ and $r(\varepsilon)$ as a function of $\Gamma(\varepsilon)$, are given by:

$$\begin{aligned} t(\varepsilon) =& \frac{Q_N}{Q_N + i\Gamma} \\ r(\varepsilon) =& \frac{i\Gamma}{Q_N - i\Gamma} \end{aligned} \tag{2.19}$$

Finally, the transmission amplitude of the equation (2.19) is multiplied by its respective complex conjugate expression ($T(\varepsilon) = tt^*$), thus obtaining, the transmission probability ($T(\varepsilon)$) given by:

$$T(\varepsilon) = \frac{Q_N^2}{Q_N^2 + \Gamma^2} \tag{2.20}$$

Taking the expression given by (2.20), will be possible to evaluate and determine the transmission probability ($T(\varepsilon)$) for $N = 1, 2, 3$, resulting the expressions respectively given by:

$$T(\varepsilon)_{(N=1)} = \frac{(\varepsilon - \varepsilon_1)^2}{(\varepsilon - \varepsilon_1)^2 + \Gamma^2}, \tag{2.21}$$

$$T(\varepsilon)_{(N=2)} = \frac{[(\varepsilon - \varepsilon_1)(\varepsilon - \varepsilon_2) - V_c^2]^2}{[(\varepsilon - \varepsilon_1)(\varepsilon - \varepsilon_2) - V_c^2]^2 + (\varepsilon - \varepsilon_2)^2\Gamma^2} \tag{2.22}$$

y

$$T(\varepsilon)_{(N=3)} = \frac{(\varepsilon - \varepsilon_1)(\varepsilon - \varepsilon_2)(\varepsilon - \varepsilon_3) - V_c^2[(\varepsilon - \varepsilon_1) + (\varepsilon - \varepsilon_3)]}{(\varepsilon - \varepsilon_1)(\varepsilon - \varepsilon_2)(\varepsilon - \varepsilon_3) - V_c^2[(\varepsilon - \varepsilon_1) + (\varepsilon - \varepsilon_3)] + [(\varepsilon - \varepsilon_2)(\varepsilon - \varepsilon_3) - V_c^2]^2\Gamma^2} \tag{2.23}$$

The figure 2.5 represents the transmission probability as a function of the incident electron energy, for $N = 1, 2$ and 3 QD_s coupled to the QW for values of $\varepsilon_l = 0\ eV$ and $V_c = \Gamma = 1.0\ eV$ [6].

[6] The results presented in this section for these values were reproduced taking into account the work of Orellana *et al.* [7]

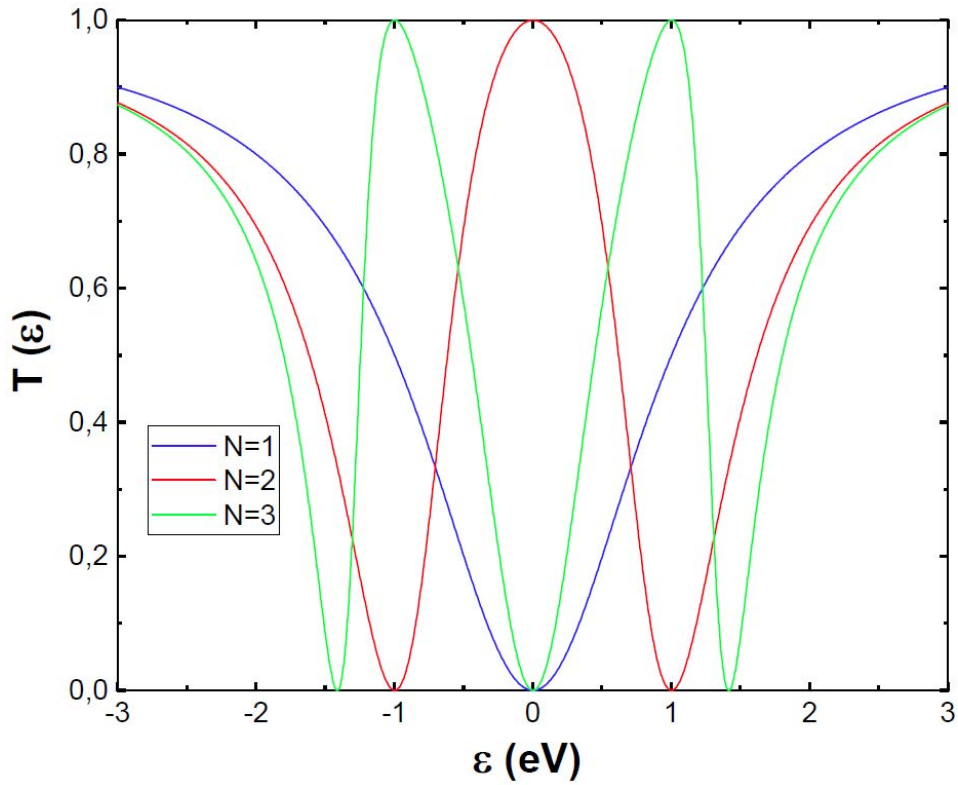

Figure 2.5: *Transmission probability as a function of the incident electron energy for $N = 1$ (blue line), $N = 2$ (red line) and $N = 3$ (black line) for values of $\varepsilon_l = 0\ eV$ and $V_c = \Gamma = 1.0\ eV$.*

As we can see, the transmission probability for $N = 1$ (blue line) presents a single antiresonance at $\varepsilon = 0\ eV$, that is, when the incident energy of the electron coincides with the energy of the only QD coupled laterally to the QW, the transmission probability is zero and the reflection is maximum [7].

In the case where $N = 2$ (Figure 2.5, red line), was taken $V_{1,2} = V_c$ (coupling between the QD_s located in sites 1 and 2), finding that the system presented two antiresonances in the energy values given by $\varepsilon = \frac{1}{2}(\varepsilon_1 + \varepsilon_2) \pm \frac{1}{2}\sqrt{(\varepsilon_1 - \varepsilon_2)^2 + 4V_c^2}$ and a single resonance in $\varepsilon = \varepsilon_2$.

Finally for $N = 3$ (Figure 2.5, green line), is observed that the sys-tem with $\varepsilon_1 = \varepsilon_2 = \varepsilon_3$ y $V_{1,2} = V_{2,3} = V_c$, has three antiresonances and two resonances. Taking into account the expression (2.23) of the transmission probability for this case, the three mentioned antiresonances are found when:

$$(\varepsilon - \varepsilon_1)(\varepsilon - \varepsilon_2)(\varepsilon - \varepsilon_3) - V_c^2[(\varepsilon - \varepsilon_1) + (\varepsilon - \varepsilon_3)] = 0, \qquad (2.24)$$

[7]The resonances and/or antiresonances presented in each of the results are explained by the Fano effect, which is described in more detail at the end of this section.

and in this case as $\varepsilon_1 = \varepsilon_2 = \varepsilon_3$ results:

$$(\varepsilon - \varepsilon_1)^3 - V_c^2(2(\varepsilon - \varepsilon_1)) = 0, \tag{2.25}$$

and doing $\lambda = \varepsilon - \varepsilon_1$ is obtained that::

$$\begin{aligned} \lambda^3 - 2V_c^2\lambda = 0, \\ \lambda(\lambda^2 - 2V_c^2) = 0, \end{aligned} \tag{2.26}$$

finding two possibilities: The first that $\lambda = 0$ and the second that $\lambda^2 - 2V_c^2 = 0$, therefore, we see that the three antiresonances are found when $\varepsilon = \varepsilon_1$, $\varepsilon = \varepsilon_1 + \sqrt{2}V_c$ and $\varepsilon = \varepsilon_1 - \sqrt{2}V_c$.

We can also find two resonances, where is known that $T(\varepsilon) = 1$ for the same conditions in which $\varepsilon_1 = \varepsilon_2 = \varepsilon_3$ in the form:

$$\frac{(\varepsilon - \varepsilon_1)^3 - 2V_c^2(\varepsilon - \varepsilon_1)}{(\varepsilon - \varepsilon_1)^3 - 2V_c^2(\varepsilon - \varepsilon_1) + [(\varepsilon - \varepsilon_1)^2 - V_c^2]^2\Gamma^2} = 1$$

$$(\varepsilon - \varepsilon_1)^3 - 2V_c^2(\varepsilon - \varepsilon_1) = (\varepsilon - \varepsilon_1)^3 - 2V_c^2(\varepsilon - \varepsilon_1) + [(\varepsilon - \varepsilon_1)^2 - V_c^2]^2\Gamma^2$$

$$0 = [(\varepsilon - \varepsilon_1)^2 - V_c^2]^2\Gamma \; (\varepsilon - \varepsilon_1)^2 - V_c^2 = 0$$

$$\begin{aligned} (\varepsilon - \varepsilon_1)^2 &= V_c^2 \\ \varepsilon - \varepsilon_1 &= \pm V_c \end{aligned} \tag{2.27}$$

getting two resonances when $\varepsilon = \varepsilon_1 + V_c$ and $\varepsilon = \varepsilon_1 - V_c$.

This result can be seen more clearly when the expression (2.23) is evaluated, where the variation of the coupling energies V_c and Γ with $\varepsilon_1 = \varepsilon_2 = \varepsilon_3 = 0\ eV$ as shown in figures 2.6(a) and 2.6(b)respectively.

For either of the two cases (figuras 2.6(a) o 2.6(b)), the antiresonances in the transmission probability are independent of Γ as could be deduced. For the case where V_c is varied and especially for three values highlighted in the upper panel of the figure 2.6(a) where $V_c = 0.5\ eV$ the antiresonances in $\varepsilon = -0.74\ eV, 0\ eV$ and $0.74\ eV$ are presented; for the case where $V_c = 1.5\ eV$ in $\varepsilon = -2.12\ eV, 0\ eV$ and $2.12\ eV$ three resonances are presented and finally for $V_c = 2.5\ eV$ the resonances are finding in $\varepsilon = -3.53\ eV, 0\ eV$ and $3.53\ eV$. For this last case, the antiresonances of the ends cannot be verified due to the energy window ($-3.0\ eV$ to $3.0\ eV$) taken in the figure.

Another characteristic to observe in the transmission profile when V_c varies, is that as said coupling between the QD_s increases, the width

of each resonance increases and therefore the bandwidth increases proportionally to $2V_c$. These results are consistent with those found by [6], for this class of low-dimensional systems.

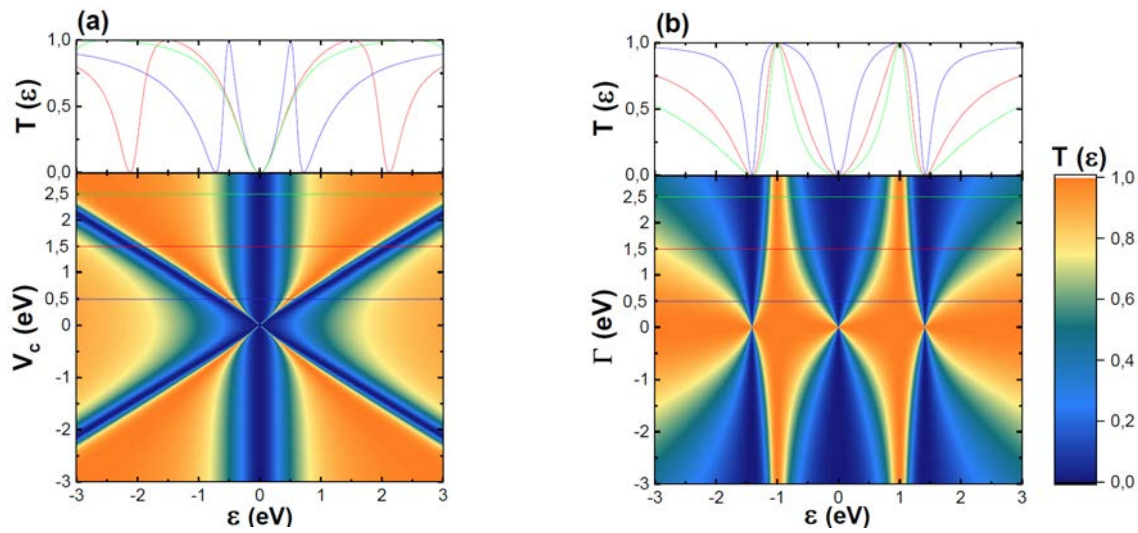

Figure 2.6: *Transmission probability as a function of the incident electron energy for $N = 3$, with $\varepsilon_1 = \varepsilon_2 = \varepsilon_3 = 0\ eV$ (a) Varying V_c, $\Gamma = 1.0\ eV$ and (b) varying Γ, $V_c = 1.0\ eV$.*

On the other hand, the transmission probability profile varying Γ and with $V_c = 1\ eV$ (Figure 2.6 (b)), is characterized by having an almost constant behavior, i.e., the antiresonances will always be found at $\varepsilon = -1.41\ eV, 0\ eV$ and $1.41\ eV$ and resonances around $\varepsilon = -1.0\ eV$ y $1.0\ eV$, with small variations in the bandwidth, which decreases as Γ increases, since, as Γ is a function of $\frac{V_0^2}{2\nu \sin(k)}$ (as mentioned), a strong coupling regime will be presented around small values of Γ where $V_0 > \nu$ and a weak coupling regime where $V_0 < \nu$ and the width of each resonance in $T(\varepsilon)$ decreases.

It is important to highlight and as observed, both Γ and V_c are parameters that can be controlled independently and at the same time experimentally in devices used in nanoelectronics [16, 19].

Continuing with the system of $N = 3$ for a array of QD_s in **T**-shaped, the effect of the variation in the site energies of the QD_s is analyzed. In the figure 2.7 the transmission probability as a function of the incident electron energy for $N = 3$ and $V_c = \Gamma$ is represented, taking into account that the energy value varies for ε_1 at site $N = 1$ (figure 2.7 a), ε_2 at site $N = 2$ (figure 2.7 b) and ε_3 at the site $N = 3$ (figure 2.7 c), for the values of $\varepsilon_{1,2,3} = 0\ eV$ when they remain constant.

In the case where ε_1 (figure 2.7a), we find that the antiresonances

have a shift to the right, and are obtained by solving the equation $\varepsilon^3 - \varepsilon_1\varepsilon^2 - 2V_c^2\varepsilon + V_c^2\varepsilon_1 = 0$. Particularly for $\varepsilon_1 = -1.0\ eV$ (blue line) the antiresonances are found at $\varepsilon = -1.8\ eV, -0.45\ eV, 1.25\ eV$; for $\varepsilon_1 = 0\ eV$ (red line), the three antiresonances are at $\varepsilon = 0\ eV$ and when $\varepsilon_1 = 1.0\ eV$ (green line) the antiresonances are at $\varepsilon = -1.25\ eV, 0.45\ eV, 1.8\ eV$ for $V_c = 1.0\ eV$.

In the same way, the resonances can be calculated, which are found at $\varepsilon = \pm V_c$, result of solving the equation $(\varepsilon - \varepsilon_2)(\varepsilon - \varepsilon_3) - V_c^2 = 0$. Said

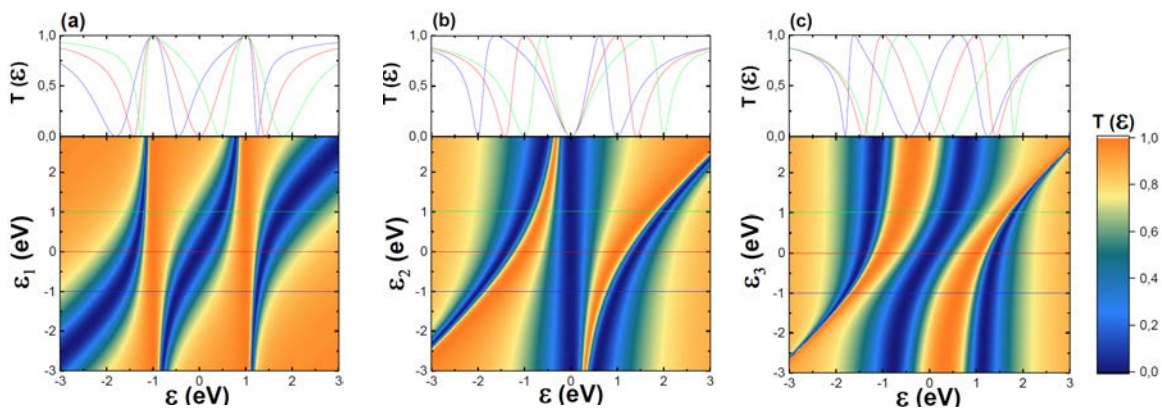

Figure 2.7: *Transmission probability as a function of the incident electron energy for $N = 3$ and $V_c = \Gamma = 1.0\ eV$. (a) Varying ε_1 and $\varepsilon_{2,3} = 0\ eV$, (b) Varying ε_2 and $\varepsilon_{1,3} = 0\ eV$, (c) Varying ε_3 and $\varepsilon_{1,2} = 0\ eV$.*

resonances can be observed in figure 2.7 a, at the energy $\varepsilon = \pm 1\ eV$, where is clear that it depends only on V_c.

In the figure 2.7b, the profile of $T(\varepsilon)$ is presented as a function of the incident electron energy and the energy ε_2 for the same system with three QD_s. In this behavior is observed that the three antiresonances are presented, together with two resonances where the transmission probability is maximum. The difference with the previous case (figure 2.7a) is that, one of its antiresonances remains constant around $\varepsilon = 0\ eV$. The above, can be deduced from the equation (2.24), where $\varepsilon_1 = \varepsilon_3 = 0$ to find the antiresonances at $\varepsilon = 0$ and $\varepsilon = \frac{\varepsilon_2 \pm \sqrt{\varepsilon_2^2 + 8V_c^2}}{2}$, solving the equation $\varepsilon^2(\varepsilon - \varepsilon_2) - 2V_c^2\varepsilon = 0$, and its corresponding resonances in $\varepsilon = \frac{\varepsilon_2 \pm \sqrt{\varepsilon_2^2 + 4V_c^2}}{2}$ solving the equation $\varepsilon(\varepsilon - \varepsilon_2) - V_c^2 = 0$ where we can see the maximums in the transmission probability.

For the case where ε_3 varies, we have the profile of $T(\varepsilon)$ for the array of QD_s with $N = 3$ in figure 2.7c. In this case, the behavior is similar to that presented in 2.7a, finding the antiresonances when solving the equation $\varepsilon^3 - \varepsilon_3\varepsilon^2 - 2V_c^2\varepsilon + V_c^2\varepsilon_3 = 0$, howeve, the difference is that

the maximums in the $T(\varepsilon)$ or resonances are in non-constant energy values equal to $\varepsilon = \frac{\varepsilon_3 \pm \sqrt{\varepsilon_3^2 + 4V_c^2}}{2}$.

On the other hand, it is important to note that when the quantum dot arrangement is greater than $N = 3$ (as analyzed), i.e., as the amount of QD_s coupled laterally to the QW increases, increases in the same way, the amount of antiresonances (N) and the number of resonances ($N - 1$), maintaining the band's width and a certain symmetry behavior with respect to the value of the energy of ε_l, showing a parity effect in the transmission function, that is, when $N = odd$ an antiresonance will occur at $\varepsilon = \varepsilon_l$ and when $N = even$ a resonance around the same value ($\varepsilon = \varepsilon_l$), as can be seen in the figure 2.8a (N = even) and 2.8b (N = odd) [16, 20].

The transmission probability profile shown in figure 2.8 for $N > 3$ is calculated using the equation (2.20), taking into account that $V_{l-1,l} = V_c$, $\varepsilon_l = \varepsilon_0$ and particularly Q_N is determined by means of the recurrence expression given by:

$$Q_N = (\varepsilon - \varepsilon_0)x_N, \tag{2.28}$$

where $x_N = 1 - \frac{\alpha}{x_{N-1}}$ and $\alpha \equiv V_c^2/(\varepsilon - \varepsilon_0)^2$. For $N = 1, 2, 3, ...$ we start with initial conditions of $x_1 = 1$, in this way the expression is generalized for any value of N QD_s, making use of the recurrence presented in the Q_N term of the transmission probability.

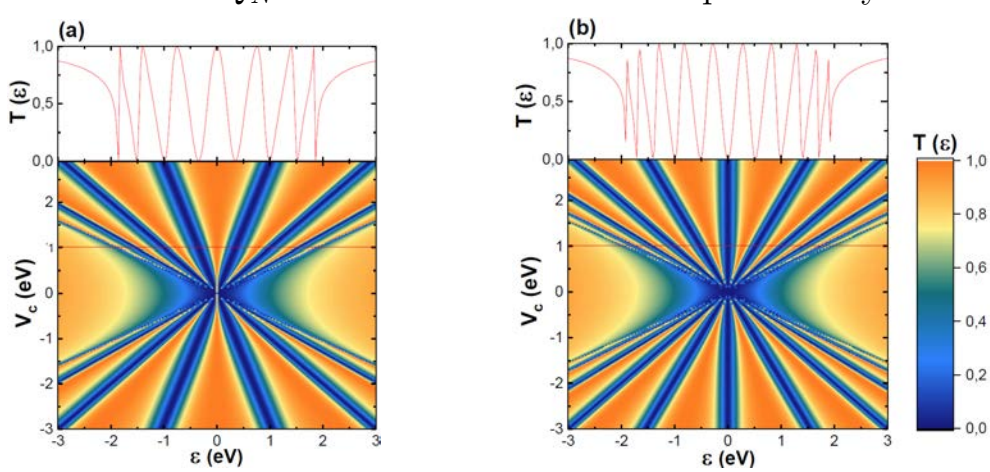

Figure 2.8: *Transmission probability as a function of the incident electron energy and V_c for values of $\varepsilon_l = 0$, $\Gamma = 1.0$ eV. (a) For $N = 8$ QD_s and (b) $N = 11$ QD_s*

It is evident that figure 2.8 shows the dependence of $T(\varepsilon)$ with the variation of V_c, showing a behavior similar to that presented in figure 2.6 (a).

Finally, and to complement this section, is essential to identify the effect generated by the antiresonances/resonances presented in quantum transport through systems such as the one presented. This effect is known as *Fano Effect*.

The Fano effect is the result of the interference between the state of a discrete energy channel and the states corresponding to the energy continuum, in this case, it happens for a quantum dot embedded in a medium that presents a continuum of its own energies.

Nanotechnology has made it possible to study many important devices (sensors, chips, fibers, etc.), opening new horizons with its applications where fundamental physical phenomena play an important role in the efficiency of most of them, such as the transport of wave excitations [16]. Often, the propagation waves are dispersed in different paths, and consequently, the phenomena of constructive interference (increase in the amplitude of the transmission resonance) and destructive interference (suppression of transmission resonance) appear.

The Fano effect, whose purpose is to analyze the main characteristics caused by a close coexistence of resonance in transmission and resonance in reflection, can be reduced to the interaction of a discrete (localized) state with a continuous state of the propagation modes, due to at the superposition principle of quantum mechanics when two states are coupled by paths different producing interferences. Therefore, Fano resonances can originate from observing the absorption spectral lines.

According to the above and using a perturbative scheme, Fano explained the appearance of asymmetric resonances. He considered a new state called "prediagonalized", generated by the coupling between a discrete bound state with another state on the continuum. Such prediagonalized state may or may not have a clear physical analogy, but serves in any case as a convenient mathematical construction to solve the problem.

As a result, Fano obtained the formula for the resonance profile of a scattering section, given by:

$$\sigma = \frac{(\epsilon + q)^2}{\epsilon + 1^2} \tag{2.29}$$

Using a phenomenological parameter q (introduced in his original document, as a ratio of probabilities of transition to the mixed and

continuous state) and a reduced energy form ϵ defined by $2(E-E_F)/\Gamma$. E_F is an energy resonant and Γ is the width of the autoionized state. The formula 2.29 suggests that there is exactly one maximum and one minimum in the Fano profile where $\sigma_{min} = 0$ when $\epsilon = -q$, and $\sigma_{max} = 1 + q^2$ when $\epsilon = 1/q$.

In the limit that $|q| \to \infty$ the transition to the continuum is very weak, and the shape of the line is fully determined by the transition through the discrete state only with the standard Lorentz profile of a Breit-Wigner resonance.

When the asymmetric parameter q is of the order of unity in both the continuous and discrete transition, they have the same resulting shape in the asymmetric profile, with a maximum value of $E_{max} = E_F + \Gamma/(2q)$ and a minimum value over $E_{min} = E_F - \Gamma q/2$.

In the case when the asymmetric parameter is zero ($q = 0$), the main characteristic of a Fano resonance is presented describing a symmetrical dip, sometimes also called an anti-resonance.

This characteristic given in the Fano resonance explains the possibility of destructive interference, which leads to asymmetric line shapes.

The effective resonance frequency of the discrete level E_F can be somewhere between the maximum and minimum of the asymmetric profile, and the parameter q defines the relative deviation. Therefore, in the situation where $|q| \to \infty$ the resonant frequency coincides with the maximum of the profile, while in the case when $q = 0$, the resonant frequency coincides with the minimum, for $q = 1$ the resonant frequency is exactly in the middle distance between the minimum and maximum.

The Fano formula has been used successfully in adaptation and explanation of experimental data in different fields of physics (from Fano 1964; to Wickenhauser et al., 2005 [19–21]), and as we saw in this section, the Fano effect, characterized by the presence of the Fano resonances, is present in the transport of charge through an array of quantum dots QD_s.

References

[1] D. K. Ferry, S. Goodnick and J. Bird, Transport in Nanostructures, Second Edit. New York: Cambridge University Press, 2009.

[2] S. Datta, Quantum Transport: Atom to Transistor. New York: Cambridge University Press, 2005.

[3] P. Bhattacharya, S. Ghosh, and A. D. Stiff-Roberts, Quantum Dot Opto-Electronic Devices, vol. 34, no. 1. Springer Nature Switzerland, 2020.

[4] J. H. Ojeda, M. Pacheco, and P. A. Orellana, "An array of quantum dots as a spin filter device by using Dicke and Fano effects," Nanotechnology, vol. 20, no. 43, 2009, doi: 10.1088/0957-4484/20/43/434013.

[5] J. H. Ojeda Silva, *Propiedades de Transporte de Hilos Moleculares y alambres cuánticos*. Tesis de Doctorado en Ciencias Mención Física. Universidad Técnica Federico Santa María, Valparaíso-Chile, 2010. https://es.overleaf.com/project/60d34955f0856b56220c1507

[6] J. H. Ojeda, M. Pacheco, L. Rosales, and P. A. Orellana, "Current and Shot noise in DNA chains," Org. Electron., vol. 13, no. 8, pp. 1420–1429, 2012, doi: 10.1016/j.orgel.2012.03.036.

[7] P. A. Orellana, F. Domínguez-Adame, I. Gómez, and M. L. Ladrón de Guevara, Transport through a quantum wire with a side quantum-dot array, Phys. Rev. B - Condens. Matter Mater. Phys., vol. 67, no. 8, 2003, doi: 10.1103/PhysRevB.67.085321.

[8] W. Z. Shangguan, T. C. Au Yeung, Y. B. Yu, and C. H. Kam, Quantum transport in a one-dimensional quantum dot array, Phys. Rev. B, Condens. Matter Mater. Phys., vol. 63, no. 23, pp. 1-9, 2001, doi: 10.1103/PhysRevB.63.235323.

[9] M. Di Ventra, Electrical Transport in Nanoscale Systems, First Edit. New York: Cambridge University Press, 2008.

[10] J. H. Davies, The Physics of Low-dimensional Semiconductors: An Introduction. New York: Cambridge University Press, 1998.

[11] L. E. Ballentine, Quantum Mechanics - A Modern Development. USA: World Scientific Publishing Co. Pte. Ltd, 1998.

[12] G. Chen, G. Klimeck, S. Datta, G. Chen, and W. A. Goddard, Resonant tunneling through quantum-dot arrays, Phys. Rev. B, vol. 50, no. 11, pp. 8035-8038, 1994, doi: 10.1103/PhysRevB.50.8035.

[13] C. Kittel, Introduction to Solid State Physics, Eighth Edi. United States of America 1098: John Wiley Sons, Inc, 2005.

[14] H. P. Myers, Introductory Solid State Physics, Second Edi. Philadelphia: Taylor Francis, 2009.

[15] A. F. J. Levi, Applied Quantum Mechanics. New York: Cambridge University Press, 2003.

[16] A. E. Miroshnichenko, S. Flach, and Y. S. Kivshar, Fano resonances in nanoscale structures, Rev. Mod. Phys., vol. 82, no. 3, pp. 2257-2298, 2010, doi: 10.1103/RevModPhys.82.2257.

[17] P. A. Orellana, M. L. De Ladrón Guevara and F. Domínguez-Adame, Electronic transmission through a quantum wire by side-attached nanowires, Phys. E Low-Dimensional Syst. Nanostructures, vol. 25, no. 4, 384-389, 2005, DOI: 10.1016/j.physe.2004.06.052.

[18] T. Hensgens et al., Quantum simulation of a Fermi-Hubbard model using a semiconductor quantum dot array, Nature, vol. 548, no. 7665, pp. 70-73, 2017, DOI: 10.1038/nature23022.

[19] A. E. Miroshnichenko and Y. S. Kivshar, "Engineering Fano resonances in discrete arrays," Phys. Rev. E - Stat. Nonlinear, Soft Matter Phys., vol. 72, no. 5, pp. 1–7, 2005, doi: 10.1103/PhysRevE.72.056611.

[20] U. Fano, Effects of configuration interaction on intensities and phase shifts, Phys. Rev., vol. 124, no. 6, pp. 1866-1878, 1961, DOI: 10.1103/PhysRev.124.1866.

[21] M. Wickenhauser, J. Burgdörfer, F. Krausz, and M. Drescher, "Time resolved fano resonances," Phys. Rev. Lett., vol. 94, no. 2, pp. 1–4, 2005, doi: 10.1103/PhysRevLett.94.023002.

Chapter 3

Green's functions and Quantum transport properties

3.1 Introduction to Green's functions

Due to their diversity, Green's functions have been applied in different fields of physics such as statistical mechanics, solid-state physics, field theory, nuclear physics, among others, turning out to be a powerful mathematical tool in obtaining the solution of physical systems involving many mutually interacting particles [1].

The Green functions contain information on relevant properties of the system including: the energy of the ground state, the energy and half-life of the excited states, the average value of any operator of a body in the ground state, the response to external disturbances, partition function and therefore of thermodynamic functions (entropy, density of levels, etc.). Regarding these external perturbations, a first analytical approach to the transport problem in disordered systems was proposed by Dyson [1], who, taking into account a disordered one-dimensional chain of harmonic oscillators [2], He was able to find an expression for the density of states using the method of the Green functions [2–4].

In this chapter, the time-independent Green functions (behaviors in the steady state) are used to determine some properties of electric transport and to compare the results with those given in the previous

[1] For which it makes use of perturbation theory to expand them into a perturbative series based on precise rules, to find the contribution of the n-th order in the disturbance, being able to represent employing Feynman diagrams.

[2] Each oscillator coupled to its nearest neighbors by harmonic forces, the inertia of each oscillator and the strength of each coupling being a random variable based on a known statistical distribution law. The theory applies equally to a chain of masses connected by elastic springs and making mechanical vibrations, or to an electrical transmission line composed of alternating inductances and capacitances with random characteristics.

section and which were determined using wave functions.

In general, the Green functions can be defined as the solutions of inhomogeneous differential equations of the type:

$$[z - L(r)]G(r, r', z) = \delta(r - r') \tag{3.1}$$

where r and r' are subject to certain boundary conditions, $z = \lambda + i\eta$ is a complex and $L(r)$ is a differential operator independent of time, hermitic and having a set complete of eigenfunctions $\phi_n(r)$, such that:

$$L(r)\phi_n(r) = \lambda\phi_n(r) \tag{3.2}$$

which satisfies the same boundary conditions of $G(r, r', z)$ and can be considered as orthonormal without loss of generality. Green's function can be written in terms of the energy eigenvalues of the form:

$$G(z) = \sum_l \frac{|\phi_l\rangle\langle\phi_l|}{z - L} = \sum_n \frac{|\phi_n\rangle\langle\phi_n|}{z - \lambda_n} + \int de_c \frac{|\phi_{e_c}\rangle\langle\phi_{e_c}|}{z - \lambda_{e_c}}, \tag{3.3}$$

where the sums and integrals run over the discrete and continuous states of energy respectively.

Considering a Tight Binding Hamiltonian operator ($L = H$) H and $z = E + i\eta$, the equation for Green's function can be written as:

$$[E - H]G(r, r', E) = \delta(r - r') \tag{3.4}$$

If the eigenvalues of H are E_n and the eigenfunctions are defined as $\psi_n(r)$, Green's function is defined by:

$$G(r, r', E) = \sum_n \frac{\psi_n(r)\psi_n^*(r')}{E - E_n} \tag{3.5}$$

For the Hamiltonian ca se given by equation (2.1), where we can define to $H_0 = \sum_{n=1}^{N} \varepsilon_n c_n^\dagger c_n$ and $V = \sum_{n=1}^{N} V_{n,n-1} c_n^\dagger c_n$, in such a way that $H = H_0 + V$ and $G_0 = \frac{1}{E - H_0}$ is the Green's function associated with H_0, therefore, the Green's function of H can be written as:

$$\begin{aligned} G(E) &= \frac{1}{E - H} = \frac{1}{E - H_0 - V} = \frac{1}{G_0^{-1} - V} \\ &= G_0(E)[1 - G_0(E)V]^{-1} \\ &= G_0(E) + G_0(E)V[G_0(E) + G_0(E)VG_0(E)...]\, G(E) \\ &= G_0(E) + G_0(E)VG(E) \end{aligned} \tag{3.6}$$

thus resulting, an equation of motion or equation known as the Dyson equation, which can be represented in real space by the completez relation ($\sum_k |k\rangle\langle k| = 1$), as follows:

$$\langle n|G(E-H)|n'\rangle = \delta_{nn'} \tag{3.7}$$

and further defining $G_{nk} = \langle n|G|k\rangle$, $H_{kn'} = \langle k|H|n'\rangle$, $\langle n|k\rangle = \delta_{nk}$ and making effective the definition of Kronecker delta ($n = k$) results:

$$EG_{nn'} - \sum_k G_{nk}H_{kn'} = \delta_{nn'} \tag{3.8}$$

Now calculating $H_{kn'} = \langle k| \quad H|n'\rangle$, using the equation (2.1) in the Dirac representation ($H = \sum_l |l\rangle\varepsilon_l\langle l| + \sum_{l,m} |l\rangle V_{l,m}\langle m|$) with dumb indices and Kronecker deltas δ_{kl} y δ_{km} results:

$$H_{kn'} = \varepsilon_k\delta_{kn'} + V_{kn'} \tag{3.9}$$

Replacing the equation (3.9) in (3.8) we have:

$$(E-\varepsilon_{n'})G_{nn'} = \delta_{nn'} + \sum_k V_{kn'}G_{nk} \tag{3.10}$$

The equation (3.10) is known as the dynamic equation for electrons. Since the Tight Binding Hamiltonian is being considered, the transfer integrals V_{nk} are different of zero only between neighbors closest to each other, so the dynamic equation can be written more explicitly as:

$$(E-\varepsilon_{n'})G_{nn'} = \delta_{nn'} + V_{n',n'-1}G_{n,n'-1} + V_{n',n'+1}G_{n,n'+1} \tag{3.11}$$

Is evident that the method of Green's functions can give a clearer idea of the bound states as well as the density of states. If the Green's function of a medium is known, in principle the Green's function for a disturbed system could be calculated. Using this formulation, we can compute the Green's function of undisturbed and perturbed periodic one-dimensional models [2, 5].

Known the formalism of Green's functions, is used in this section to calculate some transport properties in low dimensional systems such as quantum wires QW or quantum dot array QD_s

Applying the Dyson equation we analyze the transmission probability for systems of one, two and three QD_s placed in a linear position,

two and three QD_s in the form of a **T** and three QD_s in the form of a cross; each one of these systems being between two metallic contacts.

When the systems have more than one QD, in addition to the Green's functions, the real system's renormalization or decimation scheme is used to simplify its solution. The renormalization method is a method that transforms the real space into an effective space that generates the systematic reduction of the Hamiltonian dimension, that is, the set of linear equations that characterize the system becomes a set of non-linear equations with energies effective couplings and couplings with fewer degrees of freedom. For this reason, to calculate the transport properties in this work, the renormalization process is carried out under the inclusion of Feynman paths using Green functions, which can be considered as propagators that carry the information of charge transport through the quantum system and provide an alternative in the solution of the Schrödinger equation in a numerically and analytically stable way [6–12].

After having the renormalized quantum system and in the case of obtaining a one-dimensional system, the Green's function is calculated (which would be the basis for the transmission probability calculations), employing the Dyson equation (3.10), and written more generally as:

$$G_{ij}(w) = \delta_{ij} g_i(w) + g_i(w) \sum_{l \neq i} t_{il} G_{ij}(w), \tag{3.12}$$

where $w = E - i\eta$ is the analytical extension of the energy for the complex plane (with η infinitesimal), $g_i(w) = 1/(w - \varepsilon_i)$ is the atomic local green's function and the functions $G_{ij}(w)$ represent the electron propagator with energies w between the sites (i, j). Once the Green's function of the effective linear system is known, the transmission probability ($T(E)$, without taking into account the spin) is calculated given by the Fisher-Lee relation:

$$T(E) = Tr\left[\Gamma^L G^r \Gamma^R G^a\right]. \tag{3.13}$$

Here $\Gamma^\alpha = i\left(\Sigma^\alpha - \Sigma^{\alpha\dagger}\right)$ is the matrix corresponding to the spectral density of the left(right) contacts (L(R)). Due to that one-dimensional systems are analyzed, the equation (3.13) can be written as:

$$T(E) = \Gamma^L_{11} \Gamma^R_{NN} \left|G^r_{1N}\right|^2, \tag{3.14}$$

where G^r_{1N} corresponds to the matrix element of the retarded Green's function G^r of the system, and Γ^L_{11}, Γ^R_{NN} are the only non-zero elements of the spectral density Γ^α.

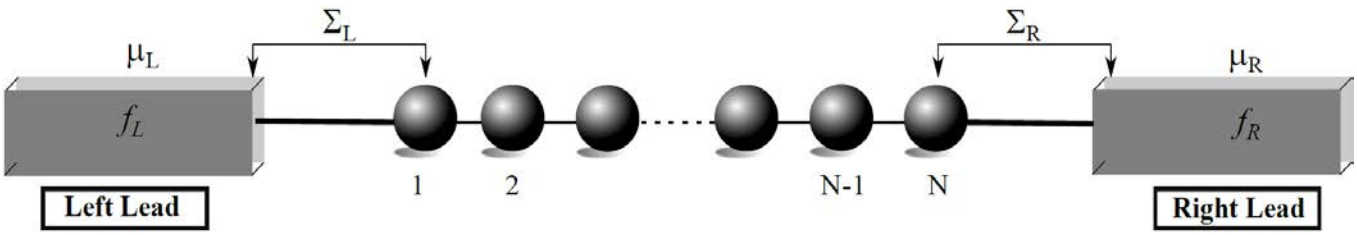

Figure 3.1: *Linear conductor between left (L) and right (R) metal contacts.*

The Green's function G^r_{1N} for those systems that are between two contacts as shown in the figure 3.1, is determined by taking the Dyson's equation of the form:

$$G_{1N} = G^0{}_{1N} + G^0_{11} \sum_k V^k{}_L G_{LN}{}^k + G^0_{1N} \sum_k V^k{}_R G_{RN}{}^k, \tag{3.15}$$

taking into account that $G_{LN}{}^k = G_L{}^{k0} V_L{}^k G_{1N}$, and, $G_{RN}{}^k = G_R{}^{k0} V_R{}^k G_{NN}$ the equation (3.15) takes the form:

$$G_{1N} = G^0{}_{1N} + G^0{}_{11} \sum_k |V^k{}_L|^2 G_L{}^{k0} G_{1N} + G^0{}_{1N} \sum_k |V^k{}_R|^2 G_R{}^{k0} + G_{NN}, \tag{3.16}$$

now defining $\Sigma_L = \sum_k |V^k{}_L|^2 G_L{}^{k0}$ and $\Sigma_R = \sum_k |V^k{}_R|^2 G_R{}^{k0}$ we obtain that:

$$G_{1N} = G^0{}_{1N} + G^0{}_{11} \Sigma_L G_{1N} + G_{1N} \Sigma_R G_{NN}. \tag{3.17}$$

However, we must leave the Green's function G_{1N} in terms of the local Green's functions G^0_{ij}, where i, j represent the sites in the chain, therefore we take G_{NN} in the expression (3.17) and is left in terms of these local Green's functions, obtaining:

$$\begin{aligned} G_{NN} =& G^0{}_{NN} + G^0_{N1} \sum_k V^k{}_L G_{LN}{}^k + G^0_{NN} \sum_k V^k{}_R G_{RN}{}^k \\ =& G^0{}_{NN} + G^0{}_{N1} \sum_k |V^k{}_L|^2 G_L{}^{k0} G_{1N} + G^0{}_{NN} \sum_k |V^k{}_R|^2 G_R{}^{k0} + G_{NN} \\ =& G^0{}_{NN} + G^0{}_{N1} \Sigma_L G_{1N} + G_{NN}{}^0 \Sigma_R G_{NN} \\ G_{NN} =& \frac{G^0{}_{NN} + G^0{}_{N1} \Sigma_L G_{1N}}{(1 - G_{NN}{}^0 \Sigma_R)}. \end{aligned} \tag{3.18}$$

Replacing 3.18 into 3.17 we have:

$$G_{1N} = G^0{}_{1N} + G^0{}_{11}\Sigma_L G_{1N} + G^0{}_{1N}\Sigma_R\Big[\frac{G^0{}_{NN} + G^0{}_{N1}\Sigma_L G_{1N}}{(1 - G_{NN}{}^0\Sigma_R)}\Big]$$

$$G_{1N} = \frac{G^0{}_{1N}}{(1 - G_{NN}{}^0\Sigma_R)}\Big[1 - G_{NN}{}^0\Sigma_R + \Sigma_R G_{NN}{}^0\Big] +$$

$$\Big[\frac{G_{11}{}^0\Sigma_L - G_{11}{}^0\Sigma_L\Sigma_R G_{NN}{}^0 + G_{1N}{}^0\Sigma_R\Sigma_L G_{N1}{}^0}{(1 - G_{NN}{}^0\Sigma_R)}\Big]G_{1N}$$

$$G_{1N} = \frac{G^0{}_{1N}}{(1 - G_{NN}{}^0\Sigma_R)} + \Big[\frac{G_{11}{}^0\Sigma_L(1 - \Sigma_R G_{NN}{}^0) + G_{1N}{}^0\Sigma_R\Sigma_L G_{N1}{}^0}{(1 - G_{NN}{}^0\Sigma_R)}\Big]G_{1N}$$

$$G_{1N}\Big[1 - G_{NN}{}^0\Sigma_R - G_{11}{}^0\Sigma_L(1 - \Sigma_R G_{NN}{}^0) - G_{N1}{}^0\Sigma_R\Sigma_L G_{1N}{}^0\Big] = G_{1N}{}^0$$

$$G_{1N}\Big[(1 - G_{11}{}^0\Sigma_L)(1 - G_{NN}{}^0\Sigma_R) - G_{N1}{}^0 G_{1N}{}^0\Sigma_R\Sigma_L\Big] = G_{1N}{}^0$$

finally,

$$G_{1N} = \frac{G_{1N}{}^0}{(1 - G_{11}{}^0\Sigma_L)(1 - G_{NN}{}^0\Sigma_R) - G_{N1}{}^0 G_{1N}{}^0\Sigma_R\Sigma_L} \tag{3.19}$$

Now, taking $\Sigma_L = \Sigma_R \equiv \Sigma = i\Gamma/2$, the equation (3.19) is reduced to:

$$G_{1N} = \frac{G^0_{1N}}{(1 + iG^0_{11}\Gamma/2)^2 + (G^0_{1N}\Gamma/2)^2} \tag{3.20}$$

Once the Green's function G_{1N} has been determined and using the Fischer-Lee relation (Equation (3.14)), the transmission probability through a linear system connected to two contacts is given by:

$$T(E) = \frac{(\Gamma G^0_{1N})^2}{\mid (1 + iG^0_{11}\Gamma/2)^2 + (G^0_{1N}\Gamma/2)^2 \mid^2} \tag{3.21}$$

which can be expressed in the form:

$$
\begin{aligned}
T(E) =& \frac{(G^0_{1N}\Gamma)^2}{|1 + i\frac{G^0_{11}\Gamma}{2} + (\frac{G^0_{11}\Gamma}{2})^2 + (\frac{G^0_{1N}\Gamma}{2})|^2} \\
=& \frac{(G^0_{1N}\Gamma)^2}{|1 + \frac{\Gamma^2}{4}[(G^0_{1N})^2 - (G^0_{11})^2] + iG^0_{11}\Gamma|^2} \\
=& \frac{(G^0_{1N}\Gamma)^2}{[1 + \frac{\Gamma^2}{4}([(G^0_{1N})^2 - (G^0_{11})^2] + iG^0_{11}\Gamma][1 + \frac{\Gamma^2}{4}([(G^0_{1N})^2 - (G^0_{11})^2] - iG^0_{11}\Gamma]} \\
=& \frac{(G^0_{1N}\Gamma)^2}{[1 + \frac{\Gamma^2}{4}[(G^0_{1N})^2 - (G^0_{11})^2]]^2 + (G_{11}\Gamma)^2}
\end{aligned}
\tag{3.22}
$$

3.2 Properties of quantum transport through systems with QD_s and QW using Green's functions.

In this section, the properties of quantum transport through systems with QD_s and QW are analyzed using Green functions, however, when obtaining the different results in the transmission probability of each of the systems, a comparison is making with the results obtained in the transmission profile using wave functions, whose results were analyzed in the previous chapter.

3.2.1 Transmission probability through a quantum dot (QD).

The system studied in this section is represented by a QD which is coupled between two leads or metal contacts left (L) and right (R) through the interface $\Gamma_{L,R}$ respectively, as can be seen in figure 3.2.

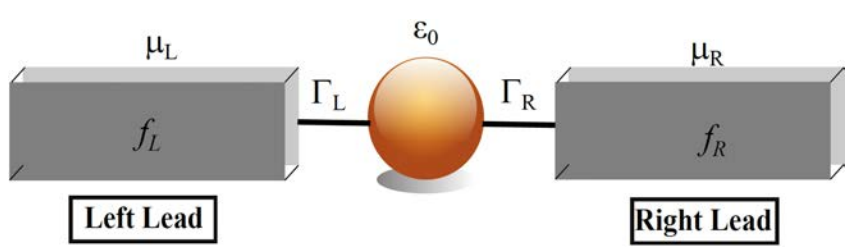

Figure 3.2: *A QD between two contacts left (L) and right (R).*

Said system of a QD is modeled through a Tight Binding Hamiltonian given by the equation (2.1) of the form:

$$H = H_{QD} + H_L + H_I \tag{3.23}$$

where H_{QD} corresponds to the Hamiltonian of the QD and (H_L, H_I) is the Hamiltonian of the leads (Left and Right) and interaction QD -Leads respectively, which are defined as :

$$\begin{aligned} H_{QD} &= \varepsilon_0 c_0^\dagger c_0 \\ H_L &= \sum_{k_L} \varepsilon_{k_L} d_{k_L}^\dagger d_{k_L} + \sum_{k_R} \varepsilon_{k_R} d_{k_R}^\dagger d_{k_R} \\ H_I &= \Gamma_L \sum_{k_L} d_{k_L}^\dagger c_0 + \Gamma_R \sum_{k_R} d_{k_R}^\dagger c_0 + h.c., \end{aligned} \tag{3.24}$$

where $c_0^\dagger$ is the operator creating an electron at the 0 place of the QD, $d_{k_{L,R}}^\dagger$ is the operator creating an electron in a $k_{L,R}$ state with energy $\varepsilon_{k_{L,R}}$, $\Gamma_{L,R}$ is the coupling between each Lead with the QD system and $h.c.$ is the complex conjugate of the Hamiltonian.

With the Hamiltonian established, the Fisher Lee's function (Equation (3.13)) is applied to calculate the transmission probability, the Green's function of the entire quantum system is determined through the Dyson equation (3.12), which takes the form:

$$G_{00} = g_0 + g_0 \nu G_{L0} + g_0 \nu G_{R0}, \tag{3.25}$$

where $g_0 = \frac{1}{z-\varepsilon_0}$, con $z = \varepsilon - i\eta$ and $\eta \to 0$, is the local Green's function of the QD with energy ε_0, and the second terms of (3.25) correspond to the bondings between the QD and the left and right leads respectively. Defining $G_{(L,R)0}$ as $G_{L0} = g_L \nu G_{00}$ and $G_{R0} = g_R \nu G_{00}$ and solving G_{00}, the equation (3.25) is given by:

$$G_{00} = \frac{g_0}{1 - g_0 \nu^2 g_L - g_0 \nu^2 g_R}, \tag{3.26}$$

which, by doing algebraic treatments and defining some physical quantities[3], we obtain the Green's function of the QD system, coupled to contacts given by:

$$G_{00} = G_0 = \frac{1}{(\varepsilon - \varepsilon_0 - \Lambda) + i\Gamma} \tag{3.27}$$

Once this Green's function (3.27) has been obtained and by means of the Fisher Lee's equation (Equation(3.13)) for the QD which is given

[3]Local Green's function: $g_0 = 1/(\varepsilon - \varepsilon_0)$; Self-energies: $\Sigma_{(L,R)} = g_{(L,R)}\nu^2 = -\nu e^{ik}$, $\Sigma_{(L,R)} = Re[\Sigma_{(L,R)}] + iIm[\Sigma_{(L,R)}]$, $\Lambda = Re[\Sigma_R] + Re[\Sigma_L]$; System-Lead coupling: $\Gamma = Im[\Sigma_R] + Im[\Sigma_L]$

by $T(\varepsilon) = Tr[\Gamma_L \Gamma_R |G_0|^2]$, where $\Gamma_L = \Gamma_R = \Gamma$ is the coupling integral between the QD and the left and right contacts respectively, finally an equation is reached for the probability of transmission of a charge that crosses the QD from the left contact to the right given by:

$$T(\varepsilon) = \frac{\Gamma^2}{(\varepsilon - \varepsilon_0 - \Lambda)^2 + \Gamma^2}. \tag{3.28}$$

With the resulting equation (3.28) of the Transmission probability through a QD, it is evaluated to obtain the Transmission profile given in figure 3.3 (black line). At the same time, is possible to compare said profile with the Transmission profile given for an impurity found inside a QW (Figure 2.2) and is represented in figure 2.3 (b). As expected and can be seen, the transmission probability through the QD shows a resonant tunneling regime and, therefore, a unit peak in transmission associated with the eigenvalue of the QD depending on the coupling (Γ) with the left and right contacts, as observed in the atomic linear chain with an impurity (Figure 2.3 (b)). The difference lies, in the methodology used with wave functions (Figure 3.3-Red line) and Green functions (Figure 3.3-black line) and some additional coupling parameters that are taken into account within the process using wave functions, and which are implicit within the self-energy parameters Σ and couplings Γ when the process with Green's functions is used. These parameters are broken down in table 3.1.

Green's Functions	**Waves Functions**
$T(\varepsilon) = \frac{\Gamma^2}{(\varepsilon-\varepsilon_0-\Lambda)^2+\Gamma^2}$	$T = 1 - \frac{[V_a(\varepsilon_a-\varepsilon_b)+2(V_a^2-V_c^2)cosk]^2}{[V_a(\varepsilon_a-\varepsilon_b)-2V_c^2cosk][V_a(\varepsilon_a-\varepsilon_b)+2(V_a^2-V_c^2)cosk]+4V_c^4}$
$\varepsilon_0 = -0.3eV$	$\varepsilon_0 = \varepsilon_b = -0.3eV$
$\Gamma = -0.2eV$	$V_c = -0.3eV$, $V_a = -0.8eV$ and $\varepsilon_a = 0.3eV$

Table 3.1: *Energy parameters and couplings used in the calculation of the transmission probability through a QD taking into account each of the methods: Green's functions and wave functions.*

3.3 Transmission probability through two QD_s.

The system of two quantum dots coupled in the growth direction to the metallic contacts (Left and Right leads) as shown in figure 3.4, is modeled through a Tight Binding Hamiltonian given by the equation (2.1) of the form:

$$H = H_{QD} + H_L + H_I \tag{3.29}$$

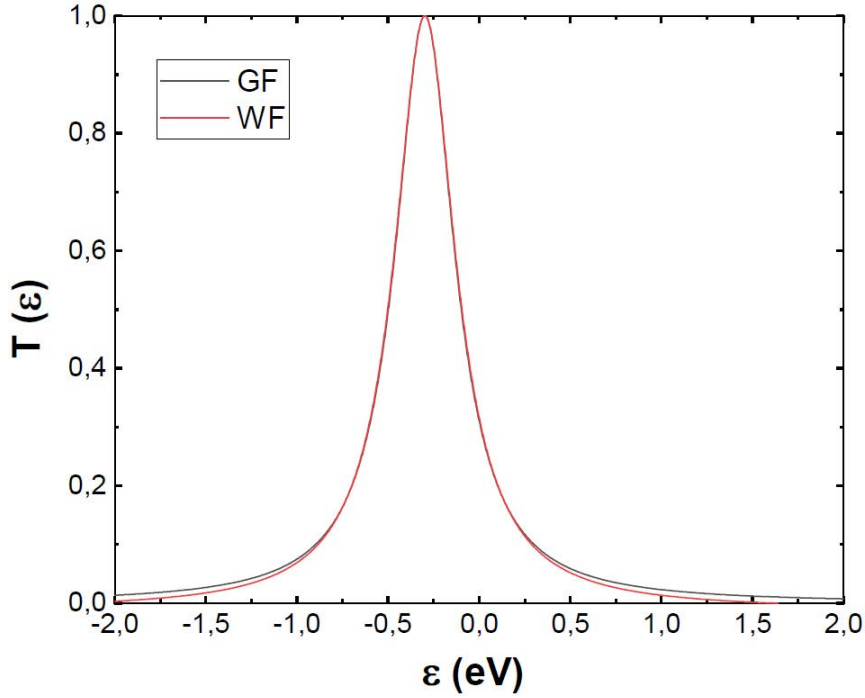

Figure 3.3: *Comparison of the transmission probability as a function of the incident electron energy: (black line) Transmission probability through a QD using Green's functions (GF), (red line) Transmission probability through impurity or QD applying Wave functions (WF).*

where H_{QD} corresponds to the Hamiltonian of the two QD_s and (H_L, H_I) are the Hamiltonians of the leads (Left and Right) and interaction QD-Leads respectively, defined by:

$$\begin{aligned} H_{QD} &= \sum_{n=1}^{2} \varepsilon_n c_n^\dagger c_n + \sum_{n=1}^{2} v_{n,n+1} c_n^\dagger c_{n+1}, \\ H_L &= \sum_{k_L} \varepsilon_{k_L} d_{k_L}^\dagger d_{k_L} + \sum_{k_R} \varepsilon_{k_R} d_{k_R}^\dagger d_{k_R} \\ H_I &= \Gamma_L \sum_{k_L} d_{k_L}^\dagger c_1 + \Gamma_R \sum_{k_R} d_{k_R}^\dagger c_2 + h.c., \end{aligned} \tag{3.30}$$

where $c_n^\dagger$ is the operator creating of an electron at the n site of the QD with energy ε_n, $d_{k_{L,R}}^\dagger$ is the operator creating an electron in a state $k_{L,R}$ with energy $\varepsilon_{k_{L,R}}$, $\Gamma_{L,R}$ is the coupling between each lead with the system of the two QD_s, $v_{n,n+1}$ is the coupling between the QD_s (which in this case is $v_{n,n+1} = V_{12}$) and $h.c.$ is the complex conjugate of the Hamiltonian. As in the case for a QD and with the Hamiltonian established for the system of two QD_s, the Fisher Lee's function (Equation (3.14), for a one-dimensional system) is applied to calculate

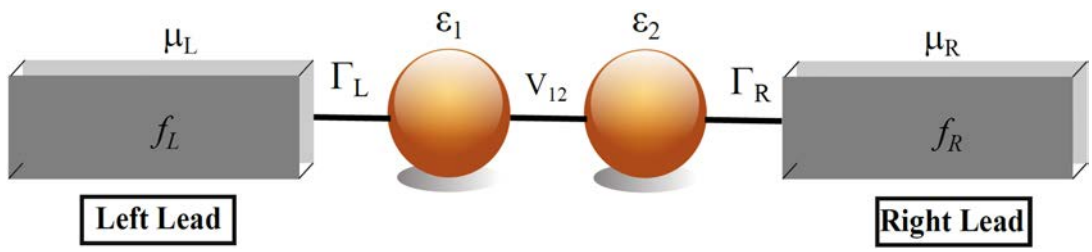

Figure 3.4: *System of two QD_s linearly connected to leads (Left and Right) respectively.*

the transmission probability, where, in this case, $N = 2$.

For this, the Green's functions $G^0_{11} = G^0_{NN}$ and G^0_{1N} of the quantum system of the two QD_s are determined through the Dyson equation (3.12), which takes the form:

$$G^0_{11} = g_1 + g_1 V_{12} G^0_{21}, \tag{3.31}$$

G^0_{21} when also calculated from the Dyson equation (3.12), resulting in $G^0_{21} = g_2 V_{21} G^0_{11}$ and replacing in the equation (3.28), the Green's function $G^0_{11} = G^0_{22}$ given by:

$$G^0_{11} = G^0_{22} = \frac{g_1}{1 - g_1 g_2 V_{12}^2} \tag{3.32}$$

Now, taking the equation $G^0_{21} = g_2 V_{21} G^0_{11}$ and replacing in it the Green's function G^0_{11} to obtain G^0_{12}, where $G^0_{12} = G^0_{21}$ y $V_{21} = V_{12}$ results:

$$G^0_{12} = \frac{g_1 g_2 V_{12}}{1 - g_1 g_2 V_{12}^2} \tag{3.33}$$

The equations (3.32) and (3.33) are replaced in the equation (3.22) with $N = 2$ (System of two QD_s coupled one-dimensionally), to obtain the Transmission probability of the total system QD_s+Leads given by:

$$T(E) = \frac{(G^0_{12}\Gamma)^2}{[1 + \frac{\Gamma^2}{4}[(G^0_{12})^2 - (G^0_{11})^2]]^2 + (G_{11}\Gamma)^2} \tag{3.34}$$

Taking $T(E) = 1$ in the equation (3.34) in order to find the resonant

peaks in the transmission for the system of two QD_s we obtain:

$$
\begin{aligned}
(G^0_{12}\Gamma)^2 &= \left[1+\frac{\Gamma^2}{4}[(G^0_{12})^2-(G^0_{11})^2]\right]^2+(G^0_{11}\Gamma)^2 \\
\Gamma^2[(G^0_{12})^2-(G^0_{11})^2]-&\left\{1+\frac{\Gamma^2}{2}[(G^0_{12})^2-(G^0_{11})^2]+\left[\frac{\Gamma^2}{4}[(G^0_{12})^2-(G^0_{11})^2]\right]^2\right\}=0 \\
&[\Gamma^2[(G^0_{12})^2-(G^0_{11})^2]]^2-8\Gamma^2[(G^0_{12})^2-(G^0_{11})^2]+16=0 \\
&[\Gamma^2[(G^0_{12})^2-(G^0_{11})^2]-4]^2=0
\end{aligned}
\tag{3.35}
$$

Replacing the equations (3.32) and (3.33) into (3.35) and taking $V_{12}=V$ for the special case where $g_1=g_2=\frac{1}{\varepsilon-\varepsilon_1}$ finally is get:

$$
\varepsilon=\varepsilon_1\pm\sqrt{\frac{4V^2-\Gamma^2}{4}} \tag{3.36}
$$

The behavior of the expression (3.34) for the transmission probability and the resonant peaks when $T(E)=1$ is observed in the figure 3.5.

In the figure 3.5(a) is possible to observe the transmission probability as a function of the energy with that the charge carrier enters the system, varying the coupling potential (Γ), where $V=0.2eV$ and the site energies of each of sites is given by $\varepsilon_1=\varepsilon_2=-0.2\ eV$. Is important to note that when $\Gamma\sim 0\ eV$ there are two resonances, which coincide with the eigenvalues of the states of each of the QD_s, equal to $-0.4\ eV$ and $0\ eV$; these values can be calculated by diagonalizing the Hamiltonian H_{QD} given in the equation (3.30) or by the equation (3.36) for $\Gamma=0\ eV$.

On the other hand, the same behavior is presented, where the bandwidth is proportional to $2V$ in this class of low-dimensionality systems, as could be observed for the system of an array of QD_s coupled to a QW [20]. This bandwidth (for the case in which the coupling (V) between the QD_s is constant) does not vary notably with the increase of Γ, however, can be seen that an increase in the amplitude is generated of $T(E)$ due to the hybridization between the delocated electronic states of the metallic contacts and the localized states of the linear system of QD_s, leading to behaviors within weak or strong regimes, depending on whether Γ is less or greater with respect to V,

i.e., if $\Gamma \leq V$ a weak coupling regime will be presented where the two resonances for any value of Γ are generated, as can be seen in the figure 3.5 (a) (upper panel-blue line), where the particular case has been

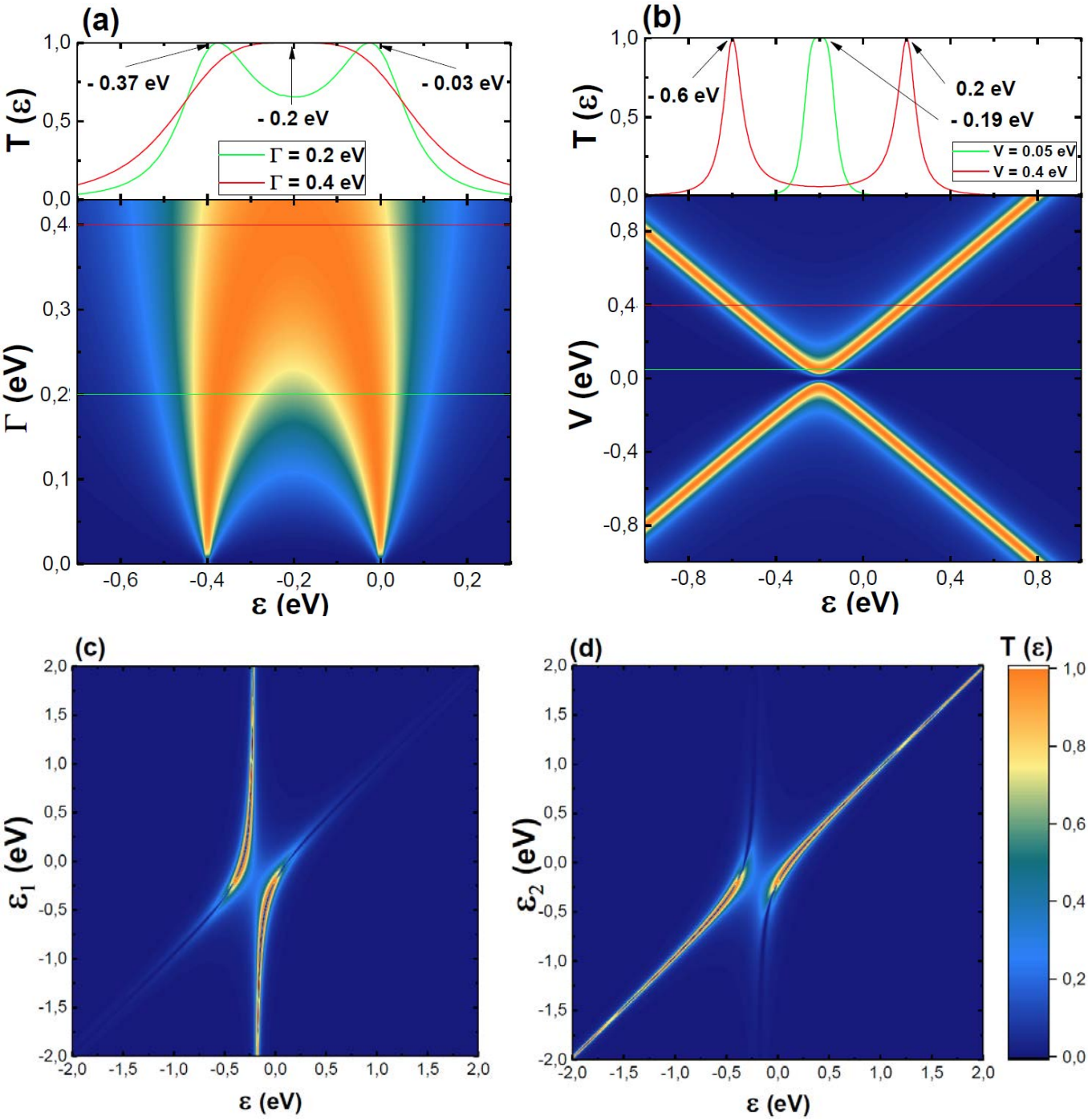

Figure 3.5: *Transmission probability as a function of energy,* ***(a)*** *varying* (Γ)*,* ***(b)*** *varying* (V)*,* ***(c)*** *varying* (ε_1)*, and* ***(d)*** *varying* (ε_2)*.*

taken in which $\Gamma = 0.2\ eV$ producing these resonant peaks in the energy values $\varepsilon = -0.37\ eV$, $-0.03\ eV$, which can be verified by evaluating the equation (3.36). Now, if $\Gamma > V$ is in a strong coupling regime and the eigenstates of the QD_s hybridize generating a single state, as can be verified by the equation (3.36) for a particular case where $\Gamma = 0.4\ eV$ resulting a resonance around $\varepsilon = -0.2\ eV$ (figure 3.5 (a), top panel-red line), with a bandwidth approximately equal to $2V$, as already mentioned.

The figure 3.5(b) shows the transmission probability $T(E)$ as a function of energy, varying the potential V between the QD_s and with energy values for each QD given by $\varepsilon_1 = \varepsilon_2 = -0.2\ eV$ and $\Gamma = 0.1\ eV$. Is clear to observe that for values $V \ll \Gamma$ the behavior is similar to that presented in figure 3.5(a), where a hybridized state occurs within a strong coupling regime (see figure 3.5(b), top panel-blue line) and whose eigenvalue is approximately equal to $\varepsilon = -0.2\ eV$. As V increases, where $V \geq \Gamma$, the bandwidth increases proportionally to $2V$ generating a separation of the resonances and keeping the intensity at the values of $T(E)$, reaching a limit where these resonant peaks are so far apart that their electronic behavior resembles a decoupled QD_s system.

Figures 3.5(c) and 3.5(d) show the profile of the transmission probability as a function of the incident electron energy, varying the site energies ε_1 and ε_2 respectively, keeping the fixed parameters of $V = 0.2\ eV$, $\Gamma = 0.1\ eV$ and $\varepsilon_{1,2} = -0.2\ eV$ when one of the two does not vary.

As can be seen and regardless of the variation of ε_1 or ε_2, there will always be two resonances that coincide with the eigenvalues of the Hamiltonian H_{QD} given in the equation (3.30) and evaluated by the expression $\varepsilon = \frac{(\varepsilon_1+\varepsilon_2)\pm\sqrt{(\varepsilon_1+\varepsilon_2)^2-4(\varepsilon_1\varepsilon_2-V^2)}}{2}$. Table 3.2 shows some of these eigenvalues for different energies of ε_1 y ε_2.

The difference between Figures 3.5(c) and 3.5(d) lies in the amplitude of each peak, due to a resonant tunneling effect. To understand these energies where resonances occur, the system of two quantum dots or impurities is taken, analogous to a system of two potential barri-

$\varepsilon_1/\varepsilon_2(eV)$	$\varepsilon(1)(eV)$	$\varepsilon(2)(eV)$
-2.0	-0.18	-2.02
-1.5	-0.17	-1.53
-1.0	-0.15	-1.05
-0.5	-0.1	-0.6
0.0	0.12	-0.32
0.5	0.55	-0.25
1.0	1.03	-0.23
1.5	1.52	-0.22

Table 3.2: Eigenvalues for different energies of ε_1 y ε_2.

ers, between which there is a finite potential well, where it is known that within this type of potentials contains a finite number of bound states [13,14], alternating from the ground state. Said bound states or energies allowed within the well make the effect of resonant tunneling possible.

When a particle penetrates the potential barriers[4], the reflections that occur between them[5] cancel out coherently, giving instead of a total transmission and, therefore, for the case where the barriers are symmetrical ($\varepsilon_1 = \varepsilon_2$), the resonant tunneling is complete generating two resonances with the same transmission amplitude and equal to unity. In the case of the figures 3.5(c) and 3.5(d) can be observed when $\varepsilon_1 = -0.2\ eV$ or $\varepsilon_2 = -0.2\ eV$ respectively.

When there are two asymmetric barriers, where $\varepsilon_1 \neq \varepsilon_2$, two resonances are generated, but one of them does not reach the unity in transmission, i.e., the system isn't transparent for this resonant energy. The asymmetry in the energy values of the barriers makes that the reflections that occur between them are not completely canceled, therefore, the resonance generated will be due to a quasi-stationary level between the asymmetric barriers, and consequently, the coherence caused by the backscatter is lost.

Figure 3.6 shows a resonant tunneling scheme for the system of the two asymmetric quantum dots, where the blue barriers represent the potential barriers with varying $\varepsilon_{1,2}$ energy.

This phenomenon of resonances can be exploited in the development of mesoscopic devices, which operate as filters [15], since when particles with energies lower than the potential barrier's height enter on the

[4]Where the energy is adjusted to the quasi-stationary levels of the well.
[5]Inside the potential well.

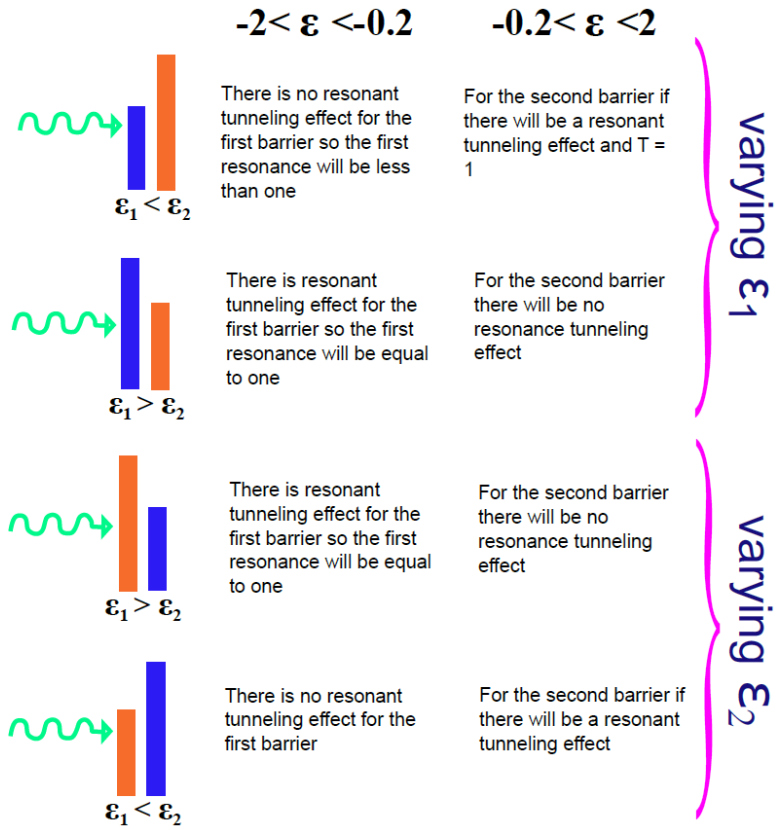

Figure 3.6: *Resonant tunneling scheme for two asymmetric barriers.*

device, only those with energy-adjusted to the resonant energy, will pass through the heterostructure containing the two barriers; while the others will be practically stopped in their entirety, and as the incidence energy increases, the transmission coefficient tends to unity. Can also be said that, when the probability of transmission is minimal or null, the particles tend to remain trapped between the barriers for a life's period [16].

3.4 Comparison with a system of wells and barriers

The transmission probability of a linear two impurities system connected to two contacts can be approximated using an analogous model of wells and barriers [17, 18] and scan the energies of the electron incident on this system and calculate the probability of transmission through it.

Figure 3.7 above shows a system of three potential barriers, all characterized by a height V_b, width L_b and two wells of width L_w in which the potential is equal to 0 eV. By connecting this system to two metal contacts, it is possible to calculate the electron probability transmission from the emitter to the collector. The transmission probability

will be maximum when the energy of these incident electrons exactly coincides with the energy of the quasi-stationary states inside the well system. Two of these states have also been included in this figure, in red the quasi-stationary state with the lowest energy which clearly corresponds to a symmetric state of energy E_1, and in blue color the following state of asymmetric behavior of energy E_2.

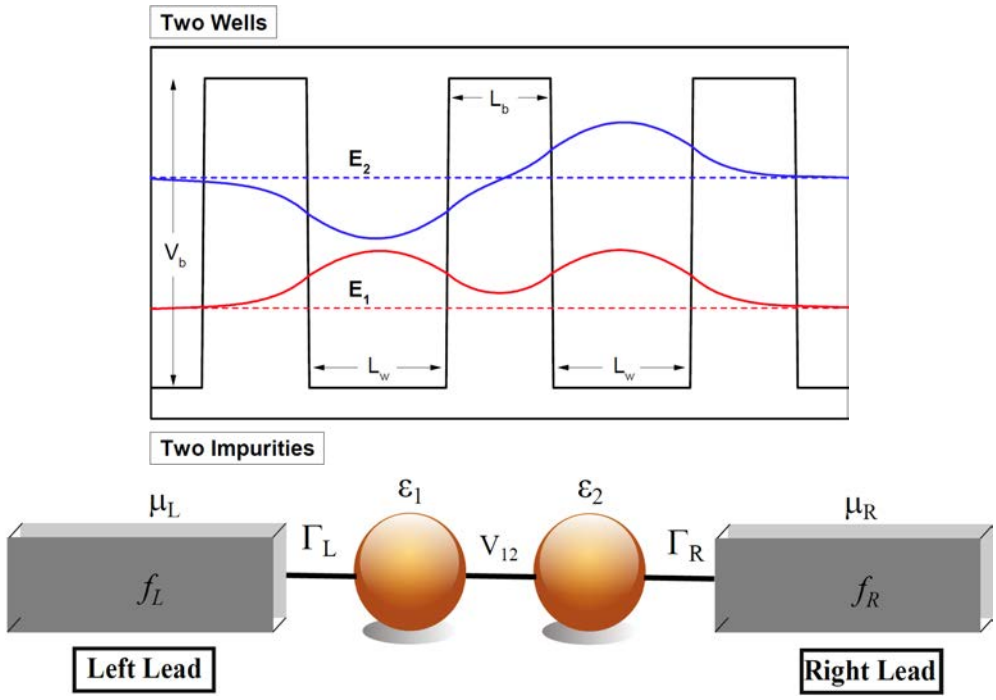

Figure 3.7: The upper figure shows a system with two wells and three barriers, two quasi-stationary electronic states with energies E_1 and E_2 are also included. The figure below is the analogous system of two linear impurities.

The wave functions of this well system are obtained by solving the Schr¨odinger equation by imposing open boundary conditions. The lower Figure 3.7 shows the modeled system that corresponds to two impurities with their energies ε_1 and ε_2, coupled via potential V_{12}, and coupled to two metallic contacts by means of the potential Γ. The figure 3.8 shows the comparison for the transmission probability of the system of two impurities in linear arrangement (dashed red curve) obtained by means of the method of Green's functions, and the transmission probability of the system of two quantum wells and three barriers (solid black line) [19] obtained by means of Schrödinger equation. The parameters used for the calculations of both models are presented in table 3.3, where the first four rows correspond to parameters of the Green functions and the last three are parameters associated with the

wells and barriers system. As is evident, for the calculated parameters, the transmission probability of the well system adequately models the system of two linear impurities that for this case are coupled since the coupling potential is about three orders of magnitude smaller than the site energy of each impurity. In this regime we see that both models account for the probability of electronic transmission in a completely equivalent way.

Figure 3.8(a) shows the transmission probability for a coupled well system, for these parameters there is an overlap between the transmission peaks due to the two states within the system or equivalently for the two site energies for the case of impurities. It should be noted that, for these parameters, the transmission function is identical for both systems, that is, the wells and barriers system adequately models the transmission probability of the two impurities system.

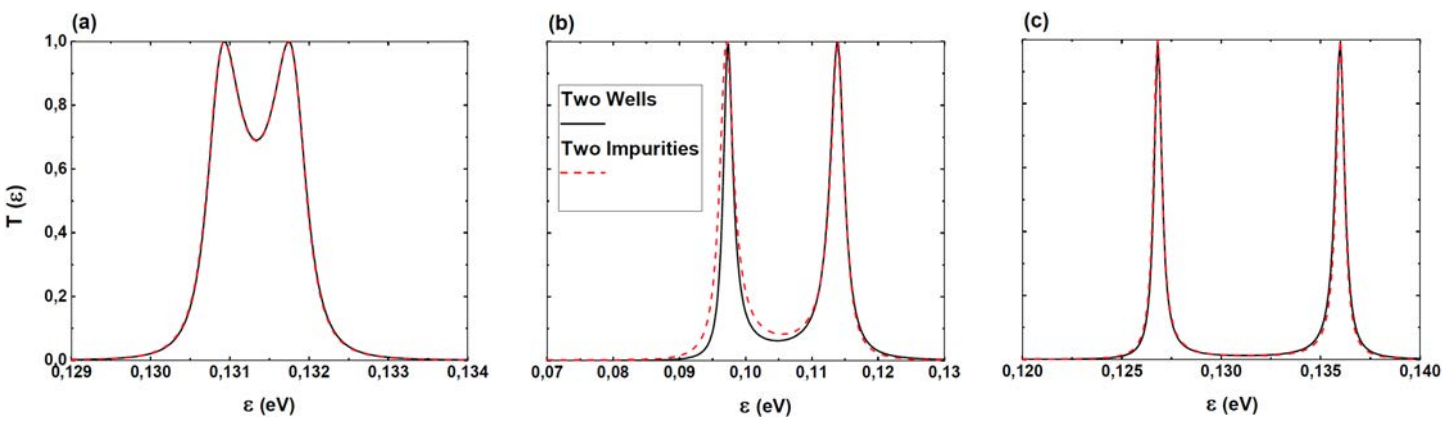

Figure 3.8: Comparison between the transmission probability for two linear impurities (dashed red line) with that obtained for a system of two quantum wells (solid black line). **(a)**, **(b)** and **(c)** correspond to the three sets of parameters presented in table 3.3.

The figure 3.8(b) again represents the transmission probability of both models, for this case the height of the potential barriers in the well system has been decreased, which has as a consequence that the transmission function no longer presents the same width for the two states in this system, and since the state with the lowest energy E_1 is the state with the longest average life time for electrons (peak on the left), it presents a small but appreciable decrease in width compared to the higher energy state E_2 (peak on the right) which is a state with a shorter average lifetime for the charge carriers. On the other hand, in the system of two impurities, this difference in the average width for the two transmission peaks does not appear. For the parameters

calculated in this case, the overlap between the transmission peaks is no longer present as in Figure 3.8(a), this indicates a decoupling between the wells and between the impurities.

Parameter	**Fig. 3.8(a)**	**Fig. 3.8(b)**	**Fig. 3.8(c)**
Γ	5.1 meV	2.5 meV	0.5 meV
V_{12}	4.8 meV	5.8 meV	4.6 meV
ε_1	0.1313 eV	0.1055 eV	0.1314 eV
ε_2	0.1313 eV	0.1055 eV	0.1314 eV
V_b	0.5 eV	0.3 eV	0.5 eV
L_b	5.4 nm	3 nm	3 nm
L_w	4 nm	4 nm	4 nm

Table 3.3: Parameters used for the simulation of figure 3.8.

In Figure 3.8(c), note again that both models are quite similar and the transmission probability of the well system fits the modeled impurity system quite well. In this case, the height of the potential barriers has been increased 0.2 eV more than in figure 3.8(b). As a consequence, the states are now both closer to the bottom of the well and therefore both have a similar average life time for charge carriers and this translates into a very close average width for both transmission peaks. For these parameters, there is again a very good similarity between the transmission probability of the well system and the two-impurity system. Note that in this case the transmission peaks are totally separated, which indicates that both the two wells and the two impurities correspond to a decoupled system.

In conclusion, it has been shown that when the potential in the well and barrier system is high enough, the electronic states are closer to the bottom of the well and, therefore, the mean width of each transmission peak is similar and is in this case in which the transmission probability of the wells and barriers system is more similar to that obtained for the system of two impurities linearly coupled to two contacts.

3.5 One-dimensional system of three QD_s

As for the case with two QD_s (figure 3.4), the system with three QD_s connected linearly with two contacts as shown in figure 3.9, is modeled through a Tight binding Hamiltonian given by the equation (3.30), the difference is that in the Hamiltonian H_{QD} the sum goes from $n = 1$

to $n = 3$ and there are couplings between the QD_s given by $v_{n,n+1} = V_{12},\ V_{23}$.

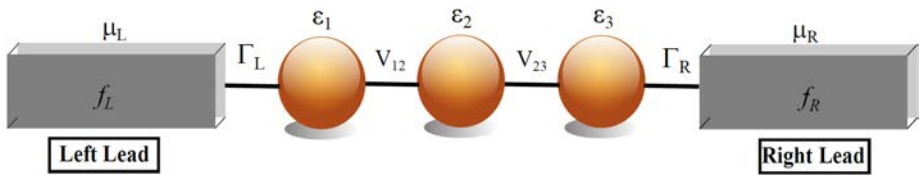

Figure 3.9: *One-dimensional system of three QD_s connected to two leads.*

With said Hamiltonian established for the system of three QD_s, the Fisher Lee function (Equation (3.14)) is applied to calculate the transmission probability (same as the previous cases with $N = 1,\ 2$ respectively), where, in this case $N = 3$.

For this, the Green functions $G^0_{11} = G^0_{NN}$ and G^0_{1N} of the quantum system of the three QD_s are determined through the Dyson equation (3.12), resulting in the expressions:

$$\begin{aligned} G^0_{13} =& \frac{g_1 g_2 g_3 V_{1,2} V_{2,3}}{1 - g_1 g_2 V^2_{1,2} - g_2 g_3 V^2_{2,3}},\ \textit{and} \\ G^0_{33} =& \frac{g_3(1 - g_1 g_2 V^2_{1,2})}{1 - g_1 g_2 V^2_{1,2} - g_2 g_3 V^2_{2,3}} \end{aligned} \tag{3.37}$$

Obtained the Green's functions G^0_{11} and G^0_{13} through the equations (3.37), they are replaced in the equation (3.22) with $N = 3$ (System of three impurities or QD_s coupled one-dimensionally), to obtain the Transmission probability of the total system QD_s+Leads given by:

$$T(E) = \frac{(G^0_{13}\Gamma)^2}{[1 + \frac{\Gamma^2}{4}[(G^0_{13})^2 - (G^0_{11})^2]]^2 + (G_{11}\Gamma)^2} \tag{3.38}$$

In the particular case of having three impurities with the same site energy, where $\varepsilon_1 = \varepsilon_2 = \varepsilon_3 \equiv \varepsilon_0$, and with the coupling between them given by $V_{1,2} = V_{2,3} \equiv v$, the Green's functions given in the equation (3.37) take the form:

$$\begin{aligned} G^0_{13} =& \frac{g_0^3 v^2}{1 - 2g_0^2 v^2},\ \textit{and} \\ G^0_{33} =& \frac{g_0(1 - g_0^2 v^2)}{1 - 2g_0^2 v^2} \end{aligned} \tag{3.39}$$

The behavior of the expression (3.38) for the transmission probability and the resonant peaks when $T(E) = 1$ is observed in the figure 3.10.

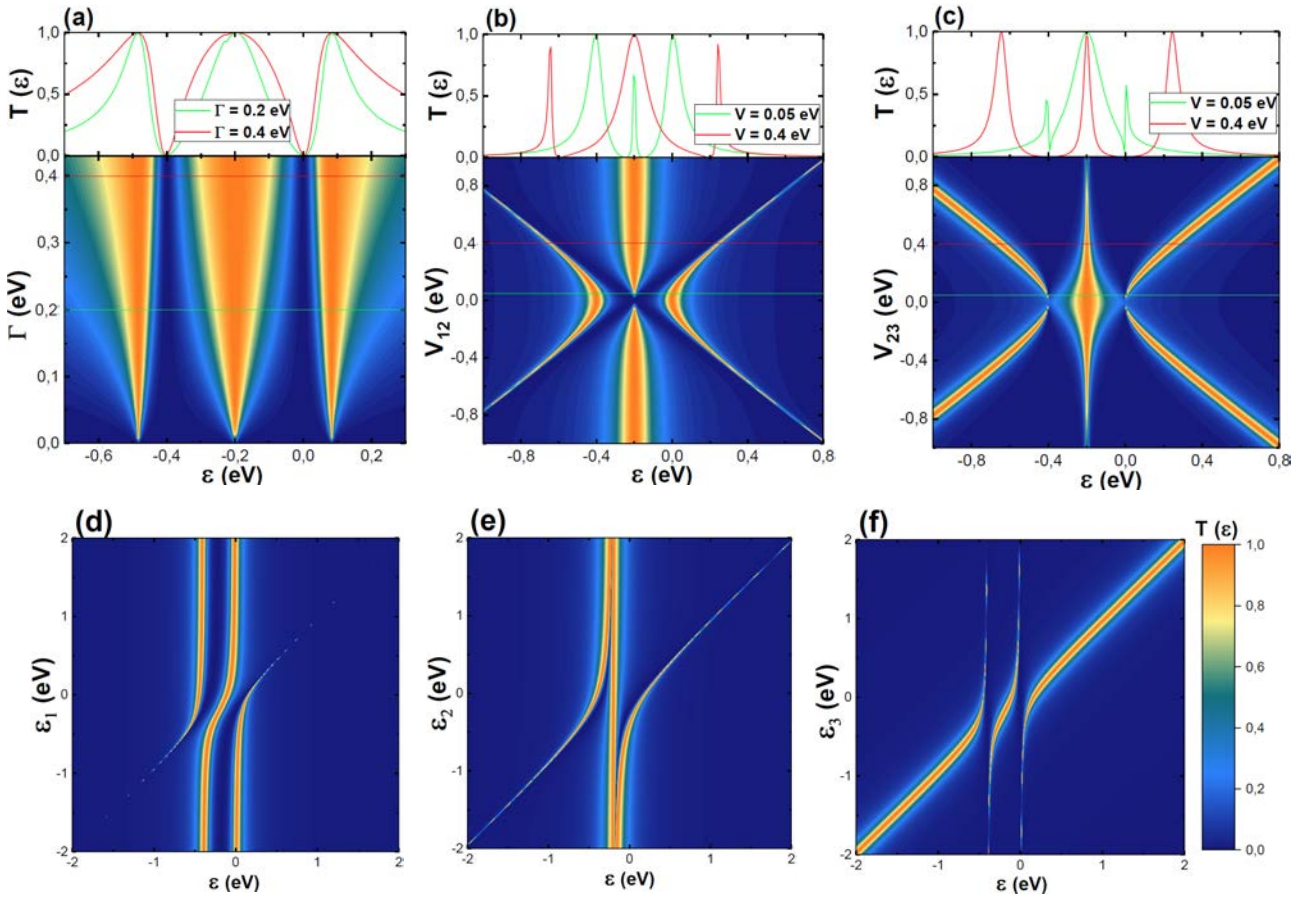

Figure 3.10: *Transmission probability,* ***(a)*** *varying* Γ ***(b)*** *varying* V_{12}*,* ***(c)*** *varying* (V_{23})*,* ***(d)*** *varying* ε_1*,* ***(e)*** *varying* ε_2 *and* ***(f)*** *varying* ε_3*.*

In the figure 3.10(a) we can see the transmission probability as a function of the energy with which the charge carrier enters the system, varying the coupling potential (Γ) of the linear system with the contacts, where $V = 0.2\ eV$ and the site energies of each of them is given by $\varepsilon_1 = \varepsilon_2 = \varepsilon_3 = -0.2\ eV$. Is important to note that when $\Gamma \sim 0\ eV$ there are three resonances, which coincide with the eigenvalues of the states of each of the QD_s, equal to $(-0.48, -0.2, 0.08)\ eV$; these values can be calculated by diagonalizing the Hamiltonian H_{QD} given in the equation (3.30).

As in the case of two impurities, the symmetrical nature of the transmission probability is noted. As Γ increases, there is an increase in the amplitude of the resonance peaks, this increase being more significant for the resonances of the extremes, while the central resonance increases in amplitude, but in a milder way. This increase in the width of each resonance is due to the hybridization between the delocated electronic states of the metallic contacts and the localized states of

the linear system of QD_s, leading to behaviors within weak or strong regimes depending on whether Γ is less than or greater than V_{12} *or* V_{23}; i.e., if Γ is less than these couplings, a weak coupling regime will occur; if Γ is greater than said couplings, a strong coupling regime will be presented and the eigenstates of the QD_s will hybridize, generating that the resonances overlap and the bandwidth increase, therefore, the charge carriers can be transported more easily from the source to drain.

On the other hand, in the figures 3.10(b) and 3.10(c) the behavior of the transmission probability can be observed (with $\Gamma = 0.1\ eV$, $\varepsilon_1 = \varepsilon_2 = \varepsilon_3 = -0.2\ eV$) as a function of the energy, varying V_{12} *and* V_{23} respectively, presenting three resonances around the eigenvalues, which can be easily determined by diagonalization of the Hamiltonian, resulting in the resonances in values of $\varepsilon = \varepsilon_1$ y $\varepsilon = \varepsilon_1 \pm \sqrt{V_{12}^2 + V_{23}^2}$.

These profiles also show a behavior similar to what occurred in the system with two QD_s, where bandwidth increases proportionally to $2V_{12}$ *or* $2V_{23}$, the difference between these two profiles lies, in that the states are hybridized in certain regions when the strong regimes are present, comparing Γ with one of the two couplings V_{12} *or* V_{23} as mentioned above. Moreover, when the value of V_{12} *or* V_{23} is very large, the system acts as if it were decoupled and therefore the conductance tends to decrease.

Figures 3.10(d), 3.10(e) and 3.10(f) show the transmission probability profile as a function of the incident electron energy, varying the site energies ε_1, ε_2 and ε_3 respectively, keeping the fixed parameters of $V = 0.2\ eV$, $\Gamma = 0.1\ eV$ and $\varepsilon_{1,2,3} = -0.2\ eV$ when one of the three does not vary. As can be seen and regardless of the variation of ε_1, ε_2 or ε_3, there will always be three resonances that coincide with the eigenvalues of the Hamiltonian H_{QD} given in the equation (3.30).

The tables 3.4, 3.5 and 3.6 show some of these eigenvalues for different energies of ε_1, ε_2 and ε_3 respectively.

As happened in the system with two QD_s, the difference of these last profiles where the energies of each QD vary, lies in the amplitude of each peak due to a resonant tunneling effect. For this system of three QD_s, it is taken analogous to a system of three potential barriers, i.e., two potential wells are formed between the three barriers.

ε_1 **(eV)**	$\varepsilon(1)(eV)$	$\varepsilon(2)(eV)$	$\varepsilon(3)(eV)$
-2.0	-2.02	-0.39	0.01
-1.5	-1.53	-0.38	0.014
-1.0	-1.05	-0.37	0.02
-0.5	-0.62	-0.32	0.04
0.0	-0.45	-0.11	0.16
0.5	-0.42	-0.03	0.56
1.0	-0.41	-0.02	1.03
1.5	-0.41	-0.01	1.52

Table 3.4: Eigenvalues for different values of ε_1.

$\varepsilon_2(eV)$	$\varepsilon(1)(eV)$	$\varepsilon(2)(eV)$	$\varepsilon(3)(eV)$
-2.0	-2.04	-0.2	-0.16
-1.5	-1.56	-0.2	-0.14
-1.0	-1.09	-0.2	-0.11
-0.5	-0.67	-0.2	-0.03
0.0	-0.4	-0.2	0.2
0.5	-0.3	-0.2	0.6
1.0	-0.26	-0.2	1.06
1.5	-0.25	-0.2	1.54

Table 3.5: Eigenvalues for different values of ε_2.

When a particle collides on the potential's barriers, the reflections that occur between them are coherently canceled, giving rise to a total transmission and therefore, for the case where the barriers are symmetric ($\varepsilon_1 = \varepsilon_2 = \varepsilon_3$), the resonant tunneling is complete, generating three resonances with the same transmission amplitude and equal to unity. In the figures 3.10(d), 3.10(e) and 3.10(f) these resonances can be observed when $\varepsilon_1 = -0.2\ eV$, $\varepsilon_2 = -0.2\ eV$ y $\varepsilon_3 = -0.2\ eV$ respectively (Central zone of each of the figures).

When there are three asymmetric barriers where $\varepsilon_1 \neq \varepsilon_2 = \varepsilon_3$, $\varepsilon_1 = \varepsilon_3 \neq \varepsilon_2$ or $\varepsilon_1 = \varepsilon_2 \neq \varepsilon_3$ three resonances are generated, but two of them do not reach the unity in transmission, that is, the system is not transparent for those resonant energies.

The asymmetry in the energy values of the barriers makes that the backward reflections that occur between them are not completely canceled. Therefore, it produces a non-zero reflection and the resonance that is generated will be due to a quasi-stationary level within the two asymmetric wells between the barriers. When the symmetry between the barriers does not exist, coherence is lost, and the transmission co-

$\varepsilon_3(eV)$	$\varepsilon(1)(eV)$	$\varepsilon(2)(eV)$	$\varepsilon(3)(eV)$
-2.0	-2.02	-0.38	0.01
-1.5	-1.53	-0.38	0.01
-1.0	-1.05	-0.37	0.02
-0.5	-0.62	-0.32	0.04
0.0	-0.45	-0.11	0.16
0.5	-0.42	-0.04	0.56
1.0	-0.41	-0.02	1.03
1.5	-0.41	-0.01	1.52

Table 3.6: Eigenvalues for different values of ε_3.

efficient does not reach the value of one, for two of three potential barriers.

3.6 T-shaped System with two QD_s between leads.

The system studied in this section is represented by two QD_s in **T**-shaped, coupled to two metal contacts left (L) and right (R) through the interface $\Gamma_{L,R}$ respectively, as can be seen in figure 3.11.

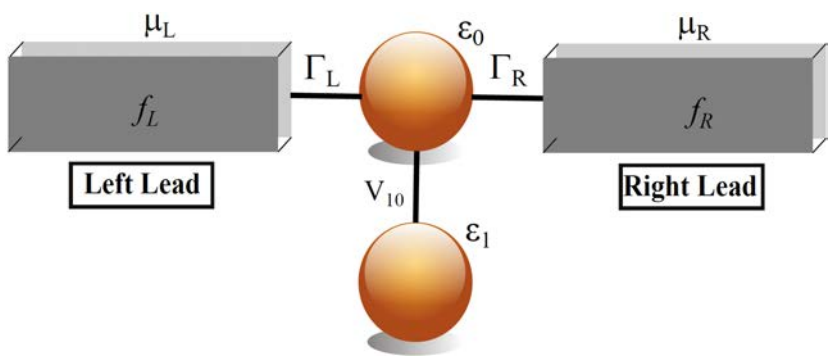

Figure 3.11: *Dos puntos cuánticos en forma de **T** acoplado a dos contactos metálicos.*

Said system is modeled through a Tight Binding Hamiltonian given by the equation (6.11) in the same way as the equation (3.23); the difference is in the Hamiltonian H_{QD}, which is given by:

$$H_{QD} = \sum_{n=1}^{2} \varepsilon_n c_n^\dagger c_n + \sum_{n=1}^{2} v_{n,n+1} c_n^\dagger c_{n+1}, \tag{3.40}$$

where $\varepsilon_n = \varepsilon_{0,1}$ and $v_{n,n+1} = V_{10}$ (see figure 3.11).

With the Hamiltonian established, the Fisher Lee's function is applied to calculate the transmission probability (Equation (3.13)), the Green's function of the entire quantum system is determined through

the Dyson equation (3.12), following the same procedure as the equations (3.25), (3.26) and (3.27), obtaining the expression for the transmission probability given by:

$$T(\varepsilon) = \frac{\Gamma^2}{(\varepsilon - \tilde{\varepsilon}_0 - \Lambda)^2 + \Gamma^2} \tag{3.41}$$

where $\tilde{\varepsilon}_0$ is the effective energy of the site, resulting from the process of renormalizing the system of two QD_s vertically coupled by V_{10} applying the Dyson equation (3.12) in the form:

$$G_{00} = g_0 + g_0 V_{10} G_{10} \tag{3.42}$$

with $G_{10} = g_1 V_{10} G_{00}$ resulting:

$$G_{00} = \frac{g_0}{1 - g_0 g_1 {V_{10}}^2} = \tilde{g} = \frac{1}{\varepsilon - \tilde{\varepsilon}_0} \tag{3.43}$$

From the expression (3.43) is easy to show that $\tilde{\varepsilon}_0 = \varepsilon_0 + \frac{V_{10}^2}{\varepsilon - \varepsilon_1}$.

Figure 3.12 shows the transmission probability calculated by the equation (3.41) (Black line), for energy and coupling values given in table 3.7 (Left column). At the same time, in this figure 3.12 the transmission probability has been graphed by evaluating the expression (2.21), which was determined using wave functions (Red line), in order to compare two methods to determine the said probability of transmission through a system of two QD_s or impurities in **T**-shaped.

Green's Functions	**Wave's Functions**
$T(\varepsilon) = \frac{\Gamma^2}{(\frac{1 - g_0 g_1 {V_{10}}^2}{g_0} - \Lambda)^2 + \Gamma^2}$	$T(\varepsilon) = \frac{(\varepsilon - \varepsilon_1)^2}{(\varepsilon - \varepsilon_1)^2 + \Gamma^2}$
$\varepsilon_0 = \varepsilon_1 = -0.3eV$	$\varepsilon_1 = -0.3eV$
$\Gamma = 8eV$	$\Gamma = \frac{V_0^2}{\nu}$, $\nu = 8eV$
$V_{10} = -0.3eV$	$V_0 = -0.3$

Table 3.7: *Expressions and values for the transmission probability function determined by the Green's functions (Left column) and wave's functions (Right column) for a T-shaped System with two QD_s between leads.*

As expected, the two methods to determine the transmission probability and shown in figure 3.12 have a large percentage of agreement, the difference lies in the parameters that are taken for the values of Γ, since that the expressions for $T(\varepsilon)$ given in table 3.7 have small variations concerning this parameter, and which is defined in each process

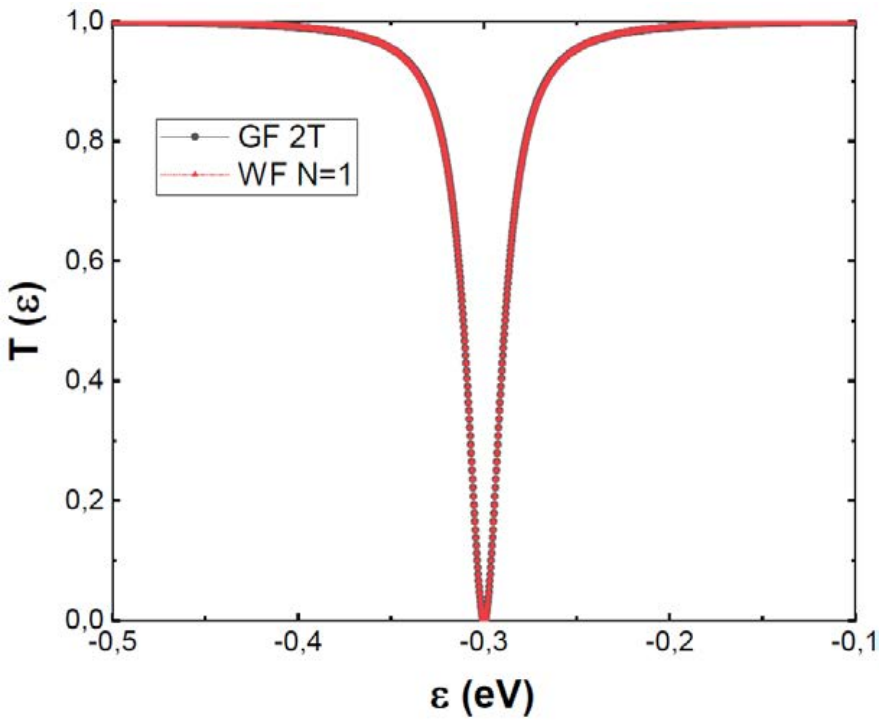

Figure 3.12: *Transmission probability as a function of the incident electron energy for the system of two QD_s in **T**-shaped, applying Green functions (Black line) and wave functions (Red line).*

when wave or Green's functions are taken respectively and from which explained earlier.

On the other hand, the behavior observed in the profile $T(\varepsilon)$ (figure 3.12), is characterized by having an antiresonance in $\varepsilon = \varepsilon_1$, which can be verified by equating to zero the expressions (2.21) using wave's functions or (3.41) using Green's functions. This antiresonance is known as Fano antiresonance, which was already explained in section 2.2.

Figure 3.13 shows the transmission probability as a function of the incident electron and Γ, for values of $\varepsilon_0 = \varepsilon_1 = 0\ eV$ and $V_{10} = \Gamma = 1.0\ eV$. As can be seen, the width of the band on the two sides of the antiresonance increases as Γ increases, and therefore the amplitude in the carrier conductance increases. This behavior is due to the hybridization of the localized states of the quantum system with the delocalized states of the contacts, as happened in the systems analyzed in the previous sections.

Figure 3.14 shows the profile of $T(\varepsilon)$ as a function of ε, for variations of ε_0 (figure 3.14 (a)), ε_1 (figure 3.14 (b)) and the coupling V_{10} between

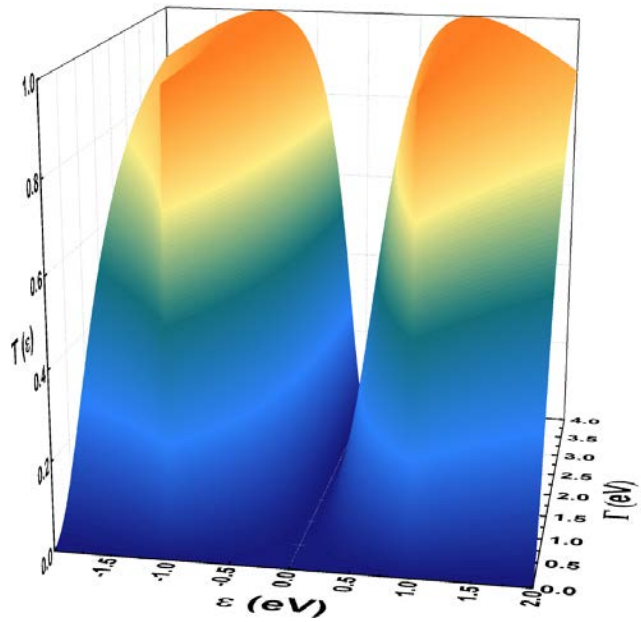

Figure 3.13: *Transmission probability as a function of the incident electron energy (ε) and the coupling (Γ), for a T-shaped system with two QD_s between contacts.*

the QD_s (figure 3.14(c)). As can be seen, for any of the three profiles, there are two resonances that coincide with the eigenvalues of the the Hamiltonian H_{QD} given in the equation (3.40) and evaluated by the expression $\varepsilon = \frac{(\varepsilon_0+\varepsilon_1)\pm\sqrt{(\varepsilon_0+\varepsilon_1)^2-4(\varepsilon_0\varepsilon_1-V_{10}^2)}}{2}$; as well as an antiresonance in $\varepsilon = \varepsilon_1$, which coincides with the value of the energy of the QD transversely coupled. In the table 3.8 some eigenvalues have been

$\varepsilon_0/\varepsilon_1(eV)$	$\varepsilon(1)(eV)$	$\varepsilon(2)(eV)$
-1.5	-2.0	0.5
-1.0	-0.4	0.62
-0.5	-1.28	0.78
0.0	-1.0	1.0
0.5	-0.78	1.28
1.0	-0.62	1.62
1.5	-0.5	2.0

Table 3.8: Eigenvalues for different energies of ε_1 y ε_2.

calculated for the variation of ε_0 and ε_1, which are the same, regardless of which of the two (ε_0 or ε_1) varies, and can be located in figures 3.14(a) and 3.14(b) respectively where the two resonances ($T(\varepsilon) = 1$) for these values are presented. At the same time in the table 3.9, some eigenvalues have been set, when V_{10} varies, which can be located in the resonances presented in the figure 3.14(c). It should be noted that the

$V_{10}(eV)$	$\varepsilon(1)(eV)$	$\varepsilon(2)(eV)$
-1.5	-1.5	1.5
-1.0	-1.0	1.0
-0.5	-0.5	0.5
0.0	0.0	0.0
0.5	-1.0	1.0
1.0	-0.5	0.5
1.5	-1.5	1.5

Table 3.9: Eigenvalues for different energies of V_{10}.

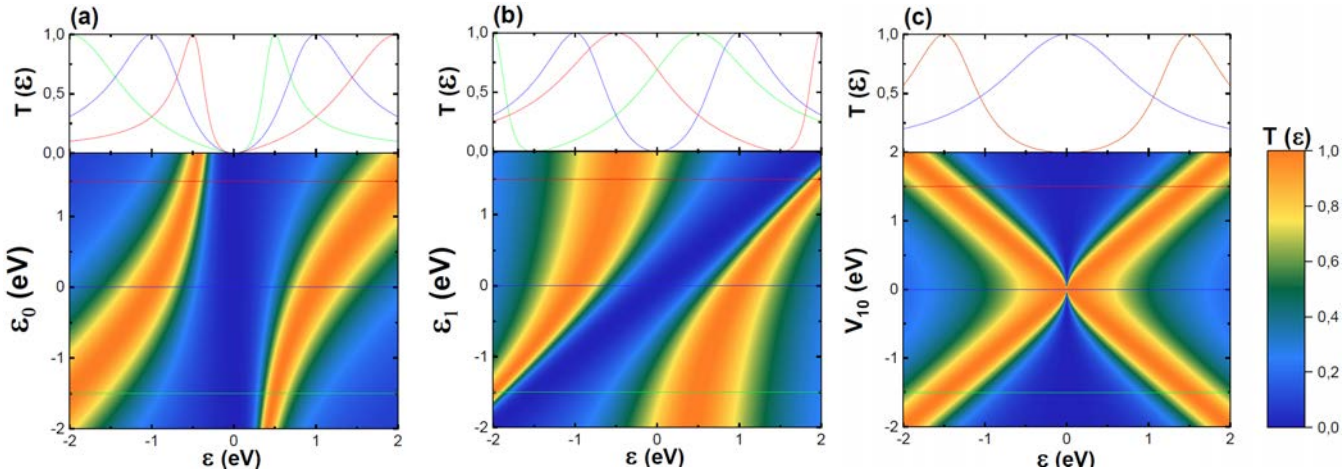

Figure 3.14: *Transmission probability for a T-shaped system with two QD_s as a function of ε, varying:* ***(a)*** *ε_0,* ***(b)*** *ε_1 and* ***(c)*** *V_{10}.*

antiresonance, which is presented at $\varepsilon = \varepsilon_1$, is constant for any value of ε_0 or V_{10} in figures 3.14(a) and 3.14(c), while for figure 3.14(b) the antiresonance varies depending on the value of ε_1, as expected.

3.7 T-shaped System with three QD_s between leads.

The system studied in this section is represented by three QD_s in **T**-shaped, coupled to two metal contacts left (L) and right (R) through the interface $\Gamma_{L,R}$ respectively, as can be seen in figure 3.15.

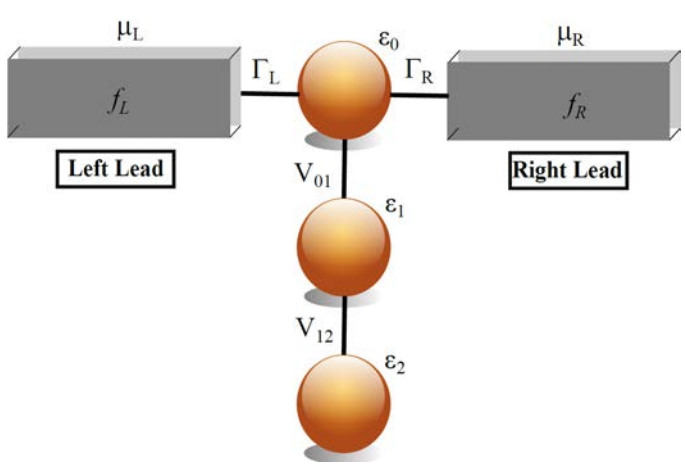

Figure 3.15: *T-shaped system with three QD_s coupled to two electrodes*

Said system is modeled through a Tight Binding Hamiltonian given by the equation (2.1) in the same way as the equation (3.23); the difference is in the Hamiltonian H_{QD}, which is given by:

$$H_{QD} = \sum_{n=1}^{3} \varepsilon_n c_n^\dagger c_n + \sum_{n=1}^{3} v_{n,n+1} c_n^\dagger c_{n+1}, \tag{3.44}$$

where $\varepsilon_n = \varepsilon_{0,1,2}$ and $v_{n,n+1} = V_{10}, V_{21}$ (see figure 3.15).

Each site with energy ε_n has an associated local undisturbed Green's function, therefore, the use of the Dyson equation (3.12) allows us to write the equations of motion of the electron at each site with the interaction of its first neighbors:

$$\begin{aligned} G_{00} =& g_0 + g_0 V_{01} G_{10} \\ G_{10} =& g_1 V_{01} G_{00} + g_1 V_{12} G_{12} \\ G_{12} =& g_2 V_{12} G_{10} \end{aligned} \tag{3.45}$$

solving the system of equations (3.45), we find that:

$$G_{00} = \frac{g_0(1 - g_1 g_2 V_{12}^2)}{1 - g_0 g_1 V_{01}^2 - g_1 g_2 V_{12}^2}. \tag{3.46}$$

In this way, the system has been reduced to a single effective site with an effective Green function $G_{00} = \tilde{g}_0$, to then apply the same equation (3.41) and evaluate the respective transmission probability.

This system is similar to a quantum wire with lateral coupling of two quantum dots ($N = 2$), which was previously studied using wave's functions and is evidenced in the transmission probability profiles found using Green's functions.

Figure 3.16 shows the transmission probability as a function of the incident electron for a T-shaped system with three QD_s for the values of $\varepsilon_0 = \varepsilon_1 = \varepsilon_2 = 1.0\ eV$, varying Γ with $V_{01} = V_{12} = 1.0\ eV$ (figure 3.16(a)), varying V_{01} with $\Gamma = V_{12} = 1.0\ eV$ (figure 3.16(b)) and varying V_{12} with $\Gamma = V_{01} = 1.0\ eV$ (figure 3.16(c)).

As can be seen, in any of the $T(\varepsilon)$ profiles, regardless of which parameter is varying, three resonance and two anti resonances are present, as expected.These resonances coincide with the eigenvalues of the system, which can be found analytically by diagonalizing the Hamiltonian of the system (equation (3.44)).

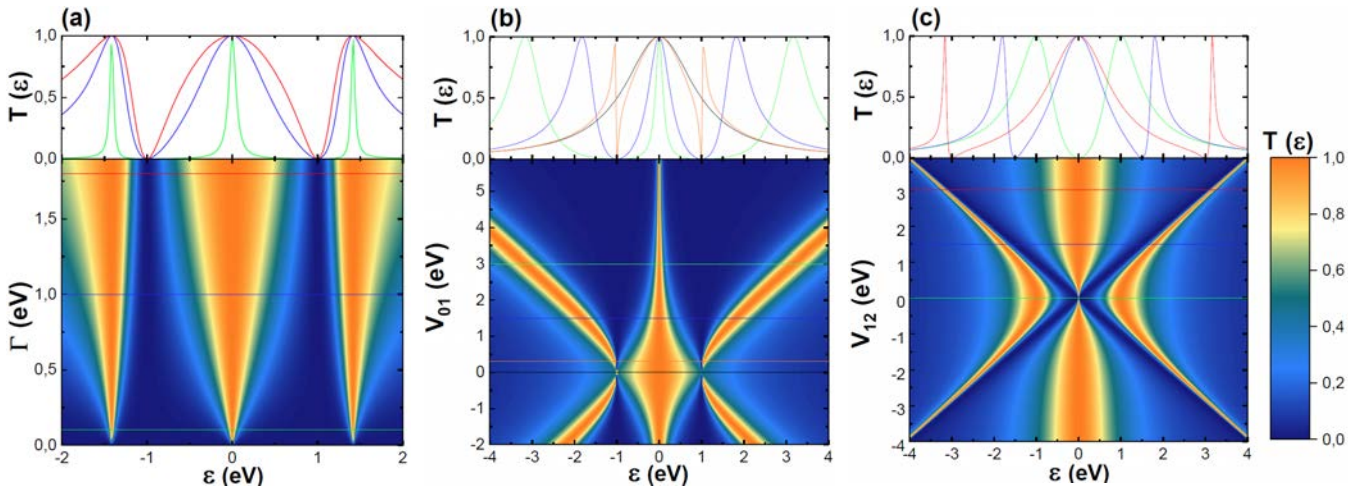

Figure 3.16: *Transmission probability $T(\varepsilon)$ for a T-shaped system with three QD_s for the values of $\varepsilon_0 = \varepsilon_1 = \varepsilon_2 = 1.0\ eV$, varying* ***(a)*** *$\Gamma$ with $V_{01} = V_{12} = 1.0\ eV$,* ***(b)*** *$V_{01}$ with $\Gamma = V_{12} = 1.0\ eV$ and* ***(c)*** *V_{12} with $\Gamma = V_{01} = 1.0\ eV$.*

As can be seen, in any of the $T(\varepsilon)$ profiles, regardless of which parameter is varying, three resonance and two anti resonances are present, as expected.These resonances coincide with the eigenvalues of the system, which can be found analytically by diagonalizing the Hamiltonian of the system (equation (3.44)).

It is important to note that the variation of Γ (Figure 3.16(a)) causes that the electron's transmission probability to change from a weak coupling regime ($\Gamma << V_{01} = V_{12}$) to a strong coupling regime ($\Gamma \sim V_{01} = V_{12}$), where the bandwidth around the resonances increases, giving clear evidence of the hybridization of the localized electronic states of the system with the delocalized states of the electrodes, as mentioned in the previous cases.

On the other hand, the variations of V_{10} and V_{21} in $T\ (\varepsilon)$ (Figures 3.16(b) and 3.16(c) respectively) generate similar behaviors, firstly, the bandwidth measured between the two extreme resonances is equal to $2V_{10}$ or $2V_{21}$, and secondly, the eigenvalues of the resonances are the same for any value of these couplings. The difference lies in the bandwidth around each resonance, because it can be in a hybridization state or not, as already mentioned.

Figure 3.17(a) shows the transmission probability as a function of the energy with variations of site energy ε_0, in which a lateral shift is observed in the maximum values of the resonant peaks, to the right for positive values and to the left for negative values of ε_0, this shift is observed

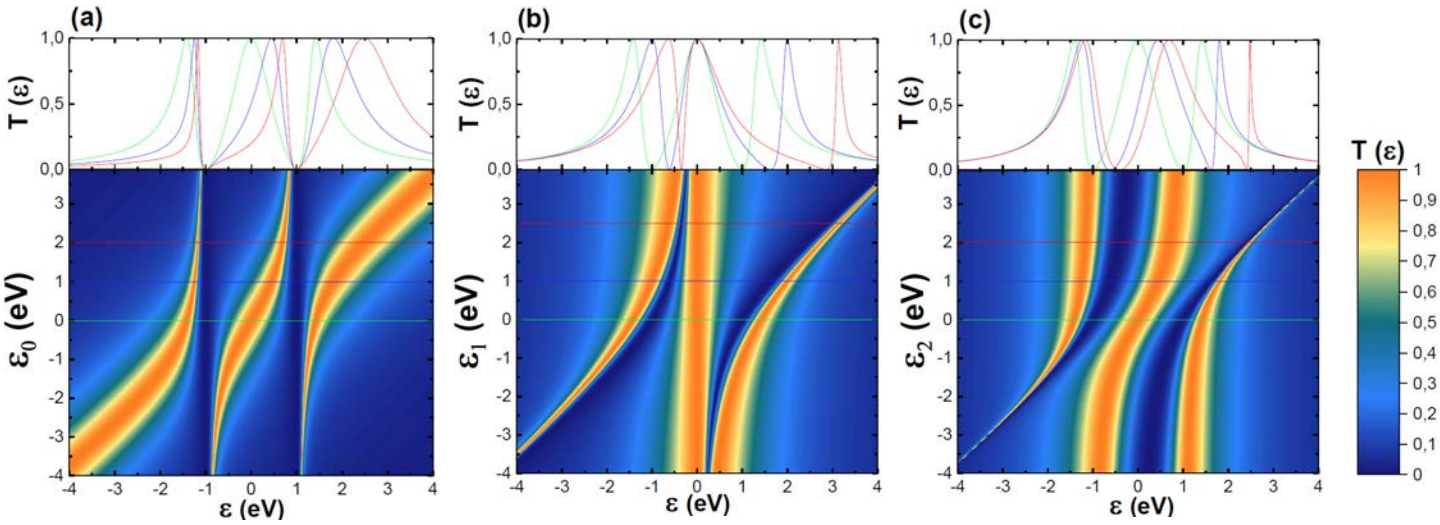

Figure 3.17: *Transmission probability T (ε) for a T-shaped system with three QDs for the values of:* $\Gamma = V_{01} = V_{12} = 1.0\ eV$, *and variations in site-specific energies.* ***(a)*** *Variaci´on energ´ıa propia* ε_0, *con* $\varepsilon_1 = \varepsilon_2 = 1.0\ eV$ ***(b)*** *Site-specific energy variation* ε_1, *with* $\varepsilon_0 = \varepsilon_2 = 1.0\ eV$, *and* ***(c)*** *Site-specific energy variation* ε_2, *with* $\varepsilon_0 = \varepsilon_1 = 1.0\ eV$

in the maximum values of the resonant peaks, to the right for positive values and to the left for negative values of ε_0, this shift represents the changes in the system's eigenenergies. It should be noted that positive values of ε_0, are taken, the shift of the resonant peaks is accompanied by a decrease in the peak width in the left and central lateral resonances, while the right lateral resonance widens with the increase in energy ε_0, in a similar way when negative values of ε_0 are taken, the shift of the resonant peaks is accompanied by a decrease in the peak width in the right and central lateral resonances, while the left lateral resonance widens with the decrease (towards values more negative) of energy ε_0. On the other hand, despite the energy shifts and variations presented by the resonant peaks, the antiresonances remain fixed for the same energy values ε, this confirms that the reflections and interferences in the electron wave are due to the configuration of Lateral coupling of sites the ε_1 and ε_2 with their coupling properties and not are due to the site ε_0.

When making variations in the energy of the ε_1 and ε_2 sites (figuras 3.17(b) y 3.17(c) respectively) the behavior observed is similar to found and analyzed in the quantum wire system with two laterally coupled sites, in which for large (and small) values of ε_1 with respect to the other site energies, the system behaves as a single site system

(with energy around ε_0), see Figure 3.17(b), and for large (and small) values of ε_2 relative to the other site energies, the system behaves as a two-site system (or a wire with lateral coupling of a QD_s or site N = 1). In the two cases of energy variations ε_1 and ε_2, the shifts in the antiresonances are observed, showing that the interference of the electronic wave depends on the laterally coupled sites.

3.8 Three-QD_s system with cross-coupling-leads at the intermediate site

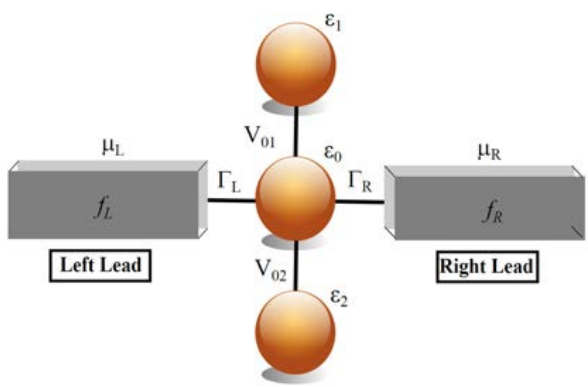

Figure 3.18: *Three-QD_s system with cross-coupling-leads at the intermediate site*

The system studied in this section is represented by three QD_s with energies ε_0, ε_1 and ε_2 in "cross-shaped" where the coupling to the metal contacts occurs at the QD with energy ε_0, as can be to seen in figure 3.18. Each site has an associated local undisturbed Green function, and as in the previous cases, the use of the Dyson equation (3.12) allows us to write the equations of motion of the electron at each site with the interaction with their first neighbors

$$\begin{aligned} G_{00} =& g_0 + g_0 V_{01} G_{10} + g_0 V_{02} G_{20} \\ G_{10} =& g_1 V_{01} G_{00} \\ G_{20} =& g_2 V_{02} G_{00} \end{aligned} \tag{3.47}$$

solving the system equations (3.47), we find that:

$$G_{00} = \frac{g_0}{1 - g_0 g_1 V_{01}^2 - g_0 g_2 V_{02}^2}. \tag{3.48}$$

In this way, the system has been reduced to a single effective site with an effective Green function $G_{00} = g^{\sim}$, to then apply the same equation (3.41) and evaluate the respective-transmission probability.

Figure 3.19 shows the transmission probability as a function of the incident electron for a "cross-shaped" system. Figure 3.19(a) corresponds to the variations of coupling Γ (with, $\varepsilon_1 = \varepsilon_2 = \varepsilon_3 = 0\ eV$ and $V_{01} = V_{02} = 1\ eV$) from the weak coupling regime to the strong coupling regime, where the characteristic shape of the transmission with two resonant peaks they are symmetrical with respect to $\epsilon = 0$, for some specific energy values that reach the maximum transmission value, while for $\epsilon = 0$ it falls to zero in a marked antiresonance. Resonances and antiresonance occur around the eigenvalues, which can be easily determined by diagonalization of the Hamiltonian, resulting in the resonances in values of $\varepsilon = \varepsilon_1$ y $\varepsilon = \varepsilon_1 \pm \sqrt{V_{12}^2 + V_{23}^2}$

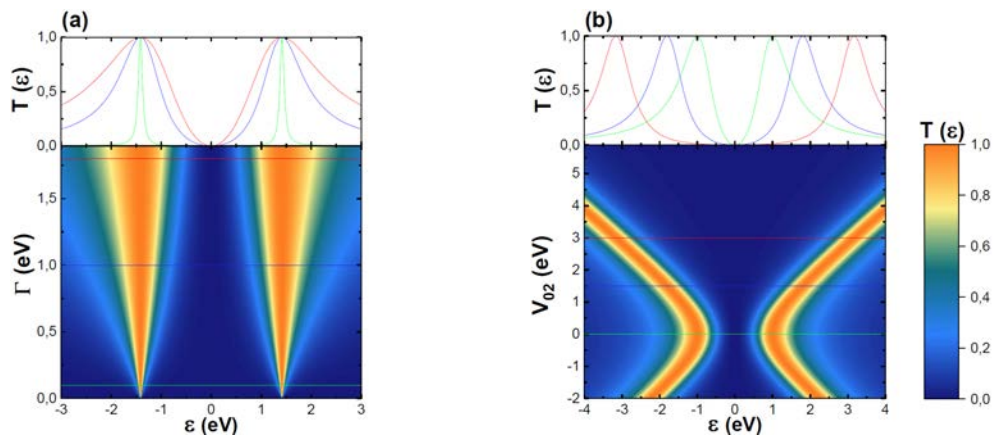

Figure 3.19: *transmission probability function T for a system of three sites in the form of a "cross" for the values: $\varepsilon_0 = \varepsilon_1 = \varepsilon_2 = 0\ eV$, and variations in the couplings* ***(a)*** *Coupling variation Γ, with $V_{01} = V_{02} = 1.0\ eV$* ***(b)*** *Coupling variation V_{02} with $\Gamma = V_{01} = 1.0\ eV$*

As in the cases previously studied in the strong coupling regime, the resonant peaks acquire a considerable width, indicating that the conduction of the electron through the system can occur for a greater range of energy values.

Despite the system is conformed by three QD_s, the transmission probability has a behavior that resembles the T-shaped system with two QD_s (it has two resonances and one antiresonance), that shows that the interference of the electron wave occurs in the same way in the two laterally coupled sites, this behavior occurs since the two coupled sites have the same site energies and couplings, marking an evident symmetry in the system.

Figure 3.19(b) corresponds to the results of the transmission probability as a function of energy with coupling variations V_{02}, where it is observed that as the coupling value V_{02} increases the central antireso-

nant peak, in $\varepsilon = 0\ eV$, remains fixed at this value, on the contrary, the two resonant peaks show a symmetric distance from the central antiresonance, increasing the energy gap generated between maximums. This behavior occurs in the same way when variations of the V_{01} coupling are made.

Figure 3.20(a) shows transmission probability as a function of the energy with variations of the energy ε_0, in which a lateral shift is observed in the maximum values of the resonant peaks, to the right for positive values and to the left for negative values from ε_0, this shift represents the changes in the system's eigenenergies. It should be noted that when positive values of ε_0 are taken, the shift of the resonant peaks is accompanied by a decrease in the peak width in the left lateral resonance, while the right lateral resonance widens with increasing energy ε_0, similarly when taking negative values of ε_0 the shift of the resonant peaks is accompanied by a decrease in the peak width in the right lateral resonances, while the left lateral resonance widens with the decrease (towards more negative values) of the energy ε_0. On the other hand, despite the energy shifts and variations that resonant peaks present, the antiresonance remains fixed for the energy value $\varepsilon = 0$.

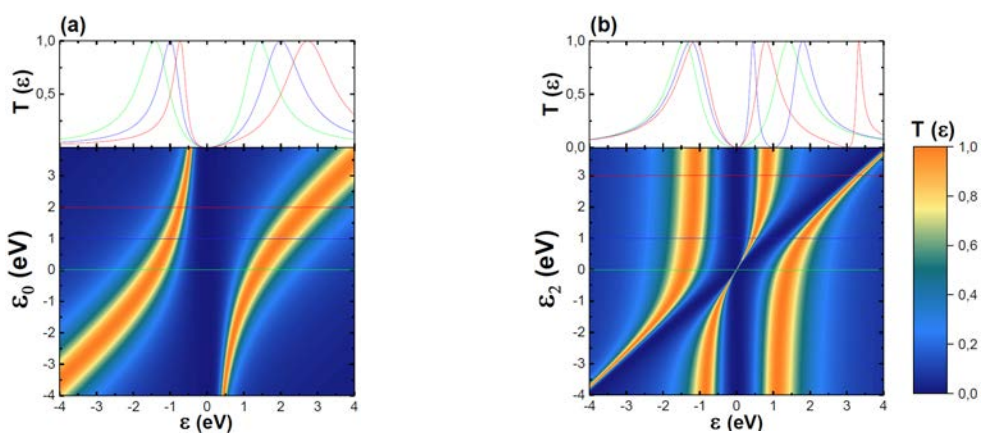

Figure 3.20: *Transmission probability T for a three-site system in the form of a "cross" for the values: $\Gamma = V_{01} = V_{02} = 1.0\ eV$, and variations in site-specific energies.* ***(a)*** *Site-specific energy variation ε_0, with $\varepsilon_1 = \varepsilon_2 = 1.0\ eV$* ***(b)*** *Variation of eigenenergy ε_2, with $\varepsilon_0 = \varepsilon_1 = 1.0\ eV$*

Figure 3.20(b), shows transmission probability as a function of the energy with variations of the energy ε_2, in which the particular case studied can be observed where $\varepsilon_1 = \varepsilon_2 = \varepsilon_0 = 0\ eV$ (green line) in which presents symmetry in the laterally coupled sites since their site energies are equal, as previously analyzed the curve presents two res-

onant peaks and an antiresonance, however as the site energy value of one of the sites increases laterally coupled (keeping the other parameters fixed) an additional antiresonance appears that presents a right lateral shift when the value of the site energy is increased and towards the left when it decreases, these variations break the symmetry that was presented in the particular case in which $\varepsilon_1 = \varepsilon_2$ and shows the interference of electrons for different values at the laterally coupled sites that coincide with the eigenvalues of energy sites. This is verified, for example in the blue curve in the upper panel, in the transmission profile shown for $\varepsilon_1 = 0\ eV$ and $\varepsilon_2 = 1\ eV$ where it is evidenced that the antiresonances have their fair minimum value in those same values, being the antiresonance at $\varepsilon = 0\ eV$ corresponding to the interference of the electron at the site ε_1 and the antiresonance at $\varepsilon = 1\ eV$ corresponding to the interference of the electron on the site ε_2.

References

[1] F. J. Dyson, "The dynamics of a disordered linear chain," Phys. Rev., vol. 92, no. 6, pp. 1331–1338, 1953, doi: 10.1103/PhysRev.92.1331.

[2] F. J. Rodríguez Dueñas, "Propiedades ópticas y de transporte de sistemas electrónicos cuasi-unidimensionales," Rev. la Acad. Colomb. Ciencias Exactas, Físicas y Nat., vol. 42, no. 163, p. 150, 2018, doi: 10.18257/raccefyn.482.

[3] E. C. Seva, *Ancho de dispersión de las resonancias multipolares gigantes*. Tesis de Doctor. Facultad de Ciencias Exactas y Naturales. Universidad de Buenos Aires (1996).

[4] R. Carrillo Bastos, "Transporte electrónico dentro y fuera de equilibrio en nanocintas de grafeno". Tesis de Doctor en Ciencias. Programa de posgrado en Ciencias en Física de Materiales. Centro de investigación Científica y de Educación superior de ensenada, Baja California, México (2014).

[5] E. Lazo Núñez, Densidad de estados de sistemas de baja dimensionalidad. Arica, Chile: Universidad de Tarapacá, (2001).

[6] J. H. Ojeda Silva, J. S. Paez Barbosa, and C. A. Duque Echeverri, "Thermo-electrical conduction of the 2,7-Di([1,1'-Biphenyl]-4-yl)-9H-fluorene molecular system: Coupling between benzene rings and stereoelectronic effects," Molecules, vol. 25, no. 14, pp. 1–17, 2020, doi: 10.3390/molecules25143215.

[7] J. A. Ashram and B. Stinchcombe, "Exact decimation approach to the Green's functions of the Fibonacci-chain quasicrystal," Phys. Rev. B 8, vol. 37, no. 10, pp. 5723–5729, 1988.

[8] J. Q. You, J. R. Yan, J. X. Zhong, and X. H. Yan, A renormalization group approach for the local electronic green's functions in two-dimensional quasi-crystals, Eur. Lett., vol. 17, no. 3, pp. 231-236, 1992, doi: 10.1209/0295-5075/17/3/008.

[9] B. B. Ruiz, Simulaciones numéricas en sistemas de baja dimensionalidad: superficies semiconductoras y nanotubos de carbono, Universidad Autónoma de Madrid, 2006.

[10] F. Guinea, C. Tejedor, F. Flores, and E. Louis, Effective two-dimensional Hamiltonian at surfaces, Phys. Rev. B, vol. 28, no. 8, pp. 4397-4402, 1983, doi: 10.1103/PhysRevB.28.4397.

[11] Q. Niu and F. Nori, Renormalization-Group Study of One-Dimensional Quasiperiodic Systems, Phys. Rev. Lett., vol. 57, no. 16, pp. 2057-2060, 1986.

[12] Q. Niu and F. Nori, Spectral splitting and wave-function scaling in quasicrystalline and hierarchical structures, Phys. Rev. B, vol. 42, no. 16, pp. 10329-10341, 1990, doi: 10.1103/PhysRevB.42.10329.

[13] L. D. Peña, Introducción a la Mecánica Cuántica. 3a ed (Fondo de Cultura Económica - UNAM, 2006. México).

[14] D. J. Griffiths, Introduction to Quantum Mechanics, 2nd ed (Pearson Prentice Hall, 2005, USA).

[15] N. G. Einsprush and W. R. Freusley, Heterostructure and Quantum Devices (Academic Press, San Diego, 1994)

[16] J. A. Arriaga Hernández, Efecto Tunel resonante a través de arreglos de barreras de potencial, Instituto Politécnico Nacional, México D.F. 2010.

[17] Abdalla AS, Eisa MH, Alhathlool R, Aldaghri O, Quantum resonant tunneling in semiconductor double-barrier structure, Optik (2018), https://doi.org/10.1016/j.ijleo.2018.05.095.

[18] Jan-Frederik Mennemann, Ansgar Jüngel, Hans Kosina,Transient Schrödinger Poisson simulations of a high-frequency resonant tunneling diode oscillator, Journal of Computational Physics, 239, 2013, 187-205, doi.org/10.1016/j.jcp.2012.12.009.

[19] Shaffa Almansour, Theoretical study of electronic properties of resonant tunneling diodes based on double and triple AlGaAs barriers, Results in Physics 17 (2020) 1030892.

[20] P. A. Orellana, F. Domínguez-Adame, I. Gómez, and M. L. Ladrón de Guevara, Transport through a quantum wire with a side quantum-dot array, Phys. Rev. B - Condens. Matter Mater. Phys., vol. 67, no. 8, 2003, doi: 10.1103/PhysRevB.67.085321.

Chapter 4

Derivation and Applications of the Numerov Method

4.1 Definition and derivation of the method

Before starting with the formal derivation of the method, we will give a brief explanation about the systems that will be taken as an example for the application of the method, these systems are known as quantum wells and can be obtained in different shapes, lengths of the well or height of potential barriers. Depending on these three parameters, as well as the materials used for its growth, changes in electronic properties may occur that lead to changes in optical properties such as absorption, refractive index, among others. Taking advantage of these characteristics, this type of system has multiple applications in devices such as solar cells [1,2], photo detectors [3,4], resonant tunneling diodes [5,6], among others.

Numerov's method is a numerical method of solving ordinary differential equations of the second order [7], particularly equations of the form:

$$\frac{d^2y(x)}{dx^2} + f(x)y(x) = 0 \tag{4.1}$$

Differential equations of this form arise naturally in many one-dimensional physical problems. In this section we will study the particular problem of an electron confined in a potential well, this physical situation is described by means of the Schrödinger equation, in which the eigenvalues and eigenfunctions will be calculated by implementing the Numerov method.

The first step is to develop the algorithm that gives us a general solution to equation (4.1). For the solution $y(x)$ in equation (4.1) let's do a Taylor expansion around the point x_0:

$$y(x) = y(x_0)+y'(x_0)(x-x_0)+\frac{1}{2}y''(x_0)(x-x_0)^2+\frac{1}{3!}y'''(x_0)(x-x_0)^3+\frac{1}{3!}y'''(x_0)(x-x_0)^3 + \frac{1}{4!}y''''(x_0)(x-x_0)^4 + \frac{1}{5!}y'''''(x_0)(x-x_0)^5 + O^6, \quad (4.2)$$

where O^6 corresponds to terms of 6 order and higher. Defining $h = x - x_0$, then the above equation can be rewritten as:

$$y(x_0+h) = y(x_0)+y'(x_0)h+\frac{1}{2}y''(x_0)h^2+\frac{1}{3!}y'''(x_0)h^3+\frac{1}{4!}y''''(x_0)h^4+\frac{1}{5!}y'''''(x_0)h^5+O^6, \quad (4.3)$$

in general, the point x_0 is an arbitrary point and it could be true that $x > x_0$, in this case $h > 0$, but in the same way it could be true that $x < x_0$, then $h < 0$, suppose that $h > 0$ in the previous equation, then to include the entire x axis we must write a similar equation for $h < 0$, taking $h = |h|$, this equation would take the form:

$$y(x_0-h) = y(x_0)-y'(x_0)h+\frac{1}{2}y''(x_0)h^2-\frac{1}{3!}y'''(x_0)h^3+\frac{1}{4!}y''''(x_0)h^4-\frac{1}{5!}y'''''(x_0)h^5+O^6, \quad (4.4)$$

the requirement now is to discretize the space in a grid of points, which in this case is one-dimensional and corresponds to the x axis. It must be taken into account that h is the difference between two successive points of the grid, then $h = x_{n+1}-x_n$, with this discretization equations (4.3) and (4.4) take the form:

$$y_{n+1} = y_n + y_n'h + \frac{1}{2}y_n''h^2 + \frac{1}{3!}y_n'''h^3 + \frac{1}{4!}y_n''''h^4 + \frac{1}{5!}y_n'''''h^5 + O^6, \quad (4.5)$$

and

$$y_{n-1} = y_n - y_n'h + \frac{1}{2}y_n''h^2 - \frac{1}{3!}y_n'''h^3 + \frac{1}{4!}y_n''''h^4 - \frac{1}{5!}y_n'''''h^5 + O^6, \quad (4.6)$$

where it has been taken into account that $y(x_n) = y_n$. Summing the equations (4.5) and (4.6),

$$y_{n+1} + y_{n-1} = 2y_n + y_n'' h^2 + \frac{1}{12} y_n'''' h^4 + O^6. \tag{4.7}$$

Using $y_n'' = -f_n y_n$, and inserting into equation (4.7):

$$y_{n+1} + y_{n-1} = 2y_n - f_n y_n h^2 + \frac{1}{12} y_n'''' h^4 + O^6, \tag{4.8}$$

to evaluate the term y_n'''', let's write (4.7) up to order 2,

$$y_{n+1} + y_{n-1} = 2y_n + y_n'' h^2 + O^4, \tag{4.9}$$

solving for the y_n'':

$$y_n'' = \frac{y_{n+1} - 2y_n + y_{n-1}}{h^2} + O^2, \tag{4.10}$$

taking into account that $y_n'''' = (y_n'')''$, then applying this to equation (4.10):

$$y_n'''' = (y_n'')'' = \frac{y_{n+1}'' - 2y_n'' + y_{n-1}''}{h^2} + O^2, \tag{4.11}$$

replacing with equation (4.1),

$$y_n'''' = \frac{-f_{n+1}y_{n+1} + 2f_n y_n - f_{n-1}y_{n-1}}{h^2} + O^2, \tag{4.12}$$

multiplying by h^4,

$$y_n'''' h^4 = -f_{n+1}y_{n+1}h^2 + 2f_n y_n h^2 - f_{n-1}y_{n-1}h^2 + O^6. \tag{4.13}$$

Now replacing (4.13) in (4.8):

$$y_{n+1} + y_{n-1} = 2y_n - f_n y_n h^2 + \frac{-f_{n+1}y_{n+1}h^2 + 2f_n y_n h^2 - f_{n-1}y_{n-1}h^2}{12} + O^6, \tag{4.14}$$

$$y_{n+1} + \frac{f_{n+1}y_{n+1}h^2}{12} = 2y_n - y_{n-1} - \frac{5f_n y_n h^2}{6} - \frac{f_{n-1}y_{n-1}h^2}{12} + O^6, \tag{4.15}$$

$$y_{n+1}\left(1 + \frac{f_{n+1}h^2}{12}\right) = 2y_n\left(1 - \frac{5f_n h^2}{12}\right) - y_{n-1}\left(1 + \frac{f_{n-1}h^2}{12}\right) + O^6, \tag{4.16}$$

$$y_{n+1} = \frac{2y_n\left(1-\frac{5f_nh^2}{12}\right) - y_{n-1}\left(1+\frac{f_{n-1}h^2}{12}\right)}{\left(1+\frac{f_{n+1}h^2}{12}\right)} + O^6\,, \tag{4.17}$$

this equation corresponds to an approximate solution of equation (4.1) with an error of order h^6. As the differential equation is of order 2, then to obtain the particular solution, it is necessary to give two initial values that are y_0 and y_1, to evaluate y_2 and follow the recurrence to obtain the term y_N for a mesh of N points.

4.1.1 Application of the method to the one-dimensional Schrödinger equation

As the objective of this chapter is to apply this method to the solution of the one-dimensional time-independent Schrödinger equation, for an electron confined to an arbitrary potential, the initial step is write this equation in atomic units, so it takes the form (4.1).

$$-\frac{\mathrm{hbar}^2}{2m_0}\frac{d^2\psi(X)}{dX^2} + V^*(X)\psi(X) = E^*\psi(X), \tag{4.18}$$

in this equation X is measured in meters, for our atomic units we must measure X in Bohr radios, that is $X = xa_0$, where x is now measured in units of a_0, taking into account that $a_0 = (4\pi\varepsilon_0\mathrm{hbar}^2)/(m_0e^2) = 0.529\times10^{-10}$ m. With this change, equation (4.18) takes the form:

$$\frac{-\mathrm{hbar}^2}{2m_0a_0^2}\frac{d^2\psi(x)}{dx^2} + V^*(x)\psi(x) = E^*\psi(x). \tag{4.19}$$

On the other hand, both V^* and E^* are measured in Joules, in our system of atomic units we require these two quantities in Rydberg which is equivalent to Ry $=\mathrm{hbar}^2/(2m_0{a^2}_0) = 13.6$ eV, then $V^* = V\,\mathrm{Ry}$ and $E^* = E$ Ry, where both V and E are measured in units of Ry. With this change, equation (4.19) takes the form:

$$-Ry\frac{d^2\psi(x)}{dx^2} + V(x)Ry\psi(x) = ERy\psi(x), \tag{4.20}$$

dividing both sides of the equality by Ry:

$$-\frac{d^2\psi(x)}{dx^2} + V(x)\psi(x) = E\psi(x), \tag{4.21}$$

defining $f(x) = E - V(x)$, we finally obtain:

$$\frac{d^2\psi(x)}{dx^2} + f(x)\psi(x) = 0. \tag{4.22}$$

This is the Schrödinger equation in atomic units, where the energy is obtained in Ry and the lengths are given in a_0. Note that this equation has exactly the same mathematical form as equation (4.1), therefore the solution for the electron wave function must also be in the form of (4.17),

$$\psi_{n+1} = \frac{2\psi_n\left(1 - \frac{5f_n h^2}{12}\right) - \psi_{n-1}\left(1 + \frac{f_{n-1}h^2}{12}\right)}{\left(1 + \frac{f_{n+1}h^2}{12}\right)}. \tag{4.23}$$

This solution corresponds to the wave function of an electron confined to a potential $V(x)$ with energy E.

4.2 Application of the method to quantum wells of different shapes

We compile a few examples of interesting finite well potentials and analyse if the resulting Schrödinger equation can be solved analytically. We also find the wavefunctions and energies for the first three quantum levels using the Numerov's method and compare them with the finite element method with the software *Comsol Multiphysics* [8, 9].

4.2.1 Finite Potential Well

The finite potential well, can be considered an extension of the infinite potential well, in which a particle is confined in a "box", but which has "walls" of finite potential. The finite square well quantum model (FSW) is a well known subject in most books of quantum mechanics (QM) [10]. The study of the solution of this type of system can be derived from the Schrödinger equation for a finite potential well, which seeks to describe the particle energy states, which are within

the well, for this type of problem there are exact solutions. In this section we found the solution for the finite square well using the Numerov's method and its first three energy states were calculated using the bisection method.

The equation for the finite potential well is given by, Fig. 5.1:

$$V(x) = \begin{cases} 0 & \text{if } |x| \leq \dfrac{L}{2}. \\ V_0 & \text{othewise} \end{cases} \tag{4.24}$$

In regions I and III, the general solution is a linear combination of exponentials with the same form, but with different constants, given by the following equations

$$\psi_0 = A \exp(k_0 x) \qquad x < 0, \tag{4.25}$$

$$\psi_2 = B \exp(-k_0 x) \qquad L < x, \tag{4.26}$$

in region II, you have the general solution for the infinite square well

$$\psi_1 = C \exp(-ik_1 x) + D \exp(ik_1 x) \qquad 0 < x < L, \tag{4.27}$$

where, A, B, C y D, are constants. k_0 and k_1, correspond to the wave numbers associated with the corresponding regions and have an implicit dependence on the energy of the electron.
The figure 5.1 show the square potencial well a function of position, in which we can observe the location of the three corresponding regions for this potential, for a shaft width $L = 4\,\text{nm}$ and $V_0 = 0.3\,\text{eV}$,

In Figure 5.2, the wave functions are shown for the three lowest states of a finite potential well. We can see that the wave function of the ground state and the second excited state show symmetry with respect to zero and that the first excited state is asymmetric with respect to the same point, this behavior of the wave functions is typical for this type of potential.

Comparison with the Finite Element Method (FEM)

Table 4.1 shows the results obtained from the first three energies using Numerov's method and finite elements, it can be noted that, for

Energy level	Numerov (eV)	FEM (eV)
1	0.0169	0.0169
2	0.0668	0.0668
3	0.1474	0.1474

Table 4.1: Comparison of the first three electronic states using Numerov's method and the finite element method (FEM) for the finite squared well.

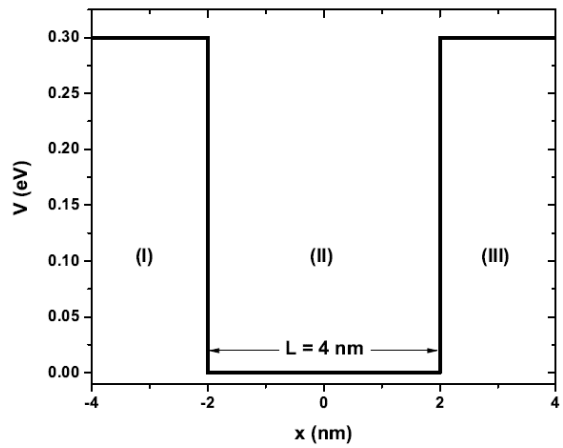

Figure 4.1: Finite potential well as a function of position x. The width of the well and the height of the potential are given by $L = 4\,\text{nm}$ and $V_0 = 0.3\,\text{eV}$ respectively.

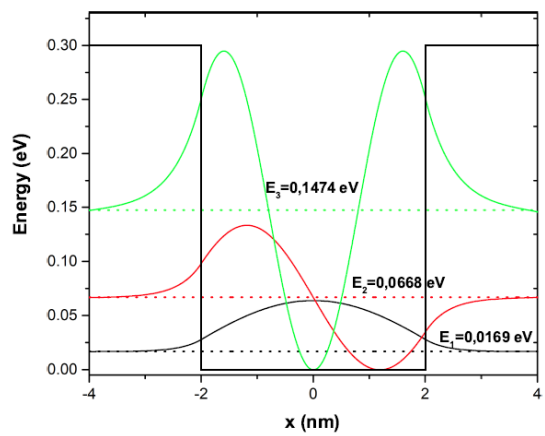

Figure 4.2: Wave functions for the three lowest states of a finite potential well, $L = 4\,\text{nm}$ and $V_0 = 0.3\,\text{eV}$.

this well, there are no differences in the corresponding energies using the two methods. With this, it can be said that Numerov's method is very precise to find the energies of the system.

4.2.2 V-shaped Potential Well

The equation for the V-shaped potential well is given by:

$$V(x) = \begin{cases} \dfrac{2V_0}{L}|x| & \text{if } |x| \leq \dfrac{L}{2} \\ V_0 & \text{othewise} \end{cases}. \tag{4.28}$$

A graph of this potential is presented in Fig. 4.3.

In Fig. 4.3, we plot Eq. 4.28, taking as parameters $L = 4\,\text{nm}$ and $V_0 = 0.3\,\text{eV}$. The well has a shape similar to a V. We notice the potencial has even symmetry, therefore we expect the wavefunctions to be either odd or even. In table 4.2, we compare the results for energies.

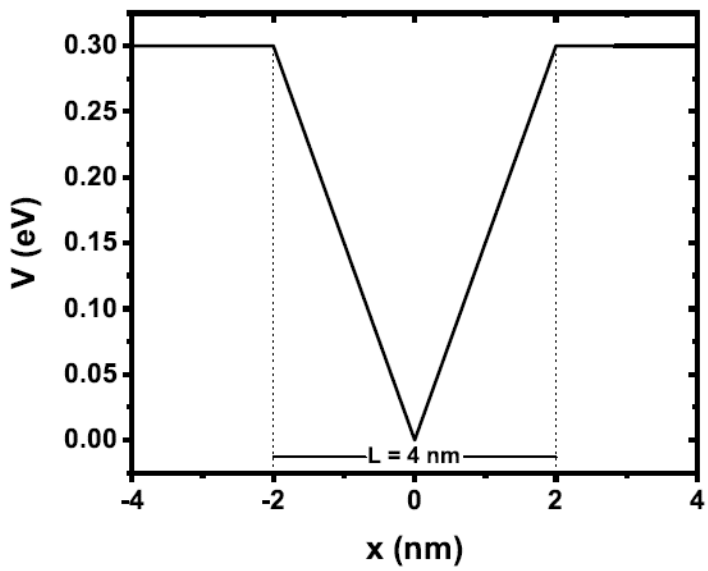

Figure 4.3: V-shaped potential well as a function of position x. For the particular example of the figure, $L = 4$nm and $V_0 = 0.3$eV.

The energies that arise from the solution of the Schrödinger equation for this system, using the two methods, are shown in Table 4.2. In this case, energy differences of $6 \times 10^{-3}\,\text{eV}$ are observed for the ground state, $1.2 \times 10^{-3}\,\text{eV}$ for the first excited state, and $1.8 \times 10^{-3}\,\text{eV}$ in the second excited state. However, the discrepancies between energies are small, so the method gives accurate results for the V-shaped well.

Energy level	**Numerov (eV)**	**FEM (eV)**
1	0.0962	0.0968
2	0.2197	0.2209
3	0.2961	0.2943

Table 4.2: Comparison of the first three electronic states using Numerov's method and the finite element method (FEM) for the V-shaped potential well.

The confining potential is symmetric about zero, therefore the wave function for the ground state and the second excited stated also symmetric, and the first excited stated is antisymmetric, with even (first and third state) and odd (second state) symmetries. For the third

state the wave function is located close to the continuum, since its corresponding energy is close to the value of the barrier (see Fig. 4.4).

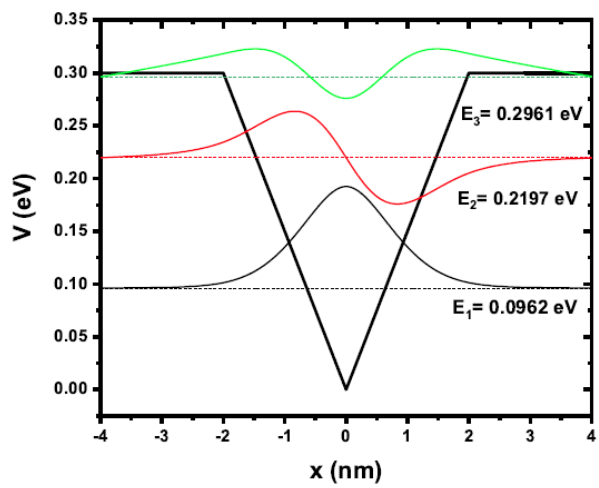

Figure 4.4: First three wave functions for the V-shaped potential as a function of position x. For the particular example of the figure, $L = 4\,\text{nm}$ and $V_0 = 0.3\,\text{eV}$.

4.2.3 Parabolic Potential

We have a parabolic potential well (see Fig. 4.5), with symmetric barriers of $V_0 = 0.3\,\text{eV}$ and length of $L = 4\,\text{nm}$, the described potential is given by the following mathematical expression:

$$V(x) = \begin{cases} \dfrac{4V_0 x^2}{L^2} & \text{if } |x| \leq \dfrac{L}{2} \\ V_0 & \text{othewise} \end{cases}. \tag{4.29}$$

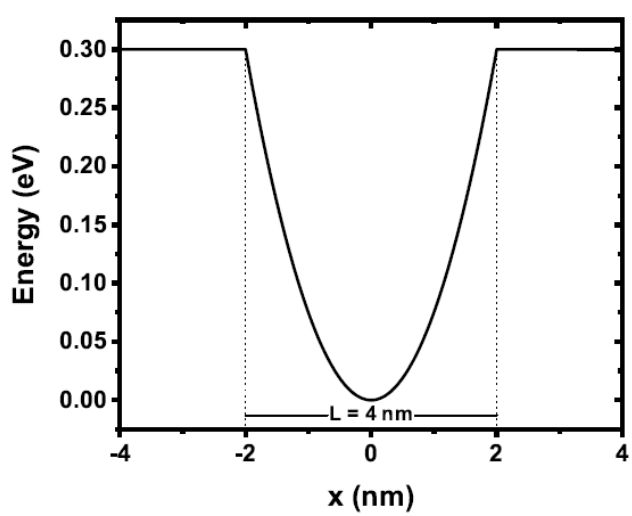

Figure 4.5: Parabolic potential well as a function of position x. For the particular example of the figure, $L = 4\,\text{nm}$ and $V_0 = 0.3\,\text{eV}$.

To solve the problem using Numerov method, a mesh composed of 4000 points spaced at 0.001 each was used. The energies and wave functions for the first 3 states are shown in Fig. 4.6. Note that potential has even symmetry, for that reason the resulting wave functions are even or odd, for example, the first state is even, the second state is odd, and so on.

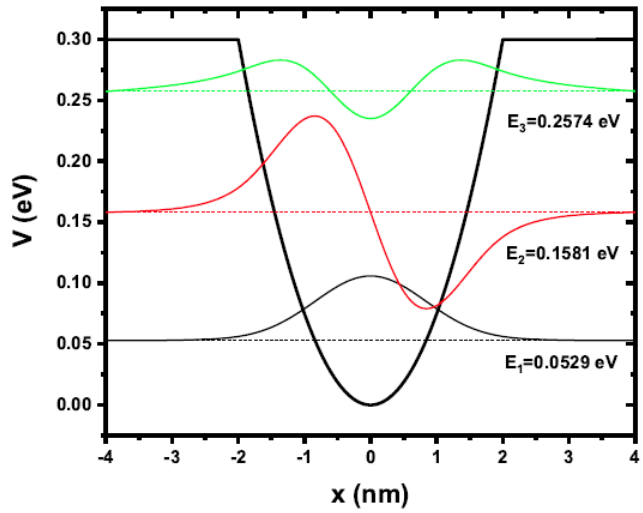

Figure 4.6: Parabolic potential well and wave functions as a function of position x. For the particular example of the figure, $L = 4\,\text{nm}$ and $V_0 = 0.3\,\text{eV}$.

Another problem with parabolic potential and exact solution is the harmonic oscillator, the difference is that the potential barriers are infinite, where the energies can be calculated by means of the expression 4.30. The characteristic of this system is that the energy levels of the particles confined in the well are spaced by the same amount $\hbar\omega$, where the basic state is $\hbar\omega/2$ [11].

$$E_n = \left(n + \frac{1}{2}\right)\hbar\omega\,. \tag{4.30}$$

Energy level	Numerov (eV)	FEM (eV)
1	0.0529	0.0534
2	0.1581	0.1595
3	0.2574	0.2590

Table 4.3: Comparison of the first three electronic states using Numerov's method and the finite element method (FEM) for the parabolic potential well.

In this case, the wave functions retain the symmetry as in the previous one (V-shaped quantum well), however, the eigenvalues obtained

are different despite having the same length and the same potential value on the barrier. This can be associated with the shape of the confinement potential.

4.2.4 Asymmetric Potential Well

We have the potential well with barriers of different heights, the Schrödinger equation of a wave function with a penetration decays exponentially in the classically forbidden region [11]. The potential well is given by the following function,

$$V(x) = \begin{cases} V_0 & \text{if } x < \dfrac{L}{2} \\ 0 & \text{if } |x| \leq \dfrac{L}{2} \\ 1.5\,V_0 & \text{if } x > \dfrac{L}{2} \end{cases} . \tag{4.31}$$

Whose corresponding graph is shown in Fig. 4.7

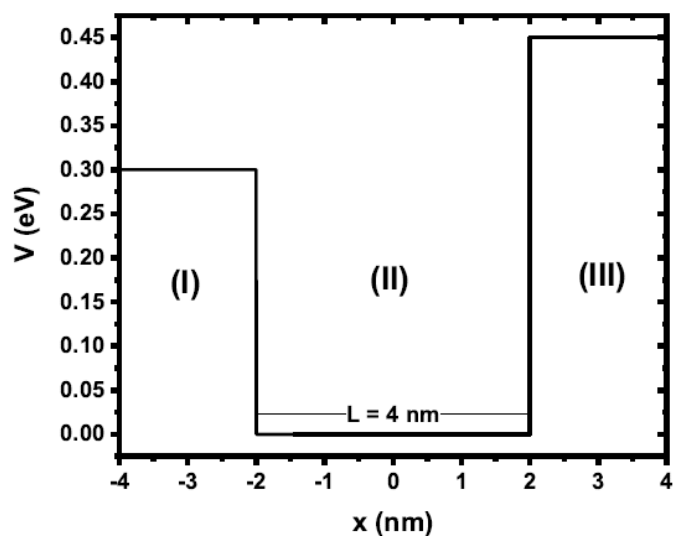

Figure 4.7: Asymmetric potential well as a function of position x. For the particular example of the figure, $L = 4\,\text{nm}$ and $V_0 = 0.3\,\text{eV}$.

The solutions of the Schrödinger equation in the regions (I), (II) and (II) are respectively,

$$\psi_I(x) = A\exp(k_I x) + B\exp(-k_I x) \qquad k_I^2 = \frac{2m\,(V_0 - E)}{\hbar^2}\,, \tag{4.32}$$

$$\psi_{II}(x) = C\exp\left(ik_{II}x\right) + D\exp\left(-ik_{II}x\right) \qquad k_{II}^2 = \frac{2mE}{\hbar^2}\,, \tag{4.33}$$

$$\psi_{III}(x) = E\exp\left(k_{III}x\right) + F\exp\left(-k_{III}x\right) \qquad k_{III}^2 = \frac{2m\left(1.5V_0 - E\right)}{\hbar^2}\,, \tag{4.34}$$

$\psi_I(x)$ and $\psi_{III}(x)$ they must tend to zero when x becomes large, for this B and E have to be zero. Then the new wave functions are

$$\psi_I(x) = A\exp\left(k_I x\right) \qquad k_I^2 = \frac{2m\left(V_0 - E\right)}{\hbar^2}\,, \tag{4.35}$$

$$\psi_{II}(x) = C\exp\left(ik_{II}x\right) + D\exp\left(-ik_{II}x\right) \qquad k_{II}^2 = \frac{2mE}{\hbar^2}\,, \tag{4.36}$$

$$\psi_{III}(x) = F\exp\left(-k_{III}x\right) \qquad k_{III}^2 = \frac{2m\left(1.5V_0 - E\right)}{\hbar^2}\,. \tag{4.37}$$

In this problem a mesh made up of 4000 points spaced at 0.001 each was used, it is possible to use a larger mesh to increase precision, but it requires more computation time. The Fig. 4.8 shows the energies and wave functions corresponding to the first three states.

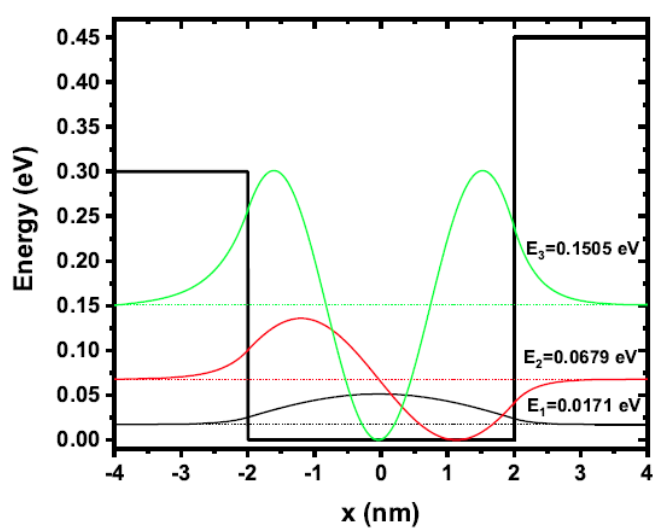

Figure 4.8: Asymmetric potential well and wave functions as a function of position x. For the particular example of the figure, $L = 4\,\mathrm{nm}$ and $V_0 = 0.3\,\mathrm{eV}$.

To check the efficiency of the method, the same problem is solved using the finite element method through the COMSOL Multiphysics

5.4 software using an extremely fine mesh for better results. The table 4.4 shows the results of the first three energies using each method.

Energy level	Numerov (eV)	FEM (eV)
1	0.0174	0.0171
2	0.0689	0.0679
3	0.1526	0.1505

Table 4.4: Comparison of the first three electronic states using Numerov's method and the finite element method (FEM) for the asymmetric potential well.

It can be noted that there is a discrepancy of 3×10^{-3} eV for the ground state, 1×10^{-3} eV for the first excited state, and 2.1×10^{-3} eV for the second excited state, this can be associated with the mesh that was used to perform the calculation using the Numerov method. However, it can be concluded that Numerov's method produces acceptable results and that it is very useful for solving Scrödinger's equation in this type of system.

The confinement potential is asymmetric with respect to the heights of the barrier. The ground state is symmetric, the first excited state is antisymmetric, since the wave function is odd and the second excited state even though the wave function is even, it is not symmetric, due to the edge effects of the barriers.

4.2.5 Sawtooth potencial

The sawtooth potential has the shape of Fig. 4.9 and its mathematical expression is given by:

$$V(x) = \begin{cases} \dfrac{V_0}{L}x + \dfrac{V_0}{2} & \text{if } |x| \leq \dfrac{L}{2} \\ V_0 & \text{othewise} \end{cases}. \tag{4.38}$$

The potential outside the well has been fixed in $V_0 = 0.3\,\text{eV}$.

By means of Numerov's method it is possible to solve the Schrödinger equation to find a set of eigenvalues and eigenfunctions of the electron confined in the potential, for the particular case of this potential, the solutions take the form presented in Fig. 4.10,

Figure 4.10 shows the form of the sawtooth potential that is included as V^* in equation 4.18, the ground state and the first two excited states

of the system are also presented with their corresponding energies and located according to the dashed lines. Note the asymmetry of the states caused by the non-symmetric form of the confining potential.

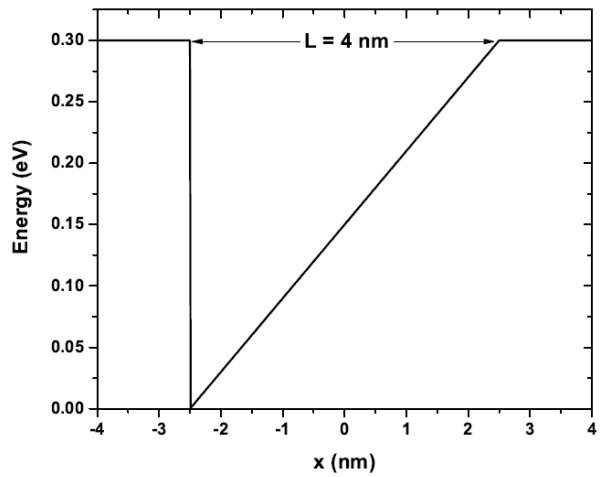

Figure 4.9: Sawtooth potential as a function of position x. With, $L = 4\,\text{nm}$ and $V_0 = 0.3\,\text{eV}$.

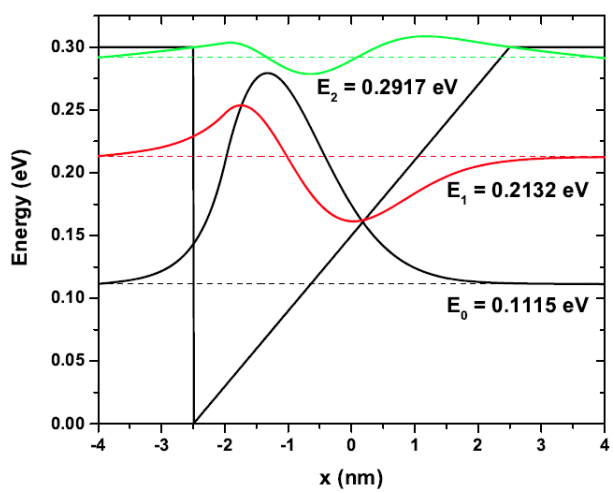

Figure 4.10: Sawtooth potential and first three wave functions as a function of position x. With, $L = 4\,\text{nm}$ and $V_0 = 0.3\,\text{eV}$.

The one-dimensional Schrödinger equation can also be solved through the finite element method (FEM), in this case, this method has been implemented by means of the COMSOL Multiphysics software, in table 4.5 the comparative results of both methods are presented for the first three confined levels,

As we can see in the previous table, the difference in energy between both methods for the ground state is only $1 \times 10^{-4}\,\text{meV}$, it must be taken into account that for the FEM a mesh of 1000 points has been taken. For the second state the difference between both methods is

Energy level	Numerov (eV)	FEM (eV)
1	0.1115	0.1114
2	0.2132	0.2131
3	0.2917	0.2893

Table 4.5: Comparison of the first three electronic states using Numerov's method and the finite element method (FEM) for the sawtooth potential well.

still 1×10^{-4} meV and for the third state, it is 2.4×10^{-3} meV, which is a greater difference and could be caused by the greater difficulty of both methods to find states with higher energies and therefore very close to the continuum.

4.3 Conclusions

Numerov's method presents quite good results in general for the case of calculated one-dimensional potentials, comparing it with the finite element method (FEM), the value for the obtained eigenvalues is quite close both for the ground state and for the first excited states. On the other hand, perhaps the fundamental advantage of this method is its easy analytical demonstration and its numerical implementation.

For the case of the finite square potential, wave functions symmetric with respect to zero were obtained for the ground state and the second excited state, and asymmetric for the first excited state with respect to the same point. The results of the energy values found by means of the numerov method and those obtained by means of the finite element method by means of the comsol program, were approximately equal, which rectifies the effectiveness of the method that we study in this chapter.

4.4 Algorithm implementation

The following is the algorithm implemented in Python for the application of the Numerov method. The first part of the code is basic to implement the calculation package, graph and export the results.

```
from numpy import *
from pylab import *
import matplotlib.pyplot as plt
import pandas as pd
```

Next, the potentials for each of the resolved structures are defined:

Squared potential

```
def V(x):
if   x<-L/2:
y=V0
if np.abs(x)<=L/2: y=0 if
x>L/2:
y=V0
return y
```

Asymmetric potential

```
def V(x):
if   x<-L/2:
y=V0
if np.abs(x)<=L/2: y=0 if
x>L/2:
y=1.5*V0
return y
```

Sawtooth potencial

```
def V(x):
if x <= -L/2:
return V0
if x >= L/2:
return V0
else:
return (V0/L)*(x + L/2)
```

Parabolic potential

```
def V(x):

if np.abs(x)<=L/2.0:

y=(4*V0/(L*L))*x*x
else:
y=V0
return y
```

V-shaped potential

```
y=V0
def V(x):
if np.abs(x)<=L/2.0:
y=V0*abs(2*x/L) else:
return y
```

The next step is to write the potential in Rydbergs and the lengths in Bohr radious since these are the inputs for the code:

```
L_well = 4              # Well length in nm #
V_well = 0.3            Potential in eV


Ry = 13.6 ao =          # 1 Ry = 13.6eV # 1 ao
0.0529                  = 0.0529nm


V0 = V_well/Ry L =      # Potential in Rydberg Ry
L_well/ao N =
                        # Well length in Bohr radious ao # Total
5001                    points in the mesh
xmin = -6*L xmax =      # left border
6*L                     # Right border


dx = (xmax - xmin)/N                          # Step
x = arange(-4/ao, 4/ao,dx)                    # Mesh
plt.plot(x, [V(i) for i in x]);   # Show the graph
df = pd.DataFrame({'x': x*ao, 'V': [V(i)*Ry for i in x]})
# Stores the data frame
np.savetxt('Potential.dat', df, delimiter="\t") # Export the potential
```

Now we must define the function $f(x)$ as in the equation 4.22,

```
def f(x,E): return E
- V(x)
```

At this point it is necessary to program the equation 4.17, which has as input parameters, the function f, the energy E, the points in the boundary of the mesh x_i and x_f, number of points a evaluate n and a vector with two inputs that gives the value of the wave function at the first two points of the mesh, these are initial values for the Numerov method,

```
def numerov(f, par_ener, xi, xf, n, psi_in): h     (xf     =
- xi)/(1.*n)
x     = arange(xi,xf+h,h)
psi   = zeros(shape(x)[0])
psi[0] = psi_in[0]
psi[1] = psi_in[1]
for i in range(2,shape(x)[0]):
f1 = (2.0 - 5.0*h**2*f(x[i-1],par_ener)/6.0)*psi[i-1] f2 = (1.0+
h**2*f(x[i-2],par_ener)/12.0)*psi[i-2] f3 = 1.0 +
h**2*f(x[i],par_ener)/12.0
psi[i] = (f1 - f2)/f3
return x, psi
```

Since an input parameter is the energy E, it can be calculated using a bisection algorithm [12],

```
def find(n):
i = 0
e = 0.0
de = 0.01
while i<n:
x, y1 = numerov(f,e,-L,L,4000,[0.0,1e-8]) x, y2 =
numerov(f,e+de,-L,L,4000,[0.0,1e-8]) if
y1[-1]*y2[-1]<0.0:
i += 1
e1 = e
e  = e + de
e2 = e
else:
e  = e + de
```

```
ea = e1
eb = e2
ec = (ea + eb)/2.0
x, ya = numerov(f, ea, -L, L, 4000, [0.0, 1e-8]) x, yc =
numerov(f, ec, -L, L, 4000, [0.0, 1e-8]) while
fabs(yc[-1]) > 1e-6:
if ya[-1]*yc[-1] < 0.0:
eb = ec
ec = (ea + eb)/2
else:
ea = ec
ec = (ea + eb) / 2.0
x, ya = numerov(f, ea, -L, L, 4000, [0.0, 1e-8]) x, yc =
numerov(f, ec, -L, L, 4000, [0.0, 1e-8]) return ec
```

At this point it only remains to call the functions to calculate the eigenvalues and the corresponding eigenfunctions,

```
e1 = find(1) e2  =
find(2)    e3    =
find(3)

print('e1      =    ',e1*Ry)
print('e2      =    ',e2*Ry)
print('e3 = ',e3*Ry)

x, psi1 = numerov(f, e1, -L, L, 4000, [0.0, 1e-8]) x, psi2  = numerov(f, e2, -L,
L, 4000, [0.0, 1e-8]) x, psi3 =  numerov(f, e3, -L, L, 4000, [0.0, 1e-8])

plt.plot(x*ao,       1000*psi1      +    e1*Ry);
plt.plot(x*ao,       1000*psi2      +    e2*Ry);
plt.plot(x*ao, 1000*psi3 + e3*Ry);

plt.plot(x*ao, [V(i)*Ry for i in x]);
```

References

[1] M. A. der Maur, G. Moses, J. M. Gordon, X. Huang, Y. Zhao, and E. A. Katz, *Temperature and intensity dependence of the open-circuit voltage of InGaN/GaN multi-quantum well solar cells*, Sol. Energy Mater. Sol. Cells **230**, 111253 (2021).

[2] M. Verma and G. P. Mishra, *Voltage preserved GaInP single junction solar cell using type-A InP multiple quantum well structure with enhanced efficiency*, Optik **220**, 165113 (2020).

[3] M. S. El Tokhy and I. I. Mahmoud, *Detectivity analysis of infrared photodetector devices under nonuniform distribution of quantum well and wire*, Optik **227**, 166113 (2021).

[4] S. Ghosh, B. Mukhopadhyay, G. Sen, and P. K. Basu, *Performance analysis of GeSn/SiGeSn quantum well infrared photodetector in terahertz wavelength region*, Physica E Low Dimens. Syst. Nanostruct. **115**, 113692 (2020).

[5] M. Ahmadzadeh, A. Ghadimi, and S. A. Sedigh Ziabari, *External quantum efficiency of a resonant tunneling diode photo detector: Structural parameters and wavelength dependencies*, Optik **221**, 165265 (2020).

[6] M. A. Md Zawawi and M. Missous, *Design and fabrication of low power GaAs/AlAs resonant tunneling diodes*, Solid State Electron. **138**, 30–34 (2017).

[7] Hairer, Ernst, Nørsett, Syvert P., Wanner, and Gerhard, *Solving Ordinary Differential Equations I. Nonstiff Problems.*, 2nd ed. Berlin: Springer, (1993).

[8] COMSOL *Multiphysics, v. 5.4*; COMSOL AB: Stockholm, Sweden, 2020.

[9] COMSOL *Multiphysics Reference Guide*; COMSOL: Stockholm, Sweden, 2012.

[10] A. Al-Ani, and K. Abid, *Solving Schrödinger Equation for Finite Potential Well Using the Iterative Method*, Al-Nahrain Journal of Science. **22**, 52-58 (2019).

[11] P. Harrison, *Quantum Wells, Wires and Dots: Theoretical and Computational Physics of Semiconductor Nanostructures, Second Edition*, John Wiley & Sons, Ltd, ISBN:9780470010792 (2005).

[12] G. Corliss, *Which Root Does the Bisection Algorithm Find?*, Siam Review **19**, 325-327 (1977).

Chapter 5

Electromagnetically Induced Transparency (EIT)

This chapter is dedicated to the development of the expression for susceptibility considering the coupling between an atomic system modeled by a three-level system (three orthogonal states) with two external electromagnetic fields [1]. This topic is extensively studied in various current works [2–8]. In Fig. (5.1) the scheme of this situation is presented, where the ground state is characterized by the vector $|b\rangle$, the highest state as $|a\rangle$ and an intermediate state $|c\rangle$, the system is immersed in two electromagnetic fields, a probe field of frequency ν that couples the states $|b\rangle$ with $|a\rangle$ and a control field of frequency ν_μ that couple the states $|c\rangle$ and $|a\rangle$ (the coupling between the $|b\rangle$ and $|c\rangle$ state is dipolarly prohibited). The calculations are based on a semi-classical approach where the atomic system is a quantum system and the external fields are classical fields. In this development a lambda-type arrangement is considered, therefore, there is no strong dipolar coupling between $|b\rangle$ and $|c\rangle$.

The Hamiltonian of the system is given by:

$$\widehat{H} = \widehat{H}_0 + \widehat{H}_1, \tag{5.1}$$

where $\widehat{H}_0$ is the Hamiltonian of the atomic system and $\widehat{H}_1$ represents the interaction of the atomic system with radiation. The three-level system corresponds to a complete basis, therefore, it is possible to write the completex relation, $\widehat{I} = |a\rangle\langle a| + |b\rangle\langle b| + |c\rangle\langle c|$, where $\widehat{I}$ is the identity operator in the base. Now, we can express the atomic system

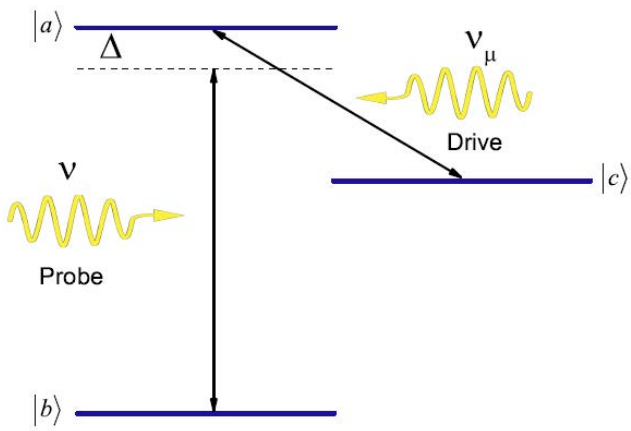

Figure 5.1: Systematic representation a three-level system in a lambda-type arrangement. ν and ν_μ are the frequencies associated with the probe and drive fields respectively.

Hamiltonian using this left and right operator,

$$\widehat{H}_0 = \widehat{I}\widehat{H}_0\widehat{I}, \tag{5.2}$$

replacing the $\widehat{I}$ operator,

$$\widehat{H}_0 = (|a\rangle\langle a| + |b\rangle\langle b| + |c\rangle\langle c|)\widehat{H}_0(|a\rangle\langle a| + |b\rangle\langle b| + |c\rangle\langle c|), \tag{5.3}$$

making the products explicitly,

$$\widehat{H}_0 = |a\rangle\langle a|\widehat{H}_0|a\rangle\langle a| + |a\rangle\langle a|\widehat{H}_0|b\rangle\langle b| + |a\rangle\langle a|\widehat{H}_0|c\rangle\langle c| + |b\rangle\langle b|\widehat{H}_0|a\rangle\langle a| + |b\rangle\langle b|\widehat{H}_0|b\rangle$$
$$\langle b| + |b\rangle\langle b|\widehat{H}_0|c\rangle\langle c| + |c\rangle\langle c|\widehat{H}_0|a\rangle\langle a| + |c\rangle\langle c|\widehat{H}_0|b\rangle\langle b| + |c\rangle\langle c|\widehat{H}_0|c\rangle\langle c|,$$

the non-diagonal terms like $\langle a|\widehat{H}_0|b\rangle$, $\langle a|\widehat{H}_0|c\rangle$, $\langle b|\widehat{H}_0|a\rangle$, $\langle b|\widehat{H}_0|c\rangle$, $\langle c|\widehat{H}_0|a\rangle$ and $\langle c|\widehat{H}_0|b\rangle$ are canceled because the atomic system Hamiltonian corresponds to a diagonal matrix. On the other hand, since each state $|n\rangle$ corresponds to an eigenstate of the Hamiltonian $\widehat{H}_0$, then it is true that, $\widehat{H}_0|n\rangle = \hbar\omega_n|n\rangle$, with $n = a, b, c$, where ω_n is the energy associated to the n state. The above result in the Hamiltonian associated to the atomic system with the form:

$$\widehat{H}_0 = \hbar\omega_a|a\rangle\langle a| + \hbar\omega_b|b\rangle\langle b| + \hbar\omega_c|c\rangle\langle c|\,. \tag{5.4}$$

For the interaction Hamiltonian, we must take into account that there are two external fields in the system (probe and drive fields). In this case, we can consider that for both fields, the radiation is given with linear polarization in x, with this consideration, we can express the interaction Hamiltonian as follows:

$$\widehat{H}_1 = -e\,\widehat{x}\,E(t) - e\,\widehat{x}\,E_\mu(t), \tag{5.5}$$

where e is the electronic charge, $E(t)$ and $E_\mu(t)$ are the electric fields associated with the probe and drive respectively. As with $\widehat{H}_0$, it is possible to act on the left and right with the identity operator to use the completex relation again,

$$\widehat{H}_1 = \widehat{I}\,\widehat{H}_1\,\widehat{I}, \tag{5.6}$$

replacing the $\widehat{I}$ operator, and by using the Eq. (6.6),

$$\widehat{H}_1 = (|a\rangle\langle a| + |b\rangle\langle b| + |c\rangle\langle c|)\widehat{H}_1(|a\rangle\langle a| + |b\rangle\langle b| + |c\rangle\langle c|)\,,$$
$$\widehat{H}_1 = -e(|a\rangle\langle a| + |b\rangle\langle b| + |c\rangle\langle c|)\widehat{x}(|a\rangle\langle a| + |b\rangle\langle b| + |c\rangle\langle c|)E(t)$$
$$-e(|a\rangle\langle a| + |b\rangle\langle b| + |c\rangle\langle c|)\widehat{x}(|a\rangle\langle a| + |b\rangle\langle b| + |c\rangle\langle c|)E_\mu(t)$$

It is clear that the terms $\langle a|\widehat{x}|a\rangle$, $\langle b|\widehat{x}|b\rangle$ and $\langle c|\widehat{x}|c\rangle$ correspond to zero integrals due to the states symmetry, what's more, the $\langle b|\widehat{x}|c\rangle$ and $\langle c|\widehat{x}|b\rangle$ terms are zero because of the lambda arrangement, thus, we obtain the following expression:

$$\widehat{H}_1 = [-|a\rangle(e\langle a|\widehat{x}|b\rangle)\langle b| - |b\rangle(e\langle b|\widehat{x}|a\rangle)\langle a|]\,E(t)+$$
$$[-|a\rangle(e\langle a|\widehat{x}|c\rangle)\langle c| - |c\rangle(e\langle c|\widehat{x}|a\rangle)\langle a|]\,E_\mu(t)\,.$$

We can define the electric dipole matrix element as $P_{ij} = e\langle i|\widehat{x}|j\rangle = (e\langle i|\widehat{x}|j\rangle)^\dagger = (e\langle j|\widehat{x}|i\rangle)^* = P^*_{ji}$, with this definition, the last equation takes the form,

$$\widehat{H}_1 = -P_{ab}\,E(t)\,|a\rangle\langle b| - P_{ac}\,E_\mu(t)\,|a\rangle\langle c| + h.c.\,, \tag{5.7}$$

where $h.c.$ is the hermitian conjugate.

The equation 5.7 is still not the most convenient to use, an expression where the Rabi frequency is associated to the excited state and the intermediate state would be convenient. The fields $E(t)$ and $E_\mu(t)$ of equation (5.5) are classical fields, we can express them as follows: $E(t) = \mathcal{E}\cos(\nu t)$ and $E_\mu(t) = \mathcal{E}_\mu\cos(\nu_\mu t)$, where $\mathcal{E}$ and $\mathcal{E}_\mu$ are the amplitudes associated with the probe and drive fields with frequencies ν and ν_μ respectively. We can define ϕ and ϕ_μ for the phases associ-ated with the dipole operator matrix elements P_{ab} and P_{ac}, obtaining $P_{ab} = |P_{ab}|e^{-i\phi}$ and $P_{ac} = |P_{ac}|e^{-i\phi_\mu}$. In this way, we can define the Rabi frequency associated with each of the couplings:

$$\Omega = \frac{|P_{ab}|\mathcal{E}}{\hbar} \quad \text{and} \quad \Omega_\mu = \frac{|P_{ac}|\mathcal{E}_\mu}{\hbar}\,. \tag{5.8}$$

To obtain the equation of the dipole electric moment for the probe and control fields we can write P_{ab} and P_{ac} in terms of the Rabi frequency,

$$P_{ab} = \frac{\hbar\Omega}{\mathcal{E}} e^{-i\phi} \qquad \text{and} \quad P_{ab} = \frac{\hbar\Omega_\mu}{\mathcal{E}_\mu} e^{-i\phi_\mu}\,, \tag{5.9}$$

it is convenient to rewrite the fields in their exponential form,

$$E(t) = \frac{\mathcal{E}}{2}(e^{-i\nu t} + e^{i\nu t}) \quad \text{and} \quad E_\mu(t) = \frac{\mathcal{E}_\mu}{2}(e^{-i\nu_\mu t} + e^{i\nu_\mu t})\,, \tag{5.10}$$

taking into account the Eqs. 5.9 and 5.10, we can express the term $P_{ab}\,E(t)$ of equation (5.7) in a new form:

$$P_{ab}\,E(t) = \frac{\hbar\Omega}{\mathcal{E}} e^{-i\phi} \cdot \frac{\mathcal{E}}{2}(e^{-i\nu t} + e^{i\nu t})\,,$$
$$P_{ab}\,E_\mu(t) = \frac{\hbar\Omega}{2}(e^{-i\phi} e^{-i\nu t}) + \frac{\hbar\Omega}{2} e^{-i\phi} e^{i\nu t}\,,$$

The second term of the expression $P_{ab}\,E(t)$ does not contribute significantly in the calculation of the electronic population, by using the rotating wave approximation we can see that the term is of high oscillations, then $P_{ab}\,E(t)$ is written as follows:

$$P_{ab}\,E(t) = \frac{\hbar\Omega}{2}\, e^{-i\phi} e^{-i\nu t}\,. \tag{5.11}$$

In the same way we calculate $P_{ac}\,E_\mu(t)$,

$$P_{ac}\,E_\mu(t) = \frac{\hbar\Omega_\mu}{2}\, e^{-i\phi_\mu} e^{-i\nu_\mu t}\,. \tag{5.12}$$

Replacing (5.11) and (5.12) in (5.7):

$$\widehat{H}_1 = -\left(\frac{\hbar\Omega}{2}\, e^{-i\phi} e^{-i\nu t}\right) |a\rangle\langle b| - \left(\frac{\hbar\Omega_\mu}{2}\, e^{-i\phi_\mu} e^{-i\nu_\mu t}\right) |a\rangle\langle c| + h.c.\,. \tag{5.13}$$

From Eq. 5.9 we obtain $\Omega e^{-i\phi} = P_{ab}\mathcal{E}/^{-}h$, replacing in Eq. (5.13) we obtain the interaction Hamiltonian between the system with the

external fields $\widehat{H}_1$ in a explicit form in terms of the amplitude of the probe field $\mathcal{E}$, the associated dipole moment P_{ab}, the external frequency ν and the Rabi frequency of the system Ω_μ,

$$\widehat{H}_1 = -\frac{P_{ab}}{2}\,\mathcal{E}e^{-i\nu t}\,|a\rangle\langle b| - \frac{\hbar\Omega_\mu}{2}\,e^{-i\phi\mu}e^{-i\nu_\mu t}\,|a\rangle\langle c| + h.c.\,. \tag{5.14}$$

We can use the Von Neumann equation to analyze the time evolution by means of the density operator,

$$\frac{\partial\widehat{\rho}}{\partial t} = -\frac{i}{\hbar}\left[\widehat{H},\widehat{\rho}\right] - \frac{1}{2}\left\{\widehat{\Gamma},\widehat{\rho}\right\}\,, \tag{5.15}$$

we must take into account that $\left[\widehat{H},\widehat{\rho}\right]$ is a commutator and $\left\{\widehat{\Gamma},\widehat{\rho}\right\}$ is an anticonmutator. To calculate the matrix elements of this equation, we must expand the products and use the completex relation between operators, with an arbitrary matrix element the last equation can be written as,

$$\dot{\rho_{ij}} = -\frac{i}{\hbar}\sum_k(H_{ik}\rho_{kj} - \rho_{ik}H_{kj}) - \frac{1}{2}\sum_k(\Gamma_{ik}\rho_{kj} + \rho_{ik}\Gamma_{kj})\,, \tag{5.16}$$

the terms Γ_{kj} and Γ_{ik} are dissipative elements and can be expressed as $\Gamma_{nm} = \langle n|\widehat{\Gamma}|m\rangle = \Upsilon_n\delta_{nm}$ with $n,m = \{a,b,c\}$ where δ_{nm} is the Kronecker delta. From the above, we see that Γ is a diagonal matrix, secondly, the term Υ_n is inversely proportional to the state decay times, additionally, since states $|b\rangle$ and $|c\rangle$ are not dipolarly coupled, thus, the decay time for these states will be very high and consequently the Γ associate with the coupling between these states will be smaller.

To calculate the matrix element of ρ_{ab} we make $i = a$ and $j = b$ in Eq. (5.16),

$$\dot{\rho_{ab}} = -\frac{i}{\hbar}\sum_k(H_{ak}\rho_{kb} - \rho_{ak}H_{kb}) - \frac{1}{2}\sum_k(\Gamma_{ak}\rho_{kb} + \rho_{ak}\Gamma_{kb})\,, \tag{5.17}$$

$$\dot{\rho_{ab}} = -\frac{i}{\hbar}[H_{aa}\rho_{ab} - \rho_{aa}H_{ab} + H_{ab}\rho_{bb} - \rho_{ab}H_{bb} + H_{ac}\rho_{cb} - \rho_{ac}H_{cb}]$$

$$-\frac{1}{2}[\Gamma_{aa}\rho_{ab}+\rho_{aa}\Gamma_{ab}+\Gamma_{ab}\rho_{bb}+\rho_{ab}\Gamma_{bb}+\Gamma_{ac}\rho_{cb}+\rho_{ac}\Gamma_{cb}]\,, \tag{5.18}$$

the non-diagonal terms of Γ have been canceled, at this point it is necessary to explicitly calculate the matrix elements associated with the complete Hamiltonian $\widehat{H}_0+\widehat{H}_1$, this is easy to do by means of equations (5.4) and (5.14),

$$H_{aa}=\langle a|\widehat{H}_0|a\rangle+\langle a|\widehat{H}_1|a\rangle=\hbar\omega_a\,, \tag{5.19}$$

$$H_{ab}=\langle a|\widehat{H}_0|b\rangle+\langle a|\widehat{H}_1|b\rangle=-\frac{P_{ab}\,\mathcal{E}}{2}\,e^{-i\nu t}\,, \tag{5.20}$$

$$H_{bb}=\langle b|\widehat{H}_0|b\rangle+\langle b|\widehat{H}_1|b\rangle=\hbar\omega_b\,, \tag{5.21}$$

$$H_{ac}=\langle a|\widehat{H}_0|c\rangle+\langle a|\widehat{H}_1|c\rangle=-\frac{\hbar\Omega_\mu}{2}\,e^{-i\phi_\mu}\,e^{-i\nu_\mu t}\,, \tag{5.22}$$

$$H_{cb}=\langle a|\widehat{H}_0|b\rangle+\langle a|\widehat{H}_1|b\rangle=0\,, \tag{5.23}$$

considering $\Gamma_{aa}=\Gamma_{bb}\equiv\Upsilon_1$ and replacing equations (5.19 - 5.23) in (5.18):

$$\begin{aligned}\dot{\rho_{ab}}=&-\frac{i}{\hbar}[\hbar\omega_a\,\rho_{ab}+\frac{P_{ab}\,\mathcal{E}}{2}\,e^{-i\nu t}\rho_{aa}-\frac{P_{ab}\,\mathcal{E}}{2}\,e^{-i\nu t}\rho_{bb}-\hbar\omega_b\,\rho_{ab}\\&-\frac{\hbar\Omega_\nu}{2}\,e^{-i\phi_\mu}\,e^{-i\nu_\mu t}\rho_{cb}]-\frac{1}{2}[\Upsilon_1\rho_{ab}+\Upsilon_1\,\rho_{ab}]\,,\\\dot{\rho_{ab}}=&-i\omega_a\,\rho_{ab}+i\omega_b\,\rho_{ab}-\frac{iP_{ab}\,\mathcal{E}}{2\hbar}\,e^{-i\nu t}\,\rho_{aa}+\frac{iP_{ab}\,\mathcal{E}}{2\hbar}\,e^{-i\nu t}\,\rho_{bb}+\frac{i}{2}\Omega_\mu\,e^{-i\phi_\mu}\,e^{-i\nu_\mu t}\,\rho_{cb}-\Upsilon_1\,\rho_{ab}\,,\end{aligned}$$

defining $\omega_{ab}=\omega_a-\omega_b$, a final equation is obtained for the matrix element ρ_{ab},

$$\dot{\rho_{ab}}=-(i\omega_{ab}+\Upsilon_1)\,\rho_{ab}-\frac{iP_{ab}\,\mathcal{E}}{2\hbar}\,e^{-i\nu t}(\rho_{aa}-\rho_{bb})+\frac{i}{2}\Omega_\mu e^{-i\phi_\mu}e^{-\nu_\mu t}\rho_{cb}\,. \tag{5.24}$$

In the same way, we can calculate the term $\dot{\rho}_{cb}$ making $i=c$ and $j=b$ in Eq. (5.16),

$$\dot{\rho_{cb}} = -\frac{i}{\hbar}\sum_k (H_{ck}\rho_{kb} - \rho_{ck}H_{kb}) - \frac{1}{2}\sum_k (\Gamma_{ck}\rho_{kb} + \rho_{ck}\Gamma_{kb})\,, \tag{5.25}$$

expanding the summation,

$$\dot{\rho_{cb}} = -\frac{i}{2}[H_{ca}\rho_{ab} - \rho_{ca}H_{ab} + H_{cb}\rho_{bb} - \rho_{cb}H_{bb} + H_{cc}\rho_{cb} - \rho_{cc}H_{cb}] -$$
$$-\frac{1}{2}[\Gamma_{ca}\rho_{ab} + \rho_{ca}\Gamma_{ab} + \Gamma_{cb}\rho_{bb} + \rho_{cb}\Gamma_{bb} + \Gamma_{cc}\rho_{cb} + \rho_{cc}\Gamma_{cb}]\,, \tag{5.26}$$

once again the terms corresponding to non-diagonal Γ have been canceled. Following the same steps as in the calculation of ρ_{ab}, the matrix elements are obtained,

$$H_{ca} = -\frac{\hbar\,\Omega_\mu}{2}\,e^{i\phi_\mu}\,e^{i\nu_\mu t}\,, \tag{5.27}$$

$$H_{ab} = -\frac{P_{ab}\,\mathcal{E}}{2}\,e^{-i\nu t}\,, \tag{5.28}$$

$$H_{cb} = 0\,, \tag{5.29}$$

$$H_{bb} = \hbar\,\omega_b\,, \tag{5.30}$$

$$H_{cc} = \hbar\,\omega_c\,, \tag{5.31}$$

considering $\Gamma_{bb} = \Gamma_{cc} \equiv \Upsilon_3$ taking into account that they are associated to the same transition, and replacing equations (5.17 - 5.31) in (5.26):

$$\dot{\rho_{cb}} = -\frac{i}{\hbar}\left[-\frac{\hbar\,\Omega_\mu}{2}\,e^{i\phi_\mu}\,e^{i\nu_\mu t}\,\rho_{ab} + \frac{P_{ab}\,\mathcal{E}}{2}\,e^{-i\nu t}\,\rho_{ca} - \hbar\omega_b\,\rho_{cb} + \hbar\omega_c\,\rho_{cb}\right] -$$
$$-\frac{1}{2}[\Upsilon_3\,\rho_{cb} + \Upsilon_3\,\rho_{cb}]\,. \tag{5.32}$$

It is pertinent to remember that Υ_3 will have a very small value because the time for electronic decay between these states will be very high, removing the parentheses in the last equation,

$$\dot{\rho_{cb}} = i\omega_b\rho_{cb} - i\omega_c\,\rho_{cb} - \frac{iP_{ab}\,\mathcal{E}}{2\hbar}\,e^{-i\nu t}\,\rho_{ca} + \frac{i\Omega_\mu}{2}\,e^{i\phi_\mu}e^{i\nu_\mu t}\,\rho_{ab} - \Upsilon_3\rho_{cb}\,, \quad (5.33)$$

defining $\omega_{cb} = \omega_c - \omega_b$, and rearranging terms, it is finally obtained,

$$\dot{\rho_{cb}} = -(i\omega_{cb} + \Upsilon_3)\,\rho_{cb} - \frac{iP_{ab}\,\mathcal{E}}{2\hbar}\,e^{-i\nu t}\,\rho_{ca} + \frac{i\Omega_\mu}{2}\,e^{i\phi_\mu}e^{i\nu_\mu t}\,\rho_{ab}\,. \quad (5.34)$$

Similarly, we can calculate the term $\dot{\rho}_{ac}$ by doing $i = a$ and $j = c$ in the equation (5.16),

$$\dot{\rho_{ac}} = -\frac{i}{\hbar}\sum_k (H_{ak}\rho_{kc} - \rho_{ak}H_{kc}) - \frac{1}{2}\sum_k (\Gamma_{ak}\rho_{kc} + \rho_{ak}\Gamma_{kc})\,, \quad (5.35)$$

expanding the summations,

$$\dot{\rho_{ac}} = -\frac{i}{\hbar}[H_{aa}\rho_{ac} - \rho_{aa}H_{ac} + H_{ab}\rho_{bc} - \rho_{ab}H_{bc} + H_{ac}\rho_{cc} - \rho_{ac}H_{cc}]$$
$$-\frac{1}{2}[\Gamma_{aa}\rho_{ac} + \rho_{aa}\Gamma_{ac} + \Gamma_{ab}\rho_{bc} + \rho_{ab}\Gamma_{bc} + \Gamma_{ac}\rho_{cc} + \rho_{ac}\Gamma_{cc}]\,, \quad (5.36)$$

the procedure is similar to the one already presented, it is easy to see that the matrix elements have the form,

$$H_{aa} = \hbar\,\omega_a\,, \quad (5.37)$$

$$H_{ac} = -\frac{\hbar\,\Omega_\mu}{2}\,e^{-i\phi_\mu}\,e^{-i\nu_\mu t}\,, \quad (5.38)$$

$$H_{ab} = -\frac{P_{ab}\,\mathcal{E}}{2}\,e^{-i\nu t}\,, \quad (5.39)$$

$$H_{bc} = 0\,, \quad (5.40)$$

$$H_{cc} = \hbar\,\omega_c\,, \quad (5.41)$$

making $\Gamma_{aa} = \Gamma_{cc} \equiv \Upsilon_2$ and replacing the Eqs. (5.37 - 5.41) in Eq. (5.36),

$$\dot{\rho_{ac}} = -\frac{i}{\hbar}\left[\hbar\omega_a\,\rho_{ac} + \frac{\hbar\,\Omega_\mu}{2}\,e^{-i\phi_\mu}\,e^{-i\nu_\mu t}\,\rho_{aa} - \frac{P_{ab}\,\mathcal{E}}{2}\,e^{-i\nu t}\,\rho_{bc} - \frac{\hbar\,\Omega_\mu}{2}\,e^{-i\phi_\mu}\,e^{-i\nu_\mu t}\,\rho_{cc} - \hbar\omega_c\,\rho_{ac}\right] - \\ - \frac{1}{2}\left[\Upsilon_2\,\rho_{ac} + \Upsilon_2\,\rho_{ac}\right]\,, \tag{5.42}$$

defining $\omega_{ac} = \omega_a - \omega_c$ and regrouping, we finally obtain,

$$\dot{\rho_{ac}} = -(i\omega_{ac} + \Upsilon_2)\,\rho_{ac} - \frac{i}{2}\Omega_\mu\,e^{-i\phi_\mu}\,e^{-i\nu_\mu t}\,(\rho_{aa} - \rho_{cc}) + \frac{iP_{ab}\,\mathcal{E}}{2\hbar}\,e^{-i\nu t}\,\rho_{bc}\,. \tag{5.43}$$

The absorption in the system is proportional to the density matrix associated with the transition $|b\rangle \to |a\rangle$, ρ_{ab}. We can consider as initial condition the system is in the ground state, this means that at time $t = 0$ all electronic population are in $|b\rangle$, this implies that $\rho_{bb}^{(0)} = 1$ and in the state $|a\rangle$ and $|c\rangle$ we will have zero $\rho_{aa}^{(0)} = \rho_{cc}^{(0)} = 0$, remembering that the diagonal terms of the density matrix are associated with the probability density of each state. In the same way we can consider $\rho_{ca}^{(0)} = 0$ which corresponds to the fact that there are no excitations in the system for $t = 0$. Let's make $\rho_{ab} = \tilde{\rho}_{ab}\,e^{i\nu t}$ and $\rho_{cb} = \tilde{\rho}_{cb}\,e^{-i(\nu+\omega_{ca})t}$ where $\tilde{\rho}_{ab}$ and $\tilde{\rho}_{cd}$ have no time dependency. By evaluating in the equation (5.24),

$$-i\nu\,\tilde{\rho}_{ab}\,e^{-i\nu t} = -(i\omega_{ab}+\Upsilon_1)\tilde{\rho}_{ab}\,e^{-i\nu t} - \frac{iP_{ab}\,\mathcal{E}}{2\hbar}(\rho_{aa}-\rho_{bb}) + \frac{i}{2}\Omega_\mu e^{-i\phi_\mu}e^{-i\nu_\mu t}\tilde{\rho}_{cb}\,e^{-i(\nu+\omega_{ca})t}\,, \tag{5.44}$$

with $t = 0$,

$$-i\nu\tilde{\rho}_{ab} = -(i\omega_{ab} + \Upsilon_1)\tilde{\rho}_{ab} - \frac{iP_{ab}\,\mathcal{E}}{2\hbar}(\rho_{aa}^{(0)} - \rho_{bb}^{(0)}) + \frac{i}{2}\Omega_\mu e^{-i\phi_\mu}\tilde{\rho}_{cb}\,,$$

reorganizing terms and applying the initial conditions for $\rho_{aa}^{(0)}$ and $\rho_{bb}^{(0)}$,

$$0 = -(\Upsilon_1 + i(\omega_{ab} - \nu))\,\tilde{\rho}_{ab} + \frac{iP_{ab}\,\mathcal{E}}{2\hbar} + \frac{i}{2}\Omega_\mu e^{-i\phi_\mu}\tilde{\rho}_{cb}\,, \tag{5.45}$$

defining the detuning $\Delta = \omega_{ab} - \nu$ as the difference between the transition energy between $|b\rangle$ and $|a\rangle$ states and the energy of the probe field, we obtain

$$0 = -(\Upsilon_1 + i\Delta)\tilde{\rho}_{ab} + \frac{iP_{ab}\,\mathcal{E}}{2\hbar} + \frac{i}{2}\Omega_\mu e^{-i\phi_\mu}\tilde{\rho}_{cb}\,. \tag{5.46}$$

Secondly, by using the expressions $\rho_{ab} = \tilde{\rho}_{ab}\, e^{i\nu t}$ and $\rho_{cb} = \tilde{\rho}_{cb}\, e^{-i(\nu + \omega_{ca})t}$ in the equation (5.34),

$$-i(\nu + \omega_{ca})\tilde{\rho}_{cb}\, e^{-i(\nu+\omega_{ca})t} = -(i\omega_{cb} + \Upsilon_3)\,\tilde{\rho}_{cb}\, e^{-i(\nu+\omega_{ca})t} - \frac{iP_{ab}\,\mathcal{E}}{2\hbar}\, e^{-i\nu t}\rho_{ca}$$
$$+\frac{i}{2}\Omega_\mu\, e^{i\phi_\mu}\, e^{i\nu_\mu t}\tilde{\rho}_{ab}\, e^{-i\nu t}\,,$$

evaluating for $t = 0$,

$$-\,i(\nu + \omega_{ca})\,\tilde{\rho}_{cb} = -(i\omega_{cb} + \Upsilon_3)\,\tilde{\rho}_{cb} - \frac{iP_{ab}\,\mathcal{E}}{2\hbar}\,\rho^{(0)}_{ca} + \frac{i}{2}\Omega_\mu\, e^{i\phi_\mu}\,\tilde{\rho}_{ab}\,, \tag{5.47}$$

rearranging terms,

$$0 = -(\Upsilon_3 + i(\omega_{cb} - \omega_{ca} - \nu))\,\tilde{\rho}_{cb} + \frac{i}{2}\Omega_\mu\, e^{i\phi_\mu}\,\tilde{\rho}_{ab}\,, \tag{5.48}$$

let's see that,

$$\omega_{cb} - \omega_{ca} = \omega_c - \omega_b - \omega_c + \omega_a\,,$$
$$\omega_{cb} - \omega_{ca} = \omega_a - \omega_b\,,$$
$$\omega_{cb} - \omega_{ca} = \omega_{ab}\,,$$

by using this result in (5.48), remembering the detuning definition,

$$0 = -(\Upsilon_3 + i\Delta)\,\tilde{\rho}_{cb} + \frac{i}{2}\Omega_\mu\, e^{i\phi_\mu}\,\tilde{\rho}_{ab}\,. \tag{5.49}$$

From this last equation, let's solve for the term $\tilde{\rho}_{cb}$,

$$\tilde{\rho}_{cb} = \frac{i\Omega_\mu\, e^{i\phi_\mu}}{2\,(\Upsilon_3 + i\Delta)}\,\tilde{\rho}_{ab}\,, \tag{5.50}$$

replacing Eq. (5.50) in (5.46):

$$0 = -(\Upsilon_1 + i\Delta)\,\tilde{\rho}_{ab} + \frac{iP_{ab}\,\mathcal{E}}{2\hbar} + \frac{i}{2}\Omega_\mu\, e^{-i\phi_\mu}\frac{i\Omega_\mu\, e^{i\phi_\mu}}{2\,(\Upsilon_3 + i\Delta)}\,\tilde{\rho}_{ab}\,,$$

simplifying,

$$0 = -(\Upsilon_1 + i\Delta)\,\tilde{\rho_{ab}} + \frac{iP_{ab}\,\mathcal{E}}{2\hbar} - \frac{\Omega_\mu^2\,\tilde{\rho}_{ab}}{4\,(\Upsilon_3 + i\Delta)}\,,$$

solving for $\tilde{\rho}_{ab}$,

$$\left[(\Upsilon_1 + i\Delta) + \frac{\Omega_\mu^2}{4\,(\Upsilon_3 + i\Delta)}\right]\tilde{\rho}_{ab} = \frac{iP_{ab}\,\mathcal{E}}{2\hbar}\,,$$

$$\frac{4\,(\Upsilon_1 + i\Delta)(\Upsilon_3 + i\Delta) + \Omega_\mu^2}{4\,(\Upsilon_3 + i\Delta)}\,\tilde{\rho}_{ab} = \frac{iP_{ab}\,\mathcal{E}}{2\hbar}\,,$$

$$\tilde{\rho}_{ab} = \frac{4\,iP_{ab}\,\mathcal{E}\,(\Upsilon_3 + i\Delta)}{2\hbar\,[4\,(\Upsilon_1 + i\Delta)\,(\Upsilon_3 + i\Delta) + \Omega_\mu^2]}\,,$$

$$\tilde{\rho}_{ab} = \frac{iP_{ab}\,\mathcal{E}\,(\Upsilon_3 + i\Delta)}{2\hbar\,[(\Upsilon_1 + i\Delta)\,(\Upsilon_3 + i\Delta) + \Omega_\mu^2/4]}\,, \tag{5.51}$$

remembering that $\rho_{ab} = \tilde{\rho}_{ab}\,e^{-\nu t}$, then we finally get,

$$\rho_{ab} = \frac{iP_{ab}\,\mathcal{E}\,(\Upsilon_3 + i\Delta)\,e^{-i\nu t}}{2\hbar[(\Upsilon_1 + i\Delta)\,(\Upsilon_3 + i\Delta) + \Omega_\mu^2/4]}\,. \tag{5.52}$$

From the Eq. (5.10), it is had that by means of the rotating wave approximation only a part of the field contributes significantly to the electronic population between the levels $|b\rangle$ and $|a\rangle$, this part is given by $E(t) = \mathcal{E}\,e^{-i\nu t}/2$, in the same way, the macroscopic polarization will be given by $P(t) = \wp\,e^{-i\nu t}/2$, where $\wp$ is the complex polarization of the system. From the above, we can write complex polarization in terms of macroscopic polarization as,

$$\wp = 2\,P(t)\,e^{i\nu t}\,. \tag{5.53}$$

To obtain an expression for the polarization of the system due to the $|b\rangle \to |a\rangle$ transition, then the wave function of the system can be approximated as a linear combination of these states,

$$|\psi(t)\rangle = C_a(t)\,|a\rangle + C_b(t)\,|b\rangle\,, \tag{5.54}$$

on the other hand, the macroscopic polarization can be calculated as,

$$P(t) = e\,\langle\psi(t)|x|\psi(t)\rangle =$$
$$P(t) = e\,\left(C_a^*(t)\,\langle a| + C_b^*(t)\,\langle b|\right) x\,\left(C_a(t)\,|a\rangle + C_b(t)\,|b\rangle\right) =$$
$$P(t) = e\,C_a^*(t)C_b(t)\,\langle a|x|b\rangle + e\,C_a(t)C_b^*(t)\,\langle b|x|a\rangle =$$
$$P(t) = C_a(t)C_b^*(t)\,P_{ba} + h.c.\,, \tag{5.55}$$

where the integrals equal to zero have been canceled and the definition of electric dipole moment that was already used in Eq. (5.7). Similarly, the density matrix associated with state in Eq. (5.54) is given by,

$$\rho = |\psi(t)\rangle\langle\psi(t)| =$$
$$\rho = \left(C_a(t)\,|a\rangle + C_b(t)\,|b\rangle\right)\,\left(C_a^*(t)\,\langle a| + C_b^*(t)\,\langle b|\right) =$$
$$\rho = |C_a(t)|^2\,|a\rangle\langle a| + C_a(t)C_b^*(t)\,|a\rangle\langle b| + C_a^*(t)C_b(t)\,|b\rangle\langle a| + |C_b(t)|^2\,|b\rangle\langle b|\,, \tag{5.56}$$

according to Eq. (5.52), let's calculate the element ρ_{ab},

$$\rho_{ab} = \langle a|\rho|b\rangle = C_a^*(t)C_b(t)\,, \tag{5.57}$$

replacing Eq. (5.57) in (5.55),

$$P(t) = P_{ba}\,\rho_{ab} + h.c. =$$
$$P(t) = P_{ab}^*\,\rho_{ab} + h.c.\,, \tag{5.58}$$

where it has been used that $P_{ba} = P_{ab}^*$. As in Eq. (5.53) the rotating wave approximation has been used, in the same way in Eq. (5.58) we must stay with only one of the terms to be consistent $P(t) \approx P_{ab}^*\,\rho_{ab}$, replacing this result in Eq. (5.53),

$$\wp = 2\,P_{ab}^*\,\rho_{ab}\,e^{i\nu t}\,, \tag{5.59}$$

this result can be equated with the complex polarization definition,

$$\wp \equiv \varepsilon_0\,\chi\,\mathcal{E} = 2\,P_{ab}^*\,\rho_{ab}\,e^{i\nu t}\,, \tag{5.60}$$

where ε_0 is the vacuum permittivity, χ the system susceptibility and $\mathcal{E}$ the field amplitude. Solving for ρ_{ab} in (5.60),

$$\rho_{ab} = \frac{\varepsilon_0\,\chi\,\mathcal{E}}{2\,P^*_{ab}}\,e^{-i\nu t}\,, \tag{5.61}$$

equating this last equation with (5.52),

$$\frac{iP_{ab}\,\mathcal{E}\,(\Upsilon_3 + i\Delta)\,e^{-i\nu t}}{2\hbar[(\Upsilon_1 + i\Delta)\,(\Upsilon_3 + i\Delta) + \Omega_\mu^2/4]} = \frac{\varepsilon_0\,\chi\,\mathcal{E}}{2\,P^*_{ab}}\,e^{-i\nu t}\,,$$

$$\chi = \frac{i|P_{ab}|^2\,(\Upsilon_3 + i\Delta)}{\hbar\varepsilon_0\,[(\Upsilon_1 + i\Delta)\,(\Upsilon_3 + i\Delta) + \Omega_\mu^2/4]}\,,$$

$$\chi = \frac{i|P_{ab}|^2\,\Upsilon_3 - |P_{ab}|^2\,\Delta}{\hbar\varepsilon_0\,\left[\Upsilon_1\,\Upsilon_3 + i\Upsilon_1\,\Delta + i\Upsilon_3\,\Delta - \Delta^2 + \Omega_\mu^2/4\right]}\,. \tag{5.62}$$

It is necessary to know the real part and the complex part of the susceptibility of the system to calculate the absorption, to obtain these expressions, let's do the substitutions,

$$\alpha = -|P_{ab}|^2\,\Delta\,,$$
$$\beta = |P_{ab}|^2\Upsilon_3\,,$$
$$\lambda = \Upsilon_1\Upsilon_3 - \Delta^2 + \Omega_\mu^2/4\,,$$
$$\sigma = \Upsilon_1\Delta + \Upsilon_3\Delta\,,$$

with these substitutions, Eq. (5.62) takes the simple form,

$$\chi = \frac{\alpha + i\beta}{\hbar\varepsilon_0\,(\lambda + i\sigma)}\,, \tag{5.63}$$

multiplying up and down by $(\lambda - i\sigma)$,

$$\chi = \frac{(\alpha + i\beta)\,(\lambda - i\sigma)}{\hbar\varepsilon_0\,(\lambda + i\sigma)\,(\lambda - i\sigma)}\,,$$

regrouping terms

$$\chi = \frac{(\alpha\lambda + \beta\sigma) - i(\alpha\sigma - \beta\lambda)}{\hbar\varepsilon_0(\lambda^2 + \sigma^2)}\,. \tag{5.64}$$

Defining the susceptibility as $\chi = \chi' + i\,\chi''$, where χ' and χ'' are the real part and imaginary part respectively, with this consideration, of Eq. (5.64) is obtained that:

$$\chi' = \frac{\alpha\lambda + \beta\sigma}{\hbar\varepsilon_0\left(\lambda^2 + \sigma^2\right)}\,, \tag{5.65}$$

and

$$\chi'' = \frac{\beta\lambda - \alpha\sigma}{\hbar\varepsilon_0\left(\lambda^2 + \sigma^2\right)}\,, \tag{5.66}$$

returning to the original variables,

$$\chi' = \frac{\left(-|P_{ab}|^2\,\Delta\right)\left(\Upsilon_1\Upsilon_3 - \Delta^2 + \Omega_\mu^2/4\right) + \left(|P_{ab}|^2\Upsilon_3\right)\left(\Upsilon_1\Delta + \Upsilon_3\Delta\right)}{\hbar\varepsilon_0\left(\left(\Upsilon_1\Upsilon_3 - \Delta^2 + \Omega_\mu^2/4\right)^2 + \left(\Upsilon_1\Delta + \Upsilon_3\Delta\right)^2\right)}\,, \tag{5.67}$$

and

$$\chi'' = \frac{\left(|P_{ab}|^2\Upsilon_3\right)\left(\Upsilon_1\Upsilon_3 - \Delta^2 + \Omega_\mu^2/4\right) - \left(-|P_{ab}|^2\,\Delta\right)\left(\Upsilon_1\Delta + \Upsilon_3\Delta\right)}{\hbar\varepsilon_0\left(\left(\Upsilon_1\Upsilon_3 - \Delta^2 + \Omega_\mu^2/4\right)^2 + \left(\Upsilon_1\Delta + \Upsilon_3\Delta\right)^2\right)}\,, \tag{5.68}$$

simplifying, the real part of the susceptibility is finally obtained as,

$$\chi' = \frac{N_a\,|P_{ab}|^2\,\Delta}{\hbar\,\varepsilon_0\,Z}\left[\Upsilon_3\,\left(\Upsilon_1 + \Upsilon_3\right) + \left(\Delta^2 - \Upsilon_1\Upsilon_3 - \Omega_\mu^2/4\right)\right]\,, \tag{5.69}$$

similarly, the imaginary part of susceptibility,

$$\chi'' = \frac{N_a\,|Pa|^2}{\hbar\,\varepsilon_0\,Z}\left[\Delta^2\,\left(\Upsilon_1 + \Upsilon_3\right) - \Upsilon_3\,\left(\Delta^2 - \Upsilon_1\Upsilon_3 - \Omega_\mu^2/4\right)\right]\,, \tag{5.70}$$

where $Z = \left(\Delta^2 - \Upsilon_1\Upsilon_3 - \Omega_\mu^2/4\right)^2 + \Delta^2(\Upsilon_1 + \Upsilon_3)^2$ and N_a is the number density of atoms in the system.

When $\Delta = 0$, which indicates that the probe field is in resonance with the transition between states $|b\rangle$ and $|a\rangle$, it is obtained,

$$\chi' = 0 \quad \text{and} \quad \chi'' = -\frac{Na\,|P_{ab}|^2}{\hbar\,\varepsilon_0\,Z}\frac{\Upsilon_3}{\Upsilon_1\Upsilon_3 + \Omega_\mu^2/4}\,. \tag{5.71}$$

It is evident that the imaginary part of the susceptibility is proportional to Υ_3, remembering that Υ_3 is the decay rate between states $|b\rangle$ and $|c\rangle$ and since these states are not coupled, then $\Upsilon_3 \to 0$ which

implies that $\chi'' \approx 0$. The above indicates that the absorption tends to zero, thus the radiation is not being absorbed when the system is in resonance with the probe field ($\omega_{ab} = \nu$), the system behaves as if it were transparent to this radiation (remembering that this should be the point of maximum absorption). This process is known as electromagnetically induced transparency. The effect depends on the Rabi frequency of the drive field and the decay rate between states $|b\rangle$ and $|c\rangle$.

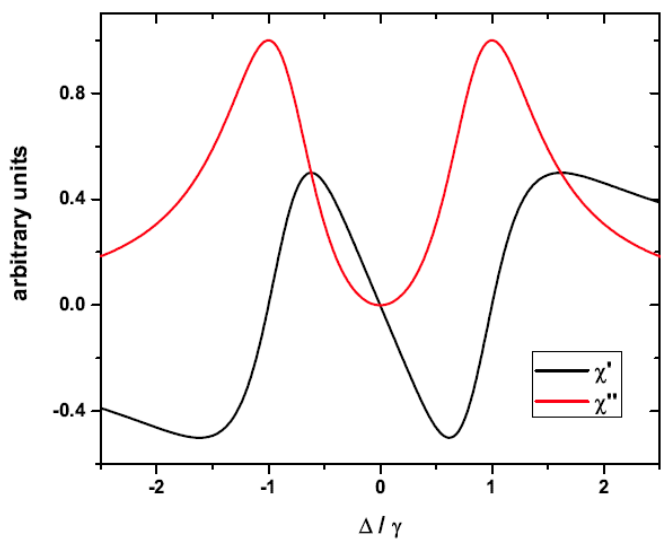

Figure 5.2: real χ' and imaginary χ'' part of susceptibility as a function of normalized detuning Δ/γ ($\gamma = \Upsilon_1$).

It is convenient to define the α and β parameters such that $\Upsilon_3 = \alpha\,\Upsilon_1$ and $\Omega_\mu = \beta\,\Upsilon_3$ are fulfilled, clearly, $\alpha << \beta$ must be met to ensure that there is no dipole coupling between states $|b\rangle$ and $|c\rangle$. The Fig. (5.2) shows the real and imaginary part of the susceptibility given by the Eqs. (5.69) and (5.70) as a function of the normalized detuning Δ/γ where $\gamma = \Upsilon_1$ has been done, $\alpha = 10^{-4}$ eV and $\beta = 2$ eV have been taken for this figure. The red curve in this figure is proportional to the absorption in the system, clearly in the resonance ($\Delta/\gamma \to 0$) the absorption tends to zero, which implies that the system is transparent under the probe field.

References

[1] M. Scully, and M. Zubairy, *Quantum Optics*, Cambridge: Cambridge University Press, ISBN-13: 978-0524235959 (1997).

[2] A. I. Bashir, *Role of intense laser-excited dressed states via electromagnetically induced transparency on the Fresnel-Fizeau photon drag through an asymmetric double quantum dot molecule (GaAs/AlGaAs) in the* Λ*-type configuration.* Physica E Low Dimens. Syst. Nanostruct. **134** 114904 (2021).

[3] R. Mukherjee and S. Konar, *Effect of quintic nonlinearity on self-phase modulation and modulation instability in multiple coupled quantum wells under electromagnetically induced transparency.* Results Phys. **17** 103090 (2020).

[4] J. Jayarubi, A. J. Peter, C. W. Lee, *Electromagnetically induced transparency in a GaAs/InAs/GaAs quantum well.* Phys. B: Condens. Matter **550** 184-188 (2018).

[5] J. Jayarubi, A. J. Peter, C. W. Lee, *Electromagnetically induced transparency in a GaAs/InAs/GaAs parabolic quantum well in the external magnetic field.* Superlattices Microstruct. **122** 9-17 (2018).

[6] D. Bejan, C. Stan, E. C. Niculescu, *Effects of electric field and light polarization on the electromagnetically induced transparency in an impurity doped quantum ring.* Opt. Mater. **75** 827-840 (2018).

[7] E. C. Niculescu, *Electromagnetically induced transparency in an asymmetric double quantum well under non-resonant, intense laser fields.* Opt. Mater. **64** 540-547 (2017).

[8] M. Gambhir, S. Gumber, P. K. Jha, M. Mohan, *Dependence of electromagnetically induced transparency on pressure and temperature in a quantum dot with flat cylindrical geometry.* Superlattices Microstruct. **71** 147–161 (2014).

Chapter 6

Nonlinear optical properties

6.1 Introduction

The general theory of the nonlinear optical response must be adapted to the situation of low dimensional systems in which the spectrum of energy states may have a contribution of discrete energies apart from the continuous states associated with subbands corresponding to free movements with effective mass along one or two dimensions. The situation in which we have a completely discrete spectrum is the quantum heteroestrucuture case, which is analogous to the resulting atomic case. The works of Rosencher and Bois [1] and Ahn and Chuang [2] were those who entered the formalism developed in the 1960 years to the situation of systems as we are concerned. Now will present a detailed derivation of the first and third-order absorption coefficients as well as the first and thir-order change in the refractive index coefficient in the scheme of reference [2] which was developed for the case of a quantum well. However, the scheme is directly extended to quantum wires, rings and dots.

6.2 Density Matrix Equations

Lets consider a system in the presence of an optical radiation of frequency ω with polarization along the z-axis. Lets denote $\hat{\rho}$, $\hat{H}_0$, $\hat{M}$ and $E(t)$ as the density matrix for one electron, the unperturbed Hamiltonian of the system, the electric dipole operator and the intensity of the electric field of the optical radiation of frequency ω respectively.

The density matrix equation for one electron with intraband relaxation is given by

$$\frac{\partial \hat{\rho}}{\partial t} = \frac{1}{i\hbar}\left[\hat{H}_0 - \hat{M}\hat{E}(t), \rho\right] - \frac{1}{2}\left[\hat{\Gamma}(\hat{\rho} - \hat{\rho}^{(0)}) + (\hat{\rho} - \hat{\rho}^{(0)})\hat{\Gamma}\right], \qquad (6.1)$$

where $\hat{\rho}^{(0)}$ is the unperturbed density matrix and $\hat{\Gamma}$ is a phenomenological operator responsible of the damping due to electron-phonon, electron-electron and other interaction processes. We assume that $\hat{\Gamma}$ is a diagonal matrix and its element Γ_{mm} is the inverse of the relaxing time for the estate $|m\rangle$. To simplify the analysis we focus on two-level systems ($|1\rangle$, $|2\rangle$).

The incident monochromatic field is defined as

$$E(t) = \Re(E_0 e^{-i\omega t}) = \frac{1}{2}E_0 e^{-i\omega t} + \frac{1}{2}E_0 e^{i\omega t} = \tilde{E}e^{-i\omega t} + \tilde{E}e^{i\omega t} \qquad (6.2)$$

The diagonal elements of the $\hat{\Gamma}$ operator are given by

$$\langle 1|\hat{\Gamma}|1\rangle = \gamma_{11} = 1/\tau_1 \quad , \quad \langle 2|\hat{\Gamma}|2\rangle = \gamma_{22} = 1/\tau_2 \qquad (6.3)$$

We can solve equation (6.1) through a perturbative series in $\hat{\rho}$ as

$$\hat{\rho}(t) = \sum_n \hat{\rho}^{(n)}(t) \qquad (6.4)$$

In thermal equilibrium, the density matrix $\hat{\rho}^{(0)}$ is a diagonal matrix where its diagonal elements are the superficial thermal population. Lets call $\hat{\rho}_{11}^{(n)} = \langle 1|\hat{\rho}|1\rangle$, $\hat{\rho}_{12}^{(n)} = \langle 1|\hat{\rho}|2\rangle$, $\hat{\rho}_{21}^{(n)} = \langle 2|\hat{\rho}|1\rangle$, $\hat{\rho}_{22}^{(n)} = \langle 2|\hat{\rho}|2\rangle$. The matrix $\hat{\rho}$ has the hermiticity property $\rho_{12}(t) = \rho_{12}^*(t)$.

Replacing equation (6.4) in equation (6.1), we obtain

$$\begin{aligned}\sum_n \frac{\partial \hat{\rho}}{\partial t} &= \frac{1}{i\hbar}\sum_n \left[(\hat{H}_0 - \hat{M}E(t))\hat{\rho}^{(n)} - \hat{\rho}^{(n)}(\hat{H}_0 - \hat{M}E(t))\right] \\ &- \frac{1}{2}\sum_n \left[\hat{\Gamma}(\hat{\rho}^{(n)} - \hat{\rho}^{(0)}) + (\hat{\rho}^{(n)} - \hat{\rho}^{(0)})\hat{\Gamma}\right] \qquad (6.5)\end{aligned}$$

Note that we can write

$$\sum_n \hat{\rho}^{(n)} - \hat{\rho}^{(0)} = \sum_n \hat{\rho}^{(n+1)} \qquad (6.6)$$

then,

$$\sum_n \frac{\partial \hat{\rho}}{\partial t} = \frac{1}{i\hbar}\sum_n \Big[(\hat{H}_0 - \hat{M}E(t))\hat{\rho}^{(n)} - \hat{\rho}^{(n)}(\hat{H}_0 - \hat{M}E(t))\Big] - \frac{1}{2}\left[\hat{\Gamma}\Big(\sum_n \hat{\rho}^{(n+1)}\Big) + \Big(\sum_n \hat{\rho}^{(n+1)}\Big)\hat{\Gamma}\right] \tag{6.7}$$

With the last expression we can calculate $\langle 2|\frac{\partial \hat{\rho}}{\partial t}|1\rangle$, so

$$\sum_n \frac{\partial \rho_{21}^{(n)}}{\partial t} = \frac{1}{i\hbar}\sum_n \Big[\langle 2|(\hat{H}_0 - \hat{M}E(t))\hat{\rho}^{(n)}|1\rangle - \langle 2|\hat{\rho}^{(n)}(\hat{H}_0 - \hat{M}E(t))|1\rangle\Big] - \frac{1}{2}\sum_n \Big[\langle 2|\hat{\Gamma}\hat{\rho}^{(n+1)}|1\rangle + \langle 2|\hat{\rho}^{(n+1)}\hat{\Gamma}|1\rangle\Big] \tag{6.8}$$

Having present that $\hat{H}_0|m\rangle = E_m|m\rangle$, we have

$$\sum_n \frac{\partial \rho_{21}^{(n)}}{\partial t} = \frac{1}{i\hbar}\sum_n \Big[E_2\langle 2|\hat{\rho}^{(n)}|1\rangle - \langle 2|\hat{M}\hat{\rho}^{(n)}|1\rangle E(t) - E_1\langle 2|\hat{\rho}^{(n)}|1\rangle + \langle 2|\hat{\rho}^{(n)}\hat{M}|1\rangle E(t)\Big] - \frac{1}{2}\sum_n \Big[\langle 2|\Gamma\hat{}\,\rho\hat{}^{(n+1)}|1\rangle + \langle 2|\rho\hat{}^{(n+1)}\Gamma\hat{}\,|1\rangle\Big] \tag{6.9}$$

Introducing the completeness relation given by,

$$|1\rangle\langle 1| + |2\rangle\langle 2| = 1, \tag{6.10}$$

we obtain

$$\sum_n \frac{\partial \rho_{21}^{(n)}}{\partial t} = \frac{1}{i\hbar}\sum_n \Big[(E_2 - E_1)\rho_{21}^{(n)} - \langle 2|\hat{M}(|1\rangle\langle 1| + |2\rangle\langle 2|)\hat{\rho}^{(n)}|1\rangle E(t) + \langle 2|\hat{\rho}^{(n)}(|1\rangle\langle 1| + |2\rangle\langle 2|)\hat{M}|1\rangle E(t)\Big] - \frac{1}{2}\sum_n \Big[\langle 2|\hat{\Gamma}(|1\rangle\langle 1| + |2\rangle\langle 2|)\hat{\rho}^{(n+1)}|1\rangle + \langle 2|\hat{\rho}^{(n+1)}(|1\rangle\langle 1| + |2\rangle\langle 2|)\hat{\Gamma}|1\rangle\Big] \tag{6.11}$$

Some algebraic steps and remembering that $\hat{\Gamma}$ only have diagonal elements we arrive at

$$\sum_n \frac{\partial \rho_{21}^{(n)}}{\partial t} = \frac{1}{i\hbar}\sum_n \Big[(E_2 - E_1)\rho_{21}^{(n)} - (M_{21}\rho_{11}^{(n)} + M_{22}\rho_{21}^{(n)})E(t) + (M_{11}\rho_{21}^{(n)} + M_{21}\rho_{22}^{(n)})E(t)\Big] - \sum_n \frac{1}{2}\Big(\frac{1}{\tau_2} + \frac{1}{\tau_1}\Big)\rho_{21}^{(n+1)} \tag{6.12}$$

Regrouping the order of some terms and setting $E_{21} = E_2 - E_1$,

$$\begin{aligned}\sum_n \frac{\partial \rho_{21}^{(n)}}{\partial t} &= \frac{1}{i\hbar}\sum_n \Big[E_{21}\rho_{21}^{(n)} - (\rho_{11}^{(n)} - \rho_{22}^{(n)})M_{21}E(t) - (M_{22} - M_{11})\rho_{21}^{(n)})E(t)\Big] \\ &- \sum_n \gamma_{12}\rho_{21}^{(n+1)} \qquad (6.13)\end{aligned}$$

where

$$\gamma_{12} = \gamma_{21} = \frac{1}{2}\Big(\frac{1}{\tau_1} + \frac{1}{\tau_2}\Big) \qquad (6.14)$$

Using the fact that $\rho_{21}^{(0)} = \rho_{12}^{(0)} = 0$ we have

$$\sum_n \rho_{21}^{(n)} = \sum_n \rho_{21}^{(n+1)} \qquad (6.15)$$

which allows us to write

$$\begin{aligned}\sum_n \frac{\partial \rho_{21}^{(n+1)}}{\partial t} &= \sum_n \Big[\frac{1}{i\hbar}E_{21} - \gamma_{12}\Big]\rho_{21}^{(n+1)} - \sum_n \frac{1}{i\hbar}(\rho_{11}^{(n)} - \rho_{22}^{(n)})M_{21}E(t) \\ &- \sum_n \frac{1}{i\hbar}(M_{22} - M_{11})E(t)\rho_{21}^{(n)}. \qquad (6.16)\end{aligned}$$

Finally, the last equation implies that — Note that it was not redefined the index of the sum. This is done with the idea of obtaining recurrence relations —

$$\begin{aligned}\frac{\partial \rho_{21}^{(n+1)}}{\partial t} &= \Big[\frac{1}{i\hbar}E_{21} - \gamma_{12}\Big]\rho_{21}^{(n+1)} - \frac{1}{i\hbar}(\rho_{11}^{(n)} - \rho_{22}^{(n)})M_{21}E(t) \\ &- \frac{1}{i\hbar}(M_{22} - M_{11})E(t)\rho_{21}^{(n)}. \qquad (6.17)\end{aligned}$$

Following an analogous procedure, we can obtain similar expressions:

$$\begin{aligned}\frac{\partial \rho_{12}^{(n+1)}}{\partial t} &= \Big[\frac{1}{i\hbar}E_{12} - \gamma_{21}\Big]\rho_{12}^{(n+1)} - \frac{1}{i\hbar}(\rho_{22}^{(n)} - \rho_{11}^{(n)})M_{12}E(t) \\ &- \frac{1}{i\hbar}(M_{11} - M_{22})E(t)\rho_{21}^{(n)}). \qquad (6.18)\end{aligned}$$

and

$$\frac{\partial \rho_{22}^{(n+1)}}{\partial t} = -\gamma_{22}\rho_{22}^{(n+1)} - \frac{1}{i\hbar}(M_{21}\rho_{12}^{(n)} - M_{12}\rho_{21}^{(n)})\tilde{E}(t), \qquad (6.19)$$

and also

$$\frac{\partial \rho_{11}^{(n+1)}}{\partial t} = -\gamma_{11}\rho_{11}^{(n+1)} - \frac{1}{i\hbar}(M_{12}\rho_{21}^{(n)} - M_{21}\rho_{12}^{(n)})\tilde{E}(t), \tag{6.20}$$

In the **last** equations we have that $M_{11} = \langle 1|\hat{M}|1\rangle$, $M_{12} = \langle 1|\hat{M}|2\rangle$, $M_{21} = \langle 2|\hat{M}|1\rangle$, and $M_{22} = \langle 2|\hat{M}|2\rangle$. Equations (6.17 – 6.20) can be solved by writing the density matrix elements in terms of sums proportional to $\exp(\pm i\omega t)$ and equating terms in both sides of the equations with same temporal dependence. In this calculations we neglect terms that correspond to higher harmonics which correspond to successive absorption and emissions of photons. We are only interested in the steady state, therefore the nth order perturbative term, $\rho^{(n)}$, is written as

$$\hat{\rho}^{(n)}(t) = \hat{\tilde{\rho}}^{(n)}(\omega)e^{-i\omega t} + \hat{\tilde{\rho}}^{(n)}(-\omega)e^{i\omega t} \tag{6.21}$$

which is valid for odd n. When n is even, only DC terms are dominant.

If we set n=1 en equation (6.21) we have

$$\hat{\rho}^{(1)}(t) = \hat{\tilde{\rho}}^{(1)}(\omega)e^{-i\omega t} + \hat{\tilde{\rho}}^{(1)}(-\omega)e^{i\omega t} \tag{6.22}$$

and taking n=0 in (6.17) we have an equation for $\rho_2^{(1)}1(t)$ as,

$$\frac{\partial \rho_{21}^{(1)}}{\partial t} = \left[\frac{1}{i\hbar}E_{21} - \gamma_{12}\right]\rho_{21}^{(1)} - \frac{1}{i\hbar}\left[(\rho_{11}^{(0)} - \rho_{22}^{(0)})M_{21}E(t) + (M_{22} - M_{11})E(t)\rho_{21}^{(0)}\right] \tag{6.23}$$

Remembering that $\rho_{21}^{(0)} = 0$, we obtain

$$\frac{\partial \rho_{21}^{(1)}}{\partial t} = \left[\frac{1}{i\hbar}E_{21} - \gamma_{12}\right]\rho_{21}^{(1)} - \frac{1}{i\hbar}(\rho_{11}^{(0)} - \rho_{22}^{(0)})M_{21}\tilde{E}(t). \tag{6.24}$$

Therefore we can replace equations (6.2) and (6.22) to solve the last equation. After performing some algebraic steps and equating coefficients of $\exp(i\omega t)$, we have

$$-i\omega\tilde{\rho}_{21}^{(1)}(\omega) = \left[\frac{1}{i\hbar}E_{21} - \gamma_{12}\right]\tilde{\rho}_{21}^{(1)}(\omega) - \frac{1}{i\hbar}(\rho_{11}^{(0)} - \rho_{22}^{(0)})M_{21}\tilde{E}(t), \tag{6.25}$$

which enables us to obtain $\tilde{\rho}_{ba}^{(1)}(\omega)$ so

$$\tilde{\rho}_{21}^{(0)}(\omega) = \frac{\tilde{E}M_{21}(\rho_{11}^{(0)} - \rho_{22}^{(0)})}{(E_{21} - \hbar\omega - i\hbar\gamma_{12})}. \tag{6.26}$$

Now, our task to calculate the term $\tilde{\rho}_{21}^{(3)}(\omega)$. For that purpose we must choose $n = 2$ in equation (6.17)

$$\frac{\partial \rho_{21}^{(3)}}{\partial t} = \left[\frac{1}{i\hbar}E_{21} - \gamma_{12}\right]\rho_{21}^{(3)} - \frac{1}{i\hbar}\left[(\rho_{11}^{(2)} - \rho_{22}^{(2)})M_{21}E(t) + (M_{22} - M_{11})E(t)\rho_{21}^{(2)}\right] \tag{6.27}$$

At the same time we take $n = 3$ in equation (6.21) to get

$$\rho^{(3)}(t) = \hat{\tilde{\rho}}^{(3)}(\omega)e^{-i\omega t} + \hat{\tilde{\rho}}^{(3)}(-\omega)e^{i\omega t} \tag{6.28}$$

Right now we proceed as before, replacing equations (6.2) and (6.28) in (6.27) and equating terms of $\exp(-i\omega t)$. We also clarify that the terms $\rho_{11}^{(2)}(t)$, $\rho_{22}^{(2)}(t)$, and $\rho_{21}^{(2)}(t)$, are rectification terms that do not change in time and we can directly replace them by $\tilde{\rho}_{11}^{(2)}(0)$, $\tilde{\rho}_{22}^{(2)}(0)$, and $\tilde{\rho}_{21}^{(2)}(0)$ respectively, therefore

$$-i\omega\tilde{\rho}_{21}^{(3)}(\omega) = \left[\frac{1}{i\hbar}E_{21} - \gamma_{12}\right]\tilde{\rho}_{21}^{(3)}(\omega) - \frac{1}{i\hbar}\left[(\tilde{\rho}_{11}^{(2)}(0) - \tilde{\rho}_{22}^{(2)}(0))M_{21}\tilde{E} + (M_{22} - M_{11})\tilde{E}\tilde{\rho}_{21}^{(2)}(0)\right] \tag{6.29}$$

Manipulating this equation allows us to obtain $\tilde{\rho}_{21}^{(3)}(\omega)$ as

$$\tilde{\rho}_{21}^{(3)}(\omega) = \frac{\tilde{E}}{E_{21} - \hbar\omega - i\hbar\gamma_{12}}\left[(\tilde{\rho}_{11}^{(2)}(0) - \tilde{\rho}_{22}^{(2)}(0))M_{21} + (M_{22} - M_{11})\tilde{\rho}_{21}^{(2)}(0)\right] \tag{6.30}$$

Our target is to find the difference $(\tilde{\rho}_{11}^{(2)}(0) - \tilde{\rho}_{22}^{(2)}(0))$. We must use equations (6.19) and (6.20) to accomplish this. So,

$$\frac{\partial \rho_{22}^{(2)}}{\partial t} = -\gamma_{22}\rho_{22}^{(2)} - \frac{1}{i\hbar}(M_{21}\rho_{12}^{(1)} - M_{12}\rho_{21}^{(1)})E(t). \tag{6.31}$$

and

$$\frac{\partial \rho_{11}^{(2)}}{\partial t} = -\gamma_{11}\rho_{11}^{(2)} - \frac{1}{i\hbar}(M_{12}\rho_{21}^{(1)} - M_{21}\rho_{12}^{(1)})E(t). \tag{6.32}$$

Focusing in equation (6.32)and knowing that $\rho_{11}^{(2)}$ is a rectification term, we have that $\frac{\partial \rho_{11}^{(2)}}{\partial t} = 0$. We also have to replace $\rho_{21}^{(1)}$ and $\rho_{12}^{(1)}$ by their steady components, i.e, taking $t = 0$ in equation (6.22). As well, we take the DC component of $E(t)$, $\tilde{E}$, then

$$0 = -\gamma_{11}\rho_{11}^{(2)}(0) - \frac{\tilde{E}}{i\hbar}\left[M_{12}(\tilde{\rho}_{21}^{(1)}(\omega) + \tilde{\rho}_{21}^{(1)}(-\omega)) - M_{21}(\tilde{\rho}_{12}^{(1)}(-\omega) + \tilde{\rho}_{12}^{(1)}(\omega))\right] \tag{6.33}$$

The terms $\tilde{\rho}_{21}^{(1)}(\omega)$ and $\tilde{\rho}_{21}^{(1)}(-\omega)$ are known as non-resonant terms which can be calculated in the same manner of equation (6.26). They are given by

$$\tilde{\rho}_{21}^{(3)}(-\omega) = \frac{\tilde{E}M_{21}(\rho_{11}^{(0)} - \rho_{22}^{(0)})}{(\hbar E_{21} + \hbar\omega - i\hbar\gamma_{ab})} \tag{6.34}$$

and

$$\tilde{\rho}_{12}^{(3)}(\omega) = \frac{\tilde{E}M_{21}(\rho_{11}^{(0)} - \rho_{22}^{(0)})}{(\hbar E_{21} + \hbar\omega + i\hbar\gamma_{ab})} \tag{6.35}$$

As we can see, these last two terms present a dependence of $\hbar E_{21}+\hbar\omega$ in their denominators, that cannot have the possibility of entering in resonance in any time. By this fact, we will neglect them in the rest of our calculations, then

$$0 = -\gamma_{11}\tilde{\rho}_{11}^{(2)}(0) - \frac{\tilde{E}}{i\hbar}\Big[M_{12}\tilde{\rho}_{21}^{(1)}(\omega) - M_{21}\tilde{\rho}_{12}^{(1)}(-\omega)\Big] \tag{6.36}$$

Manipulating this expression we obtain $\tilde{\rho}_{aa}^{(2)}(0)$ as

$$\tilde{\rho}_{11}^{(2)}(0) = \frac{i\tilde{E}}{\gamma_{11}\hbar}\Big[M_{12}\tilde{\rho}_{21}^{(1)}(\omega) - M_{21}\tilde{\rho}_{12}^{(1)}(-\omega)\Big] \tag{6.37}$$

Now, we need to replace $\tilde{\rho}_{21}^{(1)}(\omega)$, which is given by (6.26) and $\tilde{\rho}_{12}^{(1)}(-\omega)$ that can be obtained in the same way as (6.26) or simply replacing $\omega \to -\omega$ in equation (6.35). After replacing the mentioned expressions and doing some mathematical steps we have

$$\tilde{\rho}_{11}^{(2)}(0) = -\frac{2\tilde{E}^2|M_{21}|^2(\rho_{11}^{(0)}) - \rho_{22}^{(0)})\gamma_{12}}{\gamma_{12}\Big[(E_{21} - \hbar\omega)^2 + (\hbar\gamma_{12})^2\Big]} \tag{6.38}$$

Following a similar procedure and noting that $|M_{21}|^2 = |M_{12}|^2$ and $\gamma_{12} = \gamma_{21}$, we can find $\tilde{\rho}_{22}^{(2)}(0)$ as

$$\tilde{\rho}_{22}^{(2)}(0) = \frac{2\tilde{E}^2|M_{12}|^2(\rho_{11}^{(0)} - \rho_{22}^{(0)})\gamma_{12}}{\gamma_{22}\Big[(E_{21} - \hbar\omega)^2 + (\hbar\gamma_{12})^2\Big]} \tag{6.39}$$

where $|M_{21}|^2 = M_{21}M_{12}$.
Finally, using (6.38) and (6.39), we arrive at

$$\tilde{\rho}_{11}^{(2)}(0) - \tilde{\rho}_{22}^{(2)}(0) = -2\tilde{E}^2\left(\frac{1}{\gamma_{11}} + \frac{1}{\gamma_{22}}\right)\frac{|M_{12}|^2(\rho_{11}^{(0)}) - \rho_{22}^{(0)})\gamma_{12}}{\Big[(E_{21} - \hbar\omega)^2 + (\hbar\gamma_{12})^2\Big]} \tag{6.40}$$

Lets obtain now $\tilde{\rho}_{ba}^{(2)}$. We must use (6.16) with $n = 1$ and remembering that we are only interested in steady terms. Then

$$\begin{aligned}\frac{\partial \rho_{ba}^{(2)}(0)}{\partial t} &= \Big[\frac{1}{i\hbar}E_{21} - \gamma_{12}\Big]\rho_{21}^{(2)}(0) - \frac{1}{i\hbar}(\rho_{11}^{(1)}(0) - \rho_{22}^{(1)}(0))M_{21}\tilde{E} \\ &- \frac{1}{i\hbar}(M_{22} - M_{11})\tilde{E}\tilde{\rho}_{21}^{(1)}. \end{aligned} \tag{6.41}$$

Since $\frac{\partial \rho_{21}^{(2)}(0)}{\partial t} = 0$ and using (6.22) with $t = 0$, we obtain

$$\begin{aligned} 0 &= \Big[\frac{1}{i\hbar}E_{21} - \gamma_{12}\Big]\rho_{21}^{(2)}(0) - \frac{1}{i\hbar}\Big(\rho_{11}^{(1)}(\omega) + \rho_{11}^{(1)}(-\omega) - \rho_{22}^{(1)}(\omega) - \rho_{22}^{(1)}(-\omega)\Big)M_{21}\tilde{E} \\ &- \frac{1}{i\hbar}(M_{22} - M_{11})\tilde{E}(\tilde{\rho}_{21}^{(1)}(\omega) + \tilde{\rho}_{21}^{(1)}(-\omega)). \end{aligned} \tag{6.42}$$

Continuing with $\tilde{\rho}_{11}^{(1)}(\omega)$ from the use of (6.38) and taking $n = 0$, we have

$$\frac{\partial \rho_{11}^{(1)}}{\partial t} = -\gamma_{11}\rho_{11}^{(1)} - \frac{1}{i\hbar}(M_{12}\rho_{21}^{(0)} - M_{21}\rho_{12}^{(0)})E(t), \tag{6.43}$$

and emphasizing again that $\rho_{21}^{(0)} = \rho_{12}^{(0)} = 0$,

$$\frac{\partial \rho_{11}^{(1)}}{\partial t} = -\gamma_{11}\rho_{11}^{(1)}, \tag{6.44}$$

Once again, using (6.22) and equating terms of $\exp(i\omega t)$, it is possible to obtain

$$\tilde{\rho}_{11}^{(1)}(\omega)(\gamma_{11} - i\omega) = 0, \tag{6.45}$$

which implies that $\tilde{\rho}_{11}^{(1)}(\omega) = 0$. In the same way $\tilde{\rho}_{11}^{(1)}(-\omega) = \tilde{\rho}_{22}^{(1)}(\omega) = \tilde{\rho}_{22}^{(1)}(-\omega) = 0$.

With these last results and neglecting the non-resonant term $\tilde{\rho}_{21}^{(1)}(-\omega)$ we have

$$0 = \Big[\frac{1}{i\hbar}E_{21} - \gamma_{12}\Big]\tilde{\rho}_{21}^{(2)}(0) - \frac{\tilde{E}}{i\hbar}(M_{22} - M_{11})\tilde{\rho}_{21}^{(1)}(\omega). \tag{6.46}$$

Manipulating this expression we obtain $\tilde{\rho}_{ba}^{(2)}(0)$, and replacing (6.26),

$$\tilde{\rho}_{21}^{(2)} = \frac{\tilde{E}^2 M_{21}(M_{22} - M_{11})(\rho_{11}^{(0)}) - \rho_{22}^{(0)})}{(E_{21} - i\hbar\gamma_{12})(E_{21} - \hbar\omega - i\hbar\gamma_{12})}. \tag{6.47}$$

Replacing (6.40) and (6.47) in equation (6.30) and performing some mathematical steps we finally arrive at

$$\begin{aligned}\tilde{\rho}_{21}^{(3)}(\omega) &= \frac{\tilde{E}\tilde{E}^2 M_{21}(\rho_{11}^{(0)}-\rho_{22}^{(0)})}{(E_{21}-\hbar\omega-i\hbar\gamma_{12})}\Big[2\frac{(1/\gamma_{11}+1/\gamma_{22})|M_{12}|^2\gamma_{12}}{(E_{21}-\hbar\omega)^2+(\hbar\gamma_{12})^2} \\ &- \frac{(M_{22}-M_{11})^2}{(E_{21}-i\hbar\gamma_{12})(E_{21}-\hbar\omega-i\hbar\gamma_{12})}\Big]. \end{aligned} \tag{6.48}$$

In the spirit of the last derivations, and using previous results, it is possible to calculate the terms $\tilde{\rho}_{22}^{(3)}(\omega)$ and $\tilde{\rho}_{11}^{(3)}(\omega)$. However, such terms, as is mentioned in the work of Ahn and Chuang [2] are negligible at the time of evaluating the third order absorption coefficient. These terms are

$$\tilde{\rho}_{22}^{(3)}(\omega) = \frac{2i\tilde{E}\tilde{E}^2|M_{21}|^2}{(\hbar\omega+i\hbar\gamma_{22})}\Im\left[\frac{(M_{22}-M_{11})(\rho_{11}^{(0)}-\rho_{22}^{(0)})}{(E_{21}-i\hbar\gamma_{12})(E_{21}-\hbar\omega-i\hbar\gamma_{12})}\right] \tag{6.49}$$

and

$$\tilde{\rho}_{11}^{(3)}(\omega) = -\frac{2i\tilde{E}\tilde{E}^2|M_{21}|^2}{(\hbar\omega+i\hbar\gamma_{11})}\Im\left[\frac{(M_{22}-M_{11})(\rho_{11}^{(0)}-\rho_{22}^{(0)})}{(E_{21}-i^{-}h\gamma_{12})(E_{21}-{}^{-}h\omega-i^{-}h\gamma_{12})}\right] \tag{6.50}$$

Here, $\Im$ denotes imaginary part.

6.3 Linear and non-linear absorption coefficients

With the results of the last section we can calculate the linear and non-linear absorption coefficients in quantum systems. The electronic polarization $P(t)$ and the optical susceptibility $\chi(t)$ which arise as consequence of the optical field $E(t)$ can be expressed through the dipolar operator $\hat{M}$ and the density matrix as

$$P(t) = \epsilon_0\chi(\omega)\tilde{E}e^{-i\omega t} + \epsilon_0\chi(-\omega)\tilde{E}e^{i\omega t} = \frac{1}{V}Tr(\tilde{\rho}\tilde{M}), \tag{6.51}$$

where V is the volume of the system, ϵ_0 is the permittivity of the vacuum and Tr denotes the trace over the diagonal elements of the matrix $\tilde{\rho}\tilde{M}$. The susceptibility χ is related with the absorption coefficient $\alpha(\omega)$ as

$$\alpha(\omega) = \omega\sqrt{\frac{\mu}{\epsilon_R}}\Im(\epsilon_0\chi(\omega)) \tag{6.52}$$

where μ is the permeability of the system, ϵ_R is the real part of the permittivity and $\chi(\omega)$ is the Fourier component of $\chi(t)$ with dependence $\exp(?i\omega t)$. We can write the polarization as

$$P(t) = \frac{1}{V}\Big[\langle 1|\tilde{\rho}\tilde{M}|1\rangle + \langle 2|\tilde{\rho}\tilde{M}|2\rangle\Big]. \tag{6.53}$$

Introducing the completeness relation and using (6.4), we have

$$P(t) = \frac{1}{V}\sum_n \Big[\rho_{11}^{(n)} M_{11} + \rho_{12}^{(n)} M_{21} + \rho_{21}^{(n)} M_{12} + \rho_{22}^{(n)} M_{22}\Big]. \tag{6.54}$$

With the aid of (6.21)

$$P(t) = \frac{1}{V}\sum_n \left[\tilde{\rho}_{11}^{(n)}(\omega) M_{11} + \tilde{\rho}_{12}^{(n)}(\omega) M_{21} + \tilde{\rho}_{21}^{(n)}(\omega) M_{12} + \tilde{\rho}_{22}^{(n)}(\omega) M_{22}\right] e^{-i\omega i} \quad \varpi. \tag{6.55}$$

Choosing $n = 1$, using (6.51), taking away the non-resonant term, equating terms of $e^{-i\omega t}$ and remembering that $\tilde{\rho}_{11}^{(1)}(\omega) = \tilde{\rho}_{22}^{(1)}(\omega) = 0$, allow us to write

$$\epsilon_0 \chi^{(1)}(\omega)\tilde{E} = \frac{1}{V}\tilde{\rho}_{21}^{(1)}(\omega) M_{12} \tag{6.56}$$

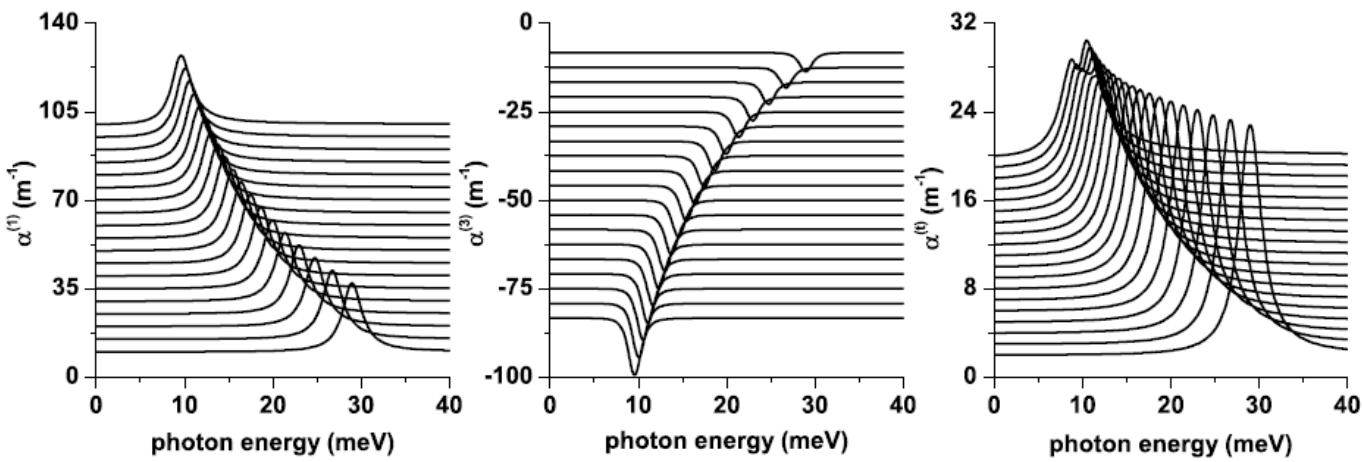

Figure 6.1: The optical absorption coefficients calculated as a function of the incident photon energy and the width of the square GaAs-AlGaAs quantum well, for linear polarization. In (a) linear absorption coefficients $\alpha^{(1)}$, (b) nonlinear absorption coefficients $\alpha^{(3)}$, (c) total absorption coefficients $\alpha^{(t)}$.

Solving for $\epsilon_0\chi^{(1)}(\omega)$, replacing (6.26), taking its imaginary part and using (6.52), we have,

$$\alpha^{(1)}(\omega) = \omega\sqrt{\frac{\mu}{\epsilon_R}}\frac{|M_{12}|^2}{V}\frac{(\rho_{11}^{(0)} - \rho_{22}^{(0)})\hbar\gamma_{12}}{(E_{21} - \hbar\omega)^2 + (\hbar\gamma_{12})^2} \tag{6.57}$$

Defining $\sigma_v = (\rho_{11}^{(0)} - \rho_{22}^{(0)})/V$ as the three-dimensional concentration of electrons in the system, we have

$$\alpha^{(1)}(\omega) = \omega\sqrt{\frac{\mu}{\epsilon_R}}\frac{|M_{12}|^2\sigma_v\hbar\gamma_{12}}{(E_{21} - \hbar\omega)^2 + (\hbar\gamma_{12})^2} \tag{6.58}$$

Following a similar procedure we can find a third-order expression, we are able to begin with

$$\epsilon_0\chi^{(3)}(\omega)\tilde{E} = \frac{1}{V}\left[\tilde{\rho}_{11}^{(3)}(\omega)M_{11} + \tilde{\rho}_{12}^{(3)}(\omega)M_{21} + \tilde{\rho}_{21}^{(3)}(\omega)M_{12} + \tilde{\rho}_{22}^{(3)}(\omega)M_{22}\right] \tag{6.59}$$

Neglecting the non-resonant term $\tilde{\rho}_{ab}^{(3)}(\omega)$, remembering that, as we said before, the terms $\tilde{\rho}_{aa}^{(3)}(\omega)$ and $\tilde{\rho}_{bb}^{(3)}(\omega)$ just induce a small contribution that we can avoid in our calculations. Solving for $\epsilon_0\chi^{(3)}(\omega)$, replacing equation (6.48), taking its imaginary part and using (6.52), we can obtain

$$\alpha^{(3)}(\omega, I) = -\omega\sqrt{\frac{\mu}{\epsilon_R}}\tilde{E}^2|M_{12}|^2\sigma_v$$

$$\Im\left[\frac{1}{(E_{21} - \hbar\omega - i\hbar\gamma_{12})}\left\{\frac{2\gamma_{12}(\gamma_{11} + \gamma_{22})|M_{12}|^2}{\gamma_{11}\gamma_{22}[(E_{21} - \hbar\omega)^2 + (\hbar\gamma_{12})^2]} - \frac{(M_{22} - M_{11})^2}{(E_{21} - i\hbar\gamma_{12})(E_{21} - \hbar\omega - i\hbar\gamma_{12})}\right\}\right]. \tag{6.60}$$

Defining the intensity I of the electromagnetic field through the equation

$$\tilde{E}^2 = \frac{I}{2\epsilon_0 n_r c} \tag{6.61}$$

where c is the speed of light of the vacuum and n_r is the refractive index of the medium, we have

In the second line of the previous equation two terms clearly can be identified. The first one is proportional to the fourth power of the inter level matrix element, whereas the second term depends of the difference between the intra level matrix elements. This second part goes to zero for symmetric heterostructures whereas is finite when

asymmetries are included via changes in the composition, via boundary conditions or via effects of external proves. Note that the third order correction depends of the intensity of the incident radiation. And that for zero energy of the incident photon also goes to zero in the same way observed for the first order term correction.

$$\alpha^{(3)}(\omega, I) = -\omega\sqrt{\frac{\mu}{\epsilon_R}}\frac{I}{2\epsilon_0 n_r c}|M_{12}|^2\sigma_\upsilon$$

$$\Im\left[\frac{1}{(E_{21}-\hbar\omega-i\hbar\gamma_{12})}\left\{\frac{2\gamma_{12}(\gamma_{11}+\gamma_{22})|M_{12}|^2}{\gamma_{11}\gamma_{22}[(E_{21}-\hbar\omega)^2+(\hbar\gamma_{12})^2]}\frac{(M_{22}-M_{11})^2}{(E_{21}-i\hbar\gamma_{12})(E_{21}-\hbar\omega-i\hbar\gamma_{12})}\right\}\right]. \tag{6.62}$$

As a fact of simplicity, lets choose $\gamma_{11} = \gamma_{22}$, which implies that $\gamma_{122} = \gamma_{11} = \gamma_{22}$, so

$$\frac{\gamma_{12}(\gamma_{11}+\gamma_{22})}{\gamma_{11}\gamma_{22}} = 2. \tag{6.63}$$

Taking the imaginary part of equation (6.62) and performing a lengthly algebra leads to a more manageable expression for the third-order absorption coefficient as

$$\begin{aligned}\alpha^{(3)}(\omega, I) &= -\omega\sqrt{\frac{\mu}{\epsilon_R}}\frac{I}{2\epsilon_0 n_r c}\frac{|M_{12}|^2\sigma_\upsilon\hbar\gamma_{12}}{[(E_{21}-\hbar\omega)^2+(\hbar\gamma_{12})^2]^2} \qquad (6.64)\\ &\times \left[4|M_{12}|^2 - \frac{(M_{22}-M_{11})^2(3E_{21}^2-4\hbar\omega E_{21}+\hbar^2(\omega^2-\gamma_{12}^2))}{E_{21}^2+(\hbar\gamma_{12})^2}\right]\end{aligned}$$

With (6.58) and (6.63), the optical absorption coefficient is given by

$$\alpha^{(t)}(\omega, I) = \alpha^{(1)}(\omega) + \alpha^{(3)}(\omega, I). \tag{6.65}$$

6.4 Linear and non-linear changes in the refractive index

In order to calculate the changes in the refractive index, we follow a procedure which is analogous to the one of the last section. In this time, we start with the fact that the change in the refractive index is related with the optical susceptibility through the equation

$$\frac{\Delta n(\omega)}{n_r} = \Re\left(\frac{\chi(\omega)}{2\,n_r^2}\right). \tag{6.66}$$

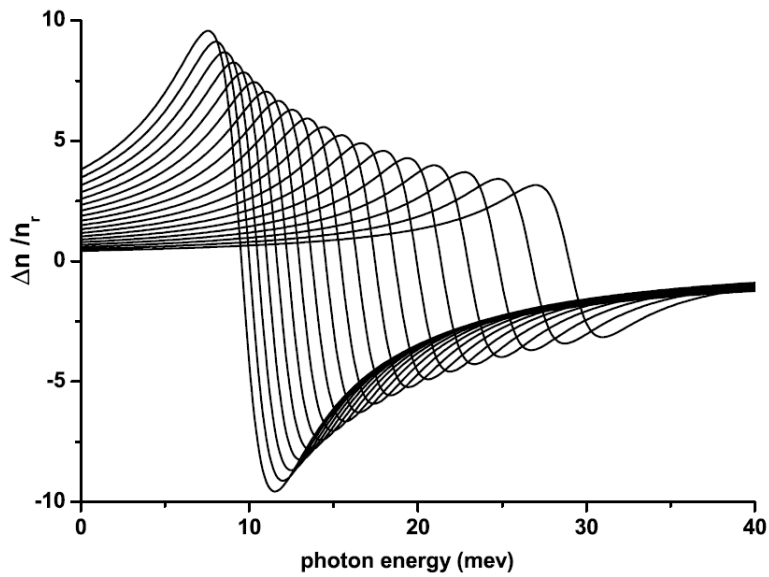

Figure 6.2: The total change in the refractive index coefficients calculated as a function of the incident photon energy and the width of the square GaAs-AlGaAs quantum well, for linear polarization.

Using equation (6.56), introducing the previous definitions and taking the real part of the expressions, allow us to find an expression for the linear change in the refractive index, therefore

$$\frac{\Delta n^{(1)}(\omega)}{n_r} = \frac{\sigma_\upsilon\,|M_{12}|^2}{2\,n_r^2\,\varepsilon_0}\frac{E_{21}-\hbar\,\omega}{(E_{21}-\hbar\,\omega)^2+(\hbar\,\gamma_{12})^2} \tag{6.67}$$

Lets calculate now the third order correction to the change in the refractive index parting from equation (6.59), which after the preliminary considerations, can be written as

$$\chi^{(3)}(\omega) = \frac{1}{V\tilde{E}\epsilon_0}\tilde{\rho}_{21}^{(3)}(\omega)M_{21}. \tag{6.68}$$

Using (6.48) and (6.68) in (6.66) and taking into account the definitions for σ_υ and I, we obtain

$$\Delta n^{(3)}(\omega) = -I|M_{12}|^2\sigma_\upsilon$$

$$n_r \qquad 4n_r^3\epsilon_0 c$$

$$\Re\left\{\frac{E_{21}-\hbar\omega-i\hbar\gamma_{12}}{[(E_{21}-\hbar\omega)^2+(\hbar\gamma_{12})^2]^2}\times\left[4|M_{12}|^2-\frac{(M_{22}-M_{11})^2(E_{21}^2+i\hbar\gamma_{12})(E_{21}-\hbar\omega+i\hbar\gamma_{12})}{E_{21}^2+(\hbar\gamma_{12})^2}\right]\right\}. \tag{6.69}$$

If use the relation $c^2 = 1/\varepsilon_0\mu$ and manipulate the equation through

a long algebra, we can arrive at

$$\frac{\Delta n^{(3)}(\omega)}{n_r} = \frac{|M_{12}|^2\sigma_v}{4n_r^3\epsilon_0 c}\frac{\mu c I}{[(E_{21}-\hbar\omega)^2+(\hbar\gamma_{12})^2]^2}\Big[4(E_{21}-\hbar\omega)|M_{12}|^2 - \frac{(M_{22}-M_{11})^2}{E_{21}^2+(\hbar\gamma_{12})^2} \times \{(E_{21}-\hbar\omega)[E_{21}(E_{21}-\hbar\omega)-(\hbar\gamma_{12})^2]-(\hbar\gamma_{12})^2[2E_{21}-\hbar\omega]\}\Big] \tag{6.70}$$

Therefore, the total change in the refractive index is given by

$$\frac{\Delta n(\omega,I)}{n_r} = \frac{\Delta n^{(1)}(\omega)}{n_r} + \frac{\Delta n^{(3)}(\omega,I)}{n_r} \tag{6.71}$$

6.5 Non-linear optical rectification, second and third harmonic generator

In Eqs. 6.72, 6.73 and 6.74 are shown the expressions for the non linear optical rectification (NOR), second harmonic generator (SHG) and third harmonic generator(THG) optical properties, with the radiation polarization taken in the z-direction following Rosencher et al. [1], this are obtained by means of the compact density matrix formalism. We use the energy structure consists of two for NOR, and three and four levels intrasubband transitions for SHG and THG,respectively.

$$\chi_0^{(2)} = \frac{4\,e^3\,\rho_v}{\varepsilon_0\,\hbar^2}\,\mu_{01}^2\,\delta_{01}\,\frac{\omega_{10}^2\,(1+\Gamma_2/\Gamma_1)+(\omega^2+\Gamma_2^2)(\Gamma_2/\Gamma_1-1)}{[(\omega_{10}-\omega)^2+\Gamma_2^2]\,[(\omega_{10}+\omega)^2+\Gamma_2^2]}\,, \tag{6.72}$$

$$\chi_{2\omega}^{(2)} = \frac{e^3\,\rho_v}{\varepsilon_0\,\hbar^2}\,\frac{M_{10}\,M_{20}\,M_{12}}{(\omega-\omega_{01}-i\,\Gamma)(2\omega-\omega_{20}-i\,\Gamma/2)}\,, \tag{6.73}$$

$$\chi_{3\omega}^{(3)} = \frac{e^4\,\rho_v}{\varepsilon_0\,\hbar^3}\,\frac{M_{10}\,M_{30}\,M_{12}\,M_{23}}{(\omega-\omega_{01}-i\,\Gamma)(2\omega-\omega_{20}-i\,\Gamma/2)}\frac{1}{(3\omega-\omega_{30}-i\,\Gamma/3)} \tag{6.74}$$

Parameters used in these equations are defined as: ρ_v is the electronic density, $M_{ij} = \langle\psi_i|e\,z|\phi_j\rangle$, $(i,j=1,2,3,4)$ is the off-diagonal matrix element, $\omega_{ij} = (E_i - E_j)/\hbar$, $(i,j=1,2,3,4)$ is the frequency associated with the transition energies, and Γ is the damping term associated with the lifetime of the electrons involved in the transitions. Note that in the expressions obtained can infer the presence of resonant peaks in optical properties coefficients when the photon energy

coincides with the transition energy between the two states involved and exactly at the same energy value, the change of refractive index it will always be zero.

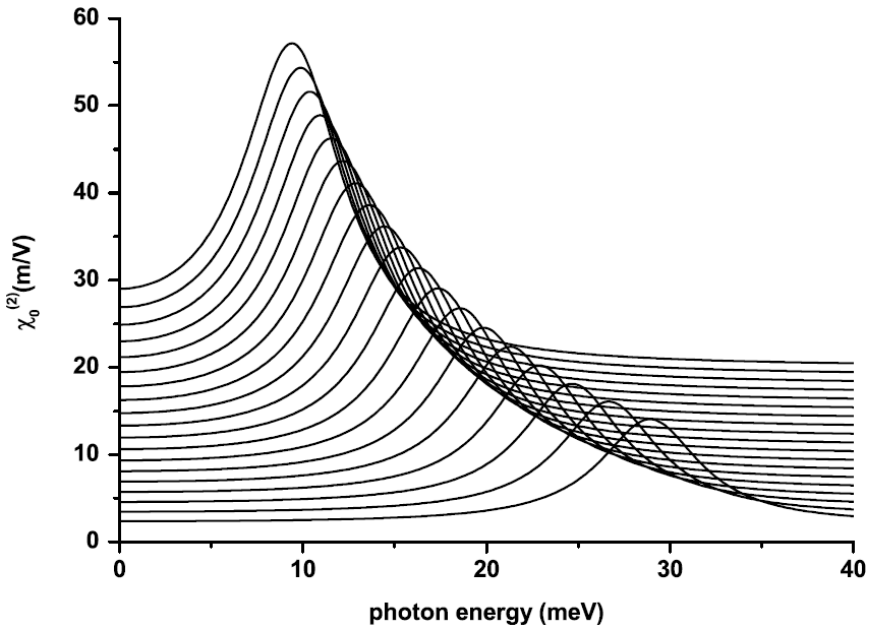

Figure 6.3: The nonlinear optical rectification coefficients calculated as a function of the incident photon energy and the width of the square GaAs-AlGaAs quantum well, for linear polarization.

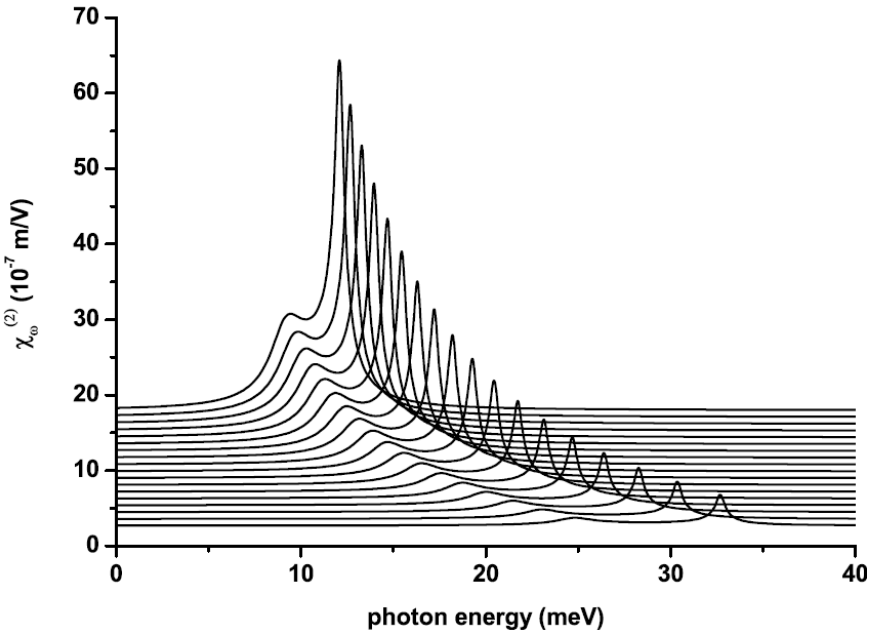

Figure 6.4: The second harmonic generator (SHG) calculated as a function of the incident photon energy and the width of the square GaAs-AlGaAs quantum well, for linear polarization.

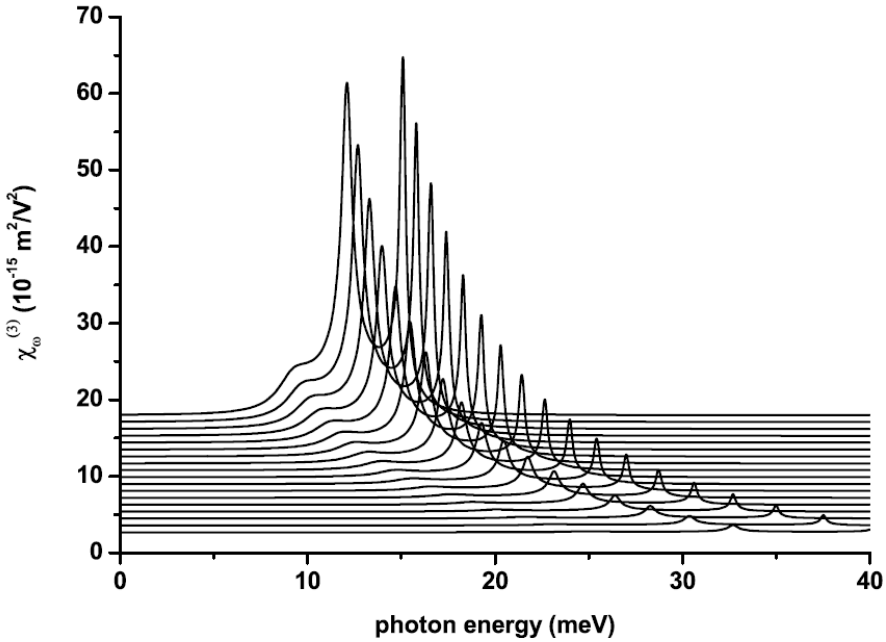

Figure 6.5: The third harmonic generator (TGH) calculated as a function of the incident photon energy and the width of the square GaAs-AlGaAs quantum well, for linear polarization.

References

[1] E. Rosencher, P. Bois, Phys. Rev. B 14 (1991), p. 11315.

[2] D. Ahn, S. Chuang, IEEEJ. Quantum Electron QE-23 (1987), p. 2169.

[3] Wen Xiong, Electronic structure and intersubband magnetoabsorption spectra of CdSe/CdS core-shell nanowires, Superlattices and Microstructures, vol. 98, pp. 158-173, 2016.

[4] M. Zavvari, K. Abedi, A. Yusefli, M. Karimi, Proposal of a quantum ring intersubband photodetector integrated with avalanche multiplication region for high performance detection of far infrared, Optik - International Journal for Light and Electron Optics, vol. 126, no. 19, pp. 1861-1864, 2015.

[5] N. Zeiri, N. Sfina, S. Abdi-Ben Nasrallah, J.-L. Lazzari, M. Said, Intersubband transitions in quantum well mid-infrared photodetectors, Infrared Physics and Technology, vol. 60, pp. 137-144, 2013.

[6] P. Bhattacharya and Z. Mi, Quantum-Dot Optoelectronic Devices, Proceedings of the IEEE, vol. 95, no. 9 pp. 1723-1740, 2007.

[7] F. M. S. Lima, M. A. Amato, O. A. C. Nunes, A. L. A. Fonseca, B. G. Enders, E. F. da Silva, Jr., J. Appl. Phys. 105 (2009), p. 123111

[8] P. F. Yuh and K. L. Wang, Optical transitions in a step quantum well, J. Appl. Phys. 65, pp. 4377 (1989)

[9] Hao Feng, Kunio Tada, Field-Induced Optical Effect in a Five-Step Asymmetric Coupled Quantum Well with Modified Potential, IEEE Journal Of Quantum Electronics, Vol. 34, No. 7, July 1998 Pp. 1197

[10] E. Kasapoglu, I. Sokmen, The effects of intense laser field and electric field on intersubband absorption in a double-graded quantum well, Physica B 403 (2008) pp. 3746–750

[11] E. Ozturk, I. Sokmen, Effect of magnetic fields on the linear and nonlinear intersubband optical absorption coefficients and refractive index changes in square and graded quantum wells, Superlattices and Microstructures 48 (2010) pp. 312–320

[12] F. Ungan, R. L. Restrepo, M. E. Mora-Ramos, A. L. Morales, C. A. Duque, Intersubband optical absorption coefficients and refractive index changes in a graded quantum well under intense laser field: Effects of hydrostatic pressure, temperature and electric field, Physica B 434 (2014) pp. 26-31

[13] H. Dakhlaoui, The effects of doping layer location on the electronic and optical properties of GaN step quantum well, Superlattices and Microstructures 97 (2016) pp. 439-447

Study of delta-doped quantum wells

Energy levels and applications in the terahertz region

First Edition

Quantum wells, quantum wires, quantum dots. These are terms that have become familiar not only to specialists in physics and semiconductor technology but also to the common public. But these structures of nanoscopic dimensions appeared several decades ago in the vision of renowned specialists in these materials and, as a reality, after it was possible to develop epitaxial crystal growth techniques and methodologies that allow ultra-precise control of the deposition of atomic monolayers. The 1980s witnessed a steady increase in research work on these structures. The subsequent decades have seen the consolidation of a branch that has redefined solid-state physics and, in particular, semiconductor physics. Although these three classes of systems began to be studied, at least from a theoretical point of view, almost simultaneously, the attention of the first years was much more inclined towards quantum wells.

©2022 Editorial Instituto Antioqueño de Investigación
Medellín – Antioquia